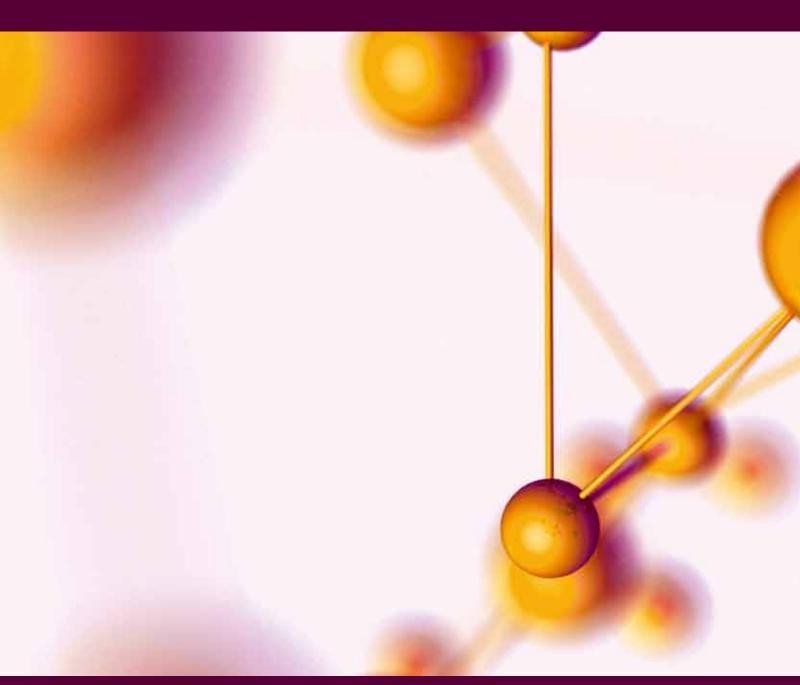
Accurate Potential Energy Surfaces and Beyond: Chemical Reactivity, Binding, Long-Range Interactions, and Spectroscopy

Guest Editors: Laimutis Bytautas, Joel M. Bowman, Xinchuan Huang, and António J. C. Varandas



Accurate Potential Energy Surfaces and Beyond: Chemical Reactivity, Binding, Long-Range Interactions, and Spectroscopy

Accurate Potential Energy Surfaces and Beyond: Chemical Reactivity, Binding, Long-Range Interactions, and Spectroscopy

Guest Editors: Laimutis Bytautas, Joel M. Bowman, Xinchuan Huang, and António J. C. Varandas



Editorial Board

János G. Ángyán, France M. Sabry Abdel-Mottaleb, Egypt Taicheng An, China J. A. Anderson, UK Panos Argyrakis, Greece Ricardo Aroca, Canada Stephen H. Ashworth, UK Biman Bagchi, India Hans Bettermann, Germany Vasudevanpillai Biju, Japan Joel Bowman, USA Wybren J. Buma, The Netherlands Sylvio Canuto, Brazil Li Ming Dai, USA Michael Deleuze, Belgium Michael Dolg, Germany D. James Donaldson, Canada Ali Eftekhari, USA Gregory S. Ezra, USA Claudio Fontanesi, Italy Michael J. Frisch, USA Paul Geerlings, Belgium Robert Gerber, Israel Jinlong Gong, China David Wayne Goodman, USA Vicki H. Grassian, USA Lawrence Harding, USA David Brynn Hibbert, Germany Kimihiko Hirao, Japan Paul L. Houston, USA Jyh-Ping Hsu, Taiwan

F. Illas, Spain Kwang S. Kim, Republic of Korea Bernard Kirtman, USA Lowell D. Kispert, USA Marc Koper, The Netherlands Alexei A. Kornyshev, UK Yuan Kou, China David Logan, UK Clare M. McCabe, USA James K. McCusker, USA Michael L. McKee, USA Robert M. Metzger, USA Michael V. Mirkin, USA David Muddiman, USA Klaus Mullen, Germany Daniel Neuhauser, USA Konstantin Neyman, Spain Minh Tho Nguyen, Belgium Hiroshi Onishi, Japan Thomas Oppenlaender, Germany Samir K. Pal, India Leonardo Palmisano, Italy Francesco Paolucci, Italy Jan Skov Pedersen, Denmark Piotr Piecuch, USA M. P. Pileni, France Simon M. Pimblott, UK Oleg Prezhdo, USA Colin Raston, Australia Benjaram M. Reddy, India Ranko Richert, USA

Eli Ruckenstein, USA Gnther Rupprechter, Austria Kenneth Ruud, Norway Viktor A. Safonov, Russia Dennis Salahub, Canada Anunay Samanta, USA Dipankar Das Sarma, India Joop Schoonman, The Netherlands Stefan Seeger, Switzerland Tamar Seideman, USA Hiroshi Sekiya, Japan Luis Serrano-Andrés, Spain Michael D. Sevilla, USA C. David Sherrill, USA Kenneth Showalter, USA Karl Sohlberg, USA Miquel Solà, Spain Vasco Teixeira, Portugal Sergei Tretiak, USA Thanh N. Truong, USA Frantisek Turecek, USA P. Unwin, UK Eric Vauthey, Switzerland David Wales, UK Peter Wolynes, USA Qiang Xu, Japan Yigzaw G Yohanis, UK Jeffrey M. Zaleski, USA Ruhong Zhou, USA

Contents

Accurate Potential Energy Surfaces and Beyond: Chemical Reactivity, Binding, Long-Range Interactions, and Spectroscopy, Laimutis Bytautas, Joel M. Bowman, Xinchuan Huang, and António J. C. Varandas Volume 2012, Article ID 679869, 4 pages

The N··· HF Interactions in the X-Pyridazine··· (HF)₂ Complexes: Substituent Effects and Energy Components, Ali Ebrahimi, Mostafa Habibi-Khorassani, Farideh Badichi Akher, and Abdolkarim Farrokhzadeh Volume 2012, Article ID 362608, 9 pages

Potential Energy Surfaces for Reactions of X Metal Atoms (X = Cu, Zn, Cd, Ga, Al, Au, or Hg) with YH₄ Molecules (Y = C, Si, or Ge) and Transition Probabilities at Avoided Crossings in Some Cases, Octavio Novaro, María del Alba Pacheco-Blas, and Juan Horacio Pacheco-Sánchez Volume 2012, Article ID 720197, 17 pages

New *ab Initio* Potential Energy Surfaces for the Renner-Teller Coupled $1^1A'$ and $1^1A''$ States of CH_2 , Haitao Ma, Chunfang Zhang, Zhijun Zhang, Xiaojun Liu, and Wensheng Bian Volume 2012, Article ID 236750, 12 pages

Applications of Potential Energy Surfaces in the Study of Enzymatic Reactions, Eric A. C. Bushnell, WenJuan Huang, and James W. Gauld Volume 2012, Article ID 867409, 15 pages

Quantum Instanton Evaluations of the Thermal Rate Constants for Complex Systems, Yi Zhao and Wenji Wang

Volume 2012, Article ID 483504, 16 pages

Improved Potential Energy Surface of Ozone Constructed Using the Fitting by Permutationally Invariant Polynomial Function, Mehdi Ayouz and Dmitri Babikov Volume 2012, Article ID 951371, 9 pages

Potential Energy Surface of NO on Pt(997): Adsorbed States and Surface Diffusion, N. Tsukahara and J. Yoshinobu

Volume 2012, Article ID 571657, 9 pages

Exploring Multiple Potential Energy Surfaces: Photochemistry of Small Carbonyl Compounds, Satoshi Maeda, Koichi Ohno, and Keiji Morokuma Volume 2012, Article ID 268124, 13 pages

Ab Initio Potential Energy Surfaces for Both the Ground (\widetilde{X}^1A') and Excited (\widetilde{A}^1A'') Electronic States of HSiBr and the Absorption and Emission Spectra of HSiBr/DSiBr, Anyang Li, Sen Lin, and Daiqian Xie Volume 2012, Article ID 572148, 20 pages

Constructing Potential Energy Surfaces for Polyatomic Systems: Recent Progress and New Problems, J. Espinosa-Garcia, M. Monge-Palacios, and J. C. Corchado Volume 2012, Article ID 164752, 19 pages

Hindawi Publishing Corporation Advances in Physical Chemistry Volume 2012, Article ID 679869, 4 pages doi:10.1155/2012/679869

Editorial

Accurate Potential Energy Surfaces and Beyond: Chemical Reactivity, Binding, Long-Range Interactions, and Spectroscopy

Laimutis Bytautas, ¹ Joel M. Bowman, ² Xinchuan Huang, ³ and António J. C. Varandas ⁴

- ¹ Department of Chemistry, Rice University, Houston, TX 77005, USA
- ² Cherry L. Emerson Center for Scientific Computation and Department of Chemistry, Emory University, Atlanta, GA 30322, USA
- ³ SETI Institute and NASA Ames Research Center, MS 245-6, Moffett Field, CA 94035, USA

Correspondence should be addressed to Laimutis Bytautas, laimutis.bytautas@rice.edu

Received 13 February 2012; Accepted 13 February 2012

Copyright © 2012 Laimutis Bytautas et al. This is an open access article distributed under the Creative Commons Attribution License, which permits unrestricted use, distribution, and reproduction in any medium, provided the original work is properly cited.

1. Background

Beginning with the seminal paper of Born and Oppenheimer (BO) [1] in 1927, the concept of the potential energy surface (PES) plays a critical role in the description, simulation, and modeling of molecular systems. It provides the basis [2] for understanding the processes associated with the nuclear motions in molecules. By going beyond the characteristic stationary points and barriers, full dimensional, accurate potential energy surfaces have a very broad range of applications in many areas of physical chemistry; for example, they provide insight into structure, reactivity, and spectroscopy of molecules. While the majority of stable structures on PES are associated with the covalent or ionic bonding [3], the regions of PES dominated by van der Waals interactions are essential for low-temperature phenomena and molecular stacking which are critical for understanding biomolecular structures involving DNA and RNA molecules [4]. Furthermore, the advances in "cold chemistry" [5] make it possible to test the theoretical predictions (see, e.g., [6]) involving very small barriers of <15 K. At such low temperatures the quantum effects, for example, tunneling, play a significant role in chemical reactivity. For instance, the large de Broglie wavelength of ultracold molecules entirely changes the nature of reaction dynamics [7], and energy barriers on the PES play a different role because, in this regime, quantum tunneling becomes the dominant reaction pathway [8]. In addition, our understanding of potential energy surfaces has benefitted greatly from the ability of experimentalists to study chemical reactions and "observe" transition states in real time using the transition-state spectroscopy [9].

Due to the recent advances in ab initio method development [10] primarily focusing on the solution of the nonrelativistic Schrödinger equation, the theoretical data representing PESs is of higher quality and the cost and timing for such calculations is considerably improved. Furthermore, the relativistic corrections [11] can be significant and should be included if high accuracy of PESs is needed. For instance, the inclusion of the spin-orbit coupling effect (relativistic phenomenon) may turn a crossing of two potential energy curves into an avoided crossing [12]. Finally, given the raw ab initio data, efficient fitting techniques [13] are capable of generating excellent analytical representations of potential energy surfaces. One example is the functional representation of a PES using the double many-body expansion method [14]. Another important class of PESs corresponds to the ones that are constructed to be explicitly invariant with respect to all permutations of equivalent atoms [15, 16]. It is well recognized that one of the most stringent criteria of the quality of the PES is its ability to reproduce the experimental rotational-vibrational spectrum with the "near-spectroscopic" accuracy [12] of about 10 cm⁻¹ or better [17]. Occasionally, the empirical refinements for ab initio PESs are used in order to achieve a very close agreement (<0.1 cm⁻¹) with experiment for rovibrational transitions [18].

In many cases the BO approximation is valid to a high degree, and a single PES is sufficient to describe the motion of nuclei. However, when several electronic states get close in energy, the coupling between different potential energy surfaces becomes significant. The crossings of several PESs

⁴Departamento de Quimica, Universidade de Coimbra, 3004535 Coimbra, Portugal

(e.g., conical intersections) or avoided crossings require a more refined treatment of nuclear dynamics which extends nuclear motion to more than one BO surface [19]. The conical intersections or "seams" [20, 21] play an important role in photochemistry, for example, contributing to the photostability of DNA and participating in the isomerization process of cofactor retinal that initiates visual reception.

2. The Present Issue

The current special issue (ten papers: six reviews and four research articles) represents an excellent collection of papers focusing on the various aspects of potential energy surfaces.

The paper "Constructing potential energy surfaces for polyatomic systems: recent progress and new problems" by J. Espinosa-Garcia, M. Monge-Palacios, and J. C. Corchado provides a comprehensive description of different methods for constructing PESs based on electronic structure calculations, and their performance is evaluated by calculating properties associated with chemical reaction dynamics. The authors conclude that at the present stage the field of small systems has become mature; however the realm of larger polyatomic systems requires considerable improvement, especially when dealing with relativistic (e.g., spin-orbit) effects.

M. Ayouz and D. Babikov in their research paper "Improved potential energy surface of ozone constructed using the fitting by permutationally invariant polynomial function" illustrate the advantages of their method by studying the formation of ozone at thermal energies and its spectroscopy near the dissociation limit. The authors demonstrate that the approach of fitting the *ab initio* data by permutationally invariant polynomial functions allows the construction of accurate global PESs for symmetric molecules using only relatively small number of points.

The research paper "Ab initio potential energy surfaces for both the ground (\tilde{X}^1A') and excited (\tilde{A}^1A'') electronic states of HSiBr and the absorption and emission spectra of HSiBr/DSiBr" by A. Li, S. Lin, and D. Xie illustrate the high quality of the PESs by calculating the vibrational energy levels for the ground and excited states of these challenging systems. The latter were found to be in good agreement with the available experimental band origins.

The surface diffusion of adsorbed atoms and molecules plays a significant role in various surface dynamical processes, e.g., in heterogeneous chemical reactions and formation of self-assembled structures. N. Tsukahara and J. Yoshinobu in the paper "Potential energy surface of NO on Pt(997): adsorbed states and surface diffusion" elucidate the PES by investigating the adsorption states and diffusion processes of NO on Pt(997) using infrared absorption spectroscopy (IRAS) and scanning tunneling microscopy (STM).

The classical transition state theory (TST) has been very popular over the years for calculating the reaction rate constants, and it has been quite successful in the high-temperature regime. However, at low temperatures, especially involving light nuclei, the quantum effects become significant. Quantum instanton (QI) approximation has been introduced as one way to quantize the TST by naturally incorporating the quantum effects, like, for example, tunneling. For this reason, the quantum instanton approximation has received much attention for estimating the chemical reaction rate constants using full-dimensional potential energy surfaces. The QI can be applied to quite complex molecular systems via well-established imaginary time path integral techniques as described by Y. Zhao and W. Wang in their paper "Quantum instanton evaluations of the thermal rate constants for complex systems." The authors demonstrate the utility of the QI method by applying it to such complex processes like H diffusion on Ni(100) surface, and surface-subsurface transport and interior migration for H/Ni.

The hydrogen bonding plays a significant role in living organisms, for example, between DNA or RNA bases. The cooperativity of hydrogen bonding and the substituent effects are very important in stabilizing biomolecules. In this issue, A. Ebrahimi, S. M. Habibi-Khorassani, F. B. Akher, and A. Farrokhzadeh in the research article "The N···HF interactions in the X-pyridazine···(HF)₂ complexes: substituent effects and energy components" investigate the strength of the hydrogen bonding between X-pyridazine (N-sites) and HF molecules depending on the substituent. The authors find that in all complexes the binding energies (N···HF) increase for electron-donating substituents and decrease for electron-withdrawing substituents. Also a negative cooperativity is observed for two hydrogen bond interactions.

In order to understand the entire photochemical reaction process of a given system, it is necessary to explore several PESs that represent ground and excited states. Within the Franck-Condon (FC) approximation, a reaction starts from the FC point on an excited-state surface. Then, depending on the topography and the available excess energy, the system may select either adiabatic or nonadiabatic pathway. In the adiabatic case, the reacting system moves on the excited PES surpassing transition state to yield products. In the nonadiabatic case, the system undergoes a nonadiabatic transition (or several transitions cascading through a number of PESs) and then moves on the PES of the lower state. In the later case, the seams of intersection between two PESs play an important role. S. Maeda, K. Ohno, and K. Morokuma in the review paper "Exploring multiple potential energy surfaces: photochemistry of small carbonyl compounds" describe the global reaction route mapping (GRRM) method to explore the critical regions such as transition states, conical intersections, intersection seams, and minima associated with multiple PESs. The authors illustrate the efficiency of the method by documenting new nonadiabatic pathways in the photochemistry of formaldehyde and acetone.

Enzymatic reactions exploring catalytic properties of enzymes represent a very intense area of chemical research. Many species encountered in enzymatic reactions, especially metalloenzymes, may have more than one electronic state lying close in energy. It is possible that as reaction progresses, the relative energy separation between states may vary, and in particular the energetic ordering of these states may change during the reaction. Such mechanisms may include

cases where the "switching" involves PESs of different spin multiplicities. The likelihood of such multistate reactivity may have important consequences in enzymatic reactions. E. A. C. Bushnell, W. Huang, and J. Gauld in the paper "Applications of potential energy surfaces in the study of enzymatic reactions" explore several states of different spin multiplicities in the catalytic activation of O_2 by alpha-ketoglutarate-dependent dioxygenase (AlkB).

The photochemical studies where the metal atom is photoexcited into an upper state and then reacts with a given molecule (e.g., methane) are quite informative since the reaction pathway and probability strongly depend on the initial electronic state of an atom. Furthermore, the reaction pathway frequently encounters several potential energy surfaces (with various multiplicities) before the final products are formed. In this issue, O. Novaro, M. del Alba Pacheco-Blas, and J. H. Pacheco-Sánchez in the paper "Potential energy surfaces for reactions of X metal atoms (X = Cu, Zn, Cd, Ga, Al, Au, or Hg) with YH₄ molecules (Y = C, Si, or Ge) and transition probabilities at avoided crossings in some cases" discuss the possible mechanisms for the reaction of the metal atom with the gas molecules. In the cases above, the authors show that reaction pathways encounter many surfaces, and the transition probabilities for going from one surface to another are calculated using timedependent Landau-Zener theory. The results indicate a good agreement with the experimental data whenever they are available.

An example of the BO approximation breakdown is the Renner-Teller effect which is due to the fact that at linear geometries many of the electronic states in molecules are twofold degenerate. This results in the coupling of the electronic motion with the nuclear motion giving rise to the so-called rovibronic coupling. H. Ma, C. Zhang, Z. Zhang, X. Liu, and W. Bian in their research article "New ab initio potential energy surfaces for the Renner-Teller coupled $1^1A'$ and $1^1A''$ states of CH₂" generate the analytical representations of the PESs using a dual-level (the lower level and the higher level which also include core and core-valence correlation effects) strategy with the inclusion of the Renner-Teller terms. The authors use these PESs for the quantum dynamical calculations and demonstrate that the calculated vibronic energy levels for the two singlet electronic states are in excellent agreement with experiment.

Finally, we would like to thank all the authors for providing the high-quality papers and also all the reviewers who donated their valuable time to this special issue.

Laimutis Bytautas Joel M. Bowman Xinchuan Huang António J. C. Varandas

References

[1] M. Born and J. R. Oppenheimer, "Zur quantentheorie kontinuierlicher spektren," *Annalen der Physik*, vol. 41, no. 8-9, pp. 457–484, 1927.

- [2] J. N. Murrell, S. Carter, S. C. Farantos, P. Huxley, and A. J. C. Varandas, *Molecular Potential Energy Functions*, John Wiley & Sons, Chichester, UK, 1984.
- [3] P. Ball, "Beyond the bond," *Nature*, vol. 469, no. 7328, pp. 26–28, 2011.
- [4] K. E. Riley, M. Pitoňák, P. Jurečka, and P. Hobza, "Stabilization and structure calculations for noncovalent interactions in extended molecular systems based on wave function and density functional theories," *Chemical Reviews*, vol. 110, no. 9, pp. 5023–5063, 2010.
- [5] D. Herschbach, "Molecular collisions, from warm to ultracold," *Faraday Discussions*, vol. 142, pp. 9–23, 2009.
- [6] L. Bytautas and K. Ruedenberg, "Ab initio potential energy curve of F₂. IV. Transition from the covalent to the van der Waals region: competition between multipolar and correlation forces," Journal of Chemical Physics, vol. 130, no. 20, Article ID 204101, 2009.
- [7] R. V. Krems, "Cold controlled chemistry," *Physical Chemistry Chemical Physics*, vol. 10, no. 28, pp. 4079–4092, 2008.
- [8] P. R. Schreiner, H. P. Reisenauer, D. Ley, D. Gerbig, C.-H. Wu, and W. D. Allen, "Methylhydroxycarbene: tunneling control of a chemical reaction," *Science*, vol. 332, no. 6035, pp. 1300–1303, 2011.
- [9] A. H. Zewail, "Femtochemistry: recent progress in studies of dynamics and control of reactions and their transition states," *Journal of Physical Chemistry*, vol. 100, no. 31, pp. 12701– 12724, 1996.
- [10] C. D. Sherrill, "Frontiers in electronic structure theory," *Journal of Chemical Physics*, vol. 132, no. 11, Article ID 110902, 2010.
- [11] P. Pyykkö, "Relativistic effects in structural chemistry," *Chemical Reviews*, vol. 88, no. 3, pp. 563–594, 1988.
- [12] L. Bytautas, N. Matsunaga, and K. Ruedenberg, "Accurate ab initio potential energy curve of O₂ II. Core-valence correlations, relativistic contributions, and vibration-rotation spectrum," *Journal of Chemical Physics*, vol. 132, no. 7, Article ID 074307, 2010.
- [13] G. C. Schatz, "The analytical representation of electronic potential-energy surfaces," *Reviews of Modern Physics*, vol. 61, no. 3, pp. 669–688, 1989.
- [14] A. J. C. Varandas, "Intermolecular and intramolecular potentials: topographical aspects, calculation, and functional representation via a double many-body expansion method," *Advances in Chemical Physics*, vol. 74, pp. 255–338, 1988.
- [15] B. J. Braams and J. M. Bowman, "Permutationally invariant potential energy surfaces in high dimensionality," *International Reviews in Physical Chemistry*, vol. 28, no. 4, pp. 577– 606, 2009.
- [16] J. M. Bowman, B. J. Braams, S. Carter et al., "Ab-initio-based potential energy surfaces for complex molecules and molecular complexes," *Journal of Physical Chemistry Letters*, vol. 1, no. 12, pp. 1866–1874, 2010.
- [17] O. L. Polyansky, A. G. Császár, S. V. Shirin et al., "High-accuracy *ab initio* rotation-vibration transitions for water," *Science*, vol. 299, no. 5606, pp. 539–542, 2003.
- [18] X. Huang, D. W. Schwenke, and T. J. Lee, "Rovibrational spectra of ammonia. I. Unprecedented accuracy of a potential energy surface used with nonadiabatic corrections," *Journal of Chemical Physics*, vol. 134, no. 4, Article ID 044320, 15 pages, 2011.
- [19] G. A. Worth and L. S. Cederbaum, "Beyond born-oppenheimer: molecular dynamics through a conical intersection," *Annual Review of Physical Chemistry*, vol. 55, pp. 127–158, 2004.

- [20] D. R. Yarkony, "Conical intersections: the new conventional wisdom," *Journal of Physical Chemistry A*, vol. 105, no. 26, pp. 6277–6293, 2001.
- [21] T. J. Martinez, "Physical chemistry: seaming is believing," *Nature*, vol. 467, no. 7314, pp. 412–413, 2010.

Hindawi Publishing Corporation Advances in Physical Chemistry Volume 2012, Article ID 362608, 9 pages doi:10.1155/2012/362608

Research Article

The N··· HF Interactions in the X-Pyridazine ··· $(HF)_2$ Complexes: Substituent Effects and Energy Components

Ali Ebrahimi, Mostafa Habibi-Khorassani, Farideh Badichi Akher, and Abdolkarim Farrokhzadeh

Department of Chemistry, University of Sistan and Baluchestan, P.O. Box 98135-674, Zahedan, Iran

Correspondence should be addressed to Ali Ebrahimi, ebrahimi@chem.usb.ac.ir

Received 31 October 2011; Revised 4 January 2012; Accepted 24 January 2012

Academic Editor: Laimutis Bytautas

Copyright © 2012 Ali Ebrahimi et al. This is an open access article distributed under the Creative Commons Attribution License, which permits unrestricted use, distribution, and reproduction in any medium, provided the original work is properly cited.

The effects of substituents on the N···HF interactions in the X-pyridazine···(HF)_n (X = N(CH₃)₂, NHCH₃, NH₂, C₂H₅, CH₃, OCH₃, OH, CN, OF, NO₂, F, Br, Cl, and n = 1, 2) complexes have been studied at the B3LYP/6-311++G(d,p) level of theory. In all complexes, the binding energies increase for the electron-donating substituents and decrease for the electron-withdrawing substituents. A negative cooperativity is observed for two hydrogen bond interactions. There are meaningful relationships between the Hammett constants and the energy data and the results of population analysis in the binary and ternary complexes. Symmetryadapted perturbation theory (SAPT) analysis was also carried out to unveil the nature of hydrogen bond in the complexes 2 and 3. The electron-donating substituents increase the magnitude of the SAPT interaction energy components and the electron-withdrawing substituents decrease those components. The highest/lowest change is observed for the $E_{\text{exch}}/E_{\text{disp}}$ component. The effect of C_2H_5 (or CH₃) on different components is higher than OCH₃ in the complex 2 while the trend is reversed in the complex 3. It is demonstrated that the electrostatic interaction plays a main role in the interaction, although induction and dispersion interactions are also important.

1. Introduction

The diazine rings are building blocks of many important natural and synthetic compounds [1]. They have been the subject of extensive research, particularly in the pharmaceutical and agrochemical areas due to their broad activities, such as antihypertensive and anti-inflammatory activity [2–5].

The hydrogen bond plays a crucial role in biology, chemistry and related disciplines [6–13]. Cooperativity is an important characteristic of hydrogen bond interactions. The role of hydrogen bond may be modified by the cooperativity of hydrogen bonds in many chemical and biological systems [14–16]. It plays an important role in controlling and regulating the processes occurring in living organisms. Many physical and chemical properties of materials are determined by hydrogen-bonding cooperativity [17–20]. For example, the hydrogen bond cooperativity is relevant for sustaining

the stable conformers of biological molecules [21, 22] and constructing the crystal structures [22, 23].

The effects of substituents on the binding energies of the X-pyridazine $\cdot \cdot \cdot (HF)_n$ (n = 1, 2) complexes (represented by 1–3 in Scheme 1) and the cooperativity of the H-bond interactions have been investigated in the present study. Substituent X is located at position 4 of pyridazine ring, which is meta relative to N₂ in 1 and 2 and para relative to N₁ in 1 and 3. The relationship between binding energies and the Hammett constants have been studied for binary and ternary complexes. Also, the cooperativity of two hydrogen bond interactions and the strength of interactions have been investigated by the results of atoms in molecules (AIMs) [24], the natural bond orbital (NBO) [25], and molecular electrostatic potential (MEP) analysis. Symmetry-adapted perturbation theory (SAPT) [26] has been employed to determine the physically significant components of the total interaction energies for the complexes 2 and 3.

SCHEME 1: The X-pyridazine··· (HF) $_n$ complexes considered in the present work (X = N(CH $_3$) $_2$, NHCH $_3$, NH $_2$, C $_2$ H $_5$, CH $_3$, OCH $_3$, OH, CN, OF, NO $_2$, F, Br, Cl, and n = 1, 2).

2. Methods

The geometries of the complexes were fully optimized with the B3LYP [27] method using the 6-311++G(d,p) basis set by the Gaussian 03 program package [28]. The single-point calculations were carried out using the MP2 [29] and PBE1-KCIS [30] methods in conjunction with the 6-311++G(d,p)and aug-cc-pVDZ basis sets. The interaction energies were corrected with the basis set superposition error (BSSE) using the counterpoise method of Boys and Bernardi [31]. The frequency calculations were performed at the B3LYP/6-311++G(d,p) level of theory. The obtained wave functions at the B3LYP/6-311++G(d,p) computational level have been used to analyze the electron density within the AIM methodology by the AIM2000 program [32]. The NBO analysis has been performed using the HF method in conjunction with the 6-311++G(d,p) basis set using the NBO3.1 program in the Gaussian03 package. Also, the ChelpG [33] charges were calculated at the B3LYP/6-311++G(d,p) level of theory to investigate the charge transfer between two units. Cube files containing the MEP information have been generated for complexes at the B3LYP/6-311++G(d,p) level of theory. The freely available MOLEKEL program [34] has been used for the visualization of the MEP data. The most negative-valued MEP point (V_{\min}) can be obtained from visual inspection of MEP data for the lone-pair region of the nitrogen atoms in pyridazine. The B3LYP-optimized geometries with the 6-311++G(d,p) basis set were then used to perform interaction energy decomposition using the SAPT scheme. Molecular integrals were first obtained with the GAMESS package [35], and the SAPT partitioning was performed using the SAPT-2008 program [36].

3. Results and Discussion

The most important geometrical parameters of complexes optimized at the B3LYP/6-311++G(d,p) level of theory are gathered in Table 1. The maximum and minimum values of the $N \cdot \cdot \cdot H$ bond length correspond to NO_2 and $N(CH_3)_2$ substituents, respectively, in all cases. Also, the $N \cdot \cdot \cdot H$ bond length in the complex 1 is longer than that in the complexes 2 and 3. On the other hand, the $N \cdot \cdot \cdot H$ bond length in the complex 2 is longer than that in the complex 3. These results show that the cooperativity of H-bond interactions leads to the elongation of the $N \cdot \cdot \cdot H$ bond lengths.

The total binding energies of complexes (ΔE) calculated at the B3LYP/6-311++G(d,p) level of theory and corrected for BSSE are summarized in Table 2. The results show that the stabilization energies of the complex 3 are larger than those of complex 2. As can be seen, the maximum and minimum values of ΔE calculated at the B3LYP/6-311++G(d,p) level of theory correspond to the N(CH₃)₂ and NO₂ substituents, respectively.

The results of single-point energy calculation at the MP2/6-311++G (d,p), MP2/aug-cc-pVDZ, PBE1KCIS/6-311++G(d,p), and PBE1KCIS/aug-cc-pVDZ levels of theory on the geometries optimized at the B3LYP/6-311++G(d,p) level of theory are also given in Table 2. The maximum and minimum ΔE values correspond to N(CH₃)₂ and NO₂ substituents, respectively, at all levels of theory.

The ΔE values calculated by the MP2 method increase by 13.8 to 7.6 percent going from 6-311++G(d,p) to aug-cc-pVDZ basis sets. The corresponding changes are in the range of -0.51 to -0.19 kcal mol⁻¹ for the values calculated by the PBE1KCIS method.

The absolute values of ΔE calculated at the MP2/6-311++G(d,p) level are 2.07 to 4.22 kcal mol⁻¹ smaller than those calculated at the B3LYP/6-311++G(d,p) level. The absolute values of ΔE calculated by the PBE1KCIS method are approximately 3.54 to 0.51 kcal mol⁻¹ larger than the values calculated by the MP2 and B3LYP methods. The ΔE values calculated at the PBE1KCIS/aug-cc-pVDZ level are approximately identical with the values calculated at the B3LYP/6-311++G(d,p) level of theory.

The BSSE-corrected binding energies of the complex 1 are lower than the sum of binding energies of the complexes 2 and 3 (see Table 2). In addition, the stabilization energies of complexes become more negative by the electron-donating substituents (with the exception of the OH substituent in the complex 2) relative to the pyridazine, while the behavior is reversed by the electron-withdrawing substituents.

The total substituent effect comprises inductive/field effects, which have electrostatic character, and resonance effects, which are not electrostatic in nature. Resonance effects are strongest at para position, while the electrostatic interactions inversely depend on distance [38, 39]. The Hammett substituent constants are presented in Table 1 [37]. For the N(CH₃)₂, NHCH₃, NH₂, CH₃, and C₂H₅ substituents, the σ_p values are more negative than the σ_m values, so, the electron donation of the aforementioned substituents in the complex 3 is higher than that in the complex 2. The high

Table 1: The N···H bond lengths optimized at the B3LYP/6-311++G(d,p) level in (Å) and the Hammett constants.

		Bond length		Hammett constants					
	Complex 1	Complex 2	Complex 3	σ_m	σ_p	$\sigma_{ m total}$	σ_I	σ_R	
$N(CH_3)_2$	1.67 (1.69)	1.64	1.63	-0.15	-0.83	-0.98	0.15	-0.98	
NHCH ₃	1.68 (1.70)	1.65	1.63	-0.52	-0.74	-1.26	0.03	-0.73	
NH_2	1.68 (1.71)	1.65	1.64	-0.16	-0.66	-0.82	0.08	-0.74	
CH_3	1.71 (1.71)	1.66	1.66	-0.07	-0.17	-0.24	0.01	-0.18	
C_2H_5	1.71 (1.71)	1.66	1.66	-0.07	-0.15	-0.22	0.00	-0.15	
OCH_3	1.70 (1.72)	1.67	1.65	0.12	-0.27	-0.15	0.29	-0.56	
OH	1.71 (1.73)	1.67	1.66	0.12	-0.37	-0.25	0.30	-0.70	
Н	1.72 (1.72)	1.67	1.67	0.00	0.00	0.00			
OF	1.73 (1.74)	1.70	1.68	0.47	0.36	0.83			
CN	1.75 (1.70)	1.71	1.70	0.56	0.66	1.22	0.51	0.15	
NO_2	1.76 (1.76)	1.72	1.71	0.71	0.78	1.49	0.60	0.13	
F	1.73 (1.74)	1.69	1.68	0.34	0.06	0.40	0.45	-0.39	
Br	1.73 (1.74)	1.69	1.69	0.39	0.23	0.62	0.40	-0.22	
Cl	1.73 (1.74)	1.69	1.68	0.37	0.23	0.60	0.42	-0.19	

The data in the parentheses correspond to the $N_2 \cdot \cdot \cdot H$ bond length. The σ values are taken from [37].

Table 2: The binding energies ($-\Delta E$ in kcal mol⁻¹) corrected for BSSE calculated at different levels.

		Complex	1		Complex 2	2		Complex 3	3
	B3LYP	MP2	PBE1KCIS	B3LYP	MP2	PBE1KCIS	B3LYP	MP2	PBE1KCIS
$N(CH_3)_2$	25.75	21.90 (23.52)	26.22 (25.86)	13.92	11.90 (12.81)	14.19 (14.03)	14.48	11.72 (12.70)	14.71 (14.49)
NHCH ₃	25.32	21.80 (23.23)	25.81 (25.42)	13.73	12.00 (12.74)	13.99 (13.82)	14.31	11.82 (12.60)	14.54 (14.31)
NH_2	24.51	20.30 (22.12)	25.06 (24.66)	13.27	11.30 (12.14)	13.55 (13.38)	13.88	11.14 (12.10)	14.15 (13.91)
CH_3	22.98	19.80 (21.10)	23.44 (23.07)	12.80	10.90 (11.63)	13.03 (12.85)	12.86	10.82 (11.50)	13.08 (12.88)
C_2H_5	23.34	19.80 (21.44)	23.88 (23.64)	13.01	10.90 (11.86)	13.32 (13.24)	13.09	10.78 (11.80)	13.40 (13.31)
OCH_3	23.19	19.90 (21.24)	23.65 (23.31)	12.61	10.90 (11.55)	12.85 (12.68)	13.20	10.99 (11.70)	13.43 (13.24)
OH	22.42	19.30 (20.69)	22.96 (22.67)	12.29	10.60 (11.34)	12.57 (12.43)	12.72	10.61 (11.30)	12.98 (12.81)
Н	22.01	19.00 (20.28)	22.45 (22.07)	12.33	10.50 (11.17)	12.55 (12.35)	12.33	10.50 (11.20)	12.55 (12.35)
OF	20.10	17.60 (18.89)	20.70 (20.56)	10.99	9.59 (10.29)	11.29 (11.21)	11.56	9.82 (10.50)	11.86 (11.76)
CN	18.33	16.00 (17.10)	18.76 (18.42)	10.21	8.66 (9.26)	10.41 (10.22)	10.43	9.03 (9.62)	10.64 (10.46)
NO_2	17.59	15.50 (16.74)	18.14 (17.95)	9.85	8.40 (9.04)	10.10 (9.99)	10.03	8.88 (9.50)	10.30 (10.19)
F	20.30	17.60 (18.86)	20.84 (20.57)	11.20	9.65 (10.28)	11.46 (11.31)	11.63	9.86 (10.50)	11.89 (11.75)
Br	20.28	17.70 (18.86)	20.79 (20.42)	11.16	9.63 (10.23)	11.41 (11.23)	11.51	9.89 (10.50)	11.75 (11.58)
Cl	20.29	17.70 (18.81)	20.80 (20.44)	11.18	9.65 (10.22)	11.43 (11.24)	11.55	9.91 (10.50)	11.80 (11.61)

The data in the parenthesis correspond to the aug-cc-pVDZ basis set.

electronegativity of oxygen makes the OCH₃ and OH substituents electron-withdrawing by the inductive effect; this is reflected in the positive value for σ_m .

Recall that the meta substituents only affect the reaction center by the inductive effects, whereas the para substituents affect it by both the inductive and resonance effects. Thus, there is a satisfactory linear relationship between ΔE and $\sigma_I(R=0.91)$, ΔE and $\sigma_I+\sigma_R(R=0.98)$, respectively, in the complexes 2 and 3. Comparing the σ values for the meta and para indicates that the electron-donating resonance effect (σ_R) dominates over the electron-withdrawing inductive effect (σ_I) . Therefore, these substituents are more electron-donating in the complex 3 in comparison to the complex 2. The σ_m and σ_p values are positive for the OF, CN, NO₂, F, Br, and Cl substituents. Thus, these substituents are electron-withdrawing in both the meta and para positions. Comparison between the σ values for the meta and para indicates that the σ_I dominates over the σ_R . Since the inductive effect

is inversely related to distance, the electron-withdrawing inductive effects are stronger in the complex 2 in comparison with the complex 3.

The σ_m and σ_p constants can be used as appropriate parameters for the description of the intermolecular interaction in the X-pyridazine···(HF)₂ complex. The linear correlation coefficient between the ΔE values and the σ_m , σ_p , and $\sigma_{\text{total}}(\sigma_m + \sigma_p)$ constants is equal to 0.95, 0.97, and 0.98, respectively. This indicates that the total electrostatic effect of the substituents as well as induction and resonance vitally impacts the two intermolecular interactions (see Figure 1).

3.1. AIM and NBO Analysis. A way to characterize the hydrogen bond is AIM analysis that interprets these interactions in terms of critical points [40, 41]. The values of electron density (ρ) calculated at the $N_2 \cdots H$ and $N_1 \cdots H$ bond critical points (BCPs) of complexes 1–3 are gathered in Table 3.

Table 3: Electron densities ρ (in e/au³) at the N···H BCP in the X-pyridazine···(HF) $_n(n=1,2)$ complexes and individual H-bond energies E (in kcal mol⁻¹) calculated for the complex 1.

	Сс	omplex 1	Complex 2	Complex 3
	$ ho_{\mathrm{BCP}} imes 10^2$	E	$ ho_{\mathrm{BCP}} imes 10^2$	$\rho_{\rm BCP} \times 10^2$
$N(CH_3)_2$	5.46 , <i>5.23</i>	−14.41 , <i>−13.44</i>	6.03	6.16
$NHCH_3$	5.40 , 5.15	- 14.23 , - <i>13.18</i>	5.95	5.95
NH_2	5.32 , 5.05	- 13.85 , - <i>12.73</i>	5.82	5.97
CH_3	4.99 , 4.95	- 12.36 , - <i>12.21</i>	5.69	5.69
C_2H_5	5.02 , 5.00	- 12.76 , - <i>12.67</i>	5.73	5.74
OCH_3	5.08 , 4.91	- 12.98 , - <i>12.29</i>	5.60	5.79
OH	5.02 , 4.79	- 12.66 , - <i>11.75</i>	5.56	5.65
Н	4.83 , 4.83	- 12.04 , - <i>12.04</i>	5.54	5.54
OF	4.70 , 4.55	-11.37, -10.81	5.19	5.35
CN	4.45 , 4.43	-10.22, -10.15	5.01	5.07
NO_2	4.42 , 4.45	-10.08, -10.19	4.90	4.90
F	4.71 , 4.57	-11.46, -10.92	5.23	5.36
Br	4.69 , 4.61	−11.33 , <i>−11.02</i>	5.24	5.33
Cl	4.69 , 4.60	−11.36, −11.02	5.25	5.35

The bold and italicized values correspond to the $N_1 \cdots H$ and $N_2 \cdots H$ hydrogen bonds, respectively.

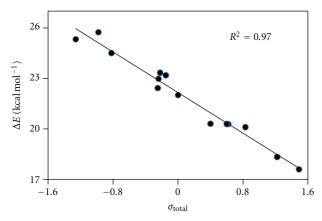


FIGURE 1: Correlation between the binding energies $(-\Delta E \text{ in kcal mol}^{-1})$ and Hammett constant σ_{total} for the complex 1.

The maximum and minimum values correspond to the $N(CH_3)_2$ and NO_2 substituents, respectively, (with the exception of ρ_{N_2H} in the complex 1 where the minimum value corresponds to the CN substituent). The topological properties of ρ calculated at the BCP of the intermolecular hydrogen bonds may be treated as a measure of the hydrogen bond strength [42–44]. The electron-withdrawing substituents pull the lone pair of nitrogen atoms of pyridazine inside the ring and decrease the ρ values at the $N \cdot \cdot \cdot$ H BCP, while the electron-donating substituents increase the ρ values and enhance the hydrogen bond strength. The ρ values calculated at the $N \cdot \cdot \cdot$ H BCP in the complex 3 are higher than those in the complex 2, and the complex 3 is more stable than the complex 2. On the other hand, the ρ values of $N \cdot \cdot \cdot$ H hydrogen bond of complex 1 are lower than the values calculated at

the $N_2\cdots H$ and $N_1\cdots H$ hydrogen bonds in the complexes 2 and 3. Thus, a negative cooperativity is predicted from the comparison between $\rho_{N\cdots H}$ values in the complex 1 and the complexes 2 and 3. The $N\cdots H$ bond length decreases linearly by the increase in the ρ values calculated at the $N\cdots H$ BCP for all categories ($R^2\simeq 0.99$). Also, there is a linear relationship between ρ and ΔE for all cases. A linear relationship ($R^2=0.99$) is observed between the ΔE values calculated at the B3LYP/6-311++G(d,p) level and the ρ values calculated at the $N\cdots H$ BCPs in the complex 1.

Because of linear relationship between ΔE and $\rho_{\rm NH}$ values, the $\Delta E = c\rho_{\rm NH}$ can be used for the calculation of individual H-bond energies in the complex 1 (see Table 4). All individual H-bond energies calculated for the complex 1 are lower than the values calculated for the complexes 2 and 3. Also, there is a linear relationship with high correlation coefficient (R=0.99) between individual H-bond energies and the N···H bond lengths.

For a better understanding of the hydrogen bond interaction in the complexes 1-3, the NBO analysis has been carried out at the HF/6-311++G(d,p) level of theory. The lp_N $\rightarrow \sigma_{HF}^*$ interaction, which can be considered as a measure of charge transfer, has been evaluated in the complexes 1-3 (see Table 5). The donor-acceptor interaction energy (E^2) value of this interaction can be used to predict the strength of the N \cdot ·· ·H hydrogen bond. In all cases, the maximum and minimum values correspond to the N(CH₃)₂ and NO₂ substituents, respectively. As can be seen in Table 4, the E^2 values of the $lp_{N_2} \rightarrow \sigma_{HF}^*$ and $lp_{N_1} \rightarrow \sigma_{HF}^*$ interactions in the complexes 2 and 3 are higher than those in the complex 1. So, the negative cooperativity decreases the E^2 values of $lp_{N_2} \rightarrow \sigma_{HF}^*$ and $lp_{N_1} \rightarrow \sigma_{HF}^*$ donor-acceptor interactions in the complex 1 relative to the complexes 2 and 3. The electron-donating substituents increase the electron density on the nitrogen atoms of pyridazine ring (with the exception of OH substituent in the complex 2) and increase their inclination on polarization of HF, which increase the E^2 value of the lp_N \rightarrow $\sigma_{\rm HF}^*$ interaction. Though OH is an electron-donating substituent, but it destabilizes the complex 2 relative to the pyridazine. This behavior is not observed for the OCH₃ functional group. The NBO atomic charge on the O (-0.71) of OH substituent is more negative than O (-0.61) of the OCH₃ substituent. Thus, electron-withdrawing induction effect is predominant over the electron-donating resonance effect by the high electronegativity of O atom in the OH substituent. Moreover, there are good linear relationships between the E^2 values and both the σ_{total} values and N··· H bond lengths.

The occupation numbers of lp_{N_2} , lp_{N_1} , and σ_{HF}^* are given in Table 4. The maximum and minimum occupancies for lp_{N_2} and lp_{N_1} correspond to NO_2 and $N(CH_3)_2$, respectively, the maximum and minimum occupancies of σ_{HF}^* correspond to $N(CH_3)_2$ and NO_2 , respectively. As can be seen in Table 4, increasing the occupation numbers of lp_{N_2} and lp_{N_1} is accompanied with the decrease in the occupation number of σ_{HF}^* for all complexes. The occupancies of lp_{N_2} and lp_{N_1} in the complex 1 are larger than those in the complexes 2 and 3, while the occupancy of σ_{HF}^* in the complexes 2 and 3 is larger than that in the complex 1. Thus, the occupancy of the first lp_N/σ_{HF}^* increases/decreases in the presence of second

25.36, 24.28

		Complex 1			Comple	ex 2		Comple	x 3
	E^2	lp_N	$\sigma_{ m HF}^*~(imes~10^2)$	E^2	lp_N	$\sigma_{ m HF}^*~(imes 10^2)$	E^2	lp_N	$\sigma_{\mathrm{HF}}^{*} (imes 10^{2})$
$N(CH_3)_2$	34.16 , <i>30.47</i>	1.911 , 1.914	4.509 , <i>5.030</i>	39.48	1.904	5.767	42.41	1.902	6.166
NHCH ₃	33.46 , 29.71	1.912 , 1.915	4.395 , 4.934	38.66	1.906	5.651	41.79	1.903	6.087
NH_2	32.52 , 28.72	1.913 , 1.917	4.236 , 4.793	37.35	1.908	5.438	40.05	1.905	5.838
CH_3	28.59 , 27.95	1.919 , 1.920	4.148 , <i>4.239</i>	36.07	1.911	5.289	36.44	1.910	5.333
C_2H_5	28.94 , 28.42	1.919 , 1.919	4.213 , <i>4.288</i>	36.62	1.910	5.394	36.91	1.910	5.399
OCH_3	29.60 , 27.51	1.917 , 1.920	5.604 , 5.946	35.08	1.912	5.101	37.70	1.900	5.503
OH	29.01 , 25.99	1.918 , 1.921	3.859 , 4.286	34.39	1.912	5.031	36.12	1.910	5.273
Н	26.79 , 26.73	1.921 , 1.921	3.982 , 3.982	34.69	1.912	5.093	34.69	1.912	5.093
OF	25.44 , 23.61	1.922 , 1.924	4.931 , <i>5.238</i>	30.95	1.918	4.520	32.49	1.915	4.760
CN	22.58 , <i>22.52</i>	1.928 , 1.926	3.348 , <i>3.352</i>	28.57	1.919	4.200	29.04	1.921	4.259
NO_2	21.48 , 21.68	1.929 , 1.928	4.566 , 4.556	27.26	1.922	3.993	27.64	1.922	4.041
F	25.50 , <i>23.92</i>	1.922 , 1.925	3.533 , <i>3.785</i>	30.95	1.918	4.520	32.63	1.914	4.774
Br	25.29 , 24.36	1.923 , 1.923	3.622 , <i>3.757</i>	31.14	1.915	4.575	32.23	1.916	4.723

31.16

1.916

4.570

Table 4: The results of NBO analysis for the X-pyridazine $\cdot \cdot \cdot (HF)_n$ (n = 1, 2) complexes at the HF/6-311++G(d,p) level of theory.

3.602, 3.763 The E^2 values are in kcal mol^{-1} . The bold and italicized values correspond to the $N_1 \cdots H$ and $N_2 \cdots H$ bonds, respectively.

Table 5: The results of MEP analysis ($V_{\min} \times 10^3$) and charge transfer ($\Delta q \times 10^3$ in au) calculated from ChelpG charges.

1.923, 1.923

	Co	mplex 1	Com	plex 2	Comp	plex 3
	V_{min}	Δq	$V_{ m min}$	Δq	$V_{ m min}$	Δq
$N(CH_3)_2$	97	205 , 194	103	295	107	309
$NHCH_3$	96	199 , 187	101	282	106	293
NH_2	94	193 , 189	99	283	103	294
CH_3	87	189 , 195	96	294	97	291
C_2H_5	88	190 , 200	97	292	98	296
OCH_3	89	181 , 204	98	288	99	295
OH	86	192 , 188	92	293	96	295
Н	84	194 , 195	94	300	94	300
OF	79	182 , 182	88	278	89	280
CN	73	175 , 185	83	277	82	279
NO_2	72	178 , 182	81	278	80	270
F	79	186 , 181	88	280	89	279
Br	80	213 , 163	89	325	90	328
Cl	80	189 , 176	89	275	90	285

The bold and italicized values correspond to the charge transfer from N₁ and N2 atoms to HF unit, respectively.

 $N \cdot \cdot \cdot HF$ interaction. This confirms the negative cooperativity in the complex 1. There is a little difference between the occupancies of lp_{N_2} and lp_{N_1} in the complexes 2 and 3. Also, the occupancy of σ_{HF}^* in the complex 3 is larger than that in the complex 2. Therefore, the changes of occupation numbers of lp_{N_2} , lp_{N_1} , and σ_{HF}^* are in agreement with the binding energies in all categories. A linear relationship (R^2 = 1.0) is observed between the ΔE values and the sum of E^2 values of $lp_{N_1} \rightarrow \sigma_{HF}^*$ and $lp_{N_1} \rightarrow \sigma_{HF}^*$ in the complex 1. The high linear correlation ($R^2=1.0$) indicates the additivity of the E^2 values of two H-bond interactions.

There is also a linear relationship between the E^2 values and the occupancies of lp_{N_2} , lp_{N_1} , and σ_{HF}^* . In addition,

there is a linear relationship between E^2 and $N \cdot \cdot \cdot H$ hydrogen bond lengths in three categories. Linear relationships are observed for the E^2 value of $\lg_{N_2} \to \sigma_{HF}^*$ versus $r_{N_2...H}(R^2 = 0.98)$ and the E^2 values of $\lg_{N_1} \to \sigma_{HF}^*$ versus $r_{N_1...H}(R^2 = 0.98)$ 0.99) in the complex 1.

32.40

1.915

4.745

On the base of charges calculated by the ChelpG method (see Table 5), the charge transfer occurred from X-pyridazine to HF unit, The electron-donating substituents promote the charge transfer from X-pyridazine to HF unit, and enhance the basicity of the nitrogen atoms in the X-pyridazine. In the complex 3, the charge transfer is larger and the basicity of N atom is higher than those in the complex 2; this can be a reason for the stability of complex 3. On the other hand, the charge transfer in the complex 1 is lower than that in complexes 2 and 3; this is in agreement with the negative cooperativity of two hydrogen bond interactions.

3.2. MEP Analysis. The MEP is an important tool in exploring the nature of intermolecular interactions [45-51]. The capability of the N2 and N1 atoms to accept hydrogen bond was estimated through the minimum of the MEP (V_{\min}) around the nitrogen atoms. As can be seen in Table 5, the MEP values become more negative with the electrondonating substituents. Thus, the electrostatic term depends on the electron donation or electron withdrawal character of the substituents. Also, a good linear relationship is observed between the V_{\min} values and the σ_{total} values (see Figure 2). Therefore, those values can be used to predict the Hammett constants. The trend in the V_{\min} values is 3 > 2 > 1; so, those values become less negative around the nitrogen atoms when both interactions coexist.

The MEP, $V_{(r)}$, is directly related to electron density $\rho(r)$ through the Poisson's equation [52]:

$$\nabla^2 V(r) = 4\pi \rho(r). \tag{1}$$

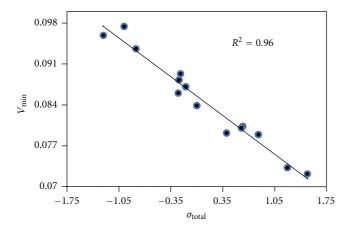


FIGURE 2: Linear correlation between molecular electrostatic potential minimum (V_{\min}) around the nitrogen atoms of the pyridazine and the Hammett electronic parameters for the complex 1.

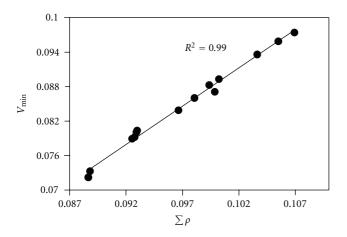


FIGURE 3: Interplay between the V_{\min} value around the nitrogen of pyridazine versus the sum of ρ values calculated at the N···H BCPs for complex 1.

Is there a liner relationship between V_{\min} and the ρ values calculated at the HBCPs? The V_{\min} values become more negative with increasing ρ values calculated at HBCPs in X-pyridazine···(HF)_n complexes. The linear correlation coefficients between the V_{\min} values and the ρ values are equal to 0.98 and 0.99, respectively, in the complexes 2 and 3. As can be seen in Figure 3, there is a good correlation between V_{\min} values and $\sum \rho$ values for the complex 1 (R = 1.00). Similarly, there is a linear relationship (R = 0.99) between V_{\min} and E^2 of $Ip_N \rightarrow \sigma_{HF}^*$ interaction, V_{\min} , and the $N_2 \cdots H$ and $N_1 \cdots H$ bond lengths. Also, there is a good linear correlation between V_{\min} values and $\sum E^2$ in the complex 1 (R = 1.00).

3.3. SAPT Energy Decomposition. The SAPT analysis is a method for investigation the nature of the intermolecular interactions [53–55]. The SAPT method provides detailed information on the intermolecular interaction, as this

method directly calculates magnitude of each term (electrostatic, dispersion, etc.) of the intermolecular interactions [56]. A detailed description of SAPT and some of its applications can be found in some recent references [57–59].

To determine the nature of the hydrogen bond in the complexes 2 and 3, the interaction energies were decomposed into physically meaningful components, including electrostatic, induction, dispersion, and exchange energies, using SAPT technique at the B3LYP/6-31G(d) level. It can be seen from Table 6 that the values of electrostatic energy $(E_{\rm els})$, induction energy $(E_{\rm ind})$, and dispersion energy $(E_{\rm disp})$ are negative, whereas the exchange energy (E_{exch}) is positive for all complexes. Thus, the stabilization/destabilization of the complexes by substitution is represented simply by the sum from E_{els} , E_{ind} , and E_{disp} contributions. In both complexes, the absolute values for these three negative terms are largest for the N(CH₃)₂ substituent and are smallest for the NO_2 substituent. In the complex 3, the absolute values of E_{els} , $E_{\rm ind}$, and $E_{\rm disp}$ are larger than those values in the complex 2. Thus, the complex 3 is more stable than the complex 2. The electron-donating substituents have positive effect and increase the magnitude of the calculated SAPT interaction energy components (with the exception of OH substituent in the complex 2 that decreases the magnitude of electrostatic energy relative to pyridazine). The electron-withdrawing substituents have negative effect and decrease the magnitude of interaction energy components, with the exception of $E_{\rm disp}$ in the complex 2 that slightly increases in the presence of mentioned substituents. The dependence of the dispersion term to the substituent is smaller than other complexes. When position of HF changes from para to meta relative to the substituent, the electrostatic term changes by 2.8%, the induction term changes by 2.2%, and the dispersion term changes by 12.5%. Thus, the dispersion energy component of the SAPT analysis was found to be very sensitive to the position of HF relative to the substituent.

In the complex 2, the electrostatic forces contribute about 52.0–54.6% to the total attractive interaction energy, the induction forces are about 35.6-43.6% of the total attractive energy, and the dispersion contribution is 9.7-11.9%. On the other hand, the electrostatic, induction, and dispersion contributions are 51.9–52.6%, 36.4–37.0%, and 10.5–11.7%, respectively, in the complex 3. Thus, we believe that the electrostatic interactions are mainly responsible for the binding energies and formation of hydrogen bonds, although the induction and dispersion interactions are also important. Since the electrostatic plays an important role, the polarization correlates with the electrostatic energy. The electronwithdrawing substituents hinder the electron transfer-driven polarization to the HF unit (which results in destabilization), whereas the electron-donating substituents allow strong polarization to the HF unit (which results in strong stabilization). It is also interesting to note that the polarization for the electron-donating and electron-withdrawing substituents in the complex 2 is slightly weaker than that in the complex 3. In the complex 3, the electron density at the para position is an important stabilizing factor, and thus the stabilization/destabilization by substituent of a pyridazine is governed mostly by the electrostatic energy. In Figure 4, a linear

			Complex 2					Complex 3		
	$E_{ m els}$	E_{ind}	$E_{ m exch}$	$E_{ m disp}$	$E_{ m int}^{ m SAPT}$	$E_{ m els}$	$E_{ m ind}$	E_{exch}	$E_{ m disp}$	$E_{ m int}^{ m SAPT}$
$N(CH_3)_2$	-25.53	-17.74	34.24	-5.16	-14.18	-26.21	-18.48	35.29	-5.27	-14.67
$NHCH_3$	-25.15	-17.41	33.69	-5.08	-13.94	-25.93	-18.29	35.00	-5.22	-14.45
NH_2	-24.34	-16.81	32.71	-4.95	-13.39	-25.16	-17.66	33.94	-5.09	-13.97
CH_3	-23.5	-16.35	31.87	-4.84	-12.83	-23.51	-16.40	31.90	-4.84	-12.84
C_2H_5	-23.73	-16.53	32.16	-4.88	-12.98	-23.75	-16.59	32.23	-4.88	-13.00
OCH_3	-22.95	-15.86	31.01	-4.75	-12.55	-23.99	-16.83	32.64	-4.94	-13.11
OH	-22.62	-15.72	30.90	-4.74	-12.19	-23.08	-16.16	31.54	-4.80	-12.51
Н	-22.80	-14.89	29.63	-4.06	-12.12	-22.70	-15.73	30.81	-4.69	-12.31
OF	-20.06	-14.07	27.96	-4.41	-10.59	-21.04	-14.78	29.27	-4.54	-11.09
CN	-18.92	-13.48	26.85	-4.28	-9.84	-19.37	-13.65	27.22	-4.31	-10.11
NO_2	-18.05	-12.92	25.87	-4.17	-9.28	-18.64	-13.06	26.27	-4.20	-9.62
F	-20.35	-14.27	28.35	-4.43	-10.71	-21.13	-14.84	29.39	-4.54	-11.12
Cl	-20.52	-14.49	28.57	-4.48	-10.93	-21.13	-14.84	29.29	-4.55	-11.23

TABLE 6: SAPT interaction energy decomposition (in kcal mol⁻¹) for the complexes 2 and 3.

All energies are in kcal mol⁻¹. $E_{\text{int}}^{\text{SAPT}} = E_{\text{els}} + E_{\text{ind}} + E_{\text{disp}} + E_{\text{exch}}$.

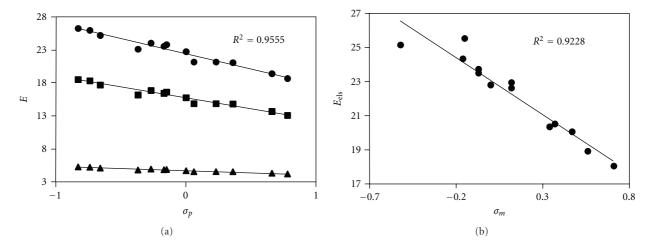


FIGURE 4: Linear relationship between the calculated SAPT interaction energy components ($\bullet E_{\text{els}}$, $\blacksquare E_{\text{ind}}$, and $\blacktriangle E_{\text{dis}}$ in kcal mol⁻¹) and σ_p for the complex **3** (a), and the electrostatic energy and σ_m for the complex **2** (b).

relationship with high correlation coefficient (R = 0.98) is observed between the calculated SAPT interaction energy components and σ_p in the complex **3**. In the complex **2**, a linear relationship with correlation coefficient 0.96 is found between the E_{els} and σ_m .

4. Conclusions

The results of quantum mechanical calculations indicate that the binding energy in the complex 3 is larger than that in the complex 2. The sum of binding energies of the complexes 2 and 3 is larger than the binding energy of the complex 1. So, there is a negative cooperativity for two hydrogen bond interactions.

Very good linear correlations are observed between the binding energies and Hammett electronic parameters σ_{total} of the substituents. The electron-donating substituents stabilize and the electron-withdrawing substituents destabilize the

complexes relative to pyridazine. According to the results of AIM analysis, the cooperativity effect decreases the electron density at the $N \cdot \cdot \cdot H$ BCPs in the X-pyridazine $\cdot \cdot \cdot (HF)_2$ complex.

On the basis of the results of SAPT analysis, the portion of electrostatic force in the complex 3 is smaller than 2, while the induction and dispersion portions are larger in the complex 3. The E^2 values of $lp_{N_2} \rightarrow \sigma_{HF}^*$ and $lp_{N_1} \rightarrow \sigma_{HF}^*$ interactions in the complex 1 are smaller than those in the complexes 2 and 3. Thus, the cooperativity effect decreases the E^2 values of $lp_{N_2} \rightarrow \sigma_{HF}^*$ and $lp_{N_1} \rightarrow \sigma_{HF}^*$ interactions in the complex 1. The occupation numbers of lp_{N_2} and lp_{N_1} in the complex 1 are larger than those in the complexes 2 and 3, respectively. The charge transfer, on the basis of ChelpG charges, is in agreement with the results of NBO and AIM analysis.

There are linear relationships between the V_{\min} and ρ_{BCP} values, the V_{\min} and the E^2 values of $lp_N \to \sigma_{HF}^*$ interaction, and between the V_{\min} and the σ_{total} values.

The SAPT calculations show that the electrostatic is the dominating interaction component in the complexes **2** and **3**, although the induction and dispersion interactions are also important. The dispersion energy component of the SAPT analysis was found to be very sensitive to the position of HF relative to the substituent. There is a good correlation between σ_p and the calculated SAPT interaction energy components in the complex **3**, while the linear relationship is only found between the $E_{\rm els}$ and σ_m in the complex **2**.

References

- [1] S. Breda, I. D. Reva, L. Lapinski, M. J. Nowak, and R. Fausto, "Infrared spectra of pyrazine, pyrimidine and pyridazine in solid argon," *Journal of Molecular Structure*, vol. 786, no. 2-3, pp. 193–206, 2006.
- [2] X. J. Zou, G. Y. Jin, and Z. X. Zhang, "Synthesis, fungicidal activity, and QSAR of pyridazinonethiadiazoles," *Journal of Agricultural and Food Chemistry*, vol. 50, no. 6, pp. 1451–1454, 2002
- [3] S. G. Lee, J. J. Kim, H. K. Kim et al., "Recent progress in pyridazin-3(2H)-ones chemistry," *Current Organic Chemistry*, vol. 8, no. 15, pp. 1463–1480, 2004.
- [4] R. V. A. Orru and M. de Greef, "Recent advances in solutionphase multicomponent methodology for the synthesis of heterocyclic compounds," *Synthesis*, no. 10, pp. 1471–1499, 2003.
- [5] N. G. Kandile, M. I. Mohamed, H. Zaky, and H. M. Mohamed, "Novel pyridazine derivatives: synthesis and antimicrobial activity evaluation," *European Journal of Medicinal Chemistry*, vol. 44, no. 5, pp. 1989–1996, 2009.
- [6] G. R. Desiraju and T. Steiner, The Weak Hydrogen Bond in Structural Chemistry and Biology, Oxford University Press, Oxford, UK, 1997.
- [7] G. R. Desiraju and T. Steiner, The Weak Hydrogen Bond, Oxford University Press, Oxford, UK, 1999.
- [8] M. Nishio, M. Hirota, and Y. Umezawa, The CH/π Interaction, Wiley-VCH, New York, NY, USA, 1998.
- [9] S. Scheiner, Ed., Molecular Interactions: from van der Waals to Strong Bound Complexes, John Wiley & Sons, Chichester, UK, 1997.
- [10] S. Scheiner, Ed., Hydrogen Bonding: A Theoretical Perspective, Oxford University Press, Oxford, UK, 1997.
- [11] G. A. Jeffrey and W. Saenger, *Hydrogen Bonding in Biological Structures*, Springer, Berlin, Germany, 1991.
- [12] G. A. Jeffrey, An Introduction to Hydrogen Bonding, Oxford University Press, Oxford, UK, 1997.
- [13] W. Wang, Y. Zhang, and K. Huang, "Unconventional interaction in N(P)-related systems," *Chemical Physics Letters*, vol. 411, no. 4–6, pp. 439–444, 2005.
- [14] W. Chen and M. S. Gordon, "Energy decomposition analyses for many-body interaction and applications to water complexes," *Journal of Physical Chemistry*, vol. 100, no. 34, pp. 14316–14328, 1996.
- [15] A. D. Kulkarni, R. K. Pathak, and L. J. Bartolotti, "Effect of additional hydrogen peroxide to $H_2O_2 \cdots (H_2O)n$, n=1 and 2 complexes: quantum chemical study," *Journal of Chemical Physics*, vol. 124, no. 21, Article ID 214309, 7 pages, 2006.
- [16] Q. Li, X. An, F. Luan et al., "Cooperativity between two types of hydrogen bond in H₃ C-HCN-HCN and H₃ C-HNC-HNC complexes," *Journal of Chemical Physics*, vol. 128, no. 15, Article ID 154102, 6 pages, 2008.

- [17] Y. L. Zhao and Y. D. Wu, "A theoretical study of β -sheet models: is the formation of hydrogen-bond networks cooperative?" *Journal of the American Chemical Society*, vol. 124, no. 8, pp. 1570–1571, 2002.
- [18] R. Wieczorek and J. J. Dannenberg, "H-bonding cooperativity and energetics of α -helix formation of five 17-amino acid peptides," *Journal of the American Chemical Society*, vol. 125, no. 27, pp. 8124–8129, 2003.
- [19] Q. Li, X. An, B. Gong, and J. Cheng, "Cooperativity between OH···O and CH···O hydrogen bonds involving dimethyl sulfoxide-H₂O-H₂O complex," *Journal of Physical Chemistry A*, vol. 111, no. 40, pp. 10166−10169, 2007.
- [20] H. Guo, N. Gresh, B. P. Roques, and D. R. Salahub, "Many-body effects in systems of peptide hydrogen-bonded networks and their contributions to ligand binding: a comparison of the performances of DFT and polarizable molecular mechanics," *Journal of Physical Chemistry B*, vol. 104, no. 41, pp. 9746–9754, 2000.
- [21] R. Viswanathan, A. Asensio, and J. J. Dannenberg, "Cooperative hydrogen-bonding in models of antiparallel β-sheets," *Journal of Physical Chemistry A*, vol. 108, no. 42, pp. 9205–9212, 2004.
- [22] F. H. Allen, J. A. K. Howard, V. J. Hoy, G. R. Desiraju, D. Shekhar Reddy, and C. C. Wilson, "First neutron diffraction analysis of an O-H $\cdots\pi$ hydrogen bond: 2-ethynyladamantan-2-ol," *Journal of the American Chemical Society*, vol. 118, no. 17, pp. 4081–4084, 1996.
- [23] B. S. Hudson, D. A. Braden, D. G. Allis et al., "The crystalline enol of 1,3-cyclohexanedione and its complex with benzene: vibrational spectra, simulation of structure and dynamics and evidence for cooperative hydrogen bonding," *Journal of Physical Chemistry A*, vol. 108, no. 36, pp. 7356–7363, 2004.
- [24] R. F. W. Bader, *Atoms in Molecules: A Quantum Theory*, Oxford University Press, Oxford, UK, 1990.
- [25] A. E. Reed, L. A. Curtiss, and F. Weinhold, "Intermolecular interactions from a natural bond orbital, donor-acceptor viewpoint," *Chemical Reviews*, vol. 88, no. 6, pp. 899–926, 1988.
- [26] B. Jeziorski, R. Moszynski, and K. Szalewicz, "Perturbation theory approach to intermolecular potential energy surfaces of van der waals complexes," *Chemical Reviews*, vol. 94, no. 7, pp. 1887–1930, 1994.
- [27] A. D. Becke, "Density-functional thermochemistry. III. The role of exact exchange," *Journal of Chemical Physics*, vol. 98, no. 7, pp. 5648–5652, 1993.
- [28] M. J. Frisch, G. W. Trucks, H. B. Schlegel et al., *Gaussian 03* (*Revision B.03*), Gaussian, Pittsburgh, Pa, USA, 2003.
- [29] C. Møller and M. S. Plesset, "Note on an approximation treatment for many-electron systems," *Physical Review*, vol. 46, no. 7, pp. 618–622, 1934.
- [30] Y. Zhao and D. G. Truhlar, "Benchmark databases for non-bonded interactions and their use to test density functional theory," *Journal of Chemical Theory and Computation*, vol. 1, no. 3, pp. 415–432, 2005.
- [31] S. F. Boys and F. Bernardi, "Calculation of small molecular interactions by differences of separate total energies—some procedures with reduced errors," *Molecular Physics*, vol. 19, no. 4, pp. 553–566, 1970.
- [32] F. B. König, J. Schönbohm, and D. Bayles, "AIM2000—A program to analyze and visualize atoms in molecules," *Journal of Computational Chemistry*, vol. 22, no. 5, pp. 545–559, 2001.

- [33] C. M. Breneman and K. B. Wiberg, "Determining atom-centered monopoles from molecular electrostatic potentials. The need for high sampling density in formamide conformational analysis," *Journal of Computational Chemistry*, vol. 11, no. 3, pp. 361–373, 1990.
- [34] P. Flukiger, H. P. Luthi, S. Portmann, and J. Weber, *Molekel 4.0*, Swiss Center for Scientific Computing, Manno, Switzerland, 2000.
- [35] M. W. Schmidt, K. K. Baldridge, J. A. Boatz et al., "General atomic and molecular electronic structure system," *Journal* of *Computational Chemistry*, vol. 14, no. 11, pp. 1347–1363, 1993.
- [36] R. Bukowski, W. Cencek, P. Jankowski et al., An Ab Initio Program for Many-Body Symmetry-Adapted Perturbation Theory Calculations of Intermolecular Interaction Energies. Sequential and Parallel Versions, University of Delaware, Newark, Del, USA; University of Warsaw, Warsaw, Poland, 2008.
- [37] C. Hansch, A. Leo, and R. W. Taft, "A survey of hammett substituent constants and resonance and field parameters," *Chemical Reviews*, vol. 91, no. 2, pp. 165–195, 1991.
- [38] L. P. Hammett, "Some relations between reaction rates and equilibrium constants," *Chemical Reviews*, vol. 17, no. 1, pp. 125–136, 1935.
- [39] F. Cozzi, F. Ponzini, R. Annunziata, M. Cinquini, and J. S. Siegel, "Polar interactions between stacked π systems in fluorinated 1,8-diarylnaphthalenes: Importance of quadrupole moments in molecular recognition," *Angewandte Chemie*, vol. 34, no. 9, pp. 1019–1020, 1995.
- [40] M. Alcamí, O. Mó, and M. Yáñez, "Modelling intrinsic basicities: the use of the electrostatic potentials and the atoms-in-molecules theory," *Theoretical and Computational Chemistry*, vol. 3, pp. 407–456, 1996.
- [41] C. H. Suresh and S. R. Gadre, "Electrostatic potential minimum on aromatic ring as a measure of substituent constant," *Inorganic Chemistry*, vol. 111, no. 4, pp. 710–714, 2007.
- [42] A. Ebrahimi, M. Habibi, and H. R. Masoodi, "Theoretical study of the influence of para- and meta-substituents on X-pyridine···HF hydrogen bonding," *Chemical Physics*, vol. 340, no. 1–3, pp. 85–92, 2007.
- [43] S. J. Grabowski and M. Małecka, "Intramolecular H-bonds: DFT and QTAIM studies on 3-(aminomethylene)pyran-2, 4-dione and its derivatives," *Journal of Physical Chemistry A*, vol. 110, no. 42, pp. 11847–11854, 2006.
- [44] S. J. Grabowski, "Ab initio calculations on conventional and unconventional hydrogen bonds-study of the hydrogen bond strength," *Journal of Physical Chemistry A*, vol. 105, no. 47, pp. 10739–10746, 2001.
- [45] E. Espinosa, C. Lecomte, N. E. Ghermani et al., "Hydrogen bonds: First quantitative agreement between electrostatic potential calculations from experimental X-(X + N) and theoretical ab initio SCF models," *Journal of the American Chemical Society*, vol. 118, no. 10, pp. 2501–2502, 1996.
- [46] B. Galabov and P. Bobadova-Parvanova, "Molecular electrostatic potential as reactivity index in hydrogen bonding: ab initio molecular orbital study of complexes of nitrile and carbonyl compounds with hydrogen fluoride," *Journal of Physical Chemistry A*, vol. 103, no. 34, pp. 6793–6799, 1999.
- [47] V. Dimitrova, S. Ilieva, and B. Galabov, "Electrostatic potential at atomic sites as a reactivity descriptor for hydrogen bonding. Complexes of monosubstituted acetylenes and ammonia," *Journal of Physical Chemistry A*, vol. 106, no. 48, pp. 11801–11805, 2002.

- [48] I. Mata, E. Molins, I. Alkorta, and E. Espinosa, "Topological properties of the electrostatic potential in weak and moderate N··· H hydrogen bonds," *Journal of Physical Chemistry A*, vol. 111, no. 28, pp. 6425−6433, 2007.
- [49] P. Politzer, J. S. Murray, and M. C. Concha, "Halogen bonding and the design of new materials: organic bromides, chlorides and perhaps even fluorides as donors," *Journal of Molecular Modeling*, vol. 13, no. 6-7, pp. 643–650, 2007.
- [50] P. W. Kenny, "Hydrogen bonding, electrostatic potential, and molecular design," *Journal of Chemical Information and Modeling*, vol. 49, no. 5, pp. 1234–1244, 2009.
- [51] D. J. R. Duarte, M. M. de las Vallejos, and N. M. Peruchena, "Topological analysis of aromatic halogen/hydrogen bonds by electron charge density and electrostatic potentials," *Journal of Molecular Modeling*, vol. 16, no. 4, pp. 737–748, 2010.
- [52] J. S. Murray, J. M. Seminario, M. C. Concha, and P. Politzer, "An analysis of molecular electrostatic potentials obtained by a local density functional approach," *International Journal of Quantum Chemistry*, vol. 44, no. 2, pp. 113–122, 1992.
- [53] G. Chałasiński and M. M. Szczęśniak, "State of the art and challenges of the ab initio theory of intermolecular interactions," *Chemical Reviews*, vol. 100, no. 11, pp. 4227–4252, 2000.
- [54] A. J. Stone, The Theory of Intermolecular Forces, Clarendon Press, Oxford, UK, 1996.
- [55] S. Tsuzuki and A. Fujii, "Nature and physical origin of CH/π interaction: significant difference from conventional hydrogen bonds," *Physical Chemistry Chemical Physics*, vol. 10, no. 19, pp. 2584–2594, 2008.
- [56] H. L. Williams and C. F. Chabalowski, "Using Kohn-Sham orbitals in symmetry-adapted perturbation theory to investigate intermolecular interactions," *Journal of Physical Chemistry A*, vol. 105, no. 3, pp. 646–659, 2001.
- [57] R. Bukowski, K. Szalewicz, and C. F. Chabalowski, "Ab initio interaction potentials for simulations of dimethylnitramine solutions in supercritical carbon dioxide with cosolvents," *Journal of Physical Chemistry A*, vol. 103, no. 36, pp. 7322– 7340, 1999.
- [58] D. Kim, S. Hu, P. Tarakeshwar, K. S. Kim, and J. M. Lisy, "Cation- π interactions: a theoretical investigation of the interaction of metallic and organic cations with alkenes, arenes, and heteroarenes," *Journal of Physical Chemistry A*, vol. 107, no. 8, pp. 1228–1238, 2003.
- [59] A. L. Ringer, M. S. Figgs, M. O. Sinnokrot, and C. D. Sherrill, "Aliphatic C-H/ π interactions: methane-benzene, methane-phenol, and methane-indole complexes," *Journal of Physical Chemistry A*, vol. 110, no. 37, pp. 10822–10828, 2006.

Hindawi Publishing Corporation Advances in Physical Chemistry Volume 2012, Article ID 720197, 17 pages doi:10.1155/2012/720197

Review Article

Potential Energy Surfaces for Reactions of X Metal Atoms (X = Cu, Zn, Cd, Ga, Al, Au, or Hg) with YH₄ Molecules (Y = C, Si, or Ge) and Transition Probabilities at Avoided Crossings in Some Cases

Octavio Novaro, María del Alba Pacheco-Blas, and Juan Horacio Pacheco-Sánchez²

¹ Instituto de Física, Universidad Nacional Autónoma de México, A.P. 20-364, 01000 Ciudad de México, DF, Mexico

Correspondence should be addressed to Octavio Novaro, novaro@fisica.unam.mx

Received 14 July 2011; Revised 4 October 2011; Accepted 22 November 2011

Academic Editor: Laimutis Bytautas

Copyright © 2012 Octavio Novaro et al. This is an open access article distributed under the Creative Commons Attribution License, which permits unrestricted use, distribution, and reproduction in any medium, provided the original work is properly cited.

We review *ab initio* studies based on quantum mechanics on the most important mechanisms of reaction leading to the C–H, Si–H, and Ge–H bond breaking of methane, silane, and germane, respectively, by a metal atom in the lowest states in C_s symmetry: $X(2nd \text{ excited state}, 1st \text{ excited state} \text{ and ground state}) + YH_4 \rightarrow H_3XYH \rightarrow H + XYH_3 \text{ and } XH + YH_3. \text{ with } X = Au, Zn, Cd, Hg, Al, and G, and Y = C, Si, and Ge. Important issues considered here are (a) the role that the occupation of the d-, s-, or p-shells of the metal atom plays in the interactions with a methane or silane or germane molecule, (b) the role of either singlet or doublet excited states of metals on the reaction barriers, and (c) the role of transition probabilities for different families of reacting metals with these gases, using the H–X–Y angle as a reaction coordinate. The breaking of the Y–H bond of YH₄ is useful in the production of amorphous hydrogenated films, necessary in several fields of industry.$

1. Introduction

Here, an overview of potential energy surface (PES) calculations for reactions of a metal atom with a gas molecule has been compiled. Among metal atoms, we consider cadmium, copper, zinc, gallium, aluminum, mercury, and gold, and among gas molecules methane, silane, and germane. The potential energy surfaces of an YH₄ molecule with a metal atom were determined using ab initio Hartree-Fock Self-Consistent Field (HF-SCF) calculations, where the atom core is represented by relativistic effective core potentials (RECPs) [1–5]. These calculations are followed by a Multiconfigurational Self Consistent Field (MC-SCF) study [6]. The correlation energy is accounted for through extensive variational and perturbative second-order multireference Moller-Plesset configuration interaction (MR-CI) analysis of selected perturbations obtained by iterative process calculations using the CIPSI program package [7]. The reference

(S) spaces used for the variational CI of the molecular states arising from the three $X + CH_4$ asymptotes contain between 108 and 428 determinants, which generate between 7 million and 111 million perturbed MP2 determinants near the region of the reactants and the equilibrium geometry of the methyl-metal-hydride intermediate, respectively. This methodology is particularly useful in the study of systems constituted by a few atoms.

Transition probabilities for the interaction of the lowest excited states of the metal X with tetrahedral gas molecules are studied through one-dimensional Landau-Zener theory. The strategy for obtaining the reaction pathways for X + YH₄ interactions has been extensively used in references [8–14] based on the original proposal by Chaquin et al. [15]. The initial approach (starting from 20 a.u.) of the X atom to one Y–H bond was done in a C_s symmetry in a plane containing the X, Y, and two hydrogen atoms. All the angles and distances obtained by a self-consistent field approach to

² División de Estudios de Posgrado e Investigación, Instituto Tecnológico de Toluca, A.P. 890, 52140 Metepec Edo. Mex, Mexico

find the molecular geometry of the HXYH3 intermediate are exhibited in Figure 1. From these parameters, $\theta = H-X-Y$ is the first angle fixed in order to optimize the other angles and distances for each point on a potential energy curve, and taking steps of 10 degrees for the θ angle. When two energy levels cross each other as a function of time, the semiclassical theory of time-dependent Landau-Zener theory [16, 17] for nonadiabatic transition can be utilized. Zener [17] proposed a transition probability from one potential energy curve to another as a linear velocity function, using the distance ras the reaction coordinate. Whereas for an angular velocity using the angle θ as the reaction coordinate, all developments established by Zener are still valid, given that for determining a time-dependent transition probability, the Schrödinger equation must be used. Thus, the transition probability from one-potential energy curve to another is an angular velocity function, using the angle θ as the reaction coordinate. Our theoretical results predict the formation of XH + YH₃ or H + XYH₃ products after breaking the intermediate HXYH₃. Some of these products are useful in the industry to get hydrogenated amorphous films (a-Y:H) among the other applications [18–30].

The complexity of the organometallic systems, aggregates, and metallic surfaces makes it difficult to determine the fundamental mechanisms which govern their interactions with hydrocarbons. In this situation, one begins with a study of the interaction of a single metallic atom with a hydrocarbon molecule as a model to understand the conditions that the metallic center in these activations requires. Thus, the study of the interaction of the different metallic atomic states with the methane, silane, or germane molecule is fundamental in elucidating the role of various d-, s-, or p-orbital occupations in a metal atom.

Experimental studies [31–38] carried out on the photolysis induced by the metallic atom excitation in a matrix of methane at low temperatures show that when the C–H bond of methane activates through photoexcited metallic atoms deposited in a matrix at low temperatures, the process only happens with radiation wavelengths previously known to be absorbed in the free atom, allowing it to achieve a transition to an excited state. The very low temperature of the matrix fixes the position and also reduces the internal movements of methane molecules contained in it, allowing the interaction of C–H bonds with deposited metallic atoms.

The photochemical studies on the metal-alkane interaction have attracted the attention of researchers for long time. It is worth mentioning that in 1985 the work entitled "Activation of Methane by Photoexcited Copper Atoms and Photochemistry of Methylcopper Hydride in Solid Methane Matrices," developed in Lash Miller laboratories of the University of Toronto in Canada by the G.A Ozin group [32] was considered in the publication analysis of Scientific Information Institute (current contents) as the most promising work of that year.

At room temperature and standard pressure, methane (CH₄) is a colorless, odorless, and flammable gas [39], in fact the simplest hydrocarbon. It is the major constituent of natural gas and is released during the decomposition of plants or other organic compounds, as in marshes and coal

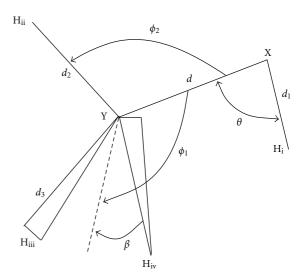


FIGURE 1: The eight $(\theta, \phi_1, \phi_2, \beta, d, d_1, d_2, \text{ and } d_3)$ geometrical parameters used for the optimal X + YH₄ reaction pathway.

mines. Methane is the first member of the alkane series. The strength of the carbon hydrogen covalent bond in methane is perhaps the strongest in all hydrocarbons, and, thus, its use as a chemical feedstock is limited. Despite the high activation barrier for breaking the C–H bond, CH₄ is still the main starting material for manufacture of hydrogen in steam reforming. The search for catalysts which can facilitate C–H bond activation in methane (105 kcal mol⁻¹ to break it) and other low alkanes is an area of research with considerable industrial significance [40].

Silane is a chemical compound (SiH₄) analogous to methane, and it is also a gas at room temperature which undergoes spontaneous combustion in air. The name "silane" is also given to a family of compounds that are silicon analogs of alkane hydrocarbons. The radical SiH₃ is termed silyl. The nomenclature parallels that of alkyl radicals. Silane may also carry certain functional group, just as alkanes do. There is (at least in principle) silicon analog for each carbon alkane. Silanes are useful for several industrial and medical applications. For instance, they are used as coupling agents to adhere glass fibers to a polymer matrix, stabilizing the composite material. They can also be used to couple a bioinert layer on a titanium implant. Other applications include water repellents, masonry protection, control of graffiti, applying polycrystalline silicon layers on silicon wafers when manufacturing semiconductors, and sealants. In addition, silane and similar compounds containing Si-H bonds are used as reducing agents in organic and organometallic chemistry [41–47].

Germane is the chemical compound with the formula GeH₄, and an analog of methane. It is the simplest germanium hydride and one of the most useful compounds of germanium. Like the related compounds silane and methane, germane is tetrahedral. It burns in the air to produce GeO₂ and water. Some processes for the industrial manufacture of germane [48], in which our calculations might be useful, are (a) chemical reduction method, (b) an electrochemical

reduction method, and (c) a plasma-based method. The gas decomposes near 600 K to germanium and hydrogen. Germane is used in the semiconductor manufacturing for epitaxial growth of germanium [49]. Organogermanium precursors have been examined as less hazardous liquid alternatives to germane for deposition of Ge-containing films [50]. Germane is flammable and toxic.

The quantum chemistry studies presented here provide valuable information about the activation of methane or silane or germane molecules with metal atoms. Products of these reactions are methyl CH₃ or silyl SiH₃ or germyl GeH₃ radicals, which are key in surface growth of amorphous hydrogenated carbon or silicon or germane films (thin films).

Methane CH₄, silane SiH₄, and Germane GeH₄ species turn out to be valuable substances in the industry of the semiconductors since the germane or silane or methane dehydrogenation in gaseous phase is one of the most current methods to obtain semiconductors in the form of amorphous hydrogenated carbon (a-C:H) [51] or silicon (a-Si:H) [52] or germane (a-Ge:H) [53] thin films. The interaction of CH3, SiH3, or GeH3 radicals and atomic hydrogen with the surfaces of carbon, silicon or germane films a-C: H, a-Si: H, or a-Ge: H plays a fundamental role in the understanding of the growth of these plasma films at low temperature. Street [54] says that the dehydrogenated material has a very high defect density which prevents doping, photoconductivity, and the other desirable characteristics of a useful semiconductor. While a real crystal contains defects such as vacancies, interstitial, and dislocations, the elementary defect of an amorphous semiconductor is the coordination defect, when an atom has too many or too few bonds [54]. Defect equilibrium is in general described by a reaction of the type

$$A + B \stackrel{\longleftarrow}{\Longrightarrow} C + D,$$
 (1)

where A–D are different configurations of point defects, dopants, electronic charges, and so forth. The properties of interest are the equilibrium state and the kinetics of the reaction [54]. Calculations as those accomplished by us mentioned previously might help to find these properties. As an example, our calculated energy of the intermediate corresponds to the defect formation energy U_d which determines the equilibrium defect density, as part of the kinetics of reaction.

Methyl radical absorption on carbon or hydrocarbon thin films is key in thin-film growth at low-temperature plasmas ($< T_{\text{room}}$) using hydrocarbon precursor gases.

The current production procedure of amorphous hydrogenated carbon (*a*-C:H) or silicon (*a*-Si:H) films is the deposition by means of the decomposition of methane or silane through glow discharges produced by radio frequency (RF). This method is known as plasma-enhanced chemical vapor deposition (PECVD) [55].

The breaking of the C–H bond of CH₄ is useful for generating amorphous hydrogenated carbon (*a*-C:H) films, which represent a class of high-technology materials with mechanical, optical, chemical, and electrical properties among polymeric, graphite, and diamondoid films.

The (*a*-C:H) is of interest to the electronic industry as a viable and cheap semiconductor that can be prepared in an ample rank of layers. The fine layer of *a*-C:H, also well-known as diamondoid carbon, is used as a revesting material of hard and low friction. The polymeric film *a*-C:H has a strong photoluminescence and is being developed as an electroluminescent material. It is also used as dielectric in metal-insulator-metal switch in screens of active matrix. The ability of deposition near to room temperatures using cheap methods of chemical vapor deposition (CVD) makes this material useful for the industry. The amorphous nature of these materials and their relative facility of deposition make them ideals for its use in a great amount of applications such as in panels of flat screen and diamondoid technology [56].

The *a*-C:H films are prepared through a glow discharge of RF in a pure methane atmosphere at different gas pressures in which the methane decomposition generates the methyl CH₃ radical, which plays a preponderant role in the generation of amorphous hydrogenated carbon surfaces [57, 58]. The electronic industry takes profit of the previous proceeding on the formation of diamondoid films.

Dense amorphous hydrocarbons have some of the highest densities among hydrocarbon and fall between crystalline diamonds and adamantanes, according to Angus [59]; this is the property that makes it so attractive to the electronic industry.

In case of diamondoid formation,

- (1) some excited metallic atoms break the C–H bond of methane with the consequent production of methyl CH₃ radicals [8, 60, 61]. Knowing that a dangling bond is an unsatisfied valence on an immobilized atom, the methyl CH₃ radicals undergo a chemisorption process controlled by the creation of dangling bonds in the *a*-C:H surface by an atom H. This is a proper process in the formation of diamondoid films in the electronic industry [62],
- (2) Ramírez and Sinclair [63] (and Velasco-Santos et al., [64]) affirm that carbonaceous natural products can have different allotropic forms of the carbon, since the amorphous carbon has graphite transitions at different temperatures when some specific metals are in contact with carbon and act as catalysts,
- (3) methyl CH₃ radicals can also be generated by photodissociation of aromatic hydrocarbon, consequently amorphous hydrogenated carbon thin films can be produced. Taguchi et al. [65] used two classes of laser (ArF or KrF) and two types of aromatics (benzene C₆H₆ or toluene C₆H₅–CH₃) to generate diamondoid films.

The breaking of Si–H bond of SiH₄ is useful in manufacture of semiconductor films of amorphous hydrogenated silicon (a-Si:H). Before the a-Si:H material has been developed, the research was on amorphous silicon without hydrogen, prepared by sputtering or by thermal evaporation.

There are at least two models for the generation of amorphous hydrogenated silicon (a-Si:H).

(i) In the thermodynamic approach [62, 66, 67], the formation of dangling bonds, the principle defect in *a*-Si:H, is attributed to the breaking of weak Si–Si bonds caused by mobile H that is released from Si–H bonds [68]:

$$H + weak bond \longrightarrow Si-H + broken bond.$$
 (2)

(ii) In the Matsuda-Gallagher-Perrin MGP model [66, 67], SiH₃ is assumed to be the only growth precursor. This assumption is based on the (presumed) dominance of this radical in plasmas leading to the device-quality a-Si: H.

The central assumption in the MGP model is that the SiH₃ reaching the *a*-Si:H can go to a weakly adsorbed (physisorbed) state forming a three-center Si–H–Si bond on a surface Si–H site. The activation of silane molecules has received a lot of attention as much in the experimental aspect [61, 69–72] as in the theoretical [9, 73]. The activation of the Si–H bond is important as much in the processes of polymerization of silane [74, 75], as in organometallic catalytic reactions [76–78].

The growth of amorphous hydrogenated silicon films *a*-Si: H in silicon substrata through PECVD in silane is widely used in the manufacture of electronic, optoelectronic, and photovoltaic devices. Amorphous semiconductors of thin films are used in an ample variety of applications such as solar cells, TFT, photoreceptors, and apparatus of images [79].

The *a*-Ge: H films are prepared through a glow discharge of RF in a pure germane atmosphere at different gas pressures in which the germane decomposition generates the germyl GeH₃ radical, which plays a preponderant role in the generation of amorphous hydrogenated germane surfaces [53].

Here we stress some important results at metal-methane, metal-silane, and metal-germane interactions grouped in three different families (coinage metals: Cu and Au. Pseudotransition metals: Zn, Cd, and Hg, and metals: Al and Ga). Castillo et al. [8, 60, 80] carried out calculations of potential energy surfaces of the interactions copper methane and zinc methane with the aim of determining the mechanisms of reaction that involve the three lowest states of the copper atom (2S, 2D, and 2P) as well as to determine the reaction routes that govern the interaction of the three lowest states of the zinc atom (¹S, ³P, and ¹P) in the process of the C–H bond activation of the methane molecule. Luna-García et al. [11, 12, 81] found the interaction potential curves of the mercury-Germane, cadmium-Germane, copper-silane, and copper-germane in the three lowest states of each metal; he improved a computational methodology to get the products of the breaking of the intermediate. Pacheco-Sánchez et al. [13, 14, 40] achieved the calculation of gallium-methane and gallium-silane interactions as much in the ground state as in the two lowest excited states of gallium; he extended Landau-Zener theory [82-85] to use the angle instead of the distance as reaction parameter in transition probability calculations at avoided crossings. Transition probability theory is described here when the reaction parameter is distance or angle. In addition, our group has considered also the following interactions: cadmium methane [86], zinc silane [9], cadmium silane [10], mercury silane [9], gold silane [87], and recently aluminum methane [88].

2. Transition Probability Theory

When two potential energy curves are very near to each other, it seems that they crossover. Actually, in the apparent crossover point, the system is degenerate, since the two different electronic configurations have the same energy [89]. This introduces a resonance energy that separates the surfaces slightly, in such way that they never intersect but only closely approach to each other before repelling. Whereas the wave function of the molecule in a given curve is of one character before the crossing point (CP) and of another character after it, the wave function of the other curve is reversed in turn; an example is given in Figure 2, where we can see that while the wavefunction ψ_1 has $6p^1$ character before CP at ξ_0 and 6s¹ character after CP at ξ_0 , the wavefunction ψ_2 has $6s^1$ character before CP at ξ_0 and $6p^1$ character after CP at ξ_0 . If ξ changes with a finite velocity, the probability that the molecule changes of a wave function to the other when passing through the crossing point is in such way that its electronic state is represented by a linear combination of the type

$$\psi = A_1(\xi)\psi_1 + A_2(\xi)\psi_2,\tag{3}$$

where $\xi = r$ or $\xi = \theta$ according to the reaction coordinate in study. By convenience in the calculation of A_1 and A_2 , the eigenfunctions ψ_1 and ψ_2 are expressed in terms of two other wave functions φ_1 and φ_2 with energies ϵ_1 and ϵ_2 , respectively, which intersect when they are plotted as functions of the internuclear distance (or angle). Due to the fact that φ_1 and φ_2 are not exact eigenfunctions of the whole Hamiltonian at the crossing point, the interaction energy ϵ_{12} between the two states φ_1 and φ_2 have to be included, then $E_1 = \epsilon_1 - \epsilon_{12}$ and $E_2 = \epsilon_2 + \epsilon_{12}$, where ϵ_{12} is the difference between the exact eigenvalues E_1 and E_2 and the approximate eigenvalues ϵ_1 , ϵ_2 : $\epsilon_{12}(\xi_0) =$ $(E_1(\xi_0) - E_2(\xi_0))/2$. Normalizing and orthogonalizing all the wavefunctions involved, and following the one-dimensional (distance as reaction coordinate) developments established by Zener [17] for a time-dependent Schrödinger equation, we obtain the transition probability as

$$P = e^{-2\pi\gamma},\tag{4}$$

where

$$\gamma = \frac{2\pi}{h} \frac{\epsilon_{12}^2}{\left| (d/dt)(\epsilon_1 - \epsilon_2) \right|^2}.$$
 (5)

The denominator can be expressed as

$$\left| \frac{d}{dt} (\epsilon_1 - \epsilon_2) \right| = \eta \left| \frac{\partial \epsilon_1}{\partial \xi} - \frac{\partial \epsilon_2}{\partial \xi} \right| = \eta |s_1 - s_2|, \quad (6)$$

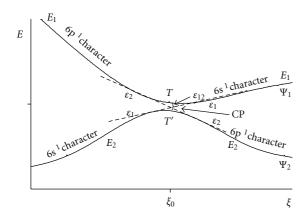


FIGURE 2: Typical graph of transition probabilities. Energy as a function of the insertion angle θ , where the two *solid lines* correspond to the avoided crossing at ξ_0 , and the *dashed lines* to the probable transitions among potential energy surfaces.

where $\eta = d\xi/dt$ is the velocity ($\eta = v$ or $\eta = \omega$, v means linear and ω means angular velocity) at which the system crosses $\xi = \xi_0$, and $|s_1 - s_2|$ is the difference of the slopes of the two potential surfaces crossing at ξ_0 . Finally, we have

$$P = e^{-(4\pi^2 \epsilon_{12}^2 / h\eta |s_1 - s_2|)} \tag{7}$$

for the transition probability of nonadiabatic behavior. The probability for a system remaining in the initial energy surface is then

$$P' = 1 - e^{-(4\pi^2 \epsilon_{12}^2 / h\eta |s_1 - s_2|)}.$$
 (8)

Rosenkewitsch [90] states that Zener [17] has obtained a similar formula to that one obtained by Landau [16] (or (7) above)

$$P \approx e^{-(\pi/2hv)(\Delta^2/F_1 - F_2)},\tag{9}$$

where $\Delta=2\epsilon_{12},v$ is the relative velocity, and F_1 and F_2 are "forces" acting on the two states. Making the identification $d/dt(\epsilon_1-\epsilon_2)=v(F_1-F_2)$ which corresponds to the change of pure kinetics energy with time, we can almost have the equation found by Zener ((7) when $\eta=\nu$), because the exponent of the Landau formula also has a factor of 2π .

Explicit calculations of transition probabilities of nonadiabatic behavior using (7) are straightforward when the reaction coordinate is the distance [91, 92] (in these cases gas is hydrogen and metal is ruthenium [91] and platinum [92]); however, when the latter is the angle, it will be necessary to calculate the angular velocity and the moment of inertia as accomplished in references [40, 82–85, 87, 88] for tetrahedral molecules interacting with metals.

2.1. Interactions of the Cu, Au Coinage Metals with YH₄. Castillo et al. [60] found that copper in its second excited state (2 P: 3 d 10 4p 1) breaks the C–H bond of methane, and its avoided crossing with the first excited state allows (2 D: 3 d 9 4s 2) to surpass a barrier of 48 kcal mol $^{-1}$. We have a transition energy of \sim 83 kcal mol $^{-1}$ between the states 2 P and 2 D and transition energy of \sim 43 kcal mol $^{-1}$ between

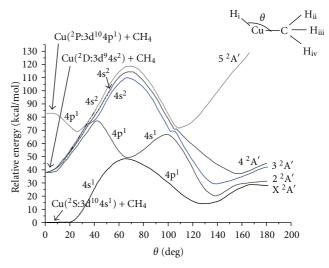


FIGURE 3: Insertion mechanism of the three lowest states of the Cu atom (2S , 2P , and 2D) into a C–H bond of methane. ${}^2A'$ interaction energy states as a function of the angle theta. The $4p^1$ character follows the path from the second excited state to the minimum in the X A' state, where the final products are formed.

the states ²D and ²S (see Table 1 and Figure 3). Transition probability (TP) values at four avoided crossings [82] are obtained when copper is photoexcited to this second excited state Cu (²P: 3d¹⁰ 4p¹), given that this copper atom is inserted in the methane molecule. It is also noteworthy [60] that the ground state is initially repulsive, but due to the avoided crossings, it became attractive after surmounting a rather high barrier. This behavior is initially exhibited at the first minimum (69 kcal mol⁻¹, 26°) of the 5 ²A' state forming the HCuCH₃ intermediate, which when continuing its path has a probability P = 0.68 of crossing towards the 4^2 A' state with $4p^1$ character and a probability P = 0.32 of continuing by the same 5 ²A' state with 4s² character. When following via 4 ²A' has a probability P = 0.61 of crossing towards the 3^2 A' state with $4p^1$ character and a probability P = 0.39 of continuing by the same 4 ²A' state with 4s² character. When continuing via 3 ²A', a very small potential barrier is surmounted with a probability P = 0.65 of crossing towards the $2^2A'$ state with $4p^1$ character, and a probability P = 0.35 of continuing by the same 3 ²A' state with 4s² character. When continuing via 2²A', it descends until reaching X²A', then it has a probability P = 0.62 of crossing towards the X^2A' state with $4p^1$ character and a probability P = 0.38 of continuing by the same 2 ²A' state (see Figure 3) with 4s¹ character. Finally, when continuing via X ²A' state (with 4p¹ character), while the theoretical energy of the HCuCH₃ intermediate is 14 kcal mol⁻¹, the experimental energy is between 15 and 25 kcal mol⁻¹. From here we can build the corresponding potential energy surfaces leading to the products by calculating the energy against the distance [60]. These products are H + CuCH₃ and HCu + CH₃, with theoretical energies 52 and 41 kcal mol⁻¹, respectively, and experimental energy values 46 and 40 kcal mol^{-1} , respectively, as mentioned in Table 1.

Pacheco-Sánchez et al. [87] have found that Gold in its second excited state (²P: 5d¹⁰ 6p¹), through a series

TABLE 1: Coinage metal family (Cu, Au). Relative energies (kcal mol ⁻¹) of the reactants, intermediary HXYH ₃ and final products for
three states of the metal. X(2nd): metal in second excited state. X(1st): metal in first excited state. X(gs): metal in ground state. $\Delta E_{\rm Exp}$:
experimentally measured energy. $\Delta E_{ m Cal}$: theoretically calculated energy.

	Y: Methane Cu ^a			Y:		Y: Germane			
X: Metal			A	Au^b		Cu ^c	Cu ^c		
	$(^{2}S, ^{2}$	D, ² P)	$(^{2}S, ^{2})$	D, ² P)	$({}^{2}S, {}^{2}$	² D, ² P)	$(^{2}S, ^{2}D,$	$({}^{2}S, {}^{2}D, {}^{2}P)$	
	$\Delta E_{ m Exp}$	$\Delta E_{ m Cal}$	$\Delta E_{ m Exp}$	$\Delta E_{ m Cal}$	$\Delta E_{ m Exp}$	$\Delta E_{ m Cal}$	Exp^d	Cal.	
X(2nd) + YH ₄	85	~83	114.3	109.8	87.8	87.7	87.8	87.7	
$X(1st) + YH_4$	34.9	~43	40.23	41.5	34.4	39.0	34.4	39	
$H + XYH_3$	46	52 ^a		30.91		36.0		33.2	
$HX + YH_3$	40	41a	18.25	21.9	27.7	33.2	21.7e	27.1	
$HXYH_3$	15-25	14^{a}		3.34		5.8		1.6	
$X(gs) + YH_4$	0	0	0	0	0	0	0	0	

^a From [80]

of avoided crossings that diminish the barriers for the ground state and first excited state, breaks the Si-H bond of silane, finally overcoming a barrier of 24.0 kcal mol⁻¹ of the ground state. The experimental transition energy between the excited state (²P: 5d¹⁰ 6p¹) and the ground state (²S: 5d¹⁰ 6s¹) is 114.28 kcal mol⁻¹, which is comparable to the transition energy of 109.8 kcal mol⁻¹ calculated by Pacheco-Sánchez et al. (Table 1). Then, the HAuSiH₃ intermediate encounters four avoided crossings between trajectories C²A', B²A', A²A', and X²A' of the energy surfaces. When gold is photoexcited to its second excited state ²P: 5d¹⁰ 6p¹, it initially passes through the avoided crossing around (77 kcal mol⁻¹, 28°) of D²A' state, and there are two possibilities of the intermediate formed for following a trajectory. Taking it to pass the avoided crossing, it has a probability P = 0.802 [87] for crossing towards C^2A' maintaining the 6p¹ character, where it finds another avoided crossing, and there is a probability of 0.737 for crossing toward B²A' also maintaining the 6p¹ character. Here it finds another avoided crossing, and there is a probability of 0.803 of crossing toward the A²A' still maintaining the 6p¹ character (see Figure 4). Henceforth, it finds the last avoided crossing, and there is a probability of 0.541 of crossing to the X ²A' maintaining the 6p¹ character too, where the products are reached at 120°. Finally, the intermediate with energy 3.34 kcal mol⁻¹ evolves toward the HAu + SiH₃ and AuSiH₃ + H products, whose energies are 21.9 and 30.91 kcal mol^{-1} . These products are of greater energy than the reactants, something typical in an endergonic reaction in which the reaction requires absorption of energy.

Luna-García et al. [12] have found that copper in its second excited state (${}^{2}P$: $3d^{10}$ $4p^{1}$) breaks the Si–H bond of silane, in a manner quite similar to the previous cases surpasses a barrier of 26.0 kcal mol⁻¹ of the ground state. The experimental transition energy between the excited state (${}^{2}P$: $3d^{10}$ $4p^{1}$) and the ground state (${}^{2}S$: $3d^{10}$ $4s^{1}$) is 87.8 kcal mol⁻¹, which agrees with the transition energy

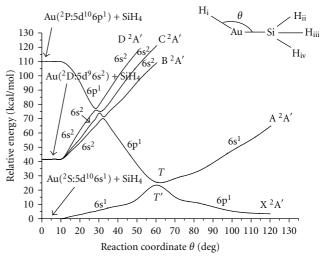


FIGURE 4: Au (2 S, 2 P, and 2 D) with SiH₄ interaction potential energy curves versus the θ insertion angle towards the HAuSiH₃ intermediate product. The 6p¹ character follows the path from the second excited state to the minimum in the X 2 A′ state, where the final products are formed.

of $87.7 \, \text{kcal mol}^{-1}$ theoretically calculated (Table 1). The initial formation of the HCuSiH₃ intermediate starts at the minimum ($70 \, \text{kcal mol}^{-1}$, 20°) with $4p^1$ character and encounters four avoided crossings among trajectories $4^2 \, \text{A}'$, $3^2 \, \text{A}'$, $2^2 \, \text{A}'$, and $X^2 \, \text{A}'$ of the energy surfaces (see Figure 5). Finally, due to the endergonic nature of this reaction, the intermediate with energy $5.8 \, \text{kcal mol}^{-1}$ (and $4p^1 \, \text{character}$) is divided into the HCu + SiH₃ and CuSiH₃ + H products with theoretical energy values of $33.2 \, \text{and} \, 36.0 \, \text{kcal mol}^{-1}$, respectively (see Table 1). In the same Table, we could only report the experimental energy value $27.7 \, \text{kcal mol}^{-1}$ of HCu + SiH₃ products.

^bFrom [87]

cFrom [12]

dFrom [93]

^eFrom [94].

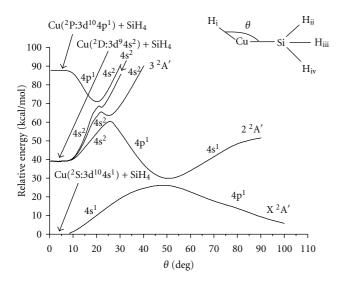


FIGURE 5: Potential energy curves of the $Cu(^2S, ^2D, ^2P)$ interaction with SiH_4 as a function of the insertion angle (θ) towards the HCuSiH $_3$ intermediate product. The $4p^1$ character follows the path from the second excited state to the minimum in the X^2A' state, where the final products take place.

Luna-García et al. [12] have found that again copper in its excited state (²P: 3d¹⁰ 4p¹) breaks a Ge–H bond of germane, overcoming a barrier of $27.0 \,\mathrm{kcal} \,\mathrm{mol}^{-1}$ of the ground state. The experimental transition energy between the excited state $(^{2}P: 3d^{10} 4p^{1})$ and the ground state $(^{2}S: 3d^{10} 4s^{1})$ is of 87.8 kcal mol⁻¹, which agrees with the transition energy of 87.7 kcal mol⁻¹ theoretically calculated (Table 1). The initial formation of the HCuGeH3 intermediate starts at the minimum (72 kcal mol⁻¹, 17°) with 4p¹ character and passes through four avoided crossings with the trajectories 4²A', $3^2A'$, $2^2A'$, and X^2A' of the energy surfaces (see Figure 6). Finally the intermediate with energy 1.6 kcal mol⁻¹ (and 4p¹ character) evolves toward HCu + GeH3 and CuGeH3 + H products with 27.1 and 33.2 kcal mol⁻¹, respectively (see Table 1). The latter is due to the endergonic nature of the reaction. In the same table, there is only the experimental energy value $21.7 \text{ kcal mol}^{-1}$ of HCu + GeH₃ products.

2.2. Interactions of the Zn, Cd, and Hg Pseudotransition Metals with YH₄. Castillo et al. [8] found that Zinc in its first excited state (1P: 3d10 4s1 4p1) lying 141 kcal mol-1 high breaks the C-H bond of methane, while the Zn ground state presents a quite high activation barrier of 90.5 kcal mol⁻¹ (see Figure 7, Table 2(a)). The TP of the potential energy surfaces $(2^{1}A' \rightarrow X^{1}A')$ is obtained for the reaction: Zn $(^{1}P:$ $4s^1 4p^1$) + CH₄ \rightarrow Zn (¹S: $4s^2$) + CH₄ through one avoided crossing; thenceforth, the products of the reaction Zn + CH₄ are reached. This happens when zinc is photoexcited to the second excited state Zn (1P: 3d10 4s1 4p1), which allows this zinc atom to be inserted in the methane molecule. The latter effect is initially exhibited at the minimum (93 kcal mol⁻¹, 59°) of the 2 ¹A' state forming the intermediate HZnCH₃, which when continuing its path has a probability [82] P =0.81 of crossing towards the X ¹A' state and a probability

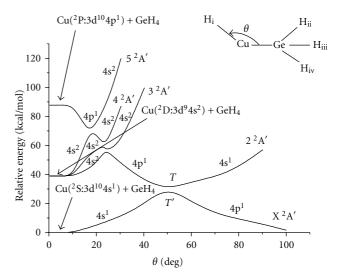


FIGURE 6: Potential energy curves of the $Cu(^2S, ^2D, ^2P)$ interaction with GeH_4 as a function of the insertion angle (θ) towards the $HCuGeH_3$ intermediate product. The $4p^1$ character goes by the path from the second excited state to the minimum in the X^2A' state, where the final products take place.

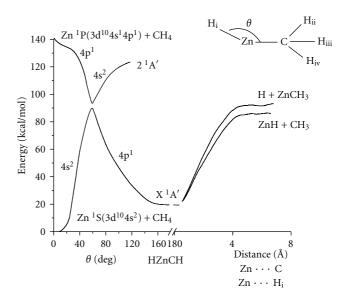


Figure 7: Potential energy surfaces of the interaction of both $Zn(^1S) + CH_4$ and $Zn(^1P) + CH_4$. The $4p^1$ character follows the path from the second excited state to the minimum in the X^1A' state, where the final products are formed. In this figure, $Zn...H_i$ means that product H + ZnCH3 arises from sending to infinity the H_i , and Zn...C means that product ZnH + CH3 arises from sending to infinity the H_iZn .

P=0.19 of continuing by the same 2 1 A' state. When following via X 1 A' (see Figure 7), at the minimum of this state, the product formation can be obtained [82]. Finally, acquiring the formation of the HZnCH₃ intermediate with a calculated energy of \sim 25 kcal mol $^{-1}$ that passes through the avoided crossing of 2 1 A' and X 1 A' sates, with the subsequent formation of HZn + CH₃ and ZnCH₃ + H final products,

Table 2 (a) Pseudotransition metal family (Zn, Cd) interacting with methane. Relative energies (kcal mol^{-1}) of the reactants, intermediate HXCH₃, and final products for three lowest states of the metals.

Monatal		n ^a	Cd ^b		
M: metal	(18, 3	P, ¹ P)	(18, 3	$ \frac{\Delta E_{\text{Cal}}}{\Delta E_{\text{Cal}}} $ 125.6 84.9 67.9 56.6 31.9°	
	$\Delta E_{ m Exp}$	$\Delta E_{ m Cal}$	$\Delta E_{ m Exp}$	ΔE_{Cal}	
$M(2nd) + CH_4$	133.7	~141	124.9	125.6	
$M(1st) + CH_4$	93.4	~94	89.3	84.9	
$H + MCH_3$		~93		67.9	
$HM + CH_3$		~82		56.6	
HMCH ₃		~25		31.9°	
$M(gs) + CH_4$	0	0	0	0	

^a From [80]

⁽b) Pseudotransition metal family (Zn, Cd, Hg) interacting with silane. Relative energies (kcal mol^{-1}) of the reactants, the HXSiH₃ intermediary and final products for threelowest states of these metals.

M: metal	Z: (1S, 3	n ^a P, ¹ P)	Cd ^b (¹ S, ³ P, ¹ P)		Hg ^b (¹ S, ³ P, ¹ P)	
	$\Delta E_{ m Exp}$	$\Delta E_{ m Cal}$	$\Delta E_{ m Exp}$	$\Delta E_{ m Cal}$	$\Delta E_{ m Exp}$	$\Delta E_{ m Cal}$
$M(2nd) + SiH_4$	133.7	141	124.9	128.5	154.6	157.6
$M(1st) + SiH_4$	93.4	93.8	89.3	84.4	119.5	114.6
$H + MSiH_3$		84		89.0		95.4
$HM + SiH_3$	70.4	74	74	75.5	83.33	87.6
HMSiH ₃		11.5		20.7		28.0
$M(gs) + SiH_4$	0	0	0	0	0	0

^aFrom [9]

⁽c) Pseudotransition metal family (Cd, Hg) interacting with germane. Relative energies (kcal mol⁻¹) of the reactants, the HXGeH₃ intermediary, and final products for three lowest states of these metals.

	C	da	Нұ	y ^a
X: metal	$({}^{1}S, {}^{3}$	P, ¹ P)	$({}^{1}S, {}^{3}I$	P, ¹ P)
	ΔExp^b	$\Delta E_{ m Cal}$	ΔExp^b	$\Delta E_{ m Cal}$
$X(2nd) + GeH_4$	124.9	128.5	154.6	157.6
$X(1st) + GeH_4$	89.3	84.4	119.5	114.6
$H + XGeH_3$		79.9		87.7
$HX + GeH_3$	68.9	70.3	75.3	80.0
$HXGeH_3$		13.6		21.0
$X(gs) + GeH_4$	0	0	0	0

^a From [10]

with the corresponding energies \sim 82 and \sim 93, respectively; as it can be seen in Table 2(a).

Ramírez-Solís and Castillo [86] compared the $C_{3\nu}$ versus $C_{2\nu}$ symmetries of Cd (1 S, 3 P, 1 P) + CH₄ interactions in the edge on geometry orientation. For $C_{3\nu}$ symmetry, they calculated two more geometry orientations. Before starting their molecular calculations, they successfully reproduced the lowest states of the atomic spectra of cadmium as mentioned in Table 2(a) which corresponds to 125.6 kcal mol $^{-1}$ for the second excited state. They did not construct the potential energy surfaces; however, they calculated the breaking of the C–H bond of methane with the consequent formation

of an intermediate with energy of $31.9 \,\text{kcal}\,\text{mol}^{-1}$ and its decomposition in possible products: $HCd + CH_3$ and $H + CdCH_3$ with energy of 56.6 and 67.9 kcal mol^{-1} , respectively (see Table 2(a)).

Luna-García et al. [9] found that Zinc in its singlet second excited state (^{1}P : $3d^{10}$ $4s^{1}$ $4p^{1}$) breaks the Si–H bond of silane, by reversing the initially repulsive ground state curve, thus, overcoming a barrier of $\sim 80 \, \text{kcal mol}^{-1}$ of the latter. The experimental transition energy between the excited state (^{1}P : $3d^{10}$ $4s^{1}$ $4p^{1}$) and the singlet ground state (^{1}S : $3d^{10}$ $4s^{2}$) is $133.7 \, \text{kcal mol}^{-1}$, which is comparable to the calculated transition energy of $141.0 \, \text{kcal mol}^{-1}$ of the second excited

^bFrom [86]

^cFrom [95].

^bFrom [10].

^bFrom [93].

state of Zinc calculated theoretically (Table 2(b), Figure 8). The formation of the HZnSiH₃ intermediate arising at the minimum (81 kcal mol⁻¹, 60°) comes with 4p¹ character and approaches the avoided crossing between 2 ¹A′ and X ¹A′ states keeping 4p¹ character until the end of the latter state with an energy 11.5 kcal mol⁻¹. Finally, due to the endergonic nature of this reaction, the intermediate leads toward the HZn + SiH₃ and ZnSiH₃ + H products with calculated energies of 74.0 and 84.0 kcal mol⁻¹, respectively (see Table 2(b)). The experimental energy for HZn + SiH₃ products is 70.4 kcal mol⁻¹ in agreement with that calculated theoretically. We have not calculated transition probabilities yet.

Luna-García et al. [10] found that cadmium in its singlet second excited state (1P: 4d10 5s1 5p1) breaks the Si-H bond of silane, creating a barrier of ~89 kcal mol⁻¹ for the ground state. The experimental transition energy between the excited state (¹P: 4d¹⁰ 5s¹ 5p¹) and the ground state (1 S: $4d^{10}$ $5s^{2}$) is 124.9 kcal mol $^{-1}$, which is comparable to the transition energy of 128.5 kcal mol⁻¹ calculated theoretically (Table 2(b), Figure 9). The formation of the HCdSiH₃ intermediate at the minimum (92 kcal mol⁻¹, 45°) comes with 5p¹ character, passes through the avoided crossing between 2 ¹A' and X ¹A' pathways, and keeps 5p¹ character until the minimum (20.7 kcal mol⁻¹, 180°) of the X ¹A' state is reached (see Figure 9). Finally, the intermediate is broken reaching the HCd + SiH₃ and CdSiH₃ + H products with calculated energies of 75.5 and 89 kcal mol⁻¹, respectively (see Table 2(b)). The experimental energy for $HCd + SiH_3$ is $74.0 \text{ kcal mol}^{-1}$. We have not calculated transition probabilities yet.

Luna-García et al. [9] found that mercury in its singlet second excited state (1P: 5d10 6s1 6p1) breaks the Si-H bond of silane, leading to a ground state barrier of $\sim 102 \,\mathrm{kcal}\,\mathrm{mol}^{-1}$. The experimental transition energy between the excited state (1P: 5d10 6s1 6p1) and the singlet ground state (1S: 5d10 6s2) is 154.6 kcal mol-1, which agrees to the transition energy of 157.6 kcal mol⁻¹ theoretically calculated (see Figure 10 and Table 2(b)). The formation of the HHgSiH₃ intermediate arising at the minimum (106 kcal mol⁻¹, 70°) comes with 6p¹ character and passes through an avoided crossing between trajectories 2 ¹A' and X ¹A' of the energy surfaces maintaining 6p¹ character. The transition probability [84] at the avoided crossing among the latter states is obtained when mercury is photoexcited to the Hg ¹P: 5d¹⁰ 6s¹ 6p¹ excited state, allowing it to be inserted in silane (SiH₄) molecule. When the reaction pathway passes the crossing point and continues its way has a probability P = 0.79 of crossing toward curve X ¹A with 6p¹ character and a probability of P = 0.21 of continuing in the same curve 2 ¹A' (see Figure 10) with 6s² character. When going toward the X ¹A' state, it allows the formation of a stable intermediate at the minimum (28 kcal mol⁻¹, 180°) of the state. Finally, the latter is broken and reaches either the HHg + SiH₃ or HgSiH₃ + H products with energies 87.6 and 95.4 kcal mol⁻¹, respectively.

Luna-García et al. [11] have found that Cadmium in its singlet second excited state (¹P: 4d¹⁰ 5s¹ 5p¹) breaks the Ge–H bond of germane, while producing a ground state

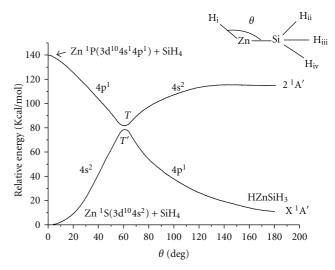


FIGURE 8: Potential energy curves of the $Zn(^1S, ^1P)$ interaction with SiH_4 as a function of the insertion angle (θ) towards the $HZnSiH_3$ intermediate product. The 4p1 character follows the path from the second excited state to the minimum in the X $^1A'$ state, where the final products are formed.

barrier of 83.6 kcal mol $^{-1}$ (see Figure 11). The experimental transition energy between the excited state (^{1}P : $4d^{10}$ 5s 1 5p 1) and the ground state (^{1}S : $4d^{10}$ 5s 2) is 124.9 kcal mol $^{-1}$, which agrees with the transition energy of 128.5 kcal mol $^{-1}$ calculated theoretically (Table 2(c)). The formation of the HCdGeH $_{3}$ intermediate at (89 kcal mol $^{-1}$, 50°) comes with 5p 1 character and goes by an avoided crossing between the 2 $^{1}A'$ and X $^{1}A'$ states maintaining a 5p 1 character until the next minimum at (13.6 kcal mol $^{-1}$, 180°) (see Figure 11). Finally the intermediate is broken in the HCd + GeH $_{3}$ and CdGeH $_{3}$ + H products with calculated energies 70.3 and 79.9 kcal mol $^{-1}$, respectively. The experimental energy for HCd + GeH $_{3}$ is 68.9 kcal mol $^{-1}$. We have not calculated the transition probabilities yet.

Luna-García et al. [11] have found that mercury in its excited state (1P: 5d10 6s1 6p1) breaks the Ge-H bond of germane, while forming a ground state barrier of 86.1 kcal mol⁻¹. The experimental transition energy between the excited state (¹P: 5d¹⁰ 6s¹ 6p¹) and the ground state (¹S: 5d¹⁰ 6s²) amounts to 154.6 kcal mol⁻¹, in good agreement with the transition energy of 157.6 kcal mol⁻¹ theoretically calculated (Table 2(c)). The transition probability [84] between the PES is obtained for the reaction Hg ¹P(5d¹⁰ 6s¹ $6p^1$) + GeH₄ \rightarrow Hg 1 S(5d¹⁰ 6s²) + GeH₄. When mercury is photoexcited to the Hg (¹P:5d¹⁰ 6s¹ 6p¹) second excited state, the mercury atom is inserted in germane (GeH₄) molecule. This effect is observed in the minimum (90 kcal mol^{-1} , 60°) of the 2 ¹A' state arriving with 6p¹ character, where the HHgGeH₃ intermediate is formed. When this intermediate continues its way, it has a probability P = 0.83 of crossing toward X 1A state with 6p1 character and a probability of P = 0.17 of continuing in the same 2^{1} A' state (see Figure 12) with 6s² character. When going toward the X¹A' state, it leads to the formation of the product at the minimum

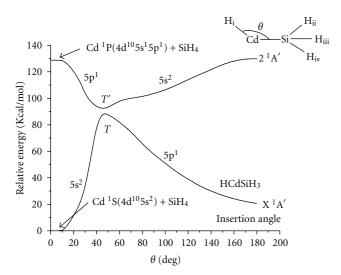


FIGURE 9: Potential energy curves of the $Cd(^1S, ^1P)$ interaction with SiH_4 as a function of the insertion angle (θ) towards the $HCdSiH_3$ intermediate product. The $5p^1$ character follows the path from the second excited state to the minimum in the X^1A' state, where the final products are formed.

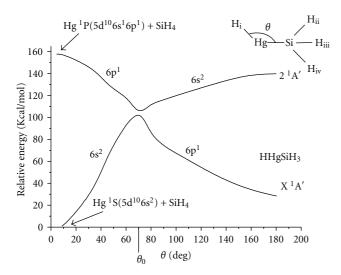


FIGURE 10: Potential energy curves of the $Hg(^1S, ^1P)$ interaction with SiH_4 as a function of the insertion angle (θ) towards the $HHgSiH_3$ intermediate product. The $6p_1$ character follows the path from the second excited state to the minimum in the X^1A' state, where the final products are formed.

(21 kcal mol $^{-1}$, 180 $^{\circ}$) of the state. Finally, the intermediate evolves towards the HHg + GeH $_3$ and HgGeH $_3$ + H products with calculated energies 80 and 87.7 kcal mol $^{-1}$, respectively, while the experimental energy for HHg + GeH $_3$ is 75.3 kcal mol $^{-1}$.

2.3. Interactions of the Al, Ga Metals with YH₄. Pacheco-Blas et al. [88] found that the aluminum in its doublet second excited state (2 D: $3s^{2}$ $3d^{1}$) breaks the C–H bond of methane, as does the $2{}^{2}$ A' state after surpassing an activation barrier of 14.0 kcal mol⁻¹ (see Figure 13). The experimental transition

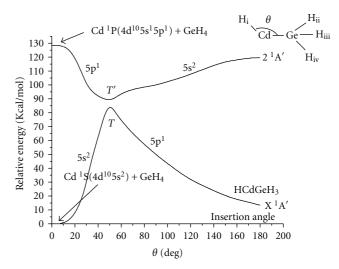


FIGURE 11: Potential energy curves of the $Cd(^1S, ^1P)$ interaction with GeH_4 as a function of the insertion angle (θ) towards the $HCdGeH_3$ intermediate product. The $5p^1$ character follows the path from the second excited state to the minimum in the X^1A' state, where the final products are formed.

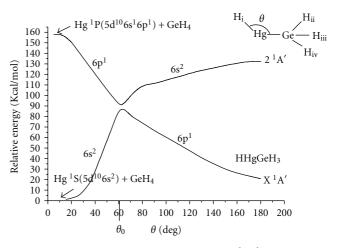


FIGURE 12: Potential energy curves of the $Hg(^1S, ^1P)$ interaction with GeH_4 as a function of the insertion angle (θ) towards the $HHgGeH_3$ intermediate product. The6 p^1 character followed the path from the second excited state to the minimum in the X^1A' state, where the final products are formed.

energy between this second excited state (2D : $^3s^2$ $^3d^1$) and the ground state (2P : $^3s^2$ $^3p^1$) is 92.5 kcal $^{-1}$ and agrees with the transition energy of 93.9 kcal $^{-1}$ theoretically calculated (see Table 3(a)). The transition probability [88] among the corresponding PES for the reaction Al $^2D(3s^2$ $^3d^1$) + CH $_4$ 3 Al $^2P(3s^2$ $^3p^1$) + CH $_4$ starts with the formation of the HAlCH $_3$ intermediate and goes through two avoided crossings with the $^3A'$, $^2A'$, and $^3A'$ states. When aluminum is photoexcited to its Al 3D : $^3s^2$ $^3d^1$ second excited state, it is inserted into a C–H bond of methane at the minimum (3R kcal 3 mol 3 character. Under these conditions, the HAlCH 3 intermediate is formed. As the latter continues its path, it

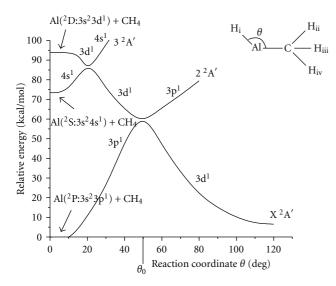


FIGURE 13: Potential energy curves of the Al (2 P, 2 S, and 2 D) interaction with CH₄ versus θ insertion angle toward the HAlCH₃ intermediate product. The 3d¹ character follows the path from the second excited state to the minimum in the X 2 A′ state, where the final products are formed.

has a probability of 0.85 of crossing toward the 2 2 A' state with 3d¹ character going to the Al 2 D: 3s² 4s¹ first state and a probability of 0.15 of continuing in the same 3 2 A' state with 4s¹ character. When the intermediate continues its pathway, there is a probability of 0.89 for crossing from the 2 2 A' state to the X 2 A' with 3d¹ character (see Figure 13), where the most stable intermediate is found at $\theta = 120^\circ$ and 6.5 kcal mol $^{-1}$. When this occurs, the final products are reached from the Al + CH₄ reaction, that is, to say, the intermediate is broken in the HAl + CH₃ and AlCH₃ + H products with calculated energies 42.8 and 48.2 kcal mol $^{-1}$, respectively. In this case, the corresponding experimental [36] energy is 45.0 kcal mol $^{-1}$ in both cases.

Pacheco-Sánchez et al. [14] have found that gallium in its doublet first excited state (2S: 4s2 5s1) breaks the C-H bond of methane, producing in the lowest state an activation barrier of 53.7 kcal mol⁻¹. The experimental transition energy among the excited state (2S: 4s2 5s1) and the ground state (²P: 4s² 4p¹) is 69.3 kcal mol⁻¹, in agreement with the transition energy 72.7 kcal mol⁻¹ theoretically calculated (see Table 3(a)), within the 3 kcal mol⁻¹ of tolerance. The transition probability [14] among the corresponding PES for the reaction Ga ${}^2S(4s^2 5s^1) + CH_4 \rightarrow Ga {}^2P(4s^2 4p^1) +$ CH₄ starts with the formation of the intermediate HGaCH₃ and passes through two avoided crossings with 3 2A', 2 ²A', and X²A' states. When gallium is photoexcited to its Ga ²S: 4s² 5s¹ first excited state, it is inserted into a C-H bond of methane at the minimum (60 kcal mol⁻¹, 25°) in the 3 ²A' state with 5s¹ character. Under these conditions, the intermediate product HGaCH3 is formed. As the latter continues its path, it has a probability of 0.715 [83] (the branching fraction is 0.73 [96]) of crossing toward the 2 ²A' state with 5s¹ character going to the Ga ²P: 4s² 4p¹ ground state and a probability of 0.285 of continuing by the

same $3^2A'$ state with $4p^1$ character. When the intermediate continues its pathway, there is a probability of 0.46 for crossing from the $2^2A'$ state to X^2A' with $5s^1$ character (see Figure 14), where the most stable intermediate is found at $\theta=120^\circ$ and $6.1\,\mathrm{kcal\,mol^{-1}}$. Finally, this intermediate is broken in the products $HGa+CH_3$ and $GaCH_3+H$ with calculated energies 40.2 and $45.7\,\mathrm{kcal\,mol^{-1}}$, respectively. The corresponding experimental energy is $38.9\,\mathrm{kcal\,mol^{-1}}$ in $HGa+CH_3$ case.

Pacheco-Sánchez et al. [13] have found that gallium in its doublet first excited state (2S: 4s2 5s1) breaks the Si-H bond of silane, overcoming a barrier of 51.0 kcal mol⁻¹ of the ground state. The experimental transition energy between the excited state (2S: 4s2 5s1) and the ground state (2P:4s2 4p¹) is 69.3 kcal mol⁻¹, which agrees to the transition energy of 71.7 kcal mol^{-1} theoretically calculated (Table 3(b)). The transition probability [13] among the corresponding PES for the reaction Ga ${}^2S(4s^2 5s^1) + SiH_4 \rightarrow Ga {}^2P(4s^2 4p^1) +$ SiH₄ starts with the formation of the intermediary molecule HGaSiH₃ passing through two avoided crossings among 3 ²A', 2 ²A', and X ²A' states. The probability [85] that it crosses from 3 2 A' state to 2 2 A' state is P = 0.701 and a probability P = 0.299 of continuing along the same 3 ²A' state. When crossing towards the 2 ²A' state in its descent, it has a probability P = 0.685 of crossing towards the X 2 A' state and a probability P = 0.315 of continuing along the same 2 2A' state (see Figure 15). Finally at the minimum (6.1 kcal mol⁻¹, 120°) of the X ²A' state, the intermediate is broken into the HGa + SiH₃ and GaSiH₃ + H products with energies 26.1 and 45.3 kcal mol⁻¹, respectively. The corresponding experimental energy is 24.5 kcal mol⁻¹ in HGa + SiH₃ case.

Lefcourt and Ozin [100] optimized geometry of Al–SiH₄ interaction for 2A_1 state in $C_{2\nu}$ symmetry with the single point SCF energy and calculated that the geometry-optimized structure does not differ very much at all from the initial geometry, a situation that is reflected in the converged energy which is only approximately 1/100 of a hartree lower (\sim 6.21 kcal/mol) than the single-point value associated with the starting structure. Calculations carried out on systems having the equivalent starting geometry but inhabiting the 2B_1 and 2B_2 electronic states yielded final energies that were considerably higher (0.17 and 0.31 hartree, resp.) than the energy obtained in the 2A_1 optimization.

3. Discussion

We have presented here a series of studies on X + YCH₄ (X = Cu, Zn, Cd, Ga, Al, Au, Hg, and Y = C, Si, Ge) reactions, attempting to identify possible general patterns. The very first study presented, the Cu + CH₄ reaction was simultaneously being studied experimentally at Toronto University in Canada [32, 33, 101–104], allowing us to make a very close comparison and correlation between their cryogenic experiments and our quantum mechanical calculations. This was due to the fact that Jaime Garcia-Prieto (a member of our group in Mexico) was working with Professor Geoffrey Ozin at Lash Miller Lab. in Toronto

Table 3 (a) Metal family (Al, Ga) interacting with methane. Relative energies (kcal mol^{-1}) of the reactants, intermediary HXCH₃ and final products for three lowest states of the metal.

X: metal		ll ^a S, ² D)	Ga ^b (² P, ² S, ² P)		
	$\Delta E_{ m Exp}$	$\Delta E_{ m Cal}$	$\Delta E_{ m Exp}$	$\Delta E_{ m Cal}$	
$X(2nd) + CH_4$	92.5	93.9	93.1	93.7	
$X(1st) + CH_4$	72.24	73.4	69.3	72.7	
$H + XCH_3$	45.0	48.2		45.7	
$HX + CH_3$	45.0	42.8	38.9°	40.2	
HXCH ₃		6.5	4.9^{d}	6.1	
$X(gs) + CH_4$	0	0	0	0	

^a From [88]

(b) Metal family (Al, Ga) interacting with silane. Relative energies (kcal mol⁻¹) of the reactants, the HXSiH₃ intermediary and final products for three lowest states of the metals.

X: metal	Al ^a (² P, ² S, ² D)		Ga ^b (² P, ² S, ² P)	
	$X(2nd) + SiH_4$	92.5		93.1
$X(1st) + SiH_4$	72.24		69.3	71.7
$H + XSiH_3$				45.3
$HX + SiH_3$			24.5°	26.1
HXSiH ₃		6.21 ^d		6.1
$X(gs) + SiH_4$	0	0	0	0

^a From [88]

on the photochemical activation of Cu in methane matrices at near-absolute zero conditions. Originally Ozin expected the open shell Cu: ²D excited state to be responsible for methane activation, but our calculations proved that the higher lying ²P was the real culprit, albeit through a series of avoided crossings a fact which was finally acknowledged in the experimental and theoretical papers [32, 60]. Since then our group, mainly through the late Sidonio Castillo and his collaborators, studied a series of transition metals. We have presented here an overview of this line of research although we evidently must accept that the list of metals studied to date is far from exhaustive. This notwithstanding, we provide here enough examples of the mechanism first advanced in our explanation of the Lash Miller Lab experiments of the activation of methane by copper [60, 82]. In short we have advanced a daring hypothesis avoided crossings and transition probabilities for curves of the same symmetry play a systematic and clear-cut role in the activation of methane, silane, and germane. Indeed, we show the evidence that in general, the most stable intermediate has a rather weak binding, thus leading to the products. The potential energy surfaces lead from the reactants climbing to this transition state which requires moderate energies, normally derived

from photoactivation processes and finally yielding the final products (XH + YH $_3$) or H + XYH $_3$). To document this, we report the configurations and bond distances as they evolve in each specific case. We kindly refer our readers to access our original papers for details. In any case, our reported energies are compatible with the spectra of reactants, intermediates, and products. For instance, the probabilities for the Ga + CH $_4$ reaction agree quite well with experimental results [83, 96], whereas those obtained for other systems reported here were widely discussed in the original papers [82–88].

The potential energy surfaces for the coinage metals Cu and Au with silane are rather similar. The main difference lies in the energies of their respective second excited states, making their potential energy wells differ from their respective intermediate complexes onward to the final products. To wit, in the Au + SiH₄ reaction, the minimum at 120 degrees has only a depth of 3.34 kcal/mol, while for Cu + SiH₄ the minimum lies at 100 degrees and is 5.58 kcal/mol deep. These results would make the study of the Ag + SiH₄ reaction all the more desirable, a valid proposition for several other metals. We explicitly state here that our work on these systems is far from complete. Take for instance our results involving Hg which are rather different from

^bFrom [14]

^cFrom [97]

^dFrom [98].

^bFrom [13]

^cFrom [97]

^dFrom [99].

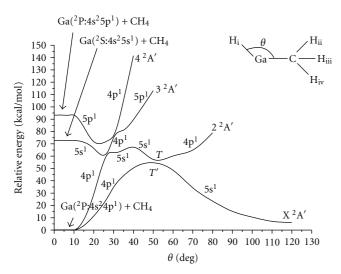


FIGURE 14: Potential energy curves of the interaction of $Ga(^2P)$, $Ga(^2S)$, and $Ga(^2P)$ with CH_4 towards the $GaCH_3$ intermediate. Energy versus insertion angle (θ) . The $5s^1$ character follows the path from the first excited state to the minimum in the X^2A' state, where the final products emerge.

the other metals, thus, naturally deserving closer scrutiny. Perhaps we may tentatively relate this peculiarity of mercury to its particularly stable ground state $^{1}S_{0}$ (with its closed $5d^{10}$ 6s² valence shell), from which stem the unique dense metal liquid character of mercury, in dire contrast with its solid metal neighbors with stable electronic arrangements. In effect we dare propose that this line of research is both valid and promising and needs much more work and attention, especially so with a close collaboration with cryogenic experiments, as we hope to establish.

Difference of PES of coinage metals interacting with silane is due to the second excited state leading to the reported well depths for the potentials for the ground state. Analogously, the PES of pseudotransition metals interacting with silane is very similar, and the main difference is the ¹P singlet energy of the pseudotransition metals at the second excited state. This causes the depth wells of potential (11.5 kcal mol⁻¹, 180°) for Zn + SiH₄, while for Cd + SiH₄ it is (20.7 kcal mol⁻¹, 180°), and for Hg it is (28 kcal mol⁻¹, 180°), since the initial formation of the intermediate until the product formation.

The methane complexes with Zn and Cd in the second excited state ^{1}P at $\theta=0$ has energies \sim 141 and 125.6 kcal mol $^{-1}$, respectively. The germane complexes with Cd and Hg in the second excited state ^{1}P at $\theta=0$ have energies 128.5 and 157.6 kcal mol $^{-1}$, respectively. The initial excitation energy of the pseudotransition metals yields the depth wells of potential, which is \sim 25 kcal mol $^{-1}$ for Zn + CH₄ and 31.9 kcal mol $^{-1}$ Cd + CH₄. The initial excitation energy of the pseudotransition metals yields the depth wells of potential, which is 13.6 and 21.0 kcal mol $^{-1}$ for Cd + GeH₄ and Hg + GeH₄, respectively.

Finally, PES of metals Al 2 D doublet and Ga 2 P doublet in the second excited state interacting with methane for $\theta = 0$ has energies 93.9 and 93.7 kcal mol $^{-1}$, respectively.

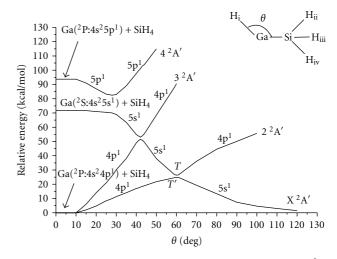


Figure 15: Potential energy curves of the interaction of $Ga(^2P)$, $Ga(^2S)$, and $Ga(^2P)$ with SiH_4 towards the $GaSiH_3$ intermediate. Energy versus insertion angle (θ) . The $5s^1$ character followed the path from the first excited state to the minimum in the X^2A' state, where the final products are formed.

The initial energy of the metals yields the depth wells of potential, of 6.5 and 6.1 kcal mol⁻¹ for Al + CH₄ and Ga + CH₄, respectively, and 6.21 taken from reference [100] and 6.1 kcal mol^{-1} for Al + SiH₄ and Ga + SiH₄, respectively. While the latter result is as expected, in the previous one there is a very small deviation. This is due to the very small energy difference at 2nd excited state between Al and Ga, and to the approximation error carried out by the numerical solutions of the system. In defense of this argumentation, it is the fact that the dissociation energy of the ionic Al⁺-CH₄ complex has been experimentally reported to be $2120 \pm 105 \,\mathrm{cm}^{1}$ $(6.06 \pm 0.3 \, \text{kcal mol}^{-1}) \, [99]$. Somewhat coincidentally we have obtained the value of 6.5 kcal mol⁻¹ for the dissociation energy of Al + CH₄ complex. It is quite remarkable that the dissociation energies for Al⁺-CH₄ and Al + CH₄ are quite close, and that the experimental value for this ionic Al⁺-CH₄ reaction is the expected value for the dissociation energy of $Al-CH_4$.

A very important issue is to get the most stable intermediate with the lowest energy on which the breaking of the intermediate is achieved. The products of the reaction emerge at the end from the X A' state, calculated using the parameter values obtained at this minimum.

The intermediate has a much lower energy than the final products due to the endergonic nature of these reactions. Initially, the metal needs a photoexcitation for taking it to an excited state for being inserted in a Y–H bond of the gas molecule, in order to surpass the activation barrier of the ground state for the reaction. After the avoided crossings, the deformed metastable intermediate arrives to the most stable arrangement, having the lowest energy with the optimal geometry. At this low energy arrangement, its internal bond orientation produces a still strong electrostatic repulsion due to the energy gained by the photoexcitation of the metal, greater than the energy of the intermediate. The metal atom

also shares its energy with the carbon and hydrogens. Thus, the new energies of the products cannot be greater than the initial excitation of the metal or lower than the energy of the reactants in their ground state.

The resulting probabilities for the case of $Ga + CH_4$ are in agreement with previous experimental results [83], whereas those obtained for the other cases are only theoretical predictions.

4. Conclusions

From the theory of transition probabilities at avoided crossings between curves of the same symmetry, we can deduce that the character of the wave function is the same at the beginning of the highest state path than at the minimum of the ground state path after all avoided crossings.

The energy value of the initial state of the metal which eventually leads to the intermediate, as well as the character of the wavefunction is crucial for the product formation. This character corresponds to the dominant excited state of the metal inserting in the gas molecule and is independent of the gas in consideration (methane, silane, or germane).

As expected the wells' potential depth is dependent on the energy level of the metal excited state in consideration, and the pathway is reflected in the character of the wavefunction revealing the electronic configuration of the corresponding excited state. This means that the higher the energy of the metal atom excited state, the deeper the potential energy well at the ground state minimum.

References

- [1] J. P. Daudey, PSHF, a HF-SCF RECP program, based on the original HONDO-76, QCPE program no. 338 by M Dupuis, J. Rys, H. F. King, 1977.
- [2] P. H. Durand and J. C. Barthelat, "A theoretical method to determine atomic pseudopotentials for electronic structure calculations of molecules and solids," *Theoretica Chimica Acta*, vol. 38, no. 4, pp. 283–302, 1975.
- [3] J. C. Barthelat, P. H. Durand, and A. Serafini, "Non-empirical pseudopotentials for molecular calculations," *Molecular Physics*, vol. 33, no. 1, pp. 159–180, 1977.
- [4] J. C. Barthelat, P. H. Durand, A. Serafini et al., "Recent progress of pseudopotentials in quantum chemistry," *Gazzetta Chimica Italiana*, vol. 108, p. 225, 1978.
- [5] M. Pelissier and P. Durand, "Testing the arbitrariness and limits of a pseudopotential technique through calculations on the series of diatoms HF, AlH, HCl, AlF, AlCl, F2, Cl2," *Theoretica Chimica Acta*, vol. 55, no. 1, pp. 43–54, 1980.
- [6] R. Carbó, M. Pélissier, J. P. Daudey, and J. Rubio, GMCP Program Based on the Elementary Jacobi Rotation Algorithm, 1993.
- [7] B. H. Huron, J. P. Malrieu, and P. Rancurel, "Iterative perturbation calculations of excited ground and excited state energies from multiconfigurational zeroth-order wavefunctions," *Journal of Chemical Physics*, vol. 58, pp. 5745–5759, 1973, CIPSI code written by J. P. Daudey, M Pélissier, J. P. Malrieu, S. Evangelisti, F. Spiegelmann, and D. Maynau.
- [8] S. Castillo, A. Ramírez-Solís, D. Díaz, E. Poulain, and O. Novaro, "Theoretical study of the activation of methane by

- photoexcited zinc atoms," *Molecular Physics*, vol. 81, no. 4, pp. 825–836, 1994.
- [9] H. Luna-García, S. Castillo, and A. Ramírez-Solís, "Ab initio study of the reactions of Zn(1S, 3P, and 1P) with SiH4," *Journal of Chemical Physics*, vol. 107, no. 17, pp. 6627–6633, 1997.
- [10] H. Luna-García, S. Castillo, and A. Ramírez-Solís, "Ab initio studies of the reactions of M(¹S, ³P, and ¹P) with SiH4 (M = Cd, Hg)," *Journal of Chemical Physics*, vol. 110, no. 23, pp. 11315–11322, 1999.
- [11] H. Luna-García, S. Castillo, and A. Ramírez-Solís, "Ab initio studies of the reactions of M(¹S, ³P, and ¹P) with GeH4 (M = Cd, Hg)," *Journal of Chemical Physics*, vol. 114, no. 6, pp. 2647–2652, 2001.
- [12] H. Luna-García, A. Ramírez-Solís, and S. Castillo, "Ab initio studies of the reactions of Cu(²S, ²D, and ²P) with SiH₄ and GeH₄," *Journal of Chemical Physics*, vol. 116, no. 3, pp. 928–935, 2002.
- [13] J. H. Pacheco-Sánchez, H. Luna-García, and S. Castillo, "Ab initio study of the reactions of Ga(²P, ²S, and ²P) with silane," *Journal of Chemical Physics*, vol. 121, no. 12, pp. 5777–5782, 2004.
- [14] J. H. Pacheco-Sánchez, H. Luna-García, and S. Castillo, "Ab initio study of the reactions of Ga(²P, ²S, and ²P) with methane," *Journal of Chemical Physics*, vol. 120, no. 9, pp. 4240–4246, 2004.
- [15] P. Chaquin, A. Papakondylis, C. Giessner-Prettre, and A. Sevin, "Theoretical study of the quenching of the low-lying excited states of lithium and magnesium by methane," *Journal of Physical Chemistry*, vol. 94, no. 19, pp. 7352–7357, 1990.
- [16] L. D. Landau, "Theory of energy transfer II," *Physikalische Zeitschrift der Sowjetunion*, vol. 2, pp. 46–51, 1932.
- [17] C. Zener, "Non-adiabatic crossing of energy levels," *Proceedings of the Royal Society A*, vol. 137, no. 833, pp. 696–702, 1932.
- [18] R. Robertson and A. Gallagher, "Mono- and disilicon radicals in silane and silane-argon dc discharges," *Journal of Applied Physics*, vol. 59, no. 10, pp. 3402–3411, 1986.
- [19] W. M. M. Kessels, A. Leroux, M. G. H. Boogaarts, J. P. M. Hoefnagels, M. C. M. van de Sanden, and D. C. Schram, "Cavity ring down detection of SiH3 in a remote SiH4 plasma and comparison with model calculations and mass spectrometry," *Journal of Vacuum Science and Technology A*, vol. 19, no. 2, pp. 467–476, 2001.
- [20] R. Nozawa, H. Takeda, M. Ito, M. Hori, and T. Goto, "In situ observation of hydrogenated amorphous silicon surfaces in electron cyclotron resonance hydrogen plasma annealing," *Journal of Applied Physics*, vol. 85, no. 2, pp. 1172–1177, 1999.
- [21] M. Abe, T. Nakajima, and K. Hirao, "A theoretical study of the low-lying states of the AuSi molecule: an assignment of the excited A and D states," *Journal of Chemical Physics*, vol. 117, no. 17, pp. 7960–7967, 2002.
- [22] N. Toshima, "Core/shell-structured bimetallic nanocluster catalysts for visible-light-induced electron transfer," *Pure and Applied Chemistry*, vol. 72, no. 1-2, pp. 317–325, 2000.
- [23] J. Westwater, D. P. Gosain, K. Yamauchi, and S. Usui, "Nanoscale silicon whiskers formed by silane/gold reaction at 335 °C," *Materials Letters*, vol. 24, no. 1–3, pp. 109–112, 1995.
- [24] G. E. Moore, "Cramming more components onto integrated circuits," *Electronics*, vol. 38, no. 8, pp. 114–117, 1965.

- [25] R. Solanki, J. Huo, J. L. Freeouf, and B. Miner, "Atomic layer deposition of ZnSe/CdSe superlattice nanowires," *Applied Physics Letters*, vol. 81, no. 20, pp. 3864–3866, 2002.
- [26] J. Westwater, D. P. Gosain, S. Tomiya, S. Usui, and H. Ruda, "Growth of silicon nanowires via gold/silane vapor-liquid-solid reaction," *Journal of Vacuum Science and Technology B*, vol. 15, no. 3, pp. 554–557, 1997.
- [27] K. Shintani and S. Kameoka, "Molecular-dynamics modelling of the tensile deformation of helical nanowires U6.12.1," in *Materials Research Society Symposium Proceed*ings, vol. 778, 2003.
- [28] L. Guczi, G. Petö, A. Beck et al., "Gold nanoparticles deposited on SiO₂/Si(100): correlation between size, electron structure, and activity in CO oxidation," *Journal of the American Chemical Society*, vol. 125, no. 14, pp. 4332–4337, 2003.
- [29] J. Guzman and B. C. Gates, "Catalysis by supported gold: correlation between catalytic activity for CO oxidation and oxidation states of gold," *Journal of the American Chemical Society*, vol. 126, no. 9, pp. 2672–2673, 2004.
- [30] M. Valden, X. Lai, and D. W. Goodman, "Onset of catalytic activity of gold clusters on titania with the appearance of nonmetallic properties," *Science*, vol. 281, no. 5383, pp. 1647– 1650, 1998.
- [31] G. A. Ozin, J. G. McCaffrey, D. F. McIntosh et al., "Activation of dihydrogen and methane by photoexcited manganese and iron atoms in low temperature matrices," *Pure and Applied Chemistry*, vol. 56, no. 1, pp. 111–128, 1984.
- [32] J. M. Parnis, S. A. Mitchell, J. García-Prieto, and G. A. Ozin, "Activation of methane by photoexcited copper atoms and the photochemistry of methylcopper hydride in solid methane matrices," *Journal of the American Chemical Society*, vol. 107, no. 26, pp. 8169–8178, 1985.
- [33] G. A. Ozin, J. G. McCaffrey, and J. M. Parnis, "Photochemistry of transition-metal atoms: reactions with molecular hydrogen and methane in low-temperature matrices," *Angewandte Chemie*, vol. 25, no. 12, pp. 1072–1085, 1986.
- [34] J. M. Parnis and G. A. Ozin, ^aPhotochemical reactions of matrix-isolated aluminum atoms with methane and molecular hydrogen. 1. Methane, "*Journal of Physical Chemistry*, vol. 93, no. 4, pp. 1204–1215, 1989.
- [35] J. M. Parnis and G. A. Ozin, "Photochemical reactions of matrix-isolated aluminum atoms with methane and molecular hydrogen. 2. Molecular hydrogen," *Journal of Physical Chemistry*, vol. 93, no. 4, pp. 1215–1220, 1989.
- [36] J. M. Parnis and G. A. Ozin, "Photochemical reactions of matrix-isolated aluminum atoms with methane and molecular hydrogen. 3. Structure, bonding, and reactivity," *Journal of Physical Chemistry*, vol. 93, no. 4, pp. 1220–1225, 1989.
- [37] J. M. Parnis and G. A. Ozin, "Photochemistry of methyl-copper hydride, CH3CuH: wavelength dependence of the product distribution," *Journal of Physical Chemistry*, vol. 93, no. 10, pp. 4023–4029, 1989.
- [38] S. A. Mitchell, P. A. Hackett, D. M. Rayner, and M. Flood, "Branching ratios for chemical reaction in collisional quenching of excited 5s¹² S_{1/2} gallium atoms," *The Journal of Chemical Physics*, vol. 86, no. 12, pp. 6852–6861, 1987.
- [39] D. A. Hensher and K. J. Button, *Handbook of Transport and the Environment*, Emerald Group Publishing, 2003.
- [40] J. H. Pacheco-Sánchez, Ab initio studies for C–H bond breaking of the methane molecule (CH4) and for Si–H bond breaking of the silane molecule (SiH4), Ph.D. thesis, Universidad Autónoma Metropolitana, (UAM-A), 2004.

- [41] M. Yasuda, Y. Onishi, M. Ueba, T. Miyai, and A. Baba, "Direct reduction of alcohols: highly chemoselective reducing system for secondary or tertiary alcohols using chlorodiphenylsilane with a catalytic amount of indium trichloride," *Journal of Organic Chemistry*, vol. 66, no. 23, pp. 7741–7744, 2001.
- [42] S. Das, D. Addis, S. Zhou, K. Junge, and M. Beller, "Zinc-catalyzed reduction of amides: unprecedented selectivity and functional group tolerance," *Journal of the American Chemical Society*, vol. 132, no. 6, pp. 1770–1771, 2010.
- [43] F. Lehmann and M. Scobie, "Rapid and convenient microwave-assisted synthesis of primary amines via reductive N-alkylation of methyl carbamate with aldehydes," *Synthesis*, no. 11, pp. 1679–1681, 2008.
- [44] Y. Kanazawa and H. Nishiyama, "Conjugate reduction of α , β -unsaturated aldehydes with rhodium(bis-oxazolinylphenyl) catalysts," *Synlett*, no. 19, pp. 3343–3345, 2006.
- [45] Y. Sumida, H. Yorimitsu, and K. Oshima, "Palladium-catalyzed preparation of silyl enolates from α, β- unsaturated ketones or cyclopropyl ketones with hydrosilanes," *Journal of Organic Chemistry*, vol. 74, no. 20, pp. 7986–7989, 2009.
- [46] H. A. Malik, G. J. Sormunen, and J. Montgomery, "A general strategy for regiocontrol in nickel-catalyzed reductive couplings of aldehydes and alkynes," *Journal of the American Chemical Society*, vol. 132, no. 18, pp. 6304–6305, 2010.
- [47] K. Sa-Ei and J. Montgomery, "Highly diastereoselective preparation of anti-1,2-diols by catalytic addition of alkynylsilanes to α-silyloxyaldehydes," *Organic Letters*, vol. 8, no. 20, pp. 4441–4443, 2006.
- [48] G. S. Girolami, T. B. Rauchfuss, and R. J. Angelici, *Synthesis and Technique in Inorganic Chemistry*, University Science Books, Mill Valley, Calif, USA, 1999.
- [49] R. Venkatasubramanian, R. T. Pickett, and M. L. Timmons, "Epitaxy of germanium using germane in the presence of tetramethylgermanium," *Journal of Applied Physics*, vol. 66, no. 11, pp. 5662–5664, 1989.
- [50] E. Woelk, D. V. Shenai-Khatkhate, R. L. DiCarlo Jr. et al., "Designing novel organogermanium OMVPE precursors for high-purity germanium films," *Journal of Crystal Growth*, vol. 287, no. 2, pp. 684–687, 2006.
- [51] A. H. Mahan, L. M. Gedvilas, and J. D. Webb, "Si-H bonding in low hydrogen content amorphous silicon films as probed by infrared spectroscopy and x-ray diffraction," *Journal of Applied Physics*, vol. 87, no. 4, pp. 1650–1658, 2000.
- [52] F. C. Marques, P. Wickboldt, D. Pang, J. H. Chen, and W. Paul, "Stress and thermomechanical properties of amorphous hydrogenated germanium thin films deposited by glow discharge," *Journal of Applied Physics*, vol. 84, no. 6, pp. 3118– 3124, 1998.
- [53] W. A. Turner, S. J. Jones, D. Pang et al., "Structural, optical, and electrical characterization of improved amorphous hydrogenated germanium," *Journal of Applied Physics*, vol. 67, no. 12, pp. 7430–7438, 1990.
- [54] R. A. Street, Hydrogenated Amorphous Silicon, Cambridge University Press, New York, NY, USA, 1991.
- [55] J. Robertson, "Deposition mechanism of hydrogenated amorphous silicon," *Journal of Applied Physics*, vol. 87, no. 5, pp. 2608–2617, 2000.
- [56] A. R. Badzian, P. K. Bachmann, T. Hartnett, T. Badzian, and R. Messier, "Amorphous hydrogenated carbon films," in *Proceedings of the E-MRS Meeting*, P. Koidl and P. Oelhafen, Eds., vol. 17, p. 63, Stasbourg, France, June 1987.
- [57] F. Demichelis, M. Fanciulli, G. Kaniadakis et al., "Amorphous hydrogenated carbon films," in *Proceedings of the E-MRS*

- Meeting, P. Koidl and P. Oelhafen, Eds., vol. 17, p. 213, Stasbourg, France, June 1987.
- [58] J. Reyes-Mena, J. González-Hernandez, R. Asomoza et al., "Amorphous hydrogenated carbon films," in *Proceedings of the E-MRS Meeting*, P. Koidl and P. Oelhafen, Eds., vol. 17, p. 229, Stasbourg, France, June 1987.
- [59] J. C. Angus, "Amorphous hydrogenated carbon films," in *Proceedings of the E-MRS Meeting*, P. Koidl and P. Oelhafen, Eds., vol. 17, p. 179, Stasbourg, France, June 1987.
- [60] S. Castillo, E. Poulain, and O. Novaro, "A theoretical study of the photochemistry of methylcopper hydride: II. Formation and stability of the HCuCH₃ intermediate complex," *International Journal of Quantum Chemistry*, vol. 40, pp. 577–585, 1991.
- [61] J. H. Wang, H. Umemoto, A. W. K. Leung, and W. H. Breckenridge, "Reactions of Zn(4s4p ³P₁) and Cd(5s5p ³P₁) with SiH₄," *Journal of Chemical Physics*, vol. 104, no. 23, pp. 9401–9407, 1996.
- [62] J. Perrin, M. Shiratani, P. Kae-Nune, H. Videlot, J. Jolly, and J. Guillon, "Surface reaction probabilities and kinetics of H, SiH₃, Si₂H₅, CH₃, and C₂H₅ during deposition of a-Si:H and a-C:H from H₂, SiH₄, and CH₄ discharges," *Journal of Vacuum Science and Technology A*, vol. 16, no. 1, pp. 278–289, 1998
- [63] A. G. Ramirez and R. Sinclair, "Wear effects on microstructural features of amorphous-carbon thin films," *Surface and Coatings Technology*, vol. 94-95, pp. 549–554, 1997.
- [64] C. Velasco-Santos, A. L. Martínez-Hernández, A. Consultchi, R. Rodríguez, and V. M. Castaño, "Naturally produced carbon nanotubes," *Chemical Physics Letters*, vol. 373, no. 3-4, pp. 272–276, 2003.
- [65] T. Taguchi, M. Morikawa, Y. Hiratsuka, and K. Toyoda, "Amorphous hydrogenated carbon films," in *Proceedings of the E-MRS Meeting*, P. Koidl and P. Oelhafen, Eds., vol. 17, p. 123, Stasbourg, France, June 1987.
- [66] W. M. M. Kessels, A. H. M. Smets, D. C. Marra, E. S. Aydil, D. C. Schram, and M. C. M. van de Sanden, "On the growth mechanism of a-Si:H," *Thin Solid Films*, vol. 383, no. 1-2, pp. 154–160, 2001.
- [67] W. M. M. Kessels, R. J. Severens, A. H. M. Smets et al., "Hydrogenated amorphous silicon deposited at very high growth rates by an expanding Ar-H₂-SiH₄ plasma," *Journal* of Applied Physics, vol. 89, no. 4, pp. 2404–2413, 2001.
- [68] K. Winer, "Chemical-equilibrium model of optimal a-Si:H growth from SiH₄," *Physical Review B*, vol. 41, no. 11, pp. 7952–7954, 1990.
- [69] W. H. Breckenridge, "Activation of H-H, Si-H, and C-H bonds by nsnp excited states of metal atoms," *Journal of Physical Chemistry*, vol. 100, no. 36, pp. 14840–14855, 1996.
- [70] B. L. Kickel and P. B. Armentrout, "Reactions of Fe+, Co+, and Ni+ with silane. Electronic state effects, comparison to reactions with methane, and M+-SiHx (x = 0-3) bond energies," *Journal of the American Chemical Society*, vol. 117, no. 2, pp. 764–773, 1995.
- [71] B. L. Kickel and P. B. Armentrout, "Guided ion beam studies of the reactions of group 3 metal ions (Sc+, Y+, La+, and Lu+) with silane. Electronic state effects, comparison to reactions with methane, and M+-SiHx (x = 0-3) Bond Energies," *Journal of the American Chemical Society*, vol. 117, no. 14, pp. 4057–4070, 1995.
- [72] A. Ferhati, T. B. McMahon, and G. Ohanessian, "Activation of silane by W+ in the gas phase: fourier-transform Ion cyclotron resonance and ab initio theoretical studies," *Journal*

- of the American Chemical Society, vol. 118, no. 25, pp. 5997–6009, 1996.
- [73] P. E. M. Siegbahn, M. Svensson, and R. H. Crabtree, "A theoretical study of mercury photosensitized reactions," *Journal of the American Chemical Society*, vol. 117, no. 25, pp. 6758–6765, 1995.
- [74] J. F. Harrod, T. Ziegler, and V. Tschinke, "Theoretical study of Cp2Ti(H)(SiH3) and Cp2TiSiH2 and their possible role in the polymerization of primary organosilanes," *Organometallics*, vol. 9, no. 4, pp. 897–902, 1990.
- [75] T. D. Tilley and H. G. Woo, "Dehydrogenative polymerization of silanes to polysilanes by zirconocene and hafnocene catalysts. A new polymerization mechanism," *Journal of the American Chemical Society*, vol. 111, no. 20, pp. 8043–8044, 1989
- [76] G. W. Parshall, Homogeneous Catalysis: the Application and Chemistry of Catalysis by Soluble Transition Metal Complexes, John Wiley & Sons, New York, NY, USA, 1992.
- [77] P. Braunstein and M. J. Knorr, "Reactivity of the metal-silicon bond in organometallic chemistry," *Journal of Organometallic Chemistry*, vol. 500, no. 1-2, pp. 21–38, 1995.
- [78] E. C. Zybill and C.Y. Liu, "Metal silicon multiple bonds: new building blocks for organic synthesis," *Synlett*, vol. 7, pp. 687–699, 1995.
- [79] F. C. Marques, P. Wickboldt, D. Pang, J. H. Chen, and W. Paul, "Stress and thermomechanical properties of amorphous hydrogenated germanium thin films deposited by glow discharge," *Journal of Applied Physics*, vol. 84, no. 6, pp. 3118– 3124, 1998.
- [80] S. Castillo, *Theoretical study of the methane activation by excited atoms of copper* (²S, ²D, and ²) and Zinc (¹S, ¹P, and ³P), Ph.D. thesis, Universidad Nacional Autonoma de Mexico (UNAM), 1992.
- [81] H. M. Luna-García, Molecular studies about the reaction mechanism for the formation of metal-silicon and metal germanium materials, Ph.D. thesis, Universidad Autonoma Matropolitana Unidad Azcapotzalco (UAM-A), 2003.
- [82] J. H. Pacheco-Sánchez and O. Novaro, "Transition probabilities found for M + CH₄ reactions (M = zinc, copper)," *International Journal of Quantum Chemistry*, vol. 108, no. 10, pp. 1645–1652, 2008.
- [83] J. H. Pacheco-Sánchez, S. Castillo, H. Luna-García, and O. Novaro, "Transition probabilities on Ga (², ²S, and ²) +CH₄ reactions," *Journal of Chemical Physics*, vol. 126, no. 10, Article ID 106103, 2007.
- [84] O. Novaro, M. A. Pacheco-Blas, and J. H. Pacheco-Sánchez, "Avoided crossings in metal (M)—gas (X) reactions (M = Hg, and X = SiH4, GeH4)," *Theoretical Chemistry Accounts*, vol. 126, no. 3, pp. 109–116, 2010.
- [85] J. H. Pacheco-Sánchez, S. Castillo, H. Luna-García, and O. Novaro, "Landau-zener theory for avoided crossings applied to the gallium-silane reactions," *International Journal of Quantum Chemistry*, vol. 107, no. 15, pp. 3053–3060, 2007.
- [86] A. Ramírez-Solís and S. Castillo, "C_{3ν} versus C_{2ν} Cd(¹S,³P, ¹P)-CH₄ van der Waals complexes: a variational and perturbational multireference configuration interaction study," *The Journal of Chemical Physics*, vol. 98, no. 10, pp. 8065–8069, 1993.
- [87] J. H. Pacheco-Sánchez, H. M. Luna-García, L. M. García-Cruz, and O. Novaro, "Transition probabilities for the Au (²S, ²D, and ²P) with SiH₄ reaction," *Journal of Chemical Physics*, vol. 132, no. 4, Article ID 044301, 2010.

- [88] M. A. Pacheco-Blas, O. A. Novaro, and J. H. Pacheco-Sánchez, "A theoretical approach to the photochemical activation of matrix isolated aluminum atoms and their reaction with methane," *Journal of Chemical Physics*, vol. 133, no. 17, Article ID 174307, 2010.
- [89] H. Eyring, Quantum Chemistry, John Wiley & Sons, New York, NY, USA, 1944.
- [90] L. Rosenkewitsch, "Zur theorie des Durchschlags von dielektriken," *Journal of Physics-USSR*, vol. 1, p. 426, 1932.
- [91] F. Colmenares, J. G. McCaffrey, and O. Novaro, "Quenching of excited 1P1 state atomic zinc by molecular nitrogen: a matrix-isolation spectroscopy/quantum chemical calculation study," *Journal of Chemical Physics*, vol. 114, no. 22, pp. 9911– 9918, 2001.
- [92] J. H. Pacheco, A. Bravo, and O. Novaro, "An ab initio study of platinum hydrogen interaction," *Revista Mexicana de Fisica*, vol. 52, no. 5, pp. 394–397, 2006.
- [93] C. E. Moore, *Atomic Energy Levels*, U.S. National Bureau of Standards, Washington, DC, USA, 1971.
- [94] K. P. Huber and G. Herzberg, Molecular Spectra and Molecular Structure IV. Spectra of Diatomic Molecules, Van Nostran, Princeton, NJ, USA, 1979.
- [95] S. Castillo, A. Ramírez-solís, and E. Poulain, "Theoretical study of the reaction of Cd(¹S, ³P, ¹P) with the methane molecule," *International Journal of Quantum Chemistry*, vol. 48, no. 27, pp. 587–598, 1993.
- [96] K. Lee, H. S. Son, S. C. Bae, and J. K. Ku, "Collisional quenching of Ga(5p) atoms by H₂, D₂ and CH₄," *Chemical Physics Letters*, vol. 288, no. 2–4, pp. 531–537, 1998.
- [97] M. Kronekvist, A. Langerquist, and H. Neuhaus, "The $A^1\Pi^{-1}\Sigma^+$ transition in the spectra of GaH and GaD," *Journal of Molecular Spectroscopy*, vol. 39, no. 3, pp. 516–518, 1971.
- [98] H. J. Himmel, A. J. Downs, and T. Greene, "Reactions of ground state and electronically excited atoms of main group elements: a matrix perspective," *Chemical Reviews*, vol. 102, no. 11, pp. 4191–4241, 2002.
- [99] P. R. Kemper, J. Bushenell, M. T. Bowers, and G. I. Gellene, "Binding between ground-state aluminum ions and small molecules: A1⁺ · (H₂/CH₄/C₂H₂/C₂H₄/C₂H₆)_n. Can Al⁺ insert into H₂?" *Journal of Physical Chemistry A*, vol. 102, no. 44, pp. 8590−8597, 1998.
- [100] M. A. Lefcourt and G. A. Ozin, "Aluminum(2P)-silane complex and photoreversible oxidative addition/reductive elimination reaction Al(2P){SiH4} .tautm. SiH3AlH. 1. Al(2P){SiH4} complex," *Journal of Physical Chemistry*, vol. 95, no. 7, pp. 2616–2623, 1991.
- [101] G. A. Ozin, D. F. McIntosh, S. A. Mitchell, and J. García-Prieto, "Methane activation. Photochemical reaction of copper atoms in solid methane," *Journal of the American Chemical Society*, vol. 103, no. 6, pp. 1574–1575, 1981.
- [102] J. M. Parnis and G. A. Ozin, "Photochemistry of methyl-copper hydride, CH3CuH: wavelength dependence of the product distribution," *Journal of Physical Chemistry*, vol. 93, no. 10, pp. 4023–4029, 1989.
- [103] R. A. Poirier, G. A. Ozin, D. F. McIntosh, I. G. Csizmadia, and R. Daudel, "Structure and bonding of H3CCuH," *Chemical Physics Letters*, vol. 101, no. 3, pp. 221–228, 1983.
- [104] G. A. Ozin and J. G. McCaffrey, "Photoinduced reductive elimination of iron atoms and methane from CH3FeH," *Journal of the American Chemical Society*, vol. 104, no. 25, pp. 7351–7352, 1982.

Hindawi Publishing Corporation Advances in Physical Chemistry Volume 2012, Article ID 236750, 12 pages doi:10.1155/2012/236750

Research Article

New ab Initio Potential Energy Surfaces for the Renner-Teller Coupled $1^1A'$ and $1^1A''$ States of CH₂

Haitao Ma,¹ Chunfang Zhang,¹ Zhijun Zhang,¹ Xiaojun Liu,² and Wensheng Bian¹

¹ Beijing National Laboratory for Molecular Sciences, Institute of Chemistry, Chinese Academy of Sciences, Beijing 100190, China

Correspondence should be addressed to Wensheng Bian, bian@iccas.ac.cn

Received 31 August 2011; Revised 31 October 2011; Accepted 9 November 2011

Academic Editor: António Varandas

Copyright © 2012 Haitao Ma et al. This is an open access article distributed under the Creative Commons Attribution License, which permits unrestricted use, distribution, and reproduction in any medium, provided the original work is properly cited.

New *ab initio* potential energy surfaces (PESs) for the two lowest-lying singlet $1^1A'$ and $1^1A''$ electronic states of CH₂, coupled by the Renner-Teller (RT) effect and meant for the spectroscopic study, are presented. The surfaces are constructed using a dual-level strategy. The internally contracted multireference configuration interaction calculations with the Davidson correction, using the *aug-cc-pVQZ* basis set, are employed to obtain 3042 points at the lower level. The core and core-valence correlation effects are taken into account in the *ab initio* calculations with a modified optimized *aug-cc-pCVQZ* basis set for the higher-level points. The analytical representations of these PESs, with the inclusion of the nonadiabatic RT terms, are obtained by the nonlinear least-squares fit of the calculated points to three-body expansion. Quantum dynamical calculations are performed on these PESs, and the computed vibronic energy levels for the two singlet electronic states are in excellent agreement with experiment.

1. Introduction

The CH₂ biradical has been the subject of many theoretical and experimental studies, due to its distinct electronic characteristics and chemical and physical properties. It is the direct chemical precursor of the widely observed CH radical [1]. As a crucial link in the photodissociation sequence of cometary methane, CH₂ plays a significant role in the chemistry of hydrocarbon combustion and the astrophysics of interstellar medium [2–5].

Since Herzberg and Johns [2] carried out a detailed analysis of the high-resolution absorption spectrum of the singlet CH_2 in the near ultraviolet region half a century ago, several groups [6–11] have observed the direct absorption spectra or subsequent monitoring of fluorescence via laser-induced fluorescence, stimulated emission pumping, dispersed fluorescence, and so forth. Experimental investigations of the spectroscopy provided abundant and precise rovibronic energy levels [12–16]. Recently, bands in the CH_2 \tilde{b}^1B_1 - \tilde{a}^1A_1 transition between 12500 and 13000 cm⁻¹ were recorded at

Doppler-limited resolution utilizing a transient frequency-modulation (FM) laser absorption spectrometer by Chang and coworkers [16]. An unexpected and particularly complicated rovibronic structure was detected for $b(1,1,0)^1$ and $b(0,3,0)^1$ vibronic levels. Comparison of the calculated spectra on the available potential energy surfaces (PESs) [17–19] with the experimental spectra of Herzberg and Johns [2] indicates that the labeling of some vibrational levels is quite inconsistent, which can be ascribed to the local perturbations from the vibrational resonances and Renner-Teller (RT) effect.

The study of the RT effect on the vibronic levels for nonlinear three-atom molecules has been an active area for several decades [8, 17, 20–24]. The \tilde{b}^1B_1 - \tilde{a}^1A_1 transition of CH₂, which is seen in the red and yellow parts of the spectrum, is one of the best examples in which the RT coupling should be observed [5]. One of the consequences of the RT coupling is the inversion of the K_a rotational structure in the lower component state (\tilde{a}^1A_1) near the barrier to linearity. As explained by Jungen et al. [25], this reordering

² Key Laboratory of Luminescence and Optical Information, Ministry of Education, Institute of Optoelectronic Technology, Beijing Jiaotong University, Beijing 100044, China

of the K_a energy levels results from the transformation at high bending levels from bent to linear configurations [8]. The two lowest-lying singlet electronic states of CH₂, which become a degenerate Δ pair at linearity, interact strongly with each other and are coupled dynamically [17, 24].

Theoretically, some researchers [3, 4, 26] examined a few electronic states of CH2 with state-of-the-art ab initio methods and provided significant clues to the understanding of the electronic structures. Bussery-Honvault and coworkers [27] computed an ab initio global PES for the first singlet state of CH₂, where a mixed numerical and analytical method was employed in the PES construction. This surface shows no barrier for the C_{2V} insertion, while a barrier of 4319 cm⁻¹ (12.35 kcal/mol) is present for the collinear approach. Unfortunately, visible discrepancies were found between the theoretical calculations on this surface and the experimental results [28]. Later, using the same ab initio methodology and similar fitting process, Bussery-Honvault and coworkers [29] constructed a PES for the second singlet state of CH₂; it should be mentioned that their two lowestlying singlet PESs are not degenerate at linearity. Joseph and Varandas [30] constructed a more accurate PES for the lowest singlet state of CH₂ with the DMBE scaled-externalcorrelations method [31] and obtained very good agreement with the experimental rate constants, which recommends it for future dynamics studies [30, 32]. Furthermore, Dawes et al. [33] constructed the lowest singlet PES using the local interpolative moving least squares method and performed further spectroscopic calculations, which yielded J = 0vibrational frequencies with a root-mean-square error of a few wavenumbers relative to available measurements.

Liu and co-workers [34] revealed various PES intersection seams among the $1^1A'$, $2^1A'$, $3^1A'$, $1^1A''$ and $2^1A''$, states in the $C(^1D)H_2$ reactive system systematically and determined the minimum energy crossing points (MECPs) accurately. The nonadiabatic interaction near MECPs may play an important role in spectroscopy and dynamics [35– 40]. The lowest MECP [34] in $C(^1D)H_2$, which is only 8797 cm⁻¹ above the CH₂ 1¹A' minimum and much lower in energy than all the other MECPs, is between the two lowlying $\tilde{a}^1 A_1$ and $\tilde{b}^1 B_1$ states, which become the degenerate Δ_g pair at linearity and hence are strongly coupled by the RT effect. All the other MECPs [34] are above or somewhat below the $C(^1D)+H_2$ asymptote in energy and thus are not expected to intervene most of the vibronic spectra of the two lowest-lying singlet electronic states. However, it is clear that the RT coupling must be taken into account in the vibronic energy level calculations of the two lowest-lying states.

A few PESs for the RT coupled \tilde{a}^1A_1 and \tilde{b}^1B_1 states have been developed to simulate the vibronic structure and electronic spectrum with the vibronic coupling included [17, 19, 24, 41]. However, the *ab initio* PESs of Green Jr. et al. [17] were empirically adjusted or shifted to fit the experimental data; other PESs [19, 24, 41] were constructed by fitting experimental data and a few *ab initio* points [13]. However, there are therefore accurate and fully *ab initio* PESs for the two lowest-lying singlet electronic states $1^1A'$ and $1^1A''$ of CH₂ with the RT terms required.

So far most of the ab initio work concerning CH2 has been based on the traditional correlated ab initio electronic structure calculations, that is, the so-called frozen core approximation, in which correlation effects involving the electrons in 1s core orbital of carbon are neglected. However, as noted by Peterson and Dunning [42], if the goals of a calculation are to obtain chemical accuracy of thermochemical properties, the effects of correlating the electrons in the core orbital generally must be addressed in the calculations. Of course, ab initio calculations including correlation effects of core electrons are very time-consuming. In this work, not only appropriate active space but also an optimized basis set with additional functions for describing core and corevalence correlation effects (called CV) is employed in our ab initio calculations, which can also guarantee that the two lowest-lying singlet PESs are degenerate at linearity. We further construct fully ab initio PESs for the two lowestlying singlet electronic states $1^1A'$ and $1^1A''$ of CH₂ with the inclusion of the nonadiabatic RT terms.

The organization of the present article is as follows. Section 2 describes the *ab initio* electronic structure calculations. The fitting of the *ab initio* energy points is presented in Section 3. The fitted PESs of CH₂ (called MZB) and vibronic energy level calculations are discussed in Section 4. Finally, a summary is given in Section 5.

2. Electronic Structure and ab Initio Calculations

2.1. Electronic Structure. For computational convenience, the molecule is placed in the yz plane, and the electronic configuration of ground state is $(1a_1)^{11}(2a_1)^{11}(1b_2)^{11}(3a_1)^{1}(1b_1)^{1}$. The $(1a_1)$ and $(2a_1)$ molecular orbitals (MOs) mostly have carbon 1s and 2s characters, respectively. The $(3a_1)$, $(1b_1)$, and $(1b_2)$ MOs mainly have the carbon 2p character lying along the twofold z axis, perpendicular and parallel with respect to the yz plane, respectively. In the C_s symmetry, the a_1 and a_2 orbitals become the a' orbitals, and the a_1 and a_2 orbitals become the a'' orbitals.

The electronic configurations of CH_2 can be represented as shown in Table 1 in the C_{2V} or C_s symmetry.

The \tilde{X}^3B_1 and \tilde{b}^1B_1 states, which share the same spatial orbital configuration with two open-shell electrons parallelly or antiparallelly distributed in the outer $3a_1$ and $1b_1$ orbitals, correspond to the triplet and singlet configurations, respectively. While the $\tilde{a}^1 A_1$ and $\tilde{c}^1 A_1$ states correspond primarily to configurations with double occupation of the $3a_1$ or $1b_1$ orbital, they could be appropriately described by the two main configuration wave functions. The two CI coefficients C_1 and C_2 for $\tilde{a}^1 A_1$ have opposite signs with $|C_1| \ge |C_2|$, while those for the $\tilde{c}^1 A_1$ state have the same sign with $|C_3| \leq$ $|C_4|$. Hence, multireference methods are required for an accurate ab initio description of the above excited states. The $\tilde{a}^1 A_1$ and $\tilde{b}^1 B_1$ states become the degenerate $1^1 \Delta_g$ pair at linearity and hence are strongly mixed by the RT coupling, which is important to the vibronic calculations. The \tilde{c}^1A_1 state correlates with the $1^1\Sigma_g^+$ state at linearity. The next two states, 1^1A_2 and 1^1B_2 , become the degenerate $1^1\Pi_u$ pair

Table 1

$\overline{\widetilde{X}}{}^{3}B_{1}:(1a_{1})^{\uparrow\downarrow}(2a_{1})^{\uparrow\downarrow}(1b_{2})^{\uparrow\downarrow}(3a_{1})^{\dagger}(1b_{1})^{\dagger}$	$X^{3}A^{\prime\prime}:(1a^{\prime})^{\uparrow\downarrow}(2a^{\prime})^{\uparrow\downarrow}(3a^{\prime})^{\uparrow\downarrow}(4a^{\prime})^{\uparrow}(1a^{\prime\prime})^{\uparrow}$
$\widetilde{a}^{1}A_{1}:C_{1}(1a_{1})^{\uparrow\downarrow}(2a_{1})^{\uparrow\downarrow}(1b_{2})^{\uparrow\downarrow}(3a_{1})^{\uparrow\downarrow}(1b_{1})^{0}+$	$1^{1}A':C_{1}(1a')^{\uparrow\downarrow}(2a')^{\uparrow\downarrow}(3a')^{\uparrow\downarrow}(4a')^{\uparrow\downarrow}(1a'')^{0}+$
$C_2(1a_1)^{\dagger\downarrow}(2a_1)^{\dagger\downarrow}(1b_2)^{\dagger\downarrow}(3a_1)^0(1b_1)^{\dagger\downarrow}$	$C_2(1a')^{\dagger\downarrow}(2a')^{\dagger\downarrow}(3a')^{\dagger\downarrow}(4a')^{0}(1a'')^{\dagger\downarrow}$
$\widetilde{b}^{1}B_{1}{:}(1a_{1})^{\uparrow\downarrow}(2a_{1})^{\uparrow\downarrow}(1b_{2})^{\uparrow\downarrow}(3a_{1})^{\uparrow}(1b_{1})^{\downarrow}$	$1^{1}A^{\prime\prime}{:}(1a^{\prime})^{\dagger\downarrow}(2a^{\prime})^{\dagger\downarrow}(3a^{\prime})^{\dagger\downarrow}(4a^{\prime})^{\dagger}(1a^{\prime\prime})^{\downarrow}$
$\widetilde{c}^{1}A_{1}:C_{3}(1a_{1})^{\dagger\downarrow}(2a_{1})^{\dagger\downarrow}(1b_{2})^{\dagger\downarrow}(3a_{1})^{\dagger\downarrow}(1b_{1})^{0}+$	$2^{1}A':C_{3}(1a')^{\uparrow\downarrow}(2a')^{\uparrow\downarrow}(3a')^{\uparrow\downarrow}(4a')^{\uparrow\downarrow}(1a'')^{0}+$
$C_4(1a_1)^{\dagger\downarrow}(2a_1)^{\dagger\downarrow}(1b_2)^{\dagger\downarrow}(3a_1)^0(1b_1)^{\dagger\downarrow}$	$C_4(1a^\prime)^{\dagger\downarrow}(2a^\prime)^{\dagger\downarrow}(3a^\prime)^{\dagger\downarrow}(4a^\prime)^0(1a^{\prime\prime})^{\dagger\downarrow}$
$1^{1}A_{2}$: $(1a_{1})^{\uparrow\downarrow}(2a_{1})^{\uparrow\downarrow}(1b_{2})^{\uparrow}(3a_{1})^{\uparrow\downarrow}(1b_{1})^{\downarrow}$	$2^{1}A^{\prime\prime}{:}(1a^{\prime})^{\dagger\downarrow}(2a^{\prime})^{\dagger\downarrow}(3a^{\prime})^{\dagger}(4a^{\prime})^{\dagger\downarrow}(1a^{\prime\prime})^{\downarrow}$
$1^{1}B_{2}:(1a_{1})^{\dagger \downarrow}(2a_{1})^{\dagger \downarrow}(1b_{2})^{\dagger}(3a_{1})^{\downarrow}(1b_{1})^{\dagger \downarrow}$	$3^{1}A':(1a')^{\uparrow\downarrow}(2a')^{\uparrow\downarrow}(3a')^{\uparrow}(4a')^{\downarrow}(1a'')^{\uparrow\downarrow}$

at linearity. The spin-orbit coupling between the \widetilde{X}^3B_1 and singlet states is small in the well region and thus is neglected in this work.

2.2. ab Initio Calculations. Two levels of ab initio calculations were performed for the PES construction which involves a dual-level strategy [43]. The electronic energies in the lower-level calculations are calculated with the state-averaged complete active space self-consistent field (SA-CASSCF) and internally contracted multireference configuration interaction (icMRCI) methods [44-47]. The active space consists of six electrons distributed among seven orbitals, which correspond to all valence electrons and valence orbitals and one additional 3s orbital of carbon which is of Rydberg character. The carbon 1s orbital is not correlated but optimized at the SA-CASSCF level. To get a good description of the two lowest-lying singlet states, especially in view of the importance of correct degeneracy between $1^1A'$ and $1^1A''$ at linear geometries and the influence of PES intersections, we simultaneously consider the five singlet states which correlate with the $C(^1D)+H_2$ asymptote in the present ab initio calculations. Consequently, the SA-CASSCF calculations including three and two roots in the A' and A''symmetries are carried out to obtain the orbitals for further icMRCI calculations. The Davidson correction (denoted as +Q) is employed to include the correlation energy due to higher excitations. Dunning's correlation-consistent polarized valence quadruple-zeta basis set augmented with diffuse functions (aug-cc-pVQZ) is used.

In the higher-level calculations, the methods and algorithm are the same as the lower-level, but the active space and basis set are different. The active space consists of all electrons distributed among eight orbitals, which include 1s, all valence, and 3s orbital of carbon. The carbon 1s orbital is correlated and also optimized at the SA-CASSCF level. To obtain the CV contribution to the energies, the aug-ccpVQZ basis set for C atom is modified. The details of this scheme could be found elsewhere [42, 48–51], and only a brief outline will be given here. The seven inner 1s functions are contracted to two functions using the coefficients from the aug-cc-pVQZ basis set. The outer five s functions are uncontracted as the six p functions. Two tight d and ffunctions are added to the (3d, 2f, 1g) polarized set given by Peterson and Dunning [42] and Woon and Dunning [48]. The additional functions are even tempered extensions of the valence sets, and the exponents of the added functions

are 5.262 and 14.984 for the *d* functions and 4.152 and 12.147 for the *f* functions which are obtained by successively multiplying the corresponding tightest functions by the ratio of the first two compact functions [50, 51]. This core basis set, developed to treat both core and valence correlations, is of the form (12s6p5d4f1g)/[7s6p5d4f1g] and is designated as optACVQZ, which is much smaller than Dunning's standard aug-cc-pCVQZ [42, 48, 49] and gives a good description of core electrons [50, 51].

For the *ab initio* calculation of nonadiabatic terms, the SA-CASSCF method is used. The active space is the same as that of the lower-level energy calculations, and the basis set employed here is the uncontracted *aug-cc-pVQZ* basis. The nonadiabatic terms, required for calculating for the RT coupling, are the matrix elements of electronic orbital angular momentum \hat{L} , and they are obtained as expectation values over the SA-CASSCF wave functions. The RT coupling takes effect when the molecule approaches linearity, that is, lies on the *z*-axis, hence the matrix elements of \hat{L}_x and \hat{L}_y can be neglected. The details of the RT Hamiltonian have been discussed in another publication [52]. So, three matrix elements of electronic angular momentum (designated as L_z^{ab} , L_{zz}^{aa} , and L_{zz}^{bb}) are calculated, where $\langle \tilde{a}^1A_1 \mid \hat{L}_z \mid \tilde{b}^1B_1 \rangle = -i\hbar L_z^{ab}$, $\langle \tilde{a}^1A_1 \mid \hat{L}_z^2 \mid \tilde{a}^1A_1 \rangle = \hbar^2 L_{zz}^{aa}$, $\langle \tilde{b}^1B_1 \mid \hat{L}_z^2 \mid \tilde{b}^1B_1 \rangle = \hbar^2 L_z^{bb}$.

All *ab initio* calculations reported in the present work were carried out using the MOLPRO2006.1 package of *ab initio* programs [53].

2.3. PES Grid. In order to cover the region of spectroscopic interest with two deep potential wells, *ab initio* calculations at icMRCI(6e, 7o)+Q/AVQZ and *ic*MRCI(8e, 8o)+Q/*optACVQZ* levels were performed at 3042 and 273 symmetry unique geometries, respectively. These were chosen carefully to accurately represent the dynamically important regions, particularly the vicinities of the minimum and near linearity. As pointed out by Liu and co-workers [34], the $1^1\Pi$ pair ($3^1A'$ and $2^1A''$) states conically cross not only the $1^1\Delta$ pair ($1^1A'$ and $1^1A''$) states at around 3.4 bohr, but also the $1^1\Sigma_g^+$ state ($2^1A'$) at 3.1 bohr in the stretching potential curves of linear H–C–H (with one of the C–H bond lengths fixed at 2.1 bohr).

We concentrate on the geometries with the CH bond length smaller than 3.0 bohrs in the process of the present PES construction. Dozens of geometries are also selected for the description of the higher energy regions. In the important regions, points were computed with small increments of 0.1–0.5 bohrs for bond length and 2.0–5.0° for bond angle, while in other regions coarser grids of 1.0-2.0 bohrs and 10.0–20.0° were used. Geometries with energies higher than 100 kcal/mol above the global minimum of \tilde{a}^1A_1 were not totally neglected but assigned a very small weight. In the calculations of icMRCI(8e, 8o)/optACVQZ, the grids were chosen as the following: 1.4, 1.8, 2.0, 2.05, 2.2, 2.6, and 3.0 bohrs for CH distance; 80, 100, 120, 143, 155, 175, and 180° for \angle HCH. In the calculations for the nonadiabatic coupling terms, almost the same grids were selected as those used in the higher-level calculations.

3. Fit of the Potential Energy Surfaces

To construct the PESs for the $1^1A'$ and $1^1A''$ states of CH₂, we choose three-body expansion functional forms for the analytical representation of the PESs with respect to the internal coordinates (R_1, R_2, θ) using a dual-level strategy, and nonadiabatic coupling terms are also taken into account. The idea of the dual-level strategy is to use two levels of ab initio calculations so as to reduce the number of higherlevel points needed for fitting [43], and the basic scheme is as follows. First, a set of lower-level ab initio points without the CV effect, which are calculated at the icMRCI(6e, 70)+Q/AVQZ level, is generated to construct a zeroth-order PES, V_x^0 (x = a, b stands for the $1^1A'$ and $1^1A''$ states of CH₂, resp.). Then, a set of higher-level points with the CV effect, calculated at the icMRCI(8e, 8o)+Q/optACVQZ level, is generated, and the data set of the energy differences of the two levels is used to construct a surface, V_x^{core} . And it should be noted that the energies of the lower level are obtained from V_r^0 , instead of the *ab initio* calculations. In addition, the nonadiabatic coupling terms, L_z^{ab} , L_{zz}^{aa} , and L_{zz}^{bb} ($\hbar = 1$ hereafter), are fitted into functions in the third stage for the future calculations. Each of these steps will now be described in more details as follows. The final adiabatic potential V is expressed as

$$V = V_x^0 + V_x^{\text{core}}. (1)$$

By applying the Levenberg-Marquardt technique for the nonlinear optimization, it was found that there are numerical problems for $M \geq 11$ due to near linear dependence of the parameters, and thus quadruple precision arithmetic was needed to obtain convergence [54]. To improve the fit, energy points below 60 kcal/mol relative to the PES minimum are weighted by a factor of 100, and energy points over 100 kcal/mol are weighted by 0.1. To accurately fit the intersection seam of the two lowest-lying singlet PESs at the linear configurations, all the points with \angle HCH larger than 170° are weighted by a factor of 100.

3.1. Analytical Representation of V^0 . For the analytical representation of V^0 , the calculated energy points were fitted to a three-body expansion in curvilinear coordinates, which

are believed to match the shape of the adiabatic PESs. For both electronic states, a Morse-type coordinate

$$\rho = 1 - e^{-\alpha(R - R_0)} \tag{2}$$

was used for the CH stretching mode, where $(R - R_0)$ is the displacement from the equilibrium geometry of the corresponding electronic state. For the angular coordinate, several types of polynomials were tested, including $\cos(\beta\theta)$, $\cos(\beta(\pi - \theta))$, $\cos(\beta(\theta - \theta_0))$, and $[(\theta - \theta_0) + \beta(\theta - \theta_0)^2 + \beta(\theta - \theta_0)^3]$. Finally, $\cos(\beta(\pi - \theta))$ was employed to describe the \angle HCH bending:

$$V_{x}^{0} = \sum_{ijk} C_{ijk}^{x} \rho_{1}^{i} \rho_{2}^{j} \rho_{3}^{k}$$

$$= \sum_{ijk} C_{ijk}^{x} \left[1 - e^{-\alpha_{1}(R_{1} - R_{0}^{x})} \right]^{i} \left[1 - e^{-\alpha_{2}(R_{2} - R_{0}^{x})} \right]^{j}$$

$$\times \left[\cos(\beta(\pi - \theta)) \right]^{k}.$$
(3)

The parameters α_1 , α_2 , β , and the C_{ijk} are determined by performing unequally weighted least squares fit to the *ab initio* data.

3.2. Analytical Representation of $V^{\rm core}$. The core correlation surface $V^{\rm core}$ was constructed in a similar way to the construction of V^0 , and the surfaces can be expressed as

$$\begin{split} V_{x}^{\text{core}} &= C_{000}^{x} + \exp\left\{\alpha \left[\left(R_{1} - R_{0}^{x}\right)^{2} + \left(R_{2} - R_{0}^{x}\right)^{2}\right]\right\} \\ &\times \sum_{ijk} C_{ijk}^{x} \rho_{1}^{i} \rho_{2}^{j} \rho_{3}^{k} \\ &= C_{000}^{x} + \exp\left\{\alpha \left[\left(R_{1} - R_{0}^{x}\right)^{2} + \left(R_{2} - R_{0}^{x}\right)^{2}\right]\right\} \\ &\times \sum_{ijk} C_{ijk}^{x} \left[\frac{\left(R_{1} - R_{0}^{x}\right)}{R_{0}^{x}}\right]^{i} \left[\frac{\left(R_{1} - R_{0}^{x}\right)}{R_{0}^{x}}\right]^{j} \\ &\times \left[\cos(\theta) - \cos(\theta_{0}^{x})\right]^{k}. \end{split} \tag{4}$$

3.3. Analytical Representation of the Nonadiabatic Coupling Terms. To fit the matrix elements of \hat{L}_z and \hat{L}_z^2 into analytical representations, several types of polynomials have been tested, and the following one provides a good description of the nonadiabatic coupling terms, L_z^{ab} , L_{zz}^{aa} , and L_{zz}^{bb} :

$$C_{000} + \cos^2\left(\frac{\theta}{2}\right) \times \sum_{ijk} C_{ijk}^n \left[1 - e^{-\alpha_1 R_1}\right]^i \left[1 - e^{-\alpha_2 R_2}\right]^j \left[\beta(\pi - \theta)\right]^k.$$

$$(5)$$

In the analytical representation above, the $\cos^2(\theta/2)$ guarantees that L^{aa}_{zz} and L^{bb}_{zz} have a correct behavior at linearity. Several types of cos functions instead of $\beta(\pi-\theta)$ were tested as angular coordinate, but very good results were not obtained. $\beta(\pi-\theta)$ is found to be suitable for the description of the bending mode.

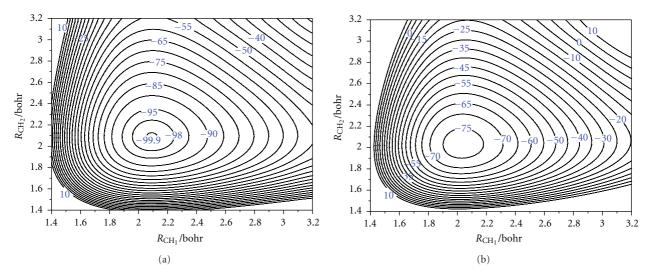


FIGURE 1: (a) Contour plot for the $1^1A'$ PES of CH₂ as a function of R_{CH_1} and R_{CH_2} (bohr) with \angle HCH fixed at the equilibrium value 102.45°. (b) Contour plot for the $1^1A''$ PES of CH₂ as a function of R_{CH_1} and R_{CH_2} (bohr) with \angle HCH fixed at the equilibrium value 144.36°. Energies (kcal/mol) are relative to the C(1D)+H₂ asymptote.

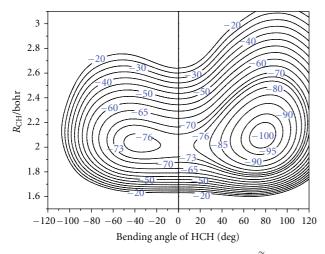


FIGURE 2: Contour plots for the \tilde{a}^1A_1 ($\rho \geq 0$) and \tilde{b}^1B_1 ($\rho \leq 0$) PESs as functions of $R_{\rm CH}$ and the bending angle of HCH. The intersection seam is shown as a bold line at $\rho = 0$, where ρ is the angle of bending. Energies (kcal/mol) are relative to the C(1D)+H₂ asymptote.

Many test calculations were performed with different polynomial orders M, and the dependences are shown in Table S1 (see Table S1 in the Supplementary Material available online at doi: 10.1155/2012/236750). Although, the RMS errors in the fit become smaller as M goes higher, we choose M=10 for the fit of V^0 due to numerical problems. The complete set of parameters amounts to a total of 286 linear coefficients and 3 nonlinear coefficients. The fit for V^0 has RMS errors of 31.88 and 142.88 cm $^{-1}$ for the $1^1A'$ and $1^1A''$ states, respectively. Below 60 kcal/mol, the RMS errors are 6.64 and 5.94 cm $^{-1}$, respectively. In the fit of $V^{\rm core}$, M is taken as 6. The complete set of parameters amounts to a total of 85 linear coefficients. The fit for $V^{\rm core}$ has

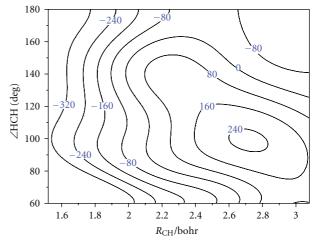


FIGURE 3: Contour plot (cm⁻¹) for V^{core} of the \tilde{a}^1A_1 state of CH₂ as a function of R_{CH} and \angle HCH.

RMS errors of 14.29 and $68.21 \, \text{cm}^{-1}$ for the $1^1A'$ and $1^1A''$ states, respectively. Below $60 \, \text{kcal/mol}$, the RMS errors are 3.15 and $11.89 \, \text{cm}^{-1}$, respectively. The numerical values of all parameters to generate the surfaces and coupling terms reported in the present study are presented in Tables S2, S3, and S4.

4. Features of the Fitted Surfaces and Vibronic Energy Level Calculations

4.1. Adiabatic PESs. Figure 1 presents the contour plots for CH bonds stretching of our PESs keeping \angle HCH fixed at 102.45° for the \tilde{a}^1A_1 state, 144.36° for the \tilde{b}^1B_1 state. We found the fitted potentials to be smooth and without any artificial oscillations. The degeneracy of the two lowestlying singlet adiabatic potentials is illustrated in Figure 2.

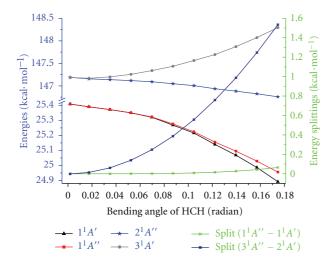


FIGURE 4: The bending potential energy curves for the four singlet states (1¹A', 1¹A'', 2¹A'', and 3¹A') of CH₂ calculated at the icMRCI(6e, 7o)+Q/AVQZ level. (The 2¹A' state, which lies between the 1¹A' and 3¹A' state, is not shown.) $R_{CH_1} = R_{CH_2} = 2.01$ bohrs. The zero energy is taken at the CH₂ (1¹A') minimum.

They are contour plots as functions of $R_{\rm CH}$ and \angle HCH. Our fitted PESs for the two singlet states are degenerate at $R_{\rm CH} = (1.6, 2.6)$ bohrs with \angle HCH = 180° . The PES difference at linear geometries in higher energy regions (with energies higher than 60 kcal/mol above the global minimum of \tilde{a}^1A_1) is due to the PES fitting error. To further improve the behavior of our PESs at linear geometries, we used an assumed angle dependence switching function to smoothly *connect* the two states above at linearity. Thus, this function is defined as follows:

$$f^{\text{sw}} = \frac{1}{2}\cos^4(\pi - \theta)\{1 - \tanh[200(1 + \cos\theta)]\}.$$
 (6)

Two adiabatic potentials for the \tilde{a}^1A_1 and \tilde{b}^1B_1 states of CH₂, which are going to be degenerate at linearity, are represented as follows:

$$V_a = \left(V_a^0 + V_a^{\text{core}}\right) + \left[\left(V_b^0 + V_b^{\text{core}}\right) - \left(V_a^0 + V_a^{\text{core}}\right)\right] f^{\text{sw}},$$

$$V_b = \left(V_b^0 + V_b^{\text{core}}\right) - \left[\left(V_b^0 + V_b^{\text{core}}\right) - \left(V_a^0 + V_a^{\text{core}}\right)\right] f^{\text{sw}}.$$
(7)

From the experimental side, a wide number of studies have led to the determination of accurate equilibrium geometries for the \tilde{a}^1A_1 and \tilde{b}^1B_1 states of CH₂. Geometries and relative energies of minima obtained from our work along with the available experimental and other theoretical values are given in Table 2. We find the PES minimum of the \tilde{a}^1A_1 state on our PESs to be located at $R_{\rm CH}=2.092$ bohrs and \angle HCH = 102.45°. Obviously, these results are in very good agreement with the experimental value CH₂ available, $R_{\rm CH}=2.092\pm0.004$ bohrs and \angle HCH = 102.38°. Despite the ground singlet state being widely studied, there have been limited research on the first excited singlet state \tilde{b}^1B_1 .

Table 2: Geometries and relative energies of the minima of the two lowest-lying singlet states of CH₂. R_e is the equilibrium interatomic distance, and θ_e is the equilibrium \angle HCH.

		Geon	netries	Relative energies	
		R _e (bohr)	$ heta_e$ (degree)	(kcal·mol ⁻¹)*	
	Ab initio without core ^a	2.0965	102.10	-100.54	
	Ab initio with core ^b	2.0914	102.38	-100.70	
	Our PESs ^c	2.0920	102.45	-100.70	
$\widetilde{a}^{1}A_{1}$	Liu et al.d	2.098	102.0	-100.3	
W 211	Flores and Gdanitz ^e	2.0917	102.31		
	Bussery-Honvault et al. ^f	2.09	102.5	-99.7	
	$DMBE^g$	2.09	102.4	-99.75	
	Exp. ^h	2.099	102.38		
	Exp.i	$2.092 \pm$	102.4 \pm		
	LAP.	0.004	0.4		
	Ab initio without core ^a	2.0316	143.12	-77.71	
	<i>Ab initio</i> with core ^b	2.0300	144.60	-77.96	
	Our PESs ^c	2.0300	144.36	-77.97	
\widetilde{b}^1B_1	Liu et al. ^d	2.032	143.2	-76.8	
	Flores and Gdanitz ^e	2.0165	143.39		
	Bussery-Honvault et al. ^f	2.02	141	-79.9	
	Exp. ^h	1.990	140 ± 15		
	Exp. ^j	2.052	139.30		

^{*} Energies are relative to the $C(^1D)+H_2$ asymptote.

As can be seen, this state is the open-shell singlet analog of the \widetilde{X}^3B_1 state. As expected, its molecular orbitals and Mulliken atomic distributions are very similar to those of the ground state, which makes the *ab initio* calculation more difficult. The PES minimum for the \widetilde{b}^1B_1 state on our PESs is located at $R_{\rm CH}=2.030\,{\rm bohrs}$ and $\angle{\rm HCH}=144.36^\circ$. In Figure 3, we have plotted the contours of the core corrections $V^{\rm core}$, as functions of $R_{\rm CH}$ and $\angle{\rm HCH}$ of the \widetilde{a}^1A_1 state. The CV effects have a geometry dependence, and the shifts can be positive or negative. The core correlations varies from -400 to $300\,{\rm cm}^{-1}$. The inclusion of core and corevalence correlation decreases the bond lengths by 0.0051 and 0.0016 bohrs and increases the bond angle by 0.28 and 1.48° for the \widetilde{a}^1A_1 and \widetilde{b}^1B_1 states, respectively.

The $1^1\Delta_g$ state of HCH at linear configuration, splitting into the two lowest-lying singlet electronic excited states

^aOur *ab initio* values using *ic*MRCI(6e, 7o)+Q/AVQZ.

^bOur ab initio values using icMRCI(8e, 8o)+Q/optACVQZ.

^cFrom our PESs.

^d Ab initio values using icMRCI(6e, 7o)/AVQZ from [34].

^eAb initio values using icMR-ACPF(8e, 7o)/ACVQZ from [55].

fPES values from [27, 29].

gPES values from [30].

hExperimental values from [2].

ⁱExperimental values from [11].

^jExperimental values from [56].

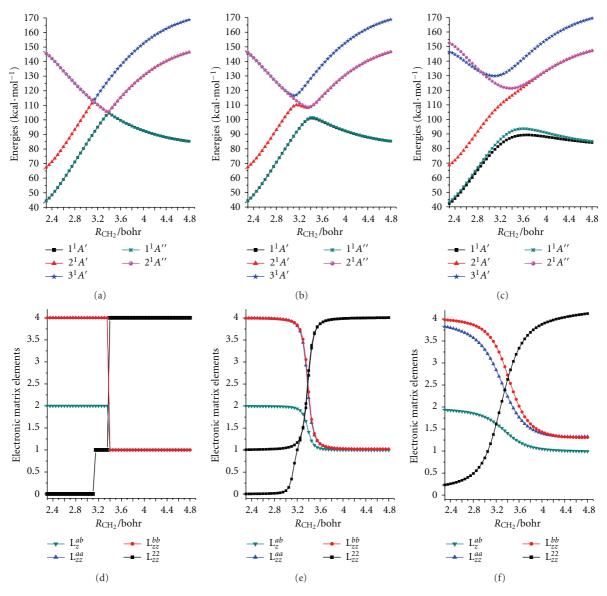


FIGURE 5: The stretching potential curves of the five singlet states $(1^1A', 2^1A', 3^1A', 1^1A'', \text{ and } 2^1A'' \text{ state})$ of CH₂ as functions of the bond length R_{CH_2} with the \angle HCH fixed at (a) 180°, (b) 175°, and (c) 160°, respectively; The Renner-Teller terms L_z^{ab} , L_{zz}^{aa} , L_{zz}^{bb} , and L_{zz}^{22} ($\langle 2^1A' \mid \hat{L}_z^2 \mid 2^1A' \rangle$) as functions of the bond length R_{CH_2} with \angle HCH fixed at (d) 180°, (e) 175°, and (f) 160°, respectively. R_{CH_1} is fixed at 2.09 bohrs, and the zero energy is taken at the CH₂ ($(1^1A')$ minimum.

 \tilde{a}^1A_1 and \tilde{b}^1B_1 as the molecule is bent, is a prime example of the vibronic RT effect. In this case, the splitting will be proportional to ρ^n , where $n=2\Lambda$ and Λ ($\Lambda=1$ for Π , and 2 for Λ state) is the eigenvalue of \hat{L}_z , the axial component of electronic angular momentum at linearity. Although the other two higher excited states ($3^1A'$ and $2^1A''$) calculated with icMRCI(6e, 70)+Q/AVQZ are not involved in the present PESs, it is clearly seen that in this region the *ab initio* computed PECs show the ρ^2 behavior for the doubly degenerate Π pair ($3^1A'$ and $2^1A''$) in Figure 4. The energy splittings between $1^1\Delta_g$ pair and $1^1\Pi_g$ pair states go quartically and quadratically, respectively, when approaching linearity.

While the energy changes with the CH bond stretched, the degeneracy of the $1^1A'$ and $1^1A''$ (or $3^1A'$ and $2^1A''$) of CH₂ is not lifted so long as the molecule is linear. The barrier to linearity plays a very important role in quantum mechanical calculations of vibronic energy levels when the RT effect is considered [18]. The height of the barrier to linearity in \tilde{a}^1A_1 CH₂ has been a long standing source of controversy. The range of reported barrier heights for linearity in the \tilde{a}^1A_1 state of CH₂ is quite large, varying from 8000 to 10000 cm⁻¹, which is summarized in Table 3. Herzberg and Johns originally gave a value of 8000 cm⁻¹, estimated from the spacing of the \tilde{b}^1B_1 bending vibrational levels [2]. Duxbury and Jungen [56] obtained a barrier of

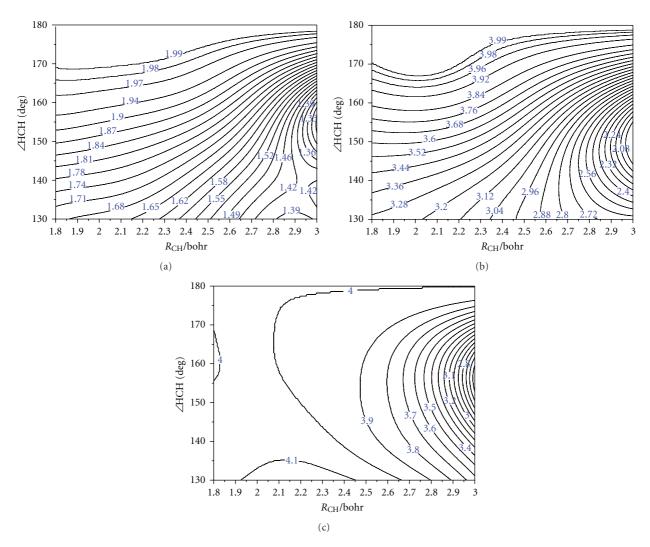


FIGURE 6: Contour plots for the Renner-Teller terms of CH₂ for the two lowest-lying singlet electronic states as functions of R_{CH} and \angle HCH: (a) L_{zz}^{ab} , (b) L_{zz}^{aa} , and (c) L_{zz}^{bb} .

 $9800 \,\mathrm{cm^{-1}}$ by fitting a bending potential function to the $(0, v_2, 0)$ levels. An earlier *ab initio* calculation gave a barrier height of $9600 \,\mathrm{cm^{-1}}$ [57]. Kalemos et al. [3] calculated this value to be $9217.7 \,\mathrm{cm^{-1}}$. In 2009, the DMBE PES predicted $9644 \,\mathrm{cm^{-1}}$ in agreement with the experimental determination of $9800 \,\mathrm{cm^{-1}}$ [56].

Green Jr. et al. [17] calculated an *ab initio* value of $9125 \, \mathrm{cm}^{-1}$ and empirically adjusted it to about $8800 \, \mathrm{cm}^{-1}$ according to the visible spectra around $15000 \, \mathrm{cm}^{-1}$. And this value is in very good agreement with the derived value of $8600 \pm 400 \, \mathrm{cm}^{-1}$ from the experiment by Hartland et al. [8]. The value of $8666 \, \mathrm{cm}^{-1}$ was obtained from the PESs constructed by Gu et al. [19] via fitting experimental data and a few *ab initio* points. Liu et al. gave the value as $8797 \, \mathrm{cm}^{-1}$ based upon the *ic*MRCI(6e, 7o)+Q/AVQZ calculations with three reference states in the A' symmetry. Our *ab initio* calculation at the same level with five reference states gives the barrier to linearity as $8895.1 \, \mathrm{cm}^{-1}$, but when the core correlation is taken into account, we obtain the *ab initio* calculated barrier to linearity as $8735.8 \, \mathrm{cm}^{-1}$. The core

correlations reduce this value by $160 \,\mathrm{cm}^{-1}$. It may be due to the fact that the Is electron is affected when the valence orbitals change from sp^2 hybridization at the minimum area to sp hybridization at linearity. Our PESs predict a height of 8715.02 and 760.2 cm⁻¹ for the barriers to linearity in the \tilde{a}^1A_1 and \tilde{b}^1B_1 states of CH₂, respectively.

4.2. Renner-Teller Nonadiabatic Coupling Terms. The fit of the RT nonadiabatic coupling terms has an RMS error of 0.0060, 0.0225, and 0.0148 for L_z^{ab} , L_{zz}^{aa} , and L_{zz}^{bb} , respectively. The polynomial order M is taken as 9. Note that $\langle 1^1A'|\hat{L}_z|1^1A''\rangle$ is imaginary and its absolute value is thus used. Figures 5(a), 5(b), and 5(c) describe the stretching potential curves of the five singlet states (1¹A', 2¹A', 3¹A', 1¹A'' and 2¹A'' state) of CH₂ as functions of bond length R_{CH_2} , with R_{CH_1} fixed at 2.09 bohrs and ∠HCH at 180°, 175° and 160°, respectively; at linearity, 1¹A' and 1¹A'' states become a degenerate Δ pair. Due to the conical intersection between Π and Δ at $R_{\text{CH}_2} = 3.38$ bohrs, L_z^{ab} , L_{zz}^{aa} , and L_{zz}^{bb} in

TABLE 3: The barrier to linearity of the \tilde{a}^1A_1 and \tilde{b}^1B_1 states.

Barrier to linearity		Note
$\widetilde{a}^1 A_1 \text{ (cm}^{-1})$	$\tilde{b}^1 B_1 \text{ (cm}^{-1})$	Note
9073.5	885.2	Our calculation at <i>ic</i> MRCI(6e, 7o)/ <i>AVQZ</i>
8895.1	907.3	Our calculation at <i>ic</i> MRCI(6e, 7o)+Q/ <i>AVQZ</i>
8735.8	706.2	Our calculation at <i>ic</i> MRCI(8e, 8o)+Q/optACVQZ
8715.1	760.2	Our PESs
8800		The empirically adjusted value based on the visible spectra ^a
8797		<i>Ab initio</i> value ^b
8666	725	The fit of empirically spectra and <i>ab initio</i> calculations ^c
8600 ± 400		The derived value from experiment ^d
8000		The derived value from experiment ^e
9217.7	953.2	<i>Ab initio</i> value ^f
9644		Ab initio value ^g
9451.1	1193.0	Others ^h
9750.0 ± 71.0	1616.6 ± 94	Others ⁱ
9600		Others ^j
9870		Others ^k
9144	879	Others ^l
9356	1049	Others ^m

^aFrom Ref. [17]. ^bFrom [34]. ^cFrom [8]. ^dFrom [19]. ^cFrom [2]. ^fFrom [3]. ^gFrom [30]. ^hFrom [5]. ⁱFrom [56]. ^jFrom [57]. ^kFrom [7]. ^lFrom [41]. ^mFrom [24].

Figure 5(d), which shows the dependence of the electronic matrix elements with $R_{\rm CH_2}$ stretching, are almost constants (2, 4, and 4) for $R_{\rm CH_2}$ < 3.38 bohrs due to quantization of the electronic angular momenta ($L_z^{ab}=2$, $L_{zz}^{aa,bb}=4$ for the Δ state); however, they change rapidly to 1 at $R_{\rm CH_2}\approx 3.38$ bohrs. Almost similar changing could be found in Figures 5(e) and 5(f) with \angle HCH = 175 and 160° due to the PESs intersections. And much more interesting rapid changing can also be found in the other three states ($2^1A'$, $3^1A'$, and $2^1A''$), for example, $\langle 2^1A' \mid \hat{L}_z^2 \mid 2^1A' \rangle$, but this is beyond the subject of the present work.

In Figure 6, the contour plots for L_z^{ab} , L_{zz}^{aa} , and L_{zz}^{bb} of the \widetilde{a}^1A_1 and \widetilde{b}^1B_1 states of CH₂ as function of CH stretching and \angle HCH bending are presented. It is well noticed that along the HCH axis, the values of $L_z^{ab} \simeq 2$ and $L_{zz}^{aa,bb} \simeq 4$ but then as the molecule deviates from linearity the values of L_z^{ab} and L_{zz}^{aa} decrease, and the values of L_{zz}^{bb} increase at the short R_{CH} region but decrease at the long R_{CH} region. The values of L_z^{ab} and $L_{zz}^{aa,bb}$ begin to drop rapidly and monotonically to 1 at $R_{\text{CH}} = 3.1$ bohrs due to the Δ/Π PES intersection at linearity. Figure 7 shows the variation of the electronic matrix elements for the two lowest-lying singlet electronic states as functions of the bending angle \angle HCH, with the CH-distance optimized for the \widetilde{a}^1A_1 state. It is shown that, as the molecule bends, the curve of L_z^{ab} decreases monotonically

Table 4: The calculated J=0 vibronic energy levels of the \widetilde{a}^1A_1 and \widetilde{b}^1B_1 states on our *ab initio* PESs employing the MCTDH method, compared with other theoretical results and experimental values. The energy levels are in cm⁻¹, relative to the zero point energy of the \widetilde{a}^1A_1 state.

$\widetilde{a}/\widetilde{b}$	ν_1	ν_2	ν_3	Green Jr. et al. ^a	Gu et al.b	Ours	Expt.
\widetilde{a}	0	1	0	1356	1351.2	1350.9	1352.6 ^d
\tilde{a}	0	2	0	2675	2664.1	2666.9	2667.7 ^d
\tilde{a}	1	0	0	2808	2807.5	2808.9	2806.0e
\tilde{a}	0	0	1	2863	2864.5	2862.5	2865.0e
\tilde{a}	0	3	0	3962	3945.6	3950.6	3950.5^{d}
\tilde{a}	1	1	0	4159	4156.5	4150.4	4152.8^{f}
\tilde{a}	0	4	0	5216	5191.5	5199.2	5196.6 ^d
\tilde{a}	1	2	0	5452	5437.6	5444.1	5444.9 ^f
\tilde{a}	2	0	0	5538	5529.3	5529.3	5531.4 ^f
\tilde{a}	0	5	0	6430	6397.9	6406.8	$6403.0^{d,f}$
\tilde{a}	1	3	0		6706.4	6712.0	6714.1 ^f
\widetilde{b}	0	0	0	8383	8354	8349	$8350^{\rm h}$
\widetilde{b}	0	1	0	9566	9537	9534	$9537^{\rm h}$
\widetilde{b}	0	2	0	10848	10831	10828	$10827^{h,i}$
\widetilde{b}	0	3	0	12231	12226	12220	$12220^{g,i,j}$
\widetilde{b}	0	4	0	13681	13684	13673	13678 ^g
\widetilde{b}	1	2	0	13850	13840	13835	13834 ^g
\widetilde{b}	1	3	0	15116	15121	15106	15114 ^g
\widetilde{b}	0	5	0	15317	15326	15313	15319 ^g
\widetilde{b}	2	2	0	16749	16749	16738	16742^{k}
\widetilde{b}	0	6	0	16929	16948	16934	16941 ^{c,g}
\widetilde{b}	1	5	0	18186	18201	18182	18192^{k}
\widetilde{b}	0	7	0	18590	18617	18603	18610 ^{c,g}

^aFrom [17]. ^bFrom [19]. ^cFrom [58]. ^dFrom [8]. ^cFrom [11]. ^fFrom [59]. ^gFrom [2]. ^hFrom [10]. ⁱFrom [12]. ^jFrom [9]. ^kFrom [60].

from 2, that of L_{zz}^{bb} rises from 4 basically in a monotonic way, but that of L_{zz}^{aa} first goes down from 4 and then goes up.

4.3. Vibronic Energy Level Calculations. We have calculated the vibronic energy levels of the \tilde{a}^1A_1 and \tilde{b}^1B_1 states on our *ab initio* PESs employing the block improved relaxation scheme [61, 62] in the multiconfiguration time-dependent Hartree (MCTDH) method [63–65]. The J=0 energy results are listed in Table 4 and are compared with experiments and calculations by other groups. The variation of the electronic matrix elements with geometry is not considered, and other groups also adopted this treatment in previous calculations. For consistency, the energy levels in Table 4 are labeled by the bent molecular notation (ν_1, ν_2, ν_3) .

Our calculated results are in excellent agreement with the experimental values, reflecting the accuracy of the constructed *ab initio* PESs. For the energy level of $\tilde{b}(0,2,0)$, our result $10828\,\mathrm{cm^{-1}}$ is closer to the experimental value $10827\,\mathrm{cm^{-1}}$ from Sears et al. [10, 12] than $10823\,\mathrm{cm^{-1}}$ from Herzberg and Johns [2]. The experimental results from Sears et al. are more reliable [10, 12, 16]. Compared with the

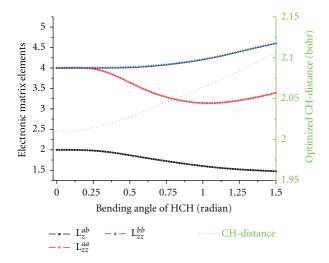


FIGURE 7: The Renner-Teller terms (L_z^{ab}, L_{zz}^{aa}) and L_{zz}^{bb}) of CH₂ for the two lowest-lying singlet electronic states as functions of the bending angle \angle HCH, with the CH-distance optimized for the \widetilde{a}^1A_1 state.

calculated results from Green Jr. et al., our results are closer to experiment [17]. Generally speaking, our results are in slightly better agreement with the experimental values than the results of Gu et al. [19], and it should be noted that the semiempirical PESs used by Gu et al. were adjusted according to the experimental values while ours are fully *ab initio* ones.

5. Summary

In this work, we report fully ab initio PESs for the RT coupled $1^1A'$ and $1^1A''$ states of CH₂ suitable for the spectroscopic study, based on the icMRCI+Q method using the AVQZ and a kind of optimized ACVQZ basis sets. The core and corevalence correlation effects are included, which are necessary for an accurate quantum chemical description of the CH₂ electronic states. The analytical representations of the two lowest-lying singlet PESs, with the inclusion of the matrix elements of electronic angular momentum L_z^{ab} , L_{zz}^{aa} , and L_{zz}^{bb} , are obtained by fitting. The obtained PESs are smooth, and the two adiabatic potentials are exactly degenerate at linearity. The minimal energy structures and the barriers to linearity predicted by our PESs are in excellent agreement with available experimental data. Furthermore, the MCTDH quantum dynamical calculations are carried out on these new PESs, and the calculated vibronic energy levels are in excellent agreement with the experimental values. Further work on the construction of the global PESs for the $1^1A'$ and $1^1A''$ states, suitable for the $C(^1D)+H_2$ reactive scattering studies, is in progress, and various PES intersections as revealed in our previous work [34], in particular conical intersections, will be included.

Acknowledgments

This work is supported by National Natural Science Foundation of China (nos. 20733005 and 21173232), Chinese

Academy of Sciences, and Beijing National Laboratory for Molecular Sciences. The authors would like to thank Professor H. Partridge for useful discussions of the modified basis set *optACVQZ* for core-valence calculations.

References

- [1] R. A. Beärda, M. C. Van Hemert, and E. F. Van Dishoeck, "Photodissociation of CH₂. I. Potential energy surfaces of the dissociation into CH and H," *The Journal of Chemical Physics*, vol. 97, no. 11, pp. 8240–8249, 1992.
- [2] G. Herzberg and J. W. C. Johns, "The Spectrum and Structure of Singlet CH₂," *Proceedings of the Royal Society of London A*, vol. 295, no. 1441, pp. 107–128, 1966.
- [3] A. Kalemos, T. H. Dunning, A. Mavridis, and J. F. Harrison, "CH₂ revisited," *Canadian Journal of Chemistry*, vol. 82, no. 6, pp. 684–693, 2004.
- [4] C. D. Sherrill, M. L. Leininger, T. J. V. Huis, and H. F. Schaefer III, "Structures and vibrational frequencies in the full configuration interaction limit: predictions for four electronic states of methylene using a triple-zeta plus double polarization (TZ2P) basis," *The Journal of Chemical Physics*, vol. 108, no. 3, pp. 1040–1049, 1998.
- [5] M. N. R. Ashfold, M. A. Fullstone, G. Hancock, and G. Duxbury, "Laser induced fluorescence spectroscopy of the CD₂ (α

 ¹A₁) radical: Renner-teller effect in CH₂ and CD₂," Molecular Physics , vol. 45, no. 4, pp. 887–896, 1982.
- [6] W. Xie, C. Harkin, H. L. Dai, W. H. Green, Q. K. Zheng, and A. J. Mahoney, "Transient vibrational spectroscopy of \tilde{a}^1A_1 CH₂ v₂ = 2," *Journal of Molecular Spectroscopy*, vol. 138, no. 2, pp. 596–601, 1989.
- [7] W. Xie, C. Harkin, and H. L. Dai, "Bending overtones and barrier height of \tilde{a}^1A_1 CH₂ by flash photolysis stimulated emission pumping," *The Journal of Chemical Physics*, vol. 93, no. 7, pp. 4615–4623, 1990.
- [8] G. V. Hartland, D. Qin, and H. L. Dai, "Renner-Teller effect on the highly excited bending levels of \(\tilde{a}^1 A_1 \) CH2," The Journal of Chemical Physics, vol. 102, no. 17, pp. 6641–6645, 1995.
- [9] B. C. Chang, M. Wu, G. E. Hall, and T. J. Sears, "Near-infrared vibronic spectrum of the CH₂ b̃¹B₁←ã¹A₁ transition," *The Journal of Chemical Physics*, vol. 101, no. 11, pp. 9236–9245, 1994.
- [10] K. Kobayashi, L. D. Pride, and T. J. Sears, "Absorption spectroscopy of singlet CH₂ near 9500 cm⁻¹," The Journal of Physical Chemistry A, vol. 104, no. 45, pp. 10119–10124, 2000.
- [11] H. Petek, D. J. Nesbitt, D. C. Darwin, P. R. Ogilby, C. B. Moore, and D. A. Ramsay, "Analysis of CH₂ \tilde{a}^1A_1 (1,0,0) and (0,0,1) Coriolis-coupled states, $\tilde{a}^1A_1-\tilde{x}^3B_1$ spin-orbit coupling, and the equilibrium structure of CH₂ \tilde{a}^1A_1 ," *The Journal of Chemical Physics*, vol. 91, no. 11, pp. 6566–6578, 1989.
- [12] G. E. Hall, A. V. Komissarov, and T. J. Sears, "Doppler-resolved spectroscopy as an assignment tool in the spectrum of singlet methylene," *The Journal of Physical Chemistry A*, vol. 108, no. 39, pp. 7922–7927, 2004.
- [13] A. J. Marr, T. J. Sears, and B. C. Chang, "Near-infrared spectroscopy of CH₂ by frequency modulated diode laser absorption," *The Journal of Chemical Physics*, vol. 109, no. 9, pp. 3431–3442, 1998.
- [14] Z. Wang, Y. Kim, G. E. Hall, and T. J. Sears, "State mixing and predissociation in the $\widetilde{c} \leftarrow \widetilde{a}$ band system of singlet methylene studied by optical-optical double resonance," *The Journal of Physical Chemistry A*, vol. 112, no. 39, pp. 9248–9254, 2008.

- [15] K. Kobayashi, G. E. Hall, and T. J. Sears, "The spectrum of CH₂ near 1.36 and 0.92 μ m: reevaluation of rotational level structure and perturbations in $\widetilde{a}(010)$," *The Journal of Chemical Physics*, vol. 124, no. 18, Article ID 184320, 2006.
- [16] C. -H. Chang, Z. Wang, G. E. Hall, T. J. Sears, and J. Xin, "Transient laser absorption spectroscopy of CH₂ near 780 nm," *Journal of Molecular Spectroscopy*, vol. 267, no. 1-2, pp. 50–57, 2011.
- [17] W. H. Green Jr., N. C. Handy, P. J. Knowles, and S. Carter, "Theoretical assignment of the visible spectrum of singlet methylene," *The Journal of Chemical Physics*, vol. 94, no. 1, pp. 118–132, 1991.
- [18] G. Duxbury, A. Alijah, B. D. McDonald, and C. Jungen, "Stretch-bender calculations of the effects of orbital angular momentum and vibrational resonances in the spectrum of singlet methylene," *The Journal of Chemical Physics*, vol. 108, no. 6, pp. 2351–2360, 1998.
- [19] J. P. Gu, G. Hirsch, R. J. Buenker et al., "A theoretical study of the absorption spectrum of singlet CH₂," *Journal of Molecular Structure*, vol. 517-518, pp. 247–264, 2000.
- [20] R. Renner, "Zur Theorie der Wechselwirkung zwischen Elektronen- und Kernbewegung bei dreiatomigen, stabförmigen Molekülen," Zeitschrift für Physik, vol. 92, no. 3-4, pp. 172– 193, 1934.
- [21] G. J. Halasz, A. Vibok, R. Baer, and M. Baer, "Renner-Teller nonadiabatic coupling terms: an *ab-initio* study of the HNH molecule," *The Journal of Chemical Physics*, vol. 124, no. 8, Article ID 081106, 4 pages, 2006.
- [22] G. J. Halász, Á. Vibók, R. Baer, and M. Baer, "D matrix analysis of the Renner-Teller effect: an accurate three-state diabatization for NH₂," *The Journal of Chemical Physics*, vol. 125, no. 9, Article ID 094102, 9 pages, 2006.
- [23] S. Zhou, Z. Li, D. Xie, S. Y. Lin, and H. Guo, "An ab initio global potential-energy surface for NH₂ (A²A') and vibrational spectrum of the Renner-TellerA²A'-X²A'' system," The Journal of Chemical Physics, vol. 130, no. 18, Article ID 184307, 10 pages, 2009.
- [24] G. Duxbury, B. D. McDonald, M. Van Gogh, A. Alijah, C. Jungen, and H. Palivan, "The effects of vibrational resonances on Renner-Teller coupling in triatomic molecules: the stretch-bender approach," *The Journal of Chemical Physics*, vol. 108, no. 6, pp. 2336–2350, 1998.
- [25] C. Jungen, D. N. Malm, and A. J. Merer, "Analysis of a $^{1}\Delta_{u} ^{1}\Sigma_{g}^{}$ transition of CS₂ in the near ultraviolet," *Canadian Journal of Physics*, vol. 51, no. 14, pp. 1471–1490, 1973.
- [26] B. Ostojić, "The dissociation of singlet methylene," *Journal of Molecular Spectroscopy*, vol. 212, no. 1, pp. 130–131, 2002.
- [27] B. Bussery-Honvault, P. Honvault, and J. M. Launay, "A study of the $C(^1D) + H_2 \rightarrow CH + H$ reaction: global potential energy surface and quantum dynamics," *The Journal of Chemical Physics*, vol. 115, no. 23, pp. 10701–10708, 2001.
- [28] L. Bañares, F. J. Aoiz, P. Honvault, B. Bussery-Honvault, and J. M. Launay, "Quantum mechanical and quasi-classical trajectory study of the $C(^1D) + H_2$ reaction dynamics," *The Journal of Chemical Physics*, vol. 118, no. 2, pp. 565–568, 2003.
- [29] B. Bussery-Honvault, J. Julien, P. Honvault, and J.-M. Launay, "Global 1 1A" potential energy surface of CH₂ and quantum dynamics of a sideways insertion mechanism for the $C(^1D) + H_2 \rightarrow CH(^2\Pi) + H$ reaction," *Physical Chemistry Chemical Physics*, vol. 7, no. 7, pp. 1476–1481, 2005.
- [30] S. Joseph and J. C. Varandas, "Accurate double many-body expansion potential energy surface for the lowest singlet state of methylene," *The Journal of Physical Chemistry A*, vol. 113, no. 16, pp. 4175–4183, 2009.

- [31] A. J. C. Varandas, "Intermolecular and intramolecular potentials: topographical aspects, calculation, and functional representation via a double many-body expansion method," Advances in Chemical Physics, vol. 74, pp. 255–338, 1988.
- [32] S. Joseph, P. J. S. B. Caridade, and A. J. C. Varandas, "Quasiclassical trajectory study of the $C(^1D) + H_2$ reaction and isotopomeric variants: kinetic isotope effect and cd/ch branching ratio," *The Journal of Physical Chemistry A*, vol. 115, no. 27, pp. 7882–7890, 2011.
- [33] R. Dawes, A. F. Wagner, and D. L. Thompson, "Ab initio wavenumber accurate spectroscopy: ¹CH₂ and HCN vibrational levels on automatically generated IMLS potential energy surfaces," *The Journal of Physical Chemistry A*, vol. 113, no. 16, pp. 4709–4721, 2009.
- [34] X. Liu, W. Bian, X. Zhao, and X. Tao, "Potential energy surface intersections in the C(¹D)H₂ reactive system," *The Journal of Chemical Physics*, vol. 125, Article ID 074306, 7 pages, 2006.
- [35] H. Zhao, W. Bian, and K. Liu, "A theoretical study of the reaction of O(³P) with isobutene," *Journal of Physical Chemistry A*, vol. 110, no. 25, pp. 7858–7866, 2006.
- [36] N. Matsunaga and D. R. Yarkony, "Energies and derivative couplings in the vicinity of a conical intersection. II. CH₂(2³A'',³3³A'') and H₂S(1¹A''2¹A''), unexpected results in an ostensibly standard case," *The Journal of Chemical Physics*, vol. 107, no. 19, pp. 7825–7838, 1997.
- [37] D. R. Yarkony, "Diabolical conical intersections," Reviews of Modern Physics, vol. 68, no. 4, pp. 985–1013, 1996.
- [38] J. Ivanic, G. J. Atchity, and K. Ruedenberg, "Violation of the weak noncrossing rule between totally symmetric closed-shell states in the valence-isoelectronic series O₃, S₃, SO₂, and S₂O," *The Journal of Chemical Physics*, vol. 107, no. 11, pp. 4307–4317, 1997.
- [39] G. J. Atchity and K. Ruedenberg, "Strong shifts in diabatic nondynamic electron correlations cause conical intersection between low-lying closed-shell adiabatic singlets of like symmetry in ozone," *The Journal of Chemical Physics*, vol. 99, no. 5, pp. 3790–3798, 1993.
- [40] H. Ma, X. Liu, W. Bian, L. Meng, and S. Zheng, "A theoretical study of the mechanism and kinetics of $F + N_3$ reactions," *ChemPhysChem*, vol. 7, no. 8, pp. 1786–1794, 2006.
- [41] P. Jensen, M. Brumm, W. P. Kraemer, and P. R. Bunker, "A treatment of the Renner effect using the MORBID hamiltonian," *Journal of Molecular Spectroscopy*, vol. 171, no. 1, pp. 31–57, 1995.
- [42] K. A. Peterson and T. H. Dunning, "Accurate correlation consistent basis sets for molecular core-valence correlation effects: the second row atoms Al-Ar, and the first row atoms B-Ne revisited," *The Journal of Chemical Physics*, vol. 117, no. 23, pp. 10548–10560, 2002.
- [43] J. Cao, Z. Zhang, C. Zhang, W. Bian, and Y. Guo, "Kinetic study on the H+SiH₄ abstraction reaction using an *ab initio* potential energy surface," *The Journal of Chemical Physics*, vol. 134, no. 2, 2011.
- [44] H. J. Werner and P. J. Knowles, "A second order multiconfiguration SCF procedure with optimum convergence," *The Journal of Chemical Physics*, vol. 82, no. 11, pp. 5053–5063, 1985
- [45] H. J. Werner and W. Meyer, "A quadratically convergent multiconfiguration-self-consistent field method with simultaneous optimization of orbitals and Cl coefficients," *The Journal* of Chemical Physics, vol. 73, no. 5, pp. 2342–2356, 1980.
- [46] H. J. Werner and W. Meyer, "A quadratically convergent MCSCF method for the simultaneous optimization of several

- states," *The Journal of Chemical Physics*, vol. 74, no. 10, pp. 5794–5801, 1981.
- [47] H. J. Werner and P. J. Knowles, "An efficient internally contracted multiconfiguration-reference configuration interaction method," *The Journal of Chemical Physics*, vol. 89, no. 9, pp. 5803–5814, 1988.
- [48] D. E. Woon and T. H. Dunning, "Gaussian basis sets for use in correlated molecular calculations. V. Core-valence basis sets for boron through neon," *The Journal of Chemical Physics*, vol. 103, no. 11, pp. 4572–4585, 1995.
- [49] A. K. Wilson, T. Van Mourik, and T. H. Dunning, "Gaussian basis sets for use in correlated molecular calculations. VI. Sextuple zeta correlation consistent basis sets for boron through neon," *Journal of Molecular Structure: THEOCHEM*, vol. 388, no. 1–3, pp. 339–349, 1996.
- [50] H. Partridge and D. W. Schwenke, "The determination of an accurate isotope dependent potential energy surface for water from extensive *ab initio* calculations and experimental data," *The Journal of Chemical Physics*, vol. 106, no. 11, pp. 4618– 4639, 1997.
- [51] O. L. Polyansky, A. G. Császár, S. V. Shirin et al., "High-accuracy *ab initio* rotation-vibration transitions for water," *Science*, vol. 299, no. 5606, pp. 539–542, 2003.
- [52] Z. Zhang, H. Ma, and W. Bian, "Accurate quantum mechanical study of the Renner-Teller effect in the singlet CH₂," *The Journal of Chemical Physics*, vol. 135, Article ID 154303, 10 pages, 2011.
- [53] H.-J. Werner, P. J. Knowles, R. Lindh et al., MOLPRO, version 2006.1, a package of *ab initio* programs.
- [54] W. Bian and H.-J. Werner, "Global *ab initio* potential energy surfaces for the CIH₂ reactive system," *The Journal of Chemical Physics*, vol. 112, no. 1, pp. 220–229, 2000.
- [55] J. R. Flores and R. J. Gdanitz, "Accurately solving the electronic Schrödinger equation of small atoms and molecules using explicitly correlated (r₁₂-)MR-CI. VIII. Valence excited states of methylene (CH₂)," *The Journal of Chemical Physics*, vol. 123, no. 14, Article ID 144316, 8 pages, 2005.
- [56] G. Duxbury and C. Jungen, "Effects of orbital angular momentum in CH₂ The Renner-Teller effect," *Journal of Polymer Science B*, vol. 63, no. 6, pp. 981–998, 1988.
- [57] D. C. Comeau, I. Shavitt, P. Jensen, and P. R. Bunker, "An ab initio determination of the potential-energy surfaces and rotation-vibration energy levels of methylene in the lowest triplet and singlet states and the singlet—triplet splitting," *The Journal of Chemical Physics*, vol. 90, no. 11, pp. 6491–6500, 1989.
- [58] H. Petek, D. J. Nesbitt, D. C. Darwin, and C. Bradley Moore, "Visible absorption and magnetic–rotation spectroscopy of ${}^{1}\text{CH}_{2}$: The analysis of the $\widetilde{b}^{1}B_{1}$ state," *The Journal of Chemical Physics*, vol. 86, no. 3, pp. 1172–1188, 1987.
- [59] G. V. Hartland, D. Qin, and H. L. Dai, "Fourier transform dispersed fluorescence spectroscopy: observation of new vibrational levels in the 5000–8000 cm⁻¹ region of ã¹A₁ CH₂," *The Journal of Chemical Physics*, vol. 98, no. 3, pp. 2469–2472, 1993
- [60] W. H. Green, I. C. Chen, H. Bitto, D. R. Guyer, and C. B. Moore, "New vibrational bands of CH_2 (\tilde{b}^1B_1)," *Journal of Molecular Spectroscopy*, vol. 138, no. 2, pp. 614–629, 1989.
- [61] L. J. Doriol, F. Gatti, C. Iung, and H. D. Meyer, "Computation of vibrational energy levels and eigenstates of fluoroform using the multiconfiguration time-dependent Hartree method," *The Journal of Chemical Physics*, vol. 129, no. 22, Article ID 224109, 9 pages, 2008.

- [62] H. D. Meyer, F. L. Quéré, C. Léonard, and F. Gatti, "Calculation and selective population of vibrational levels with the Multiconfiguration Time-Dependent Hartree (MCTDH) algorithm," *Chemical Physics*, vol. 329, no. 1-3, pp. 179–192, 2006
- [63] H.-D. Meyer, U. Manthe, and L. S. Cederbaum, "The multiconfigurational time-dependent Hartree approach," *Chemical Physics Letters*, vol. 165, no. 1, pp. 73–78, 1990.
- [64] M. H. Beck, A. Jäckle, G. A. Worth, and H. D. Meyer, "The multiconfiguration time-dependent Hartree (MCTDH) method: a highly efficient algorithm for propagating wavepackets," *Physics Report*, vol. 324, no. 1, pp. 1–105, 2000.
- [65] G. A. Worth, M. H. Beck, A. Jäckle, and H.-D. Meyer, The MCTDH Package, Version 8.2, 2000, University of Heidelberg, Germany. H.-D. Meyer, Version 8.3, 2002, Version 8.4, 2007, http://mctdh.uni-hd.de.

Hindawi Publishing Corporation Advances in Physical Chemistry Volume 2012, Article ID 867409, 15 pages doi:10.1155/2012/867409

Review Article

Applications of Potential Energy Surfaces in the Study of Enzymatic Reactions

Eric A. C. Bushnell, WenJuan Huang, and James W. Gauld

Department of Chemistry and Biochemistry, University of Windsor, Windsor, ON, Canada N9B 3P4

Correspondence should be addressed to James W. Gauld, gauld@uwindsor.ca

Received 26 June 2011; Revised 23 August 2011; Accepted 29 August 2011

Academic Editor: Laimutis Bytautas

Copyright © 2012 Eric A. C. Bushnell et al. This is an open access article distributed under the Creative Commons Attribution License, which permits unrestricted use, distribution, and reproduction in any medium, provided the original work is properly cited.

From a generated PES, one can determine the relative energies of species involved, the sequence in which they occur, and the activation barrier(s) associated with individual steps or the overall mechanism. Furthermore, they can provide more insights than a simple indication of a path of sequential mechanistic structures and their energetic relationships. The investigation into the activation of O_2 by alpha-ketoglutarate-dependent dioxygenase (AlkB) clearly shows the opportunity for spin inversion, where one can see that the lowest energy product may be formed via several possible routes. In the investigation of uroporphyrinogen decarboxylase III (UROD), the use of QM/MM methods allowed for the inclusion of the anisotropic protein environment providing greater insight into the rate-limiting barrier. Lastly, the mechanism of 6-phospho- α -glucosidase (GlvA) was discussed using different active site models. In particular, a continuum model PES was compared to the gas-phase PES.

1. Introduction

For a chemical reaction, enzymatic or nonenzymatic, the reactants, intermediates, and products all exist on a multidimensional surface. With this surface, a reaction is perfectly described by the statistical average of all possible paths from reactants to products via all possible intermediates [1]. However, a system with N atoms would require computing a (3N-6)-dimensional surface. Hence, if X number of points are to be computed for each of the (3N-6) dimensions, then X^{3N-6} calculations must be done [1]. Thus, such an undertaking is usually only computationally feasible for chemical models that consist of a few atoms. In contrast, studies on enzymatic mechanisms often necessarily require large chemical models consisting of important active site functional groups and cofactors and the substrate. Indeed, the cluster-based approach for investigating biochemical reactions typically use chemical models containing 200 atoms or more [2]. Thus, for such systems, it is impossible to determine the complete PES. Instead, a "slice" of the surface is typically constructed that involves only two coordinates, energy and reaction coordinate, and is commonly referred to as the PES [3].

The use and applicability of such "reduced-dimensionality" PESs reflects the fact that chemists and biochemists are usually only interested in key, mechanistically relevant structures including, for example, the (i) isolated reactants, (ii) reactive complex, (iii) transition structures (TS), (iv) intermediate(s), (v) product complex, and (vi) the separated products (Figure 1) [1]. It is noted that in general, computational studies on enzymatic reactions are investigated with the enzyme-substrate complex already formed. This is due in part to the inherent difficulties associated with modeling substrate binding and product release such as, for instance, consideration of clathrate waters. Furthermore, as previously stated [4], in some cases substrate binding is "seldom the most interesting part of the potential surface".

A "reduced dimensionality" PES can provide a considerable amount of information and insight into a chemical system. For example, a common goal of computational chemistry is the accurate determination of the thermochemistry of a particular system. From a PES, one can determine the relative energies of species involved, the sequence in which they occur, and the activation barrier(s) associated with individual steps or the overall mechanism. Consequently, one can determine if a reaction step or pathway is

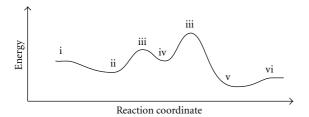


FIGURE 1: A generic PES showing (i) isolated reactants, (ii) reactive complex, (iii) TSs, (iv) intermediate complex, (v) product complex, and (vi) separated products.

feasible under the given conditions. With the appropriate corrections, these potential energies can be converted to enthalpies or free energies as has been previously discussed in detail [3]. For enzyme-catalysed reactions, free energy barriers between 55–75 kJ mol⁻¹ are typical with the upper thermodynamic limit generally held to be 84–105 kJ mol⁻¹ [4]. For barriers greater than 40 kJ mol⁻¹, transition state theory is sufficiently accurate to enable determination of the associated rate constant, albeit perhaps to within several orders of magnitude (1) [4]

$$k = \frac{k_B T}{h} e^{-\Delta G^{\ddagger}/RT}. \tag{1}$$

The reliability and accuracy of any PES is dependent on the computational model used; that is, the choice of computational method plus chemical model. A common approach, in particular for investigations of enzymatic processes, is the use of "cluster chemical models" in combination with a reliable quantum mechanical (QM) or density functional theory (DFT) methods. Typically, in such cases, only those regions of the active site-substrate complex involved in bond making and breaking processes and active site residues or functional groups that play a direct role are included [5]. For the study of biocatalytic processes, DFT methods, in particular, B3LYP, are presently the most widely used [6-8]. This is due to the fact that they include electron correlation effects yet are computationally less expensive than more conventional wave function-based electron correlation methods. Hence, they can be applied to comparatively large chemical models [4, 9]. Furthermore, they have been shown to often be able to provide accurate and reliable structures and thermochemistry. Indeed, B3LYP has been shown to often be highly accurate [5] with relative energy errors for 1st and 2nd row atom and transition metal-containing systems of just ~ 13.0 and ~ 21.0 kJ mol⁻¹, respectively [4]. The surrounding protein environment, more specifically its general polarity, is then included via use of a polarizable continuum model (e.g., IEF-PCM) [10, 11].

More recently, QM/MM methods have been increasingly applied to the elucidation of enzymatic reaction PESs. This is due in part to the fact that (i) they are able to model a greater portion of the enzyme through their combined use of QM and molecular mechanics (MM) methods, and thus (ii) are able to model the polar and steric nonhomogeneity of the protein environment surrounding the active site. Furthermore, the computed energetics of the system have

been shown to often converge faster with increasing chemical model size than for the above cluster/QM-based approach [12]. In addition, the role of the residues and mechanism is also less sensitive to increasing or varying model size [13]. However, QM/MM-based approaches suffer some of the same limitations as the alternative cluster/DFT approach such as the fact that the dynamic behaviour of the enzyme is not fully taken into account [13, 14]. The application of these methods to the elucidation of enzymatic pathways has been previously reviewed; see, for example, Senn and Thiel [15] and Llano and Gauld [16].

There are computational techniques available to determine a statistical average of possible alternative pathways of an enzymatic reaction [1, 3, 12, 17]. One common approach is to use a semiempirical (SE) method to describe the QM layer, while an MM method is used to describe the outer layer. The use of SE methods is due to the fact that extensive sampling of the protein, substrate, and solvent must be performed in order to calculate the free energies. This sampling requires large numbers of calculations that also include the inner layer, hence the need for highly efficient methods that describe this region. Alternatively, the CPMD method typically describes the inner layer using DFT methods. However, due to the added computational costs, simulation timescales are limited to 0.1 ns, significantly shorter than those noted above using SE methods [18]. In addition, QM/MM MD can also be used to determine free energies. Similar to CPMD, QM/MM MD uses DFT methods to describe the inner layer, where the complete QM/MM model is simulated for a period of time [19]. For electron transfer (ET) processes, a combined QM/MM and MD approach can be used to obtain free energies [20]. More specifically, structures of the ET reactant and product are obtained using QM/MM. An MD simulation is then run on these structures, where the equilibrium averages of the MD trajectories are used to calculate the free energies. It is noted that Zhang et al. [13] investigated the effects of structural fluctuations on the reaction energy barrier in the catalytic mechanism of acetylcholinesterase. Using eight different starting conformations obtained from a 1 ns MD simulation, they found that while the enzyme-substrate structural fluctuations led to differences in the calculated barrier of approximately ± 8 kJ mol⁻¹, the mechanistic details remained very consistent.

Potential energy surfaces, however, can provide more insights than a simple indication of a path of sequential mechanistic structures and their energetic relationships. For example, species found along an enzymatic mechanism may have more than one electronic state that lie close in energy and within the boundaries imposed by the "enzyme thermodynamic limit" (see above), particularly in the case of metalloenzymes. Often, such species contain one or more unpaired electrons. Importantly, however, it is possible that as a reaction progresses, the energy differences between states may vary, and in fact, may even change in their energetic ordering. Thus, a mechanism may proceed via "switching" between states, that is, undergoing a spin inversion (SI). Such reactions are termed multistate reactions (MSR). Hence, in the case of MSR pathways, a fundamental property is that

Scheme 1: Examples of alkylated nucleobases known to be repaired under physiological conditions by the AlkB family of enzymes [21].

the PES for each state may cross or may remain in close proximity due to the near degeneracy of the d-orbitals of metals within the complex [22]. The ability in changing of states may have a significant impact on the reaction. For example, for a given transition metal complex, a particular reaction may have a significant barrier, and thus may not feasibly occur. However, for another possible state of the complex, this reaction may have a markedly lower barrier such that it may now be feasible. While SI is typically forbidden, it has been suggested that it may be common in transition metal chemistry [23] and by extension, metalloenzymes. The points at which SI may occur on a full-dimensionality PES are challenging to describe accurately due to the possibility of strong spin-orbit coupling between the two states. However, these crossing points are not generally at stationary points [23]. Fortunately, modern computational tools are good at locating stationary points [23]. Thus, one can map a "reduced-dimensionality" PES for each state, and where they cross indicates a possible region in which SI may occur [23].

In this present paper, some of the ways in which PESs may be exploited to provide insights into enzymatic mechanisms and some factors that may influence their accuracy and reliability are discussed. These are illustrated through a review of several enzymatic systems that we have recently examined. More specifically, this article highlights three major topics in the application of PES in the elucidation of enzymatic mechanisms through examples: (i) the use of multistate reactivity PESs in elucidating possible pathways of O₂ activation in the nonheme iron DNA repair metalloenzyme alpha-ketoglutarate-dependent dioxygenase (AlkB) and the movement of electrons within the active site during the reactions progression [21], (ii) how differences in model and method (QM versus QM/MM) choice influence the mechanistic PES of Uroporphyrinogen Decarboxylase III (UROD), a key "protein-only" enzyme in porphyrin biosynthesis, [24, 25], and (iii) the influence of solvation and the use of "broken" PESs in investigations on the mechanism of the NAD⁺ and Mn²⁺ dependent metalloenzyme 6phospho- α -glucosidase (GlvA) [26].

2. Multistate Reactivity Potential Energy Surfaces: Activation of O₂ in AlkB

An organisms "blueprint" is encoded in its DNA, in particular the sequence of its nucleobases. Thus, the fidelity and integrity of these DNA components is essential to its proper functioning and genetic transmission. However, both internal (e.g., metabolic byproducts) and external (e.g.,

radiation) factors can damage nucleobases via depurination, oxidation or deamination processes [27–34]. Alternatively, they may be alkylated at their oxygen or nitrogen centres [35]. Consequently, cells have developed several approaches to mediate or repair such alkylation damage [36–40]. In particular, the AlkB family of enzymes have evolved a novel mechanism by which they oxidatively dealkylate several such damaged nucleobases, specifically 1-meA, 3-meC, 3-meT, and 1-meG (Scheme 1).

The AlkB proteins belong to the α -ketoglutarate-Fe(II)-dependent dioxygenase superfamily but are the only members to catalyze oxidative dealkylation [41, 42]. More specifically, they are nonheme iron containing proteins in which the Fe(II) ion is ligated by a facial triad of residues consisting of two histidines (His131, and His187) and an aspartate (Asp133) [43, 44]. In addition, they also require α -ketoglutarate (α -KG) as a cosubstrate [41, 42] that is converted to succinate during the mechanistic activation of O₂.

The overall mechanism of AlkB is thought to occur in three stages: [21] (i) O_2 activation to give an ferryl-oxo (Fe^{IV} = O) moiety, (ii) reorientation of the Fe^{IV} = O oxygen from the axial to an equatorial position, and (iii) oxidative dealkylation of the alkylated nucleobase [45]. It is noted that a reorientation of the Fe^{IV} = O has been suggested to occur in other enzymes of this superfamily such as the clavaminate synthase [46], while the dealkylation step has been previously computationally studied [21].

The overall proposed mechanism by which the O_2 moiety is activated with concomitant oxidation of α -KG to succinate and CO_2 is shown in Scheme 2. In particular, following binding of α -KG and O_2 , a self-redox process results in formation of a ferric-superoxide Fe^{III} - O_2 * species [47, 48]. This then nucleophilically attacks the α -keto group of α -KG, resulting in its decarboxylation (i.e., loss of CO_2) and the formation of succinate with concomitant generation of an "axial-positioned" $Fe^{IV} = O$ intermediate. However, the exact details by which the electrons released from the α -KG cosubstrate are used in the O_2 activation process, as well as the influence of the systems electronic state upon the choice of preferred pathway, remain unclear.

We examined [21] this key stage using a cluster/DFT-based computational model. In particular, optimized geometries were obtained at the PB-SCRF-B3LYP/LACVP(d) level of theory with a dielectric constant of 4.0. Frequency calculations were performed on these structures in order to characterize them as minima or transition states. Relative total energies were calculated via single-point energy

H187
$$\longrightarrow$$
 D133 FeIII \longrightarrow D133 FeIV \longrightarrow D133 Succinate

SCHEME 2: Proposed O₂ activation mechanism as catalyzed by AlkB [21].

Scheme 3: Chemical model used in the study on the mechanism of AlkB. The substrate and cosubstrate (α -KG) are modeled as 3-methyl-4-amino pyrimidinyl cation and pyruvate, respectively. Atoms marked by an * were held fixed at their crystal structure (PDB: 2FD8) positions [21].

calculations at the PB-SCRF/B3LYP/LACV3P+(d,p) level of theory based on the above geometries. All calculations were performed using the *Gaussian 03* [49] and *Jaguar 5.5* [50] software packages. For the chemical model, the coordinates of the key active site residues and groups were obtained from a crystal structure of AlkB (PDB: 2FD8) and is shown in Scheme 3 [45]. In order to maintain integrity of the model, a minimum number of atoms remote from the reactive regions were held fixed at their crystal structure positions. Complete computational details are provided in the article by Liu et al. [21].

The potential energy surfaces obtained for activation of O₂ in AlkB to give the highly reactive oxo- and oxyl-type intermediates (**IC4**) are shown in Figure 2. It should be noted that the oxidation state of the Fe centre in each complex was in part determined by calculating its spin density [21]. In addition, in order to provide further insights into electron transfer processes, a stylized electronic representation of the bond making/breaking region is also shown for the minimum energy path. Assuming the commonality of spin changes in transition metal chemistry, this minimum energy path involves spin inversion from the septet to quintet surface [23].

The preferred mode for O_2 binding to the Fe(II) centre is end-on (η^1) . Four overall spin combinations are possible for the resulting dioxygen-bound α -KG-Fe(II) active-site complex (**RC**): singlet, triplet, quintet, and septet. The overall spin-triplet complex, 3 **RC**, was chosen to be the reference energy level throughout this work.

In both the singlet and triplet states, O2 binding has occurred without electron transfer from the Fe(II) to O₂ moiety. The spin-singlet state, ¹RC, lies significantly higher in energy than ³RC by 57.1 kJ mol⁻¹ (not shown). This is likely due to less favourable antiferromagnetic alignment of the unpaired electrons of ${}^{1}\mathrm{O}_{2}({}^{1}\Sigma_{g}^{+})$ with the low-spin Fe(II) centre in 1 RC, compared to ${}^{3}O_{2}({}^{3}\Sigma_{q}^{-})$ with the highspin Fe(II) centre in ³RC [21]. In contrast, in the quintet and septet spin states, O2 binding occurs with charge transfer. That is, a high-spin sextet Fe(III) ion (S = 5/2) is formed with concomitant reduction of ³O₂ (valence electron configuration $\sigma_x^2 \pi_y^2 \pi_z^2 \pi_y^{*1} \pi_z^{*1} \sigma_x^{*0}$ in a fragment orbital picture) to $O_2^{\bullet -}(\sigma_x^2 \pi_y^2 \pi_z^2 \pi_y^{*2} \pi_z^{*1} \sigma_x^{*0})$. Importantly, the spinseptet ⁷[Fe^{III}-O₂• ⁻] complex (⁷RC) lies 12.5 kJ mol⁻¹ lower in energy than ³RC, while the spin-quintet complex ⁵RC is just $5.7 \text{ kJ} \text{ mol}^{-1}$ higher in energy than ${}^{3}\text{RC}$.

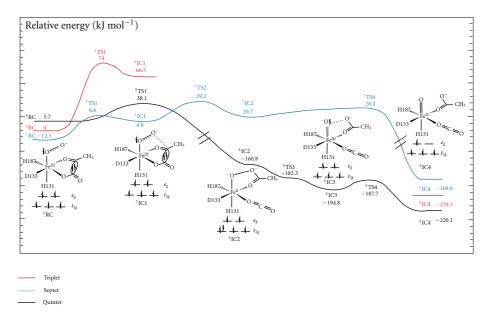


FIGURE 2: Potential energy surfaces for activation of oxygen through formation of the ferryl-oxo Fe^{IV} = O and ferric-oxyl Fe^{III}-O* compounds.

While ³RC was chosen as the "reference relative energy" for all complexes, the mechanistic details of the spin-triplet PES are not discussed herein due to its considerably higher activation barriers compared to the spin-quintet and spin-septet surfaces (Figure 2).

For ⁷RC, the lowest energy reactant complex, the first step is nucleophilic attack of the ferric-superoxide (7 [Fe^{III}-O2 •-]) group at the pyruvate's C2-carbon. It is noted that the ability of Fe^{III}-O₂ • to act as a strong nucleophile has been previously investigated by both experimental [51-54] and theoretical [55–58] studies. This step proceeds via ⁷TSI with a barrier of only 19.1 kJ mol⁻¹ to give the intermediate complex ⁷IC1 lying just 1.8 kJ mol⁻¹ lower in energy than ⁷TSI (Figure 2). In ⁷IC1, the O₂ moiety forms a peroxy bridge between Fe(III) and the pyruvate cosubstrates C2centre [21]. In the subsequent step, the cosubstrate's C2-COO⁻ bond is cleaved with the electrons formally moving into the Fe-peroxo moiety. As a result, the iron is reduced to Fe(II), while the peroxy moiety now has a charge of -2, and consequently, its O-O bond lengthens considerably. This step proceeds via ⁷TS2 with a barrier of 34.4 kJ mol⁻¹ to give the ferric-peroxide intermediate ⁷IC2 lying 15.9 kJ mol⁻¹ higher than ⁷IC1. The peroxide O-O bond is then cleaved with concomitant two-electron oxidation of the Fe(II) centre to Fe(IV) via ⁷TS4 at a cost of just 5.7 kJ mol⁻¹ with respect to ⁷IC2. The resulting Fe(IV)-oxo-type product complex ⁷IC4 is considerably lower in energy than ${}^{3}RC$ by 168.6 kJ mol $^{-1}$. Thus, overall, this pathway is enzymatically feasible.

On the quintet-state PES, the first step is also found to be nucleophilic attack of the ${}^{5}[Fe^{III}-O_{2}{}^{\bullet-}]$ group at the cosubstrate's C2 centre. However, this now occurs with decarboxylation of the pyruvate and concomitant reduction of both Fe(III) and $O_{2}{}^{\bullet-}$ to Fe(II) and $O_{2}{}^{2-}$, respectively. Importantly, this reaction proceeds via ${}^{5}TSI$ with a barrier of only $32.4 \, \text{kJ} \, \text{mol}^{-1}$ to give the energetically very low lying intermediate ${}^{5}IC2$ ($-160.8 \, \text{kJ} \, \text{mol}^{-1}$). Based on their

structural similarity, it is suggested that ⁷IC1 could be regarded as the reaction-coordinate equivalent of ⁵TSI [21]. Subsequently, 5IC2 can undergo a stepwise two-electron transfer from Fe(II) to the O-O unit [21]. The first electron transfer occurs via 5TS3 without a barrier. It is noted that optimized structures are obtained by minimization of the electronic energy at 0 K. As a result, on flat PESs the inclusion of energy corrections via, for example, singlepoint calculations, enthalpy, or Gibb's free energy corrections can result in TSs having lower relative energies than the reactant or product which it interconnects. This is typically taken to indicate that the particular reaction essentially occurs without a barrier. In the resulting intermediate ⁵IC3, the electron has transferred from the Fe(II) into the $\sigma_{\text{o-o}}^*$ orbital. As a result, the peroxo moiety, in a fragment MO picture, has the electronic configuration $\sigma_x^2 \pi_y^2 \pi_z^2 \pi_y^{*2} \pi_z^{*2} \sigma_x^{*1}$. The second electron transfer proceeds via ⁵TS4 at a cost of 7.1 kJ mol⁻¹ to give the ferryl-oxo product complex. ⁵IC4 is the ferryl-oxo compound and is found to lie 25.3 kJ mol⁻¹ lower in energy than ⁵IC3. This one-electron oxidation of Fe(III) again promotes an electron into to the σ_{o-o}^* orbital, thus giving the peroxo moiety the highly unstable electron configuration $\sigma_x^2 \pi_y^2 \pi_z^2 \pi_y^{*2} \pi_z^{*2} \sigma_x^{*2}$ and resulting in scission of the O-O linkage. The complex ⁵IC4 lies significantly lower in energy than ³RC by 220.1 kJ mol⁻¹. Importantly, however, it is also markedly lower in energy than both ⁷IC4 and ³IC4 by at least 40.8 kJ mol^{-1} (Figure 2).

Thus, by elucidating the pathways for the various possible spin states one can see that the lowest energy product ⁵IC4 may in fact be formed via several possible low energy routes. In particular, it may occur either at the beginning of the mechanism via an initial spin inversion from ⁷RC to ⁵RC, and thus providing a pathway with an overall barrier of 50.6 kJ mol⁻¹. Alternatively, spin inversion may occur along the pathway, for example, as ⁷IC1 reacts and proceeds towards ⁷TS2 and thus to directly give ⁵IC2, allowing for

Scheme 4: Proposed general acid-base mechanism for the UROD-catalyzed decarboxylation of the acetates of URO-III [59–61]. HA and HB represent general acids.

cleavage of the peroxo O–O bond with a possible pathway barrier of less than 50.6 kJ mol⁻¹. Importantly, spin inversion would enable the mechanism to access and proceed via considerably more exoergic intermediates, for example, ⁵IC2 lies 181.3 kJ mol⁻¹ lower in energy than ⁷IC2 [21]. The probability of SI occurring at a crossing-point is determined by the strength of spin-orbit coupling between the two states. Fortunately, as noted in the introduction, such crossing-points are not generally stationary points [23]. In addition, it is rarely found that the spin-orbit coupling is so strong that it affects the adiabatic energies of the PESs of the two states [23].

3. Effects of Explicitly Modeling the Protein Environment on the Catalytic Mechanism of Uroporphyrinogen Decarboxylase III

Porphyrin is an important biomolecule for all organisms. It plays a range of diverse key roles in, for example, proteins and enzymes involved in ligand transport, electron transfer, light harvesting, and redox mechanisms [62–65]. Within cells, its biosynthesis occurs via a multistage multienzymatic process in which Uroporphyrinogen Decarboxylase III (UROD) catalyses the first branching point, the fifth step. Specifically, it catalyses the sequential nonsymmetric decarboxylation of the four acetates of uroporphyrinogen III (URO-III) to give coproporphyrinogen III (CP-III) [62–64, 66].

UROD exists as a homodimer, and it has been shown experimentally that each active site is independent from the other [24]. Three electrostatic regions have been identified

within each active site: a negative, a polar-positive, and a hydrophobic region [62]. The negatively charged region contains an invariant aspartyl (hUROD: Asp86) that is thought to help orientate the substrate for catalysis as well as stabilize various mechanistic intermediates [62, 67]. Helping in substrate binding and recognition, the polar-positive region contains several residues that interact with the carboxylates of URO-III [67, 68]. Importantly, of these polar-positive residues, it has been found that one or more active-site arginyl residues (hUROD: Arg37, Arg41 and Arg50) are catalytically essential [62, 68–71]. While all four acetate decarboxylations are believed to involve the same catalytic residues, unfortunately, the exact mechanistic role of various active site residues remains unclear.

A general mechanism has been proposed for decarboxylation of the pyrrole-acetate and is shown in Scheme 4 [59–61]. Specifically, two acids are thought to be involved. In the first step, an acid (HA) protonates the C2 carbon of the pyrrole ring. This destabilizes the carboxylate group, resulting in cleavage of the C3′–C3″OO⁻ bond, that is, decarboxylation. The second acid (HB) then protonates the newly formed methylene C3′ carbon, while the first acid, now in its conjugate base form (A⁻), abstracts a proton from the–C2H2⁺-group, thus regenerating HA.

Several experimental X-ray crystal structure and kinetic studies, based on this "blueprint", have proposed possible identities for the two mechanistic acids. Specifically, from enzyme X-ray structures they obtained coupled with manual docking of the substrate, Martins et al. [64] suggested that HA is Asp86, while HB is Tyr164. In contrast, based on a X-ray crystal structure of a UROD··· product complex,

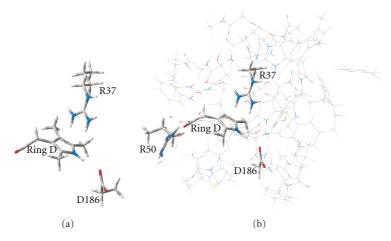


FIGURE 3: Representative images for the (a) DFT/Cluster + PCM model used by and Silva and Ramos [25] and (b) QM/MM model used by Bushnell et al. [24].

Phillips et al. [67] suggested that HA is an H_2O but were unable to conclusively determine HB. More recently, Lewis and Wolfenden, [69] using kinetics and pK_a measurements, suggested that HA and HB are Asp86 and Arg37, respectively.

Silva and Ramos [25] performed a computational investigation on the first acetate decarboxylation of URO-III as catalysed by UROD. More specifically, they used a cluster/DFT-type approach with a chemical model consisting of the aspartyl (Asp86) and arginyl (Arg37) R-groups and 1,3,4-methyl-2-acetyl pyrrole for the URO-II substrate (Figure 3). This model was derived from a crystal structure of a UROD...product complex [67]. A PCM-solvation approach was used to model the general affects of the surrounding protein environment. Using this computational model, they concluded that decarboxylation could proceed in accordance with the "blueprint" mechanism and that it was thermodynamically and enzymatically feasible with an overall barrier of 89.5 kJ mol⁻¹ [25]. Notably, this energy corresponded to the initial step, that is, proton transfer from Arg37 onto C2 of the substrate pyrrole ring. Thus, the R-group guanidinium of the active-site residue Arg37 was concluded to be both suitably positioned and capable of acting as the general acid HA that protonates the substrate's C2 centre. They further concluded that the second proton, from HB, is donated by the solvent. However, based on the experimental observation that stereochemistry is retained at the C3' centre from which the CO2 is lost, it has been concluded that HB must be an active site residue [59, 60, 72].

We reexamined the catalytic mechanism of UROD using an alternate computational approach. In particular, it was investigated [24] through combined QM and MM methods in the ONIOM formalism with mechanical embedding [73–81] as implemented in the *Gaussian 03* [44] program suite. Such an approach enabled us to consider the role of a second arginyl (Arg50) residue as well to take into account the anisotropic environment surrounding the active site. The resulting QM/MM chemical model included the substrate URO-III and all active site residues immediately surrounding it, that is, first-shell residues (Figure 3). In

addition, for those portions of the substrate exposed to solvent, the first solvation shell was retained. A subset of the complete model centered on the reactive region of the active site was then selected for the high-level QM treatment consisting of two arginyls (Arg37 and 50), an aspartyl (Asp86) residue, and the first substrate pyrrole that is decarboxylated [24]. Optimized geometries were obtained at the ONIOM(B3LYP/6-31G(d):AMBER94) level of theory [82]. However, in order to obtain more reliable calculated relative Gibbs free energies, single-point energy calculations on the above optimized structures were performed at the ONIOM(B3LYP/6-311+G(2df,p):AMBER94) level of theory. The free energies were obtained by adding the necessary energy corrections calculated at standard ambient temperature and pressure (SATP) as implemented in Gaussian 03.

Using this larger and more complete model, the initial step is again proton transfer from the guanidinium of Arg37 onto the C2 centre of the substrate pyrrole. However, this step now occurs via **TS1** at a cost of 43.1 kJ mol⁻¹ relative to the initial substrate-bound active site complex **RC** (Figure 4). This is approximately half the size of the barrier for this initial step obtained by Silva and Ramos [25] using a cluster/DFT approach. Experimentally, human UROD has been measured to have a k_{cat} value of 0.16 s⁻¹ [5, 69, 83], corresponding to an overall barrier of 77.4 kJ mol⁻¹. Thus, the smaller cluster/DFT approach would appear to give better agreement than the above larger and more extensive QM/MM-based approach. However, as summarized by Juárez et al. [84], decarboxylation of URO-III generating the 7-carboxylate intermediate, that is, the first decarboxylation, is most likely not the rate-limiting step. In fact, for several variants of UROD, the rate-limiting step appears to be the decarboxylation of the 7-carboxylate intermediate, that is, the second acetate decarboxylation. It is noted that for UROD from various species, the experimentally determined barriers for the first decarboxylation lie in the range of 8.4–51.5 kJ mol⁻¹ [68, 84]. Thus, the QM/MM calculated barrier is in fact in better agreement with related experimentally reported values for the decarboxylation of ring D.

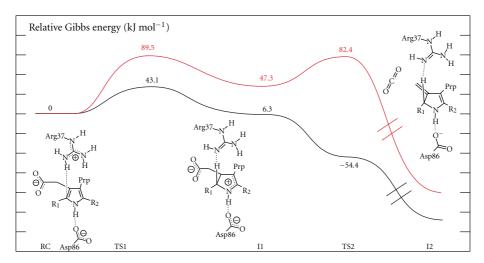


FIGURE 4: Free energy PES for the initial proton transfer and decarboxylation of ring **D** obtained using a QM/MM model (black surface with relative energies) and cluster/DFT model (red surface with relative energies) [24, 25].

The resulting C2-protonated intermediate (I1) lies higher in energy than RC by just 6.3 kJ mol⁻¹. Importantly, with the explicit addition of the protein environment (as opposed to the use of a PCM approach), a stabilizing effect occurs. This stabilizing effect is seen to reduce the relative energy of I1 by 41.0 kJ mol⁻¹ in comparison to that obtained using the cluster/DFT approach in which I1 was calculated to lie higher in energy than RC by 47.3 kJ mol⁻¹ [25].

Following protonation of C2 by Arg37, the next step is the decarboxylation of the acetate moiety (Scheme 4). Using a cluster/DFT-based approach, Silva and Ramos [25] obtained a barrier for this step of 82.4 kJ mol⁻¹. Furthermore, based on the optimized structures obtained, they concluded that the release of CO2 was hindered by the hydrogen bond interaction between the carboxylate of Asp86 and the pyrrole ring's HN moiety. In contrast, using a QM/MM-based approach, we found that this occurs via TS2 with a relative energy barrier lower than that of I1 (again due to inclusion of single-point energy and Gibb's free energy corrections; see section on Multistate Reactivity PESs) [24]. That is, the loss of CO₂ from the acetate essentially occurs without a barrier. Furthermore, a more complete and explicit inclusion of the protein environment enables a lengthening of the Asp86···C2-protonated pyrrole interaction. In turn, this leads to a destabilization of the C2-protonated pyrrole and thus enhancement of the rate of decarboxylation [25].

The subsequent and final step is protonation of the newly formed methylene carbon from which the CO_2 was lost. Unfortunately, direct comparison of the results obtained using the cluster/DFT-based [25] and QM/MM-based [24] approaches for this step is not possible. Using the former approach, the proton transferred to $\mathrm{C}'3$ was proposed to originate from the solvent. In contrast, for the latter QM/MM-based study, it was found that a second arginyl active site residue (Arg50) could act as the second required mechanistic acid HB (Scheme 4) that protonates the methylene carbon. Furthermore, the barrier for this step was just $3.1\,\mathrm{kJ}\,\mathrm{mol}^{-1}$ [24]. It is noted that the identification of an

active site residue as HB is supported by experimental conclusions based on the observed retention of stereochemistry at the pyrrole-CH3 group formed [59–61].

4. Elucidating the Catalytic Redox Mechanism and "Driving Force" in 6-Phospho-α-Glucosidase (GlvA)

In aqueous solution under standard conditions, glycosidic bonds are remarkably resistant to hydrolysis [85-89]. Glycoside hydrolases (GH) are the family of enzymes that catalyse their hydrolytic cleavage within organisms and, in fact, are amongst some of the most efficient enzymes known [90-100]. In general, these enzymes are highly stereospecific; however, the GH4 subfamily is able to catalyse the hydrolysis of either or both α - and β -glycosidic bonds [101, 102]. The enzyme 6-phospho- α -glucosidase (GlvA) is a member of this subfamily that uses NAD+ and a divalent Mn²⁺ as cofactors in its redox mechanism of glycosidic bond cleavage [97, 103, 104]. In particular, the mechanism has been proposed to proceed via two half-reactions shown in Scheme 5 [99, 105-107]. The first is thought to be initiated by proton transfer from the C3-OH group to an Mn2+ bound hydroxyl and hydride transfer from C3–H to the NAD⁺ moiety, ultimately resulting in cleavage of the glycosidic bond at C1. The cleaved product moiety ROH is then replaced within the active site by a water molecule. The second half-reaction is believed to essentially be the reverse of the first with the H₂O moiety in place of the ROH.

In order to investigate the proposed [99, 105–107] catalytic mechanism of GlvA, we employed [26] a cluster/DFT-based approach in which a large active site model was used with the surrounding protein simply modeled using a PCM-based solvation method. In particular, optimized geometries were obtained at the B3LYP/6-31G(d) 5D level of theory. Relative energies were obtained at the B3LYP/6-311+G(2df,p)//B3LYP/6-31G(d) 5D level of theory (i.e., gasphase). Corrections for the surrounding environment were

SCHEME 5: Schematic illustration of the two half-reactions in the proposed catalytic mechanism of GlvA [99, 105–107].

obtained at the same level of theory using the integral equation formalism (IEF-) PCM method with a dielectric constant of $\varepsilon=4.0$; a value typically used to model the polarity of an internal protein environment [26]. The chemical model used (Scheme 6) was derived from an X-ray crystal structure of GlvA cocrystallized with the substrate analog 6-phospho- β -glucose bound within its active site (PDB ID: 1U8X) [100]. The coordinates of proposed key mechanistic residues were then extracted, and a minimum number of atoms remote from the reaction region were held fixed at these positions in order to maintain integrity of the model during computations. Full computational details are provided in [22].

The PESs obtained for the two half-reactions are illustrated in Figure 5. The relative energies given in parenthesis were obtained in the gas phase, that is, without use of the PCM-based approach to model the general effects of the surrounding polar protein environment, and are included for comparison (see below). The catalytic mechanism of GlvA is initiated by an oxidation of the glucopyranose ring at the 3-position. Specifically, the 3'-OH group first transfers its proton to the metal bound hydroxide ligand $(Mn^{2+}\cdots OH^{-})$ to give a metal-bound water and a now negatively charged 3'-O⁻ moiety on the sugar ring (IC1). This step occurs with a barrier of 22.7 kJ mol⁻¹ when within the protein environment ("solution phase"), while the resulting intermediate IC1 lies 46.3 kJ mol⁻¹ lower in energy than the **RC**. This is then followed by a hydride transfer from the 3'C-H group to the pro-R face of the C4 centre of the NAD⁺ [26] cofactor via **TS2** at a cost of 80.8 kJ mol⁻¹ with

respect to **IC1**. This results in the formation of the 3-keto intermediate **IC2** which lies only slightly higher in energy than **IC1** by 7.2 kJ mol⁻¹.

With the formation of IC2, a double bond has now been introduced into the substrate via the formation of a keto group. In the subsequent steps, the double bond is then effectively shifted around the ring via a series of ketoenol tautomerizations coupled with proton transfers. First, a glutamyl-tyrosyl catalytic diad deprotonates the 2'C-H group of IC2 via TS3 to form the enolate (2'C = 3'C-O⁻) containing intermediate **IC3** (Figure 5). The barrier for this process is $54.0 \,\mathrm{kJ} \,\mathrm{mol}^{-1}$, while IC3 lies $14.6 \,\mathrm{kJ} \,\mathrm{mol}^{-1}$ lower in energy than RC. This is subsequently followed by proton abstraction from the C2-OH group by an adjacent aspartyl (Asp172) residue. Simultaneously, however, the Asp172 donates its proton to the leaving CH₃O⁻ moiety. Importantly, it is in this step that the actual cleavage of the glycosidic bond occurs via **TS4** at cost of only 58.9 kJ mol⁻¹ with respect to IC3. NBO and second-order perturbation analyses were used to analyse the "driving force" that leads to this greatly reduced barrier for heterolytic glycosidic bond cleavage and the regioselectivity of GlvA [22]. In particular, it was found that in the first half-reaction, electronic destabilizing effects within the sugar ring are enhanced due to several electron delocalizations that strongly favour the heterolytic cleavage of glycosidic bonds. Furthermore, this effect was greater in the case of axial (α) compared to equatorial (β) glycosidic bonds. It is noted that the first half-reaction is exothermic as the resulting product complex IC4··· MeOH lies 29.9 kJ mol^{-1} , respectively, lower in energy than **RC**.

Scheme 6: The substrate-bound active site model derived from the X-ray crystal structure PDB ID: 18UX and used in our computational investigation on GlvA. Atoms marked by an * were held fixed at their crystal structure positions.

For the second half-reaction, the cleaved MeOH moiety must first be replaced by a water to give $IC4 \cdot \cdot \cdot H_2O$. By comparing the energies of $[IC4 \cdot \cdot \cdot MeOH + H_2O]$ versus $[IC4 \cdots H_2O + MeOH]$, it is found that this replacement is slightly exothermic by 7.3 kJ mol⁻¹. Thus, while this exchange requires a "splitting" of the calculated overall PES, one is still able to maintain an energetic relationship between the two surfaces. With the formation of $IC4 \cdot \cdot \cdot H_2O$ the second half-reaction is effectively the reverse of the first halfreaction [26]. For instance, it is initiated by nucleophilic attack of the water oxygen at the C1 centre of **IC4**. This occurs via TS5 at a cost of 77.7 kJ mol⁻¹ in which the attacking H2O simultaneously transfers a proton to the Asp172 residue which itself transfers its proton onto the C2-O oxyanion centre. Similar to the analogous complex IC3, the resulting intermediate IC5 lies only slightly lower in energy than RC by 18.4 kJ mol⁻¹. In the subsequent step, the C2 centre is reprotonated by the catalytic tyrosyl-glutamyl diad via TS6 at a cost of 79.5 kJ mol⁻¹ to give the keto intermediate IC6 lying 39.6 kJ mol⁻¹ lower in energy than **RC.** The last two steps in the overall mechanism begin with a hydride transfer from the NADH moiety onto the C3 centre via **TS7**, with a barrier of 72.2 kJ mol⁻¹, to give the oxyanionic intermediate IC7. Notably, both IC7 and the preceding intermediate IC6 are essentially thermoneutral with their analogous first half-reaction complex IC2 and IC1, respectively (see Figure 5). The next and final step is a proton transfer from the metal-bound H₂O onto the newly formed $C3-O^-$ group via **TS8** at a cost of 98.6 kJ mol⁻¹. The overall mechanism is slightly exothermic, with the product-bound active site complex **PC** lying just 4.0 kJ mol⁻¹ lower in energy than RC.

Comparison of the above "solution-phase" relative energies with the gas-phase energies enables one to gain insight the role and effect of the general protein environment. It can be seen from Figure 5 that the effect of the polar environment is not systematic. For example, inclusion of the polar environment stabilizes **IC1** and **TS7** by 17.3 and 42.3 kJ mol⁻¹, respectively, but destabilizes **IC2** and **TS4** by 0.5 and 10.0 kJ mol⁻¹. In general, however, larger effects are observed for transition structures; the observed absolute changes in relative energies for TSs range from 3.3–42.3 kJ mol⁻¹ while for the intermediates and product complexes, they range from 0.5–27.3 kJ mol⁻¹.

More importantly, however, the inclusion of the general protein environment can have marked effect on the catalytic mechanism. For example, in the gas phase the overall mechanism is endothermic with the **PC** lying 11.4 kJ mol⁻¹ higher in energy than RC. However, in the "solution-phase", it is now slightly exothermic by 4.0 kJ mol⁻¹ (Figure 5). Moreover, with the inclusion of the protein environment the rate-limiting step has changed. Specifically, in the gas phase, the proton transfer from the Mn²⁺-bound water to the 3'C-O group via TS8 represents the rate-limiting step with a reaction barrier relative to **RC** of 78.3 kJ mol⁻¹. However, with inclusion of the protein environment (i.e., use of a PCM-based approach), the energy of TS8 is reduced significantly by $\sim 26.2 \text{ kJ} \text{ mol}^{-1}$ to $52.1 \text{ kJ} \text{ mol}^{-1}$ respect to **RC.** As a consequence, **TS6** (61.1 kJ mol⁻¹) now has the highest energy relative to RC. Thus, reprotonation of C2 by the catalytic tyrosyl-glutamyl diad has become the ratelimiting step. In agreement with experiment, glycosidic bond cleavage is not the rate-controlling step.

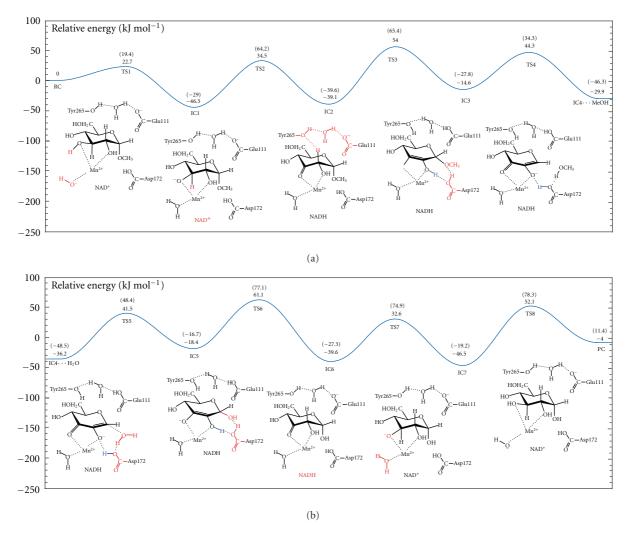


FIGURE 5: Potential energy surfaces for the catalytic mechanism of redox hydrolysis of α Glc1Me by GlvA. Single-point energies calculated in solvation and gas phase (parenthesis).

5. Summary

Potential energy surfaces (PESs) are powerful tools for elucidating the catalytic mechanisms of enzymes. Indeed, they can be more than a simple indication of a path of sequential mechanistic structures and their energetic relationships. In this paper the application of the tools and techniques of computational chemistry in combination with PES investigations has been described. Through a review of several of our recently published studies on enzymatic systems, how such an approach may be applied in order to provide deeper insights into the movement of electrons during the course of a reaction, the mechanistic role of active site residues and the surrounding environment, and the utility of multistate PESs in metalloenzymes has been highlighted. In addition, some of the challenges that these studies may encounter, such as appropriate choice of computational model on the reliability and accuracy of a PES, have also been discussed.

For example, the catalytic activation of O_2 by AlkB to give the highly reactive oxo- and oxyl-type intermediates was examined for several possible spin states. It was found that

at least in the initial steps of the process, multiple states were close in energy with each other and, furthermore, within the enzymatic thermochemical limit. As a result, and considering the likelihood of spin changes in transition metal chemistry, several minimum energy pathways to give the lowest energy product complex ⁵IC4 were identified, each involving spin inversion (SI) from a septet to quintet PES [23]. Importantly, SI enables the catalytic mechanism of AlkB to access and proceed via highly exoergic intermediates.

For the enzyme UROD, a comparison was made of its catalytic mechanism as elucidated using a combined QM and MM method in the ONIOM formalism with mechanical embedding and a cluster/DFT+PCM approach. [25] Use of a QM/MM approach enables one to more directly and extensively model the anisotropic environment surrounding an enzyme active site. In the case of UROD, with the QM/MM-based approach, it was found that the stabilizing effect of the surrounding environment provided a significant reduction in both the calculated rate-limiting proton transfer as well as the barrier for acetate decarboxylation. In fact, the more accurate inclusion of the environment enabled us

[19] to obtain an energy for the rate-limiting barrier in good agreement with related experimentally determined values.

The applicability of cluster/DFT-based approaches to the study of enzymatic systems was examined further using the case of the glycosidic hydrolase GlvA. In particular, such an approach was shown to be able to provide reliable and accurate insights when used in combination with a well-chosen chemical model. Inclusion of the general effects (polarity) of the environment surrounding the active site was shown to be important in choosing a suitable model. Indeed, its inclusion had significant effects on the mechanism obtained such as shifting it from an overall endothermic to exothermic process. More importantly, however, the rate-limiting step changed. Specifically, in the gas phase, a proton transfer from a metal-bound water to the 3'C-O- group represented the rate-limiting step. However, with the inclusion of the polar protein environment using a PCM-based approach, the ratelimiting step was instead protonation of the sugar ring's C2 centre by the catalytic tyrosyl-glutamyl diad.

Acknowledgments

The authors gratefully acknowledge the Natural Sciences and Engineering Research Council (NSERC, Canada) for funding and CGS & PGSD scholarships (E. A. C. Bushnell). SHARCNET (Canada) is acknowledged for a graduate scholarship (W.-J. Huang) and additional computational resources.

References

- [1] D. Young, Computational Chemistry: A Practical Guide for Applying Techniques to Real World Problems, Wiley-Interscience, New York, NY, USA, 2001.
- [2] P. E. M. Siegbahn and F. Himo, "Recent developments of the quantum chemical cluster approach for modeling enzyme reactions," *Journal of Biological Inorganic Chemistry*, vol. 14, no. 5, pp. 643–651, 2009.
- [3] C. J. Cramer, Essentials of Computational Chemistry: Theories and Models, John Wiley & Sons, New York, NY, USA, 2002.
- [4] P. E. M. Siegbahn and T. Borowski, "Modeling enzymatic reactions involving transition metals," *Accounts of Chemical Research*, vol. 39, no. 10, pp. 729–738, 2006.
- [5] F. Himo, "Quantum chemical modeling of enzyme active sites and reaction mechanisms," *Theoretical Chemistry Accounts*, vol. 116, no. 1–3, pp. 232–240, 2006.
- [6] A. D. Becke, "A new mixing of Hartree-Fock and local density-functional theories," *The Journal of Chemical Physics*, vol. 98, no. 2, pp. 1372–1377, 1993.
- [7] A. D. Becke, "Density-functional thermochemistry. III. The role of exact exchange," *The Journal of Chemical Physics*, vol. 98, no. 7, pp. 5648–5652, 1993.
- [8] C. Lee, W. Yang, and R. G. Parr, "Development of the Colle-Salvetti correlation-energy formula into a functional of the electron density," *Physical Review B*, vol. 37, no. 2, pp. 785–789, 1988.
- [9] P. E. M. Siegbahn, "The performance of hybrid DFT for mechanisms involving transition metal complexes in enzymes," *Journal of Biological Inorganic Chemistry*, vol. 11, no. 6, pp. 695–701, 2006.
- [10] B. Mennucci and J. Tomasi, "Continuum solvation models: a new approach to the problem of solute's charge distribution

- and cavity boundaries," *Journal of Chemical Physics*, vol. 106, no. 12, pp. 5151–5158, 1997.
- [11] J. Tomasi, B. Mennucci, and E. Cancès, "The IEF version of the PCM solvation method: an overview of a new method addressed to study molecular solutes at the QM ab initio level," *Journal of Molecular Structure: THEOCHEM*, vol. 464, no. 1–3, pp. 211–226, 1999.
- [12] L. Hu, P. Söderhjelm, and U. Ryde, "On the convergence of QM/MM energies," *Journal of Chemical Theory and Computation*, vol. 7, no. 3, pp. 761–777, 2011.
- [13] Y. Zhang, J. Kua, and J. A. McCammon, "Influence of structural fluctuation on enzyme reaction energy barriers in combined quantum mechanical/molecular mechanical studies," *Journal of Physical Chemistry B*, vol. 107, no. 18, pp. 4459–4463, 2003.
- [14] M. Klähn, S. Braun-Sand, E. Rosta, and A. Warshel, "On possible pitfalls in ab initio quantum mechanics/molecular mechanics minimization approaches for studies of enzymatic reactions," *Journal of Physical Chemistry B*, vol. 109, no. 32, pp. 15645–15650, 2005.
- [15] H. M. Senn and W. Thiel, "QM/MM methods for biomolecular systems," *Angewandte Chemie International Edition*, vol. 48, no. 7, pp. 1198–1229, 2009.
- [16] J. Llano and J. W. Gauld, Mechanistics of Enzyme Catalysis: From Small to Large Active-Site Models, vol. 2, Wiley-VCH, Weinheim, Germany, 2010.
- [17] O. Acevedo and W. L. Jorgensen, "Advances in quantum and molecular mechanical (QM/MM) simulations for organic and enzymatic reactions," *Accounts of Chemical Research*, vol. 43, no. 1, pp. 142–151, 2010.
- [18] M. Dal Peraro, P. Ruggerone, S. Raugei, F. L. Gervasio, and P. Carloni, "Investigating biological systems using first principles Car-Parrinello molecular dynamics simulations," *Current Opinion in Structural Biology*, vol. 17, no. 2, pp. 149– 156, 2007.
- [19] Y. Hagiwara, M. J. Field, O. Nureki, and M. Tateno, "Editing Mechanism of Aminoacyl-tRNA synthetases operates by a hybrid ribozyme/protein catalyst," *Journal of the American Chemical Society*, vol. 132, no. 8, pp. 2751–2758, 2010.
- [20] J. Blumberger, "Free energies for biological electron transfer from QM/MM calculation: method, application and critical assessment," *Physical Chemistry Chemical Physics*, vol. 10, no. 37, pp. 5651–5667, 2008.
- [21] H. Liu, J. Llano, and J. W. Gauld, "A DFT study of nucleobase dealkylation by the DNA repair enzyme AlkB," *Journal of Physical Chemistry B*, vol. 113, no. 14, pp. 4887–4898, 2009.
- [22] S. Shaik, H. Hirao, and D. Kumar, "Reactivity of high-valent iron-oxo species in enzymes and synthetic reagents: a tale of many states," *Accounts of Chemical Research*, vol. 40, no. 7, pp. 532–542, 2007.
- [23] R. Poli and J. N. Harvey, "Spin forbidden chemical reactions of transition metal compounds. New ideas and new computational challenges," *Chemical Society Reviews*, vol. 32, no. 1, pp. 1–8, 2003.
- [24] E. A. C. Bushnell, E. Erdtman, J. Llano, L. A. Eriksson, and J. W. Gauld, "The first branching point in porphyrin biosynthesis: a systematic docking, molecular dynamics and quantum mechanical/molecular mechanical study of substrate binding and mechanism of uroporphyrinogen-III decarboxylase," *Journal of Computational Chemistry*, vol. 32, no. 5, pp. 822–834, 2011.
- [25] P. J. Silva and M. J. Ramos, "Density-functional study of mechanisms for the cofactor-free decarboxylation performed

- by uroporphyrinogen III decarboxylase," *Journal of Physical Chemistry B*, vol. 109, no. 38, pp. 18195–18200, 2005.
- [26] W. Huang, J. Llano, and J. W. Gauld, "Redox mechanism of glycosidic bond hydrolysis catalyzed by 6-phospho-αglucosidase: a DFT study," *Journal of Physical Chemistry B*, vol. 114, no. 34, pp. 11196–11206, 2010.
- [27] R. De Bont and N. van Larebeke, "Endogenous DNA damage in humans: a review of quantitative data," *Mutagenesis*, vol. 19, no. 3, pp. 169–185, 2004.
- [28] Y. Wang, "Bulky DNA lesions induced by reactive oxygen species," *Chemical Research in Toxicology*, vol. 21, no. 2, pp. 276–281, 2008.
- [29] J. S. Taylor, "Unraveling the molecular pathway from sunlight to skin cancer," *Accounts of Chemical Research*, vol. 27, no. 3, pp. 76–82, 1994.
- [30] H. Kamiya, S. Iwai, and H. Kasai, "The (6-4) photoproduct of thymine-thymine induces targeted substitution mutations in mammalian cells," *Nucleic Acids Research*, vol. 26, no. 11, pp. 2611–2617, 1998.
- [31] M. Lysetska, A. Knoll, D. Boehringer, T. Hey, G. Krauss, and G. Krausch, "UV light-damaged DNA and its interaction with human replication protein A: an atomic force microscopy study," *Nucleic Acids Research*, vol. 30, no. 12, pp. 2686–2691, 2002.
- [32] W. L. Neeley and J. M. Essigmann, "Mechanisms of formation, genotoxicity, and mutation of guanine oxidation products," *Chemical Research in Toxicology*, vol. 19, no. 4, pp. 491–505, 2006.
- [33] E. C. Friedberg, L. D. McDaniel, and R. A. Schultz, "The role of endogenous and exogenous DNA damage and mutagenesis," *Current Opinion in Genetics and Development*, vol. 14, no. 1, pp. 5–10, 2004.
- [34] T. Lindahl, "Instability and decay of the primary structure of DNA," *Nature*, vol. 362, no. 6422, pp. 709–715, 1993.
- [35] F. Drabløs, E. Feyzi, P. A. Aas et al., "Alkylation damage in DNA and RNA—repair mechanisms and medical significance," *DNA Repair*, vol. 3, no. 11, pp. 1389–1407, 2004.
- [36] Y. Mishina, E. M. Duguid, and C. He, "Direct reversal of DNA alkylation damage," *Chemical Reviews*, vol. 106, no. 2, pp. 215–232, 2006.
- [37] B. Sedgwick, P. A. Bates, J. Paik, S. C. Jacobs, and T. Lindahl, "Repair of alkylated DNA: recent advances," *DNA Repair*, vol. 6, no. 4, pp. 429–442, 2007.
- [38] T. Lindahl, B. Sedgwick, M. Sekiguchi, and Y. Nakabeppu, "Regulation and expression of the adaptive response to alkylating agents," *Annual Review of Biochemistry*, vol. 57, pp. 133–157, 1988.
- [39] A. K. McCullough, M. L. Dodson, and R. S. Lloyd, "Initiation of base excision repair: glycosylase mechanisms and structures," *Annual Review of Biochemistry*, vol. 68, pp. 255–285, 1999.
- [40] P. J. O'Brien and T. Ellenberger, "Human alkyladenine DNA glycosylase uses acid-base catalysis for selective excision of damaged purines," *Biochemistry*, vol. 42, no. 42, pp. 12418– 12429, 2003.
- [41] S. C. Trewick, T. F. Henshaw, R. P. Hausinger, T. Lindahl, and B. Sedgwick, "Oxidative demethylation by Escherichia coli AlkB directly reverts DNA base damage," *Nature*, vol. 419, no. 6903, pp. 174–178, 2002.
- [42] P. Ø. Falnes, R. F. Johansen, and E. Seeberg, "AlkB-mediated oxidative demethylation reverses DNA damage in Escherichia coli," *Nature*, vol. 419, no. 6903, pp. 178–182, 2002.
- [43] T. Duncan, S. C. Trewick, P. Koivisto, P. A. Bates, T. Lindahl, and B. Sedgwick, "Reversal of DNA alkylation damage by two

- human dioxygenases," *Proceedings of the National Academy of Sciences of the United States of America*, vol. 99, no. 26, pp. 16660–16665, 2002.
- [44] L. Aravind and E. V. Koonin, "The DNA-repair protein AlkB, EGL-9, and leprecan define new families of 2-oxoglutarate-and iron-dependent dioxygenases," *Genome biology*, vol. 2, no. 3, Article ID RESEARCH0007, 2001.
- [45] B. Yu, W. C. Edstrom, J. Benach et al., "Crystal structures of catalytic complexes of the oxidative DNA/RNA repair enzyme AlkB," *Nature*, vol. 439, no. 7078, pp. 879–884, 2006.
- [46] Z. Zhang, J.-S. Ren, K. Harlos, C. H. McKinnon, I. J. Clifton, and C. J. Schofield, "Crystal structure of a clavaminate synthase-Fe(II)-2-oxoglutarate-substrate-NO complex: evidence for metal centred rearrangements," *FEBS Letters*, vol. 517, no. 1–3, pp. 7–12, 2002.
- [47] R. Nakajima and I. Yamazaki, "The mechanism of oxyper-oxidase formation from ferryl peroxidase and hydrogen peroxide," *Journal of Biological Chemistry*, vol. 262, no. 6, pp. 2576–2581, 1987.
- [48] G. I. Berglund, G. H. Carlsson, A. T. Smith, H. Szöke, A. Henriksen, and J. Hajdu, "The catalytic pathway of horseradish peroxidase at high resolution," *Nature*, vol. 417, no. 6887, pp. 463–468, 2002.
- [49] M. J. Frisch, G. W. Trucks, H. B. Schlegel et al., Gaussian 03, Revision D.02, Gaussian, Inc., Wallingford, Conn, USA, 2004.
- [50] Jaguar, Schrodinger, L. L. C., Portland, Ore, USA, 5.5 edition, 1991–2003.
- [51] J. San Filippo Jr., L. J. Romano, C. I. Chern, and J. S. Valentine, "Cleavage of esters by superoxide," *Journal of Organic Chemistry*, vol. 41, no. 3, pp. 586–588, 1976.
- [52] J. San Filippo Jr., C. I. Chern, and J. S. Valentine, "Oxidative cleavage of α -keto, α -hydroxy, and α -halo ketones, esters, and carboxylic acids by superoxide," *Journal of Organic Chemistry*, vol. 41, no. 6, pp. 1077–1078, 1976.
- [53] Y. M. Chiou and L. Que, "Models for α-keto acid-dependent non-heme iron enzymes: structures and reactivity of [Fe^{II}CL(O₂CCOPh)](ClO₄) complexes," *Journal of the American Chemical Society*, vol. 117, no. 14, pp. 3999–4013, 1995.
- [54] M. P. Mehn, K. Fujisawa, E. L. Hegg, and L. Que, "Oxygen activation by nonheme iron(II) complexes: α-keto carboxylate versus carboxylate," *Journal of the American Chemical Society*, vol. 125, no. 26, pp. 7828–7842, 2003.
- [55] T. Borowski, A. Bassan, and P. E. M. Siegbahn, "Mechanism of dioxygen activation in 2-oxoglutarate-dependent enzymes: a hybrid DFT study," *Chemistry: A European Journal*, vol. 10, no. 4, pp. 1031–1041, 2004.
- [56] T. Borowski, A. Bassan, and P. E. M. Siegbahn, "A hybrid density functional study of O-O bond cleavage and phenyl ring hydroxylation for a biomimetic non-heme iron complex," *Inorganic Chemistry*, vol. 43, no. 10, pp. 3277–3291, 2004.
- [57] A. Bassan, T. Borowski, and P. E. M. Siegbahn, "Quantum chemical studies of dioxygen activation by mononuclear non-heme iron enzymes with the 2-His-1-carboxylate facial triad," *Dalton Transactions*, no. 20, pp. 3153–3162, 2004.
- [58] T. Borowski, A. Bassan, and P. E. M. Siegbahn, "4-hydroxyphenylpyruvate dioxygenase: a hybrid density functional study of the catalytic reaction mechanism," *Biochemistry*, vol. 43, no. 38, pp. 12331–12342, 2004.
- [59] G. F. Barnard and M. Akhtar, "Stereochemistry of porphyrinogen carboxy-lyase reaction in haem biosynthesis," *Journal of the Chemical Society, Chemical Communications*, no. 13, pp. 494–496, 1975.

- [60] G. F. Barnard and M. Akhtar, "Stereochemical and mechanistic studies on the decarboxylation of uroporphyrinogen III in haem biosynthesis," *Journal of the Chemical Society, Perkin Transactions* 1, pp. 2354–2360, 1979.
- [61] M. Akhtar, "The modification of acetate and propionate side chains during the biosynthesis of haem and chlorophylls: mechanistic and stereochemical studies," *Ciba Foundation symposium*, vol. 180, pp. 131–152, 1994.
- [62] J. Fan, Q. Liu, Q. Hao, M. Teng, and L. Niu, "Crystal structure of uroporphyrinogen decarboxylase from Bacillus subtilis," *Journal of Bacteriology*, vol. 189, no. 9, pp. 3573–3580, 2007.
- [63] I. U. Heinemann, M. Jahn, and D. Jahn, "The biochemistry of heme biosynthesis," *Archives of Biochemistry and Biophysics*, vol. 474, no. 2, pp. 238–251, 2008.
- [64] B. M. Martins, B. Grimm, H. P. Mock, R. Huber, and A. Messerschmidt, "Crystal structure and substrate binding modeling of the uroporphyrinogen-III decarboxylase from Nicotiana tabacum: implications for the catalytic mechanism," *Journal of Biological Chemistry*, vol. 276, no. 47, pp. 44108–44116, 2001.
- [65] H. P. Mock, L. Trainotti, E. Kruse, and B. Grimm, "Isolation, sequencing and expression of cDNA sequences encoding uroporphyrinogen decarboxylase from tobacco and barley," *Plant Molecular Biology*, vol. 28, no. 2, pp. 245–256, 1995.
- [66] A. H. Jackson, H. A. Sancovich, A. M. Ferramola et al., "Macrocyclic intermediates in the biosynthesis of porphyrins," *Philosophical Transactions of the Royal Society of London. Series B*, vol. 273, no. 924, pp. 191–206, 1976.
- [67] J. D. Phillips, F. G. Whitby, J. P. Kushner, and C. P. Hill, "Structural basis for tetrapyrrole coordination by uroporphyrinogen decarboxylase," *The EMBO Journal*, vol. 22, no. 23, pp. 6225–6233, 2003.
- [68] G. Chaufan, M. C. Ríos de Molina, and L. C. San Martín de Viale, "How does hexachlorobenzene treatment affect liver uroporphyrinogen decarboxylase?" *International Journal of Biochemistry and Cell Biology*, vol. 33, no. 6, pp. 621–630, 2001.
- [69] C. A. Lewis and R. Wolfenden, "Uroporphyrinogen decarboxylation as a benchmark for the catalytic proficiency of enzymes," *Proceedings of the National Academy of Sciences of the United States of America*, vol. 105, no. 45, pp. 17328– 17333, 2008.
- [70] S. Billi de Catabbi, M. C. Ríos de Molina, and L. C. San Martín de Viale, "Studies on the active centre of rat liver porphyrinogen carboxylase in vivo effect of hexachlorobenzene," *International Journal of Biochemistry*, vol. 23, no. 7-8, pp. 675–679, 1991.
- [71] K. M. Jones and P. M. Jordan, "Purification and properties of the uroporphyrinogen decarboxylase from Rhodobacter sphaeroides," *Biochemical Journal*, vol. 293, no. 3, pp. 703– 712, 1993.
- [72] M. Akhtar, New Comprehensive Biochemistry: Biosynthesis of Tetrapyrroles, vol. 19, Elsevier, London, UK, 1991.
- [73] M. J. Bearpark, F. Ogliaro, T. Vreven et al., "CASSCF calculations for excited states of large molecules: choosing when to use the RASSCF, ONIOM and MMVB approximations," in *Computation in Modern Science and Engineering, Parts A and B*, T. E. Simos and G. Maroulis, Eds., vol. 2, pp. 583–585, Amer Inst Physics, Melville, NY, USA, 2007.
- [74] S. Dapprich, I. Komáromi, K. S. Byun, K. Morokuma, and M. J. Frisch, "A new ONIOM implementation in Gaussian98. Part I. The calculation of energies, gradients, vibrational frequencies and electric field derivatives," *Journal*

- of Molecular Structure: THEOCHEM, vol. 461-462, pp. 1–21, 1999.
- [75] S. Humbel, S. Sieber, and K. Morokuma, "The IMOMO method: integration of different levels of molecular orbital approximations for geometry optimization of large systems: test for *n*-butane conformation and *S*_N2 reaction: RCl+Cl⁻," *Journal of Chemical Physics*, vol. 105, no. 5, pp. 1959–1967, 1996.
- [76] F. Maseras and K. Morokuma, "IMOMM—a new integrated ab-initio plus molecular mechanics geometry optimization scheme of equilibrium structures and transition-states," *Journal of Computational Chemistry*, vol. 16, no. 9, pp. 1170– 1179, 1995.
- [77] K. Morokuma, D. G. Musaev, T. Vreven, H. Basch, M. Torrent, and D. V. Khoroshun, "Model studies of the structures, reactivities, and reaction mechanisms of metalloenzymes," *IBM Journal of Research and Development*, vol. 45, no. 3-4, pp. 367–395, 2001.
- [78] M. Svensson, S. Humbel, R. D. J. Froese, T. Matsubara, S. Sieber, and K. Morokuma, "ONIOM: a multilayered integrated MO + MM method for geometry optimizations and single point energy predictions. A test for Diels-Alder reactions and Pt(P(t-Bu)₃)₂ + H₂ oxidative addition," *Journal of Physical Chemistry*, vol. 100, no. 50, pp. 19357–19363, 1996.
- [79] T. Vreven, K. S. Byun, I. Komáromi et al., "Combining quantum mechanics methods with molecular mechanics methods in ONIOM," *Journal of Chemical Theory and Computation*, vol. 2, no. 3, pp. 815–826, 2006.
- [80] T. Vreven and K. Morokuma, "On the application of the IMOMO (integrated molecular orbital + molecular orbital) method," *Journal of Computational Chemistry*, vol. 21, no. 16, pp. 1419–1432, 2000.
- [81] T. Vreven, K. Morokuma, O. Farkas, H. B. Schlegel, and M. J. Frisch, "Geometry optimization with QM/MM, ONIOM, and other combined methods. I. Microiterations and constraints," *Journal of Computational Chemistry*, vol. 24, no. 6, pp. 760–769, 2003.
- [82] D. A. Case, T. E. Cheatham, T. Darden et al., "The Amber biomolecular simulation programs," *Journal of Computational Chemistry*, vol. 26, no. 16, pp. 1668–1688, 2005.
- [83] H. de Verneuil, S. Sassa, and A. Kappas, "Purification and properties of uroporphyrinogen decarboxylase from human erythrocytes. A single enzyme catalyzing the four sequential decarboxylations of uroporphyrinogens I and III," *Journal of Biological Chemistry*, vol. 258, no. 4, pp. 2454–2460, 1983.
- [84] A. B. Juárez, C. Aldonatti, M. S. Vigna, and M. C. Ríos de Molina, "Studies on uroporphyrinogen decarboxylase from Chlorella kessleri (Trebouxiophyceae, Chlorophyta)," *Canadian Journal of Microbiology*, vol. 53, no. 2, pp. 303–312, 2007
- [85] R. Wolfenden, X. Lu, and G. Young, "Spontaneous hydrolysis of glycosides," *Journal of the American Chemical Society*, vol. 120, no. 27, pp. 6814–6815, 1998.
- [86] D. L. Zechel and S. G. Withers, "Glycosidase mechanisms: anatomy of a finely tuned catalyst," *Accounts of Chemical Research*, vol. 33, no. 1, pp. 11–18, 2000.
- [87] J. M. Stubbs and D. Marx, "Glycosidic bond formation in aqueous solution: on the oxocarbenium intermediate," *Journal of the American Chemical Society*, vol. 125, no. 36, pp. 10960–10962, 2003.
- [88] J. M. Stubbs and D. Marx, "Aspects of glycosidic bond formation in aqueous solution: chemical bonding and the

- role of water," Chemistry: A European Journal, vol. 11, no. 9, pp. 2651–2659, 2005.
- [89] K. Das, D. Ray, N. R. Bandyopadhyay, T. Ghosh, A. K. Mohanty, and M. Misra, "A study of the mechanical, thermal and morphological properties of microcrystalline cellulose particles prepared from cotton slivers using different acid concentrations," *Cellulose*, vol. 16, no. 5, pp. 783–793, 2009.
- [90] Q. P. Liu, G. Sulzenbacher, H. Yuan et al., "Bacterial glycosidases for the production of universal red blood cells," *Nature Biotechnology*, vol. 25, no. 4, pp. 454–464, 2007.
- [91] B. Capon, "Mechanism in carbohydrate chemistry," *Chemical Reviews*, vol. 69, no. 4, pp. 407–498, 1969.
- [92] B. Henrissat, "A classification of glycosyl hydrolases based on amino acid sequence similarities," *Biochemical Journal*, vol. 280, no. 2, pp. 309–316, 1991.
- [93] J. D. McCarter and S. G. Withers, "Mechanisms of enzymatic glycoside hydrolysis," *Current Opinion in Structural Biology*, vol. 4, no. 6, pp. 885–892, 1994.
- [94] B. Henrissat and G. Davies, "Structural and sequence-based classification of glycoside hydrolases," *Current Opinion in Structural Biology*, vol. 7, no. 5, pp. 637–644, 1997.
- [95] M. L. Sinnott, "Catalytic mechanisms of enzymic glycosyl transfer," *Chemical Reviews*, vol. 90, no. 7, pp. 1171–1202, 1990.
- [96] G. J. Davies, T. M. Gloster, and B. Henrissat, "Recent structural insights into the expanding world of carbohydrate-active enzymes," *Current Opinion in Structural Biology*, vol. 15, no. 6, pp. 637–645, 2005.
- [97] B. P. Rempel and S. G. Withers, "Covalent inhibitors of glycosidases and their applications in biochemistry and biology," *Glycobiology*, vol. 18, no. 8, pp. 570–586, 2008.
- [98] J. Thompson, C. R. Gentry-Weeks, N. Y. Nguyen, J. E. Folk, and S. A. Robrish, "Purification from Fusobacterium mortiferum ATCC 25557 of a 6-phosphoryl-O-α-D-glucopyranosyl:6-phosphoglucohydrolase that hydrolyzes maltose 6-phosphate and related phospho-α-D-glucosides," *Journal of Bacteriology*, vol. 177, no. 9, pp. 2505–2512, 1995.
- [99] A. Varrot, V. L. Y. Yip, Y. Li et al., "NAD+ and metal-ion dependent hydrolysis by family 4 glycosidases: structural insight into specificity for phospho-β-D-glucosides," *Journal* of Molecular Biology, vol. 346, no. 2, pp. 423–435, 2005.
- [100] J. Thompson, S. B. Ruvinov, D. I. Freedberg, and B. G. Hall, "Cellobiose-6-phosphate hydrolase (CelF) of Escherichia coli: characterization and assignment to the unusual family 4 of glycosylhydrolases," *Journal of Bacteriology*, vol. 181, no. 23, pp. 7339–7345, 1999.
- [101] F. Kunst, N. Ogasawara, I. Moszer et al., "The complete genome sequence of the gram-positive bacterium Bacillus subtilis," *Nature*, vol. 390, no. 6657, pp. 249–256, 1997.
- [102] J. Thompson, A. Pikis, S. B. Ruvinov, B. Henrissat, H. Yamamoto, and J. Sekiguchi, "The gene glvA of Bacillus subtilis 168 encodes a metal-requiring, NAD(H)-dependent 6-phospho-α-glucosidase. Assignment to family 4 of the glycosylhydrolase superfamily," *Journal of Biological Chemistry*, vol. 273, no. 42, pp. 27347–27356, 1998.
- [103] B. G. Hall, A. Pikis, and J. Thompson, "Evolution and biochemistry of family 4 glycosidases: implications for assigning enzyme function in sequence annotations," *Molecular Biology and Evolution*, vol. 26, no. 11, pp. 2487–2497, 2009.
- [104] B. I. Cantarel, P. M. Coutinho, C. Rancurel, T. Bernard, V. Lombard, and B. Henrissat, "The Carbohydrate-Active EnZymes database (CAZy): an expert resource for glycogenomics," *Nucleic Acids Research*, vol. 37, no. 1, pp. D233– D238, 2009.

- [105] S. S. Rajan, X. Yang, F. Collart et al., "Novel catalytic mechanism of glycoside hydrolysis based on the structure of an NAD+/Mn²⁺-dependent phospho-α-glucosidase from Bacillus subtilis," *Structure*, vol. 12, no. 9, pp. 1619–1629, 2004
- [106] V. L. Y. Yip, J. Thompson, and S. G. Withers, "Mechanism of GlvA from Bacillus subtilis: a detailed kinetic analysis of a 6-phospho-α-glucosidase from glycoside hydrolase family 4," *Biochemistry*, vol. 46, no. 34, pp. 9840–9852, 2007.
- [107] V. L.Y. Yip and S. G. Withers, "Family 4 glycosidases carry out efficient hydrolysis of thioglycosides by an α,β -elimination mechanism," *Angewandte Chemie International Edition*, vol. 45, no. 37, pp. 6179–6182, 2006.

Hindawi Publishing Corporation Advances in Physical Chemistry Volume 2012, Article ID 483504, 16 pages doi:10.1155/2012/483504

Review Article

Quantum Instanton Evaluations of the Thermal Rate Constants for Complex Systems

Yi Zhao¹ and Wenji Wang²

¹ State Key Laboratory for Physical Chemistry of Solid Surfaces and Fujian Provincial Key Lab of Theoretical and Computational Chemistry, College of Chemistry and Chemical Engineering, Xiamen University, Xiamen 361005, China

Correspondence should be addressed to Yi Zhao, yizhao@xmu.edu.cn and Wenji Wang, wjwang@nwsuaf.edu.cn

Received 28 June 2011; Revised 26 August 2011; Accepted 10 September 2011

Academic Editor: Laimutis Bytautas

Copyright © 2012 Y. Zhao and W. Wang. This is an open access article distributed under the Creative Commons Attribution License, which permits unrestricted use, distribution, and reproduction in any medium, provided the original work is properly cited.

Quantum instanton (QI) approximation is recently proposed for the evaluations of the chemical reaction rate constants with use of full dimensional potential energy surfaces. Its strategy is to use the instanton mechanism and to approximate time-dependent quantum dynamics to the imaginary time propagation of the quantities of partition function. It thus incorporates the properties of the instanton idea and the quantum effect of partition function and can be applied to chemical reactions of complex systems. In this paper, we present the QI approach and its applications to several complex systems mainly done by us. The concrete systems include, (1) the reaction of $H + CH_4 \rightarrow H_2 + CH_3$, (2) the reaction of $H + SiH_4 \rightarrow H_2 + SiH_3$, (3) H diffusion on Ni(100) surface; and (4) surface-subsurface transport and interior migration for H/Ni. Available experimental and other theoretical data are also presented for the purpose of comparison.

1. Introduction

The accurate and efficient evaluation of chemical reaction rate constant is one of prime objectives of theoretical reaction dynamics. Since rigorous quantum mechanical approaches are limited to small molecular (several atoms) reactions, a variety of approximation approaches have been proposed. Benefited from the small recrossing dynamics at not-toohigh temperatures, the transition state theories (TSTs), originally proposed by Eyring [1, 2] and Wigner [3], have become a possible and popular way to estimate rate constants. Due to their practical simplicity, they have been broadly applied to numerous reactions. The TST is inherently a classical theory and suitable at sufficiently high temperatures, where the classical description of nuclear motions may be adequate. At low temperatures, especially for the reactions involving the motions of light atoms (i.e., hydrogen), however, quantum effects become quite significant. To make the TST still valid for such low temperature reactions, many approaches have been proposed to quantize it [4-14]. However, there is no absolutely unambiguous way to do it.

To develop a more accurate and less ad hoc quantum version of TST, with a specific focus on the tunneling regime, Miller et al. [15-17] have proposed a quantum instanton (QI) approach recently. The QI is based on an earlier semiclassical (SC) TST [18] that became known as the instanton [19, 20]. The similarity between the QI and SC instanton lies in using the steepest descent approximation to evaluate relevant integrals in the quantum rate formula, while the crucial difference is that the Boltzmann operator is evaluated by the quantum mechanics and semiclassical approximation, respectively. The QI theory thus incorporates the tunneling, corner cutting [21–24], and anharmonicity correctly and is expected to overcome the quantitative deficiency of the SC instanton model. In particular, the QI theory considers all tunneling paths and automatically gives each path its naturally weight factor from the quantum Boltzmann operator, instead of choosing a single optimal tunneling path, which is taken into account in the SC instanton and TSTs with SC tunneling corrections. Indeed, it has been numerically demonstrated that the QI predicts accurate quantum rates for one-dimensional and

² College of Science, Northwest A&F University, Yangling 712100, Shaanxi Province, China

two-dimensional models within 20% error over a wide temperature range, from the deep tunneling to overbarrier regimes.

A lot of developments and applications [25–39] have been made since the QI theory is proposed. The original QI [15] involves the second time derivative of the flux-flux correlation at time zero. It has been further improved [29] by taking into account the higher derivatives of the flux-flux function. For the 1D and collinear reactions, the improved model is considerable accuracy, giving the rates to within 5%–10% errors. For a practical purpose, a simple and general way for choosing dividing surfaces used in the QI is suggested [31], namely, using the family of (hyper)planes normal to the minimum energy path at various distances s. A "simplest" QI model [26] has also been suggested with one dividing surface, slightly less accurate than the original QI. To reveal the relationship with conventional TSTs, the classical limit of the QI has been derived [37]. It is found that the classical TST is just a special case of the QI in high temperature limit; moreover, the quantum correction of the prefactor is more important than that of the activation energy in the TST.

Since the OI solely involves the Boltzmann operator and its relevant quantities, it can be applied to quite complex molecular systems (from gas phase [17, 37], liquid [28], to surface [38, 39]) via well-established imaginary time path integral techniques. The first implementation of QI with path integral Monte Carlo and adaptive umbrella sampling techniques is applied to the three-dimensional hydrogen exchange reaction D + $H_2 \rightarrow HD + H$ [16]. Soon, the techniques are further extended to the reaction of $H+CH_4 \rightarrow$ $H_2 + CH_3$ [17]. The thermodynamic integration with respect to the mass of the isotope and the inverse temperature is also proposed to compute the kinetic isotope effects [30] and rate constants [34] directly. To improve the convergence of the Monte Carlo simulation, the efficient "virial" estimators [32] have been derived from the logarithmic derivatives of the partition function and the delta-delta correlation functions, and it is found that their statistical errors do not increase with the number of discrete time slices in the path integral. Most recently, the QI has been compared with other conventional approaches [36] for an intramolecular proton transfer on a full-dimensional potential energy surface that incorporates high-levels ab initio calculations along the reaction path. The obtained kinetic isotope effects from the QI are in reasonable agreement with those from the path-integral quantum TST.

In this paper, we firstly illustrate the QI formula and its path integral representation. Then, we display several applications, which are mainly done by ourselves. The systems include two gas phase reactions $H + CH_4 \rightarrow H_2 + CH_3$ [17] and $H + SiH_4 \rightarrow H_2 + SiH_3$ [37], H diffusion on Ni(100) surface [38], and surface-subsurface transport and interior migration for H/Ni [39].

2. Method

In this section, we summarize the rate formula for the QI evaluation. The detailed derivation can be found in [15–17]. The QI model proposes the following thermal rate

constant:

$$k_{\rm QI} = \frac{1}{Q_r} \frac{\sqrt{\pi}\hbar}{2} \frac{C_{ff}(0)}{\Delta H(\beta)}.$$
 (1)

Here, Q_r is the reactant partition function per unit volume. $C_{ff}(0)$ is zero time value of the flux-flux correlation function

$$C_{ff}(t) = \operatorname{tr} \left[e^{-\beta \hat{H}/2} \hat{F}_{a} e^{-\beta \hat{H}/2} e^{i\hat{H}t/\hbar} \hat{F}_{b} e^{-i\hat{H}t/\hbar} \right], \qquad (2)$$

where β is the inverse temperature $1/(k_BT)$, \hat{H} is the Hamiltonian operator of the reaction system, and \hat{F}_a and \hat{F}_b are the flux operators given by

$$\hat{F}_{\gamma} = \frac{i}{\hbar} \Big[\hat{H}, h \Big(s_{\gamma}(\hat{r}) \Big) \Big], \tag{3}$$

with y = a, b. In (3), h is the step-side function, r represents the Cartesian coordinates of the reaction system, and $s_a(r)$ and $s_b(r)$ define two separate dividing surfaces via the equations $s_a(r) = 0$ and $s_b(r) = 0$, both $s_a(r)$ and $s_b(r)$ being positive (negative) on the product (reactant) side of the dividing surfaces.

 $\Delta H(\beta)$ in (1) is a specific type of energy variance given by

$$\Delta H(\beta) = \hbar \sqrt{\frac{-\ddot{C}_{dd}(0)}{2C_{dd}(0)}}.$$
 (4)

In order to get the correct free particle (high temperature) limit (that would be 25% too large otherwise), an ad hoc term is added to $\Delta H(\beta)$, $\Delta H_{\rm mod}(\beta) = \Delta H(\beta) + (\sqrt{\pi} - \sqrt{2})/\beta$, which has very little effect in the low temperature regime. $C_{dd}(0)$ and $\ddot{C}_{dd}(0)$ are zero time value and its second time derivative, respectively, of the "delta-delta" correlation function

$$C_{dd}(t) = \operatorname{tr}\left[e^{-\beta \hat{H}/2} \Delta(s_a(\hat{r})) e^{-\beta \hat{H}/2} e^{i\hat{H}t/\hbar} \Delta(s_b(\hat{r})) e^{-i\hat{H}t/\hbar}\right], \tag{5}$$

where the generalized delta-function operator is

$$\Delta(s_{\gamma}(\hat{r})) = \delta(s_{\gamma}(\hat{r})) \sqrt{\sum_{i=1}^{N} \frac{1}{m_i} (\nabla_i s_{\gamma}(\hat{r}))^2} \quad (\gamma = a, b). \quad (6)$$

Here, *N* is the total number of atoms, $\nabla_i = \partial/\partial r_i$, r_i denotes the Cartesian coordinates of the *i*th atom, and m_i is its atomic mass.

The dividing surfaces are determined by the stationary condition

$$\frac{\partial}{\partial c_k} C_{dd}(0; \{c_k\}) = 0, \tag{7}$$

where $\{c_k\}$ is a collection of parameters that is involved in the location of the dividing surfaces. This condition originates from the SC instanton model, and the resulting dividing surfaces correspond qualitatively to the turning points of the periodic orbit that runs on an upside down PES in imaginary time (see Appendix A in [15, 18]).

Since all the relevant quantities in the QI expression (1) involved only the quantum Boltzmann operator, they can be readily evaluated using imaginary time path integral Monte Carlo (PIMC) [40] method.

We begin with the simplest quantity, $C_{dd}(0)$, which can be discretized according to the standard procedure [41–43] to give

$$C_{dd}(0) = C \int dr^{(1)} \int dr^{(2)} \cdots \int dr^{(P)} \Delta \left(s_a \left(r^{(0)} \right) \right)$$

$$\times \Delta \left(s_b \left(r^{(P/2)} \right) \right) \exp \left[-\beta \Phi \left(\left\{ r^{(s)} \right\} \right) \right],$$
(8)

where C is a multiplicative constant, P the number of imaginary time slices, and $r^{(s)} = (r_1^{(s)}, r_2^{(s)}, \dots, r_N^{(s)})$ the Cartesian coordinates of the system associated with the sth time slice. $\Phi(\{r^{(s)}\})$ is the discretized action given by

$$\Phi(\left\{r^{(s)}\right\}) = \frac{P}{2\hbar^2 \beta^2} \sum_{s=1}^{P} \sum_{i=1}^{N} m_i \left(r_i^{(s)} - r_i^{(s-1)}\right)^2 + \frac{1}{P} \sum_{s=1}^{P} V(r^{(s)}),$$
(9)

where $r^{(0)} = r^{(P)}$ and $\{r^{(s)}\}$ represents $\{r^{(1)}, r^{(2)}, \dots, r^{(P)}\}$. Path integral expressions for $C_{ff}(0)$ and $\ddot{C}_{dd}(0)$ are somewhat more complicated but can be obtained in a straightforward manner. The appropriate expressions are

$$C_{ff}(0) = C \int dr^{(1)} \int dr^{(2)} \cdots \int dr^{(P)} \Delta \left(s_a \left(r^{(0)} \right) \right)$$

$$\times \Delta \left(s_b \left(r^{(P/2)} \right) \right) \exp \left[-\beta \Phi \left(\left\{ r^{(s)} \right\} \right) \right] f_v \left(\left\{ r^{(s)} \right\} \right), \tag{10}$$

with

$$\begin{split} f_{\nu}\Big(\Big\{r^{(s)}\Big\}\Big) &= \left(\frac{iP}{2\hbar\beta}\right)^2 \frac{\sum_{i=1}^N \nabla_i s_a\Big(r^{(0)}\Big) \cdot \Big(r_i^{(1)} - r_i^{(P-1)}\Big)}{\sqrt{\sum_{i=1}^N m_i^{-1}(\nabla_i s_a(r^{(0)}))^2}} \\ &\times \frac{\sum_{i=1}^N \nabla_i s_b\Big(r^{(P/2)}\Big) \cdot \Big(r_i^{(P/2+1)} - r_i^{(P/2-1)}\Big)}{\sqrt{\sum_{i=1}^N m_i^{-1}(\nabla_i s_b(r^{(P/2)}))^2}}, \end{split}$$

$$\ddot{C}_{dd}(0) = -\frac{1}{\hbar^2} C \int dr^{(1)} \int dr^{(2)} \cdots \int dr^{(P)} \Delta \left(s_a \left(r^{(0)} \right) \right)
\times \Delta \left(s_b \left(r^{(P/2)} \right) \right) \exp \left[-\beta \Phi \left(\left\{ r^{(s)} \right\} \right) \right]
\times \left\{ F \left(\left\{ r^{(s)} \right\} \right)^2 + G \left(\left\{ r^{(s)} \right\} \right) \right\},$$
(11)

with

$$F(\lbrace r^{(s)} \rbrace) = -\frac{P}{\hbar^{2}\beta^{2}} \left\{ \sum_{s=1}^{P/2} - \sum_{s=P/2+1}^{P} \right\} \sum_{i=1}^{N} m_{i} (r_{i}^{(s)} - r_{i}^{(s-1)})^{2}$$

$$+ \frac{2}{P} \left\{ \sum_{s=1}^{P/2-1} - \sum_{s=P/2+1}^{P-1} \right\} V(r^{(s)}),$$

$$G(\lbrace r^{(s)} \rbrace) = \frac{2fP}{\beta^{2}} - \frac{4P}{\hbar^{2}\beta^{3}} \sum_{s=1}^{P} \sum_{i=1}^{N} m_{i} (r_{i}^{(s)} - r_{i}^{(s-1)})^{2},$$

$$(12)$$

with f being the total number of degrees of freedom (i.e., f = 3N).

In realistic calculations, we rewrite (1) as the product of several ratios

$$k_{\rm QI} = \frac{\sqrt{\pi}\hbar}{2} \frac{C_{dd}(0)}{Q_r} \frac{C_{ff}(0)}{C_{dd}(0)} \frac{1}{\Delta H(\beta)}.$$
 (13)

The terms of $C_{ff}(0)/C_{dd}(0)$ and ΔH are directly calculated as a constrained average over the same ensemble of paths [16, 17]

$$\frac{C_{ff}(0)}{C_{dd}(0)} = \langle f_{\nu} \rangle,$$

$$\Delta H^{2} = \frac{1}{2} \langle F^{2} + G \rangle,$$
(14)

with

$$\langle \cdots \rangle = \frac{\int dr^{(1)} \int dr^{(2)} \cdots \int dr^{(P)} \Delta \left(s_a \left(r^{(0)} \right) \right) \Delta \left(s_b \left(r^{(P/2)} \right) \right) \exp \left[-\beta \Phi \left(\left\{ r^{(s)} \right\} \right) \right] (\cdots)}{\int dr^{(1)} \int dr^{(2)} \cdots \int dr^{(P)} \Delta \left(s_a \left(r^{(0)} \right) \right) \Delta \left(s_b \left(r^{(P/2)} \right) \right) \exp \left[-\beta \Phi \left(\left\{ r^{(s)} \right\} \right) \right]}.$$
 (15)

The evaluation of $C_{dd}(0)/Q_r$, however, meets a challenge because the $C_{dd}(0)$ is the quantity associated with the transition state, while Q_r with the asymptotic reactant domain, we evaluate it using adaptive umbrella sampling techniques [44].

The QI approximation uses the short-time information of the flux-flux correlation function. Predescu and Miller [45] demonstrate that in the classical limit, Wigner's variational principle and the quantum variational criterion

based on the minimization of flux-flux correlation function produce the same optimal surface. Recently, Wang et al. [37] have shown that in the classical limit, the QI formula is the same as the classical transition state theory. These situations motivate us to write the QI formula (13) as the Arrhenius form

$$k_{\rm OI} = A_{\rm OI} \cdot e^{-\beta \Delta F}. \tag{16}$$

Here, the free energy ΔF is defined by

$$\Delta F = \frac{-1}{\beta} \cdot \log\left(\frac{C_{dd}(0)}{Q_r}\right). \tag{17}$$

This two-dimensional free energy is related to Q_r (the reactant partition function) and $C_{dd}(0; \xi_a, \xi_b)$, and it is corresponding to the quality of probability density at (ξ_a, ξ_b) . $C_{dd}(0; \xi_a, \xi_b)$ has a similar property to the partition function at the transition state. The prefactor is given by

$$A_{\rm QI} = \frac{\sqrt{\pi}}{2} \frac{C_{ff}(0)}{C_{dd}(0)} \frac{\hbar}{\Delta H}.$$
 (18)

The advantage of (16) allows us to investigate the respective quantum contributions to the rates from the quantum free energy and prefactor by comparing their quantum and classical values, since other factors such as the vibrationalrotational coupling and anharmonicity are automatically involved.

3. Results and Discussions

3.1. The Reaction of $H + CH_4 \rightarrow H_2 + CH_3$. The $H + CH_4$ reaction is a prototype of polyatomic hydrogen abstraction reaction. Quantum dynamical studies of this reaction have become possible only recently, because it involves 12 internal degrees of freedom and thus poses difficulties to quantum dynamics calculations as well as construction of the potential surface. We apply the QI methodology to this reaction using the potential energy surface constructed by Espinosa-García [46]. All calculations are performed in terms of the Cartesian coordinates of all the atoms (i.e., 18 degrees of freedom).

In the path integral simulations, the number of imaginary time slices P is chosen to be 20 and 100 at temperatures $T = 1000 \,\text{K}$ and 200 K, respectively, while $3 \times 10^7 \,\text{Monte}$ Carlo cycles are run to achieve <10% statistical convergence.

3.1.1. Reaction Coordinate. For this reaction, we define a generalized reaction coordinate $s(r;\xi)$, where ξ is an adjustable parameter that shifts the location of the dividing surface (defined by $s(r;\xi) = 0$). $s(r;\xi)$ is defined by a linear interpolation between two constituent reaction coordinates $s_0(r)$ and $s_1(r)$ through the parameter ξ ,

$$s(r;\xi) = \xi \cdot s_1(r) + (1 - \xi) \cdot s_0(r). \tag{19}$$

 $s_1(r)$ is a reaction coordinate whose dividing surface is designed to pass through the top of the classical potential barrier, which is defined here as

$$s_1(r) = \max \left\{ s_{\alpha}(r), s_{\beta}(r), s_{\gamma}(r), s_{\delta}(r) \right\}, \tag{20}$$

with $s_x(r)(x = \alpha, \beta, \gamma, \delta)$ being the reaction coordinate that describes the abstraction process of one of the methane hydrogens H_x by the incident one H

$$s_x(r) = r(C - H_x) - r(H_x - H) - [r^{\dagger}(C - H_x) - r^{\dagger}(H_x - H)],$$
(21)

where r(X - Y) denotes the interatomic distance between atoms X and Y and $r^{\dagger}(X - Y)$ is the value at the transition state geometry. $s_0(r)$, on the other hand, describes a dividing surface that is located far in the asymptotic reactant valley, which is given by

$$s_0(r) = R_{\infty} - |R|. \tag{22}$$

Here, R is the scattering vector that connects the incident hydrogen and the center of mass of the methane. R_{∞} is an adjustable parameter which is chosen to be 9 Å in order to guarantee that the interaction potential energy between H and CH₄ is negligible.

Now, the term $C_{dd}(0)$ (5) becomes a function of two parameters, ξ_a and ξ_b , as follows:

$$C_{dd}(0;\xi_a,\xi_b) = \operatorname{tr}\left[e^{-\beta \hat{H}/2} \Delta(s(\hat{r};\xi_a)) \times e^{-\beta \hat{H}/2} \Delta(s(\hat{r};\xi_b))\right],\tag{23}$$

and thus, one seeks a stationary point of $C_{dd}(0; \xi_a, \xi_b)$ in the two-dimensional (ξ_a, ξ_b) space to obtain the corresponding "optimal" values.

3.1.2. Free Energy Surface. The quantity $C_{dd}(0; \xi_a, \xi_b)$ varies exponentially as a function of (ξ_a, ξ_b) , it is convenient to define a quantum "free energy surface" as follows:

$$F(\xi_a, \xi_b) = -k_B T \log C_{dd}(0; \xi_a, \xi_b), \tag{24}$$

and locate the saddle point of $F(\xi_a, \xi_b)$ by visual inspection.

Figure 1 shows the free energy surfaces for the H + CH₄ reaction. It exhibits a barrier-like profile along the direction $\overline{\xi}=(\xi_a+\xi_b)/2$, while it grows approximately quadratically with the increasing of the absolute value of $\Delta\xi=\xi_a-\xi_b$. From this figure, it is seen that at a higher temperature $T=1000\,\mathrm{K}$ (Figure 1(a)), there appears only a single saddle point at $(\overline{\xi},\Delta\xi)=(1.02,0.0)$, while at a low temperature $T=200\,\mathrm{K}$ (Figure 1(b)), the saddle point bifurcates into a distinct pair at $(\overline{\xi},\Delta\xi)=(1.1,\pm0.35)$, which indicates the existence of nonnegligible tunneling effects in the rate constant [15, 16].

3.1.3. Rate Constants. Having obtained the "optimal" values of the (ξ_a, ξ_b) at each temperature, one can now compute the quantum instanton rate by combining various quantities as in (8). The calculated QI rates are tabulated in Table 1 as well as other theoretical and experimental ones.

Comparing the quantum instanton rates with others, we find that $k_{\rm QI}$ is in good agreement with the experimental data more specifically, it is closer to the rates obtained by Baulch et al. [47] than those by Sutherland et al. [48], and $k_{\rm QI}$ agrees with $k_{\rm CVT/\mu OMT}$ within 10% for the temperature range T=600-2000 K, but it becomes somewhat larger than the latter as the temperature is decreased (the deviation becomes 30% and 55% for T=500 and 300 K, resp.). It should be noted that the differences between $k_{\rm QI}$ and $k_{\rm CVT/\mu OMT}$ are much smaller than the uncertainty of the experimental data.

Figure 2 displays the Arrhenius plots of the rate constants. In Figure 2, we also plot the accurate quantum dynamics results of MCTDH (the multiconfigurational

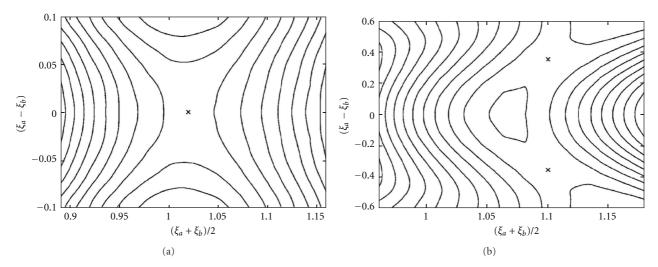


FIGURE 1: Local topography of the quantum free energy surface defined by (24) near the top of the barrier. (a) $T = 1000 \,\text{K}$; (b) $T = 200 \,\text{K}$. The cross symbols show the location of the saddle points. The values of ξ_a and ξ_b at the saddle points are used as input for computing the quantum instanton rate.

Table 1: Theoretical and experimental rate constants obtained for the H + CH₄ \rightarrow H₂ + CH₃ reaction. (ξ_a, ξ_b) is the saddle point of the quantum free energy surface. $k_{\rm QI}$ is the quantum instanton rate constant. $k_{\rm CVT/\mu OMT}$ is the rate constant of the canonical variational theory with microcanonical optimized multidimensional tunneling (CVT/ μ OMT) [46]. $k_{\rm exp\,t}^a$ are the experimental Arrhenius fits, $k(T) = 2.18 \times 10^{-20} \, T^{3.0} \, {\rm exp}(-4045/T)$ [47] and $k(T) = 6.78 \times 10^{-21} \, T^{3.156} \, {\rm exp}(-4406/T)$ [48], respectively. Unit: cm³s⁻¹ for rates.

T (K)	(ξ_a, ξ_b)	$k_{ m QI}$	$k_{ ext{CVT}/\mu ext{OMT}}$	$k_{\exp t}^a$	$k_{\exp t}^b$
200	(0.93, 1.28)	3.30 (-22)		2.87 (-22)	3.36 (-23)
300	(1.05, 1.05)	7.80 (-19)	5.03 (-19)	8.20 (-19)	1.86 (-19)
400	(1.05, 1.05)	6.00 (-17)	4.16 (-17)	5.66 (-17)	1.82 (-17)
500	(1.04, 1.04)	9.00 (-16)	6.96 (-16)	8.35 (-16)	3.33 (-16)
600	(1.03, 1.03)	5.42 (-15)	5.00 (-15)	5.56 (-15)	2.57 (-15)
700	(1.02, 1.02)	2.40 (-14)		2.31 (-14)	1.19 (-14)
800	(1.02, 1.02)	7.13 (-14)	6.72 (-14)	7.10(-14)	4.00 (-14)
900	(1.02, 1.02)	1.85(-13)		1.78 (-13)	1.07 (-13)
1000	(1.02, 1.02)	3.97 (-13)	3.58 (-13)	3.82 (-13)	2.43 (-13)
2000	(1.00, 1.00)	1.52 (-11)	1.70 (-11)	2.31 (-11)	1.96 (-11)

time-dependent Hartree approach) [49]. Compared to the MCTDH ones, our QI rate constants are larger by factors of about 2 to 3 over the temperature range 300–400 K. This difference may partly be due to the recrossing effect which is not considered in QI theory and partly arise from the use of the J-shifting approximation and the neglect of the vibrational angular momenta Hamiltonian in MCTDH method [49].

3.2. The Reaction of $H + SiH_4 \rightarrow H_2 + SiH_3$. The $H + SiH_4$ reaction is an important step in the radical mechanism of thermal decomposition of monosilane. We calculate the rates and kinetic isotope effects (KIEs) of this reaction with the quantum instanton method in full Cartesian space, on the basis of analytical potential energy surface constructed by Espinosa-García et al. [50].

The reaction coordinate of $H + SiH_4$ has the same form as that of $H + CH_4$ (Section 3.1.1). In our QI calculations,

the number of time slices, P, is set to be 20 (1000 K) and 120 (200 K) for the quantum evaluations. In our classical evaluations, the formula is the same as QI, but the number of time slices in the path integral is set to be 1. The number of Monte Carlo is about $(6-10) \times 10^6$ for computing a single ensemble average, and it converges the relevant quantities within 10% statistical errors.

3.2.1. Free Energy and Prefactor. We have rewritten the QI formula (8) in the Arrhenius form (16), which consists of the free energy and prefactor. In this section, we calculate the corresponding quantum and classical quantities so as to investigate the respective quantum contributions to the rates from the quantum free energy and prefactor. Our calculated results are plotted in Figures 3 and 4.

Now, we look into the quantum effects from both the free energy and prefactor. Figure 3 plots the quantum and classical free energies as a function of temperature

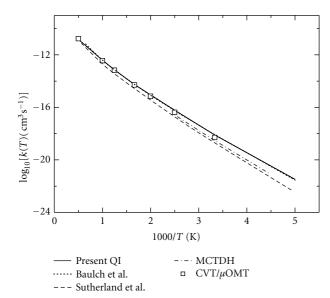


FIGURE 2: Arrhenius plots of the thermal rate constant for the $H + CH_4 \rightarrow H_2 + CH_3$ reaction. The solid line is the quantum instanton rate. Dotted and dashed lines are the Arrhenius fits of the experimental data from [47, 48], respectively. The dot-dashed line is the result of the multiconfigurational time-dependent Hartree approach (MCTDH) [49]. The open squares are the results of the canonical variational theory with microcanonical optimized multidimensional tunneling (CVT/ μ OMT) [46].

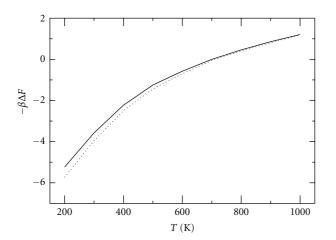


FIGURE 3: The temperature dependence of the free energy. The solid and dotted lines correspond to the quantum and classical calculations, respectively.

at the optimized stationary point. One immediately observes that the quantum effect becomes significant at $T < 600\,\mathrm{K}$, whereas both quantum and classical results nearly coincide at $T > 600\,\mathrm{K}$. As expected, the quantum effect always decreases the classical free energy. The difference of the contributions to the rates is about 40% at 200 K.

Figure 4 shows the temperature dependence of the quantum and classical prefactors. Compared with Figure 3, one easily finds that this quantum contribution is much larger than that for the free energy correction. Even at 1000 K,

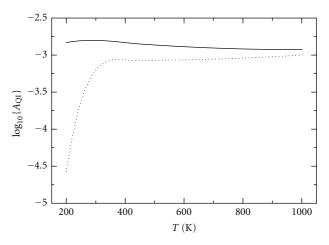


FIGURE 4: The temperature dependence of the prefactor. The solid and dotted lines correspond to the quantum and classical calculations, respectively.

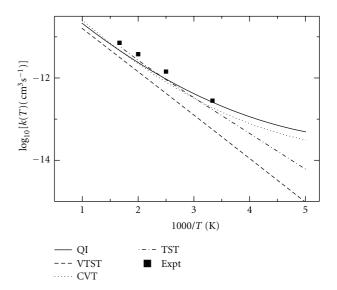


FIGURE 5: Arrhenius plot of the thermal rate constants for the H+SiH₄ reaction. Solid line, the QI results; dashed line, the classical VTST results; dotted line, CVT/CD-SCSAG results from [50]; dot-dashed, the values from the conventional TST with a simple Wigner tunneling factor [51]; filled squares are the experimental values from [52].

the difference is observable. At 200 K, the difference is about several orders of magnitude.

In the QI theory, it is not possible to explicitly distinguish the quantum contributions from the partition function and nuclear tunneling, but we can conclude that it is insufficient to estimate the accurate rate by only replacing the activation energy in the TST with its quantum analog, because the quantum prefactor plays more important rule in determining the quantum rate.

3.2.2. Rate Constants. In Table 2, we summarize the rate constants obtained from the QI theory and classical VTST (this kind of results are performed by setting the time slices

T (K)	Present QI	VTST	CVT/CD-SCSAG	DD	Expt.
200	4.82 (-14)	8.88 (-16)	3.07 (-14)	6.1 (-15)	
300	2.74(-13)	1.38 (-14)	2.09 (-13)	1.7 (-13)	2.81 (-13)
400	9.67 (-13)	4.32 (-13)	7.96 (-13)	9.1 (-13)	1.43 (-12)
500	2.37 (-12)	1.23 (-12)	2.11 (-12)	2.7 (-12)	3.78 (-12)
600	3.99 (-12)	2.55 (-12)	4.43 (-12)	5.9 (-12)	7.18 (-12)
700	7.60 (-12)	5.18 (-12)	8.00 (-12)		
800	1.18(-11)	8.63 (-12)			
900	1.76 (-11)	1.29 (-11)			
1000	2.39(-11)	1.99(-11)	2.80(-11)		

Table 2: Rate constants for the H+SiH₄ reaction (cm³s⁻¹). The CVT/CD-SCSAG results from [50]. DD is the conventional TST with simple Wigner tunneling factor [51]. Expt. is the experimental Arrhenius fits, $k(T) = 1.78 \times 10^{-10} \exp(-3820/RT)$ (T = 290-660 K) [52].

in the path integral to be 1 in the QI calculations) as well as those from the canonical variational TST with the centrifugal-dominant small curvature SC adiabatic ground-state (CVT/CD-SCSAG) approach [50], the conventional TST with simple Wigner tunneling factor [51] and the experiment [52]. The corresponding Arrhenius plots are displayed in Figure 5.

Table 2 and Figure 5 display comparable results of the CVT/CD-SCSAG to the QI values, with 36% maximal errors at 200 K and a slightly different Arrhenius slope. Both results are in good agreement with experimental data in the tested temperature range. This manifests that the PES used is reasonable accurate. However, the values from the classical VTST are always smaller than the QI results especially in the deep tunneling regions. The conventional TST results have similar tendency to those from the classical VTST. Although the classical VTST can be much improved by evaluating the partition functions quantum mechanically, we do not focus on this improvement. However, it is noted that the anharmonicity, rotational-vibrational coupling are involved in the classical simulation. It is thus expected that these large errors come from the pure quantum effects.

3.2.3. Kinetic Isotope Effects. Kinetic isotope effect (KIE) is the characteristic of chemical reactions which may reveal the quantum effect. We consider the following isotopic reactions:

(R1)
$$H + SiH_4 \longrightarrow SiH_3 + H_2$$

(R2)
$$D + SiH_4 \longrightarrow SiH_3 + HD$$
 (25)

(R3)
$$H + SiD_4 \longrightarrow SiD_3 + HD$$
.

The calculated values are tabulated in Table 3.

The KIEs of $k_{\rm QI}({\rm R1})/k_{\rm QI}({\rm R2})$ and $k_{\rm QI}({\rm R1})/k_{\rm QI}({\rm R3})$ in the temperature range of 200–1000 K are summarized in Table 3. Besides the QI values, this table also displays comparable results of the CVT/CD-SCSAG [50]. It is easily found that the $k({\rm R1})/k({\rm R2})$ KIEs predicted by the QI are smaller than 1, in agreement with the CVT/CD-SCSAG values. The detailed comparison reveals that the CVT/CD-SCSAG predicts smaller values than those from QI theory. Again, the maximal error occurs at 200 K and is about 23%. For $k({\rm R1})/k({\rm R3})$ KIEs, we find that although both approaches

predict the values larger than 1 at 200 to 1000 K, the QI values are smaller than those from CVT/CD-SCSAG. Espinosa-García and coworkers [50] have pointed out that the CVT/CD-SCSAG rates may have been overestimated because of the high vibrational and tunneling contributions. This manifests that the QI approach indeed correctly accounts for the quantum effects.

3.3. H Diffusion on Ni(100) Surface. Diffusion plays a fundamental role in surface process. It reveals characteristics about the underlying surface potential and is intimately involved in determining the kinetics of surface catalyzed chemical reactions. The hydrogen atom and its isotopes are ideal candidates to exhibit quantum tunneling behavior due to their small masses. We explore the evaluation of the quantum instanton approximation to the process of H diffusion on Ni(100) surface using the EAM4 potential energy surface constructed by Truong and Truhlar [53].

In the path integral calculations, the numbers of time slices, P and P_{bath} , for the degrees of freedom of H and quantized Ni atoms, respectively, are set to $(P, P_{\text{bath}}) = (24-40, 6-8)$ in the temperature range of 40-300 K. The number of Monte Carlo cycle employed is $(1-10) \times 10^6$, which converges most of the relevant quantities within 10% statistical error (some of the statistical errors are within 20% below 100 K).

3.3.1. Model. Nickel crystallizes in a face-centered-cubic (fcc) lattice structure. The structural model used consists of 162 Ni atoms over four layers: 40 atoms are in each of the first and third layers, and 41 atoms are in each of the second and fourth layers.

Figure 6 shows the platform and profile chart of Ni(100) lattice. In the simulations, 89 Ni atoms (orange), in the four sides of the bulk metal and the bottom layer, are fixed. The 48 atoms (blue) closest to the fixed ones are considered to be movable and treated classically. The last 25 ones (red), surrounding the reactant and product sites and lying directly beneath the reactant and product sites, are treated quantum mechanically.

In our calculations, the lattice (see Figure 6) is rotated by 45 degrees counterclockwise, and we chose the *x* coordinate of H atom (along the reaction path) to be reaction coordinate.

T (K)	QI KIE (R1/R2)	CVT KIE (R1/R2)	QI KIE (R1/R3)	CVT KIE (R1/R3)
200	0.56	0.69	30.10	33.60
300	0.73	0.71	8.57	9.81
400	0.77	0.76	4.39	5.07
500	0.85	0.81	3.11	3.46
600	0.90	0.84	2.41	2.72
700	0.92	0.86	2.15	2.32
800	0.94		1.78	
900	0.94		1.68	
1000	0.95	0.90	1.64	1.80

TABLE 3: The kinetic isotope effects (KIEs) at different temperatures. CVT is the CVT/CD-SCSAG values from [50].

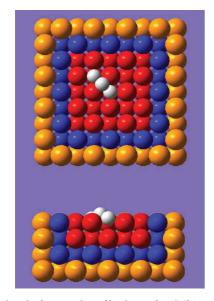


FIGURE 6: The platform and profile chart of H diffusion on Ni(100) lattice. The gray circles represent H atom on different surface sites, and the orange circles represent the fixed Ni atoms. Blue circles are Ni atoms treated classically, while the red ones are treated quantum mechanically.

3.3.2. Probability Distribution of Paths. The path integral has an advantage that the paths of the particles can display the character of the diffusive process. We extract the probability distributions for the paths of H and Ni atoms (two reaction coordinate beads (x_0 and $x_{P/2}$) of H path are fixed at the two dividing surfaces) for the purpose of guaranteeing the instanton property (the instanton is a periodic orbit between the two dividing surfaces). The dividing surfaces can be obtained from the free energy surface (24), their values at different temperatures are shown in Table 4.

Figure 7 displays the probability distributions for both H and Ni atoms at several temperatures. It is found that the probability distribution of H is localized at 300 K, and it becomes more and more delocalized as the temperature decreases. Below 80 K, the distribution rapidly becomes obvious in both sides of the transition state, and the path begins to continuously distribute between the two hollow sites at lower temperatures. This phenomenon indicates that

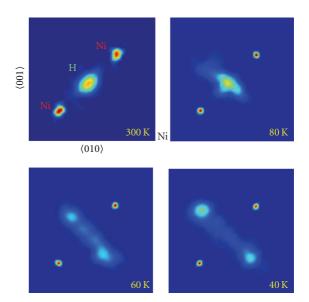


FIGURE 7: Distribution of H and Ni quantum paths on the surface with two reaction coordinate beads (x_0 and $x_{P/2}$) of H path fixed at the two dividing surfaces. Labels of <010> and <001> denote the crystal directions of nickel. The probabilities are normalized for both H and Ni.

H tunneling becomes remarkable at the temperatures lower than 80 K. The probability distributions of Ni atoms have small changes in the whole temperature range, and they seem to be frozen at very low temperature.

3.3.3. Diffusion Coefficients. According to the hopping model [54], the diffusion coefficient *D* is related to the rates through

$$D = k_{\rm OI} \cdot b^2, \tag{26}$$

where b is the hop length and is equal to 2.489 Å for the Ni(100) surface. We have calculated the diffusion coefficients at temperatures ranging from 40 to 300 K, and the results are plotted in Figure 8.

We plot two kinds of QI diffusion coefficients in Figure 8, one is the result on a rigid lattice, the other is the result on a quantized lattice. At high temperatures, these two kinds of diffusion coefficients are nearly the same; however, at low temperatures, the ones on a rigid lattice are bigger than that

Table 4: The positions of two dividing surfaces. (Unit in Å. The position 0.00 corresponds to the bridge site and the positions ± 1.24 Å correspond to two hollow sites.)

T (K)	300	80	60	50	40
x_a^{\dagger}	0.00	0.00	-0.75	-1.00	-1.08
x_b^\dagger	0.00	0.00	0.75	1.00	1.08

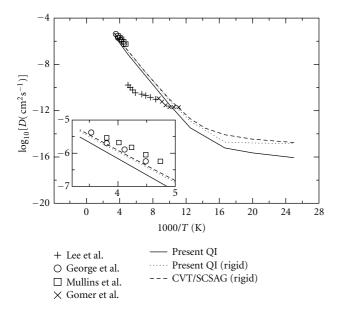


FIGURE 8: Arrhenius plots of the diffusion coefficients in the range 40–300 K. Solid line: the QI results for the quantized lattice; dotted line: the QI results for the rigid lattice; dashed line: the CVT/SCSAG results for the rigid lattice [55]. Pluses, circles, squares, and crosses are experimental results of Lee et al. [58], George et al. [56], Mullins et al. [57], and Lin and Gomer [59], respectively.

on a quantized lattice, and this is mainly due to the fact that the free energy on a quantized lattice is higher than that on a rigid lattice [38]. Comparing the QI diffusion coefficients with the CVT/SCSAG ones [55] on a rigid lattice, we find that our QI results on a rigid lattice are very similar to those from the CVT/SCSAG. Now, we compare the present theoretical results with experimental ones. It is found that the QI results as well as the CVT/SCSAG results are in good agreement with the experiments of George et al. [56] and Mullins et al. [57] at 200 K and 300 K. However, at low temperatures, the theoretical results are significantly larger than Lee et al. [58] and Lin and Gomer [59]. The experimental transition temperature (100 K–160 K) is also different from the present calculations. The QI predicts it to be 70 K for the quantized lattice, while it is about 66 K for the rigid lattice obtained from both the QI and the CVT/SCSAG approaches. These discrepancies between theories and experiments may be attributed to the interaction potential. It is likely that the accuracy of the potential energy surfaces needs further improvement.

3.4. Surface-Subsurface Transport and Interior Migration for H/Ni. A full-dimensional potential energy surface (EAM6),

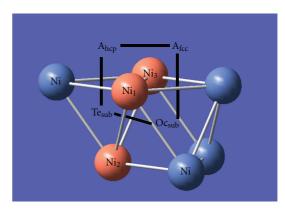


FIGURE 9: A lattice model with a few Ni atoms for the circle reaction processes of hydrogen. A_{hcp} , A_{fcc} , Oc_{sub} , and Te_{sub} are the abbreviations for a hcp hollow site, a fcc hollow site, a subsurface octahedral vacancy, and a subsurface tetrahedral vacancy, respectively. The black lines stand for the directions of the reaction paths. The atoms of Ni₁, Ni₂, and Ni₃ colored in orange are specially used to determine the reaction coordinate of the process $Oc_{sub} \rightarrow Te_{sub}$.

constructed by Wonchoba and Truhlar [60], using the embedded diatomics-in-molecules (EDIMs) [61] potential energy function, is used in this QI calculations.

In path integral calculations, the numbers of time slices, P and P_{bath} for the degrees of freedom of the H and quantized Ni atoms, respectively, are set to $(P, P_{bath}) = (30-40, 6-8)$ in the temperature range of 100-400 K. The number of Monte Carlo is about $(2-6) \times 10^6$ for computing a single ensemble average. It converges most of the values within 10% statistical errors (some of the statistical errors are within 20% at 100 K).

3.4.1. Model. Figures 9 and 10 show H diffusion processes in the nickel crystal with a face-centered-cubic (fcc) lattice structure. For a given rate process, we construct a lattice cell (each cell contains more than 200 Ni atoms) in which all atoms are treated to be movable to incorporate the effect of the crystal fluctuation on the rates. To be concrete, the Ni atoms in the four sides of the bulk metal and at the bottom layers are fixed, the Ni atoms surrounding the reactant and product sites and lying along the reaction path are treated quantum mechanically, and the others are treated classically. It should be noted that the lattice for the interior diffusion process has a structure of sphere and the outer layers are fixed.

In the QI calculations, we need to define the reaction coordinate operators \hat{s} (6). For the systems considered in this section, the hydrogen coordinates are essentially good choices. We thus adopt the following reaction coordinates for different rate processes. In the H diffusion on Ni(111) surface

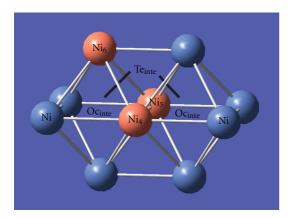


Figure 10: A lattice model with a few Ni atoms for the process of H diffusion in interior of bulk Ni. Oc_{inte} and Te_{inte} are the abbreviations for an interior octahedral vacancy and an interior tetrahedral vacancy, respectively. The black lines stand for the general directions of the reaction paths. The atoms of Ni₄, Ni₅, and Ni₆ colored in orange are specially used to determine the reaction coordinate of the process $Oc_{inte} \rightarrow Te_{inte}$.

from a hcp site to a fcc site ($A_{hcp} \rightarrow A_{fcc}$), the x coordinate of the H atom is chosen, whose direction is showed in Figure 9 as the black line connecting the A_{hcp} site to A_{fcc} site. In the H resurfacing from a subsurface octahedral vacancy to the fcc site ($Oc_{sub} \rightarrow A_{fcc}$) and from a subsurface tetrahedral vacancy to the hcp site ($Te_{sub} \rightarrow A_{hcp}$), the z coordinate of the H atom (vertical to Ni(111) surface) is taken. In the H diffusion between the adjacent subsurface octahedral and tetrahedral vacancies ($Oc_{sub} \rightarrow Te_{sub}$) and between the adjacent interior octahedral vacancy and interior tetrahedral vacancy ($Oc_{inte} \rightarrow Te_{inte}$), the reaction coordinates are along the directions that perpendicular to the planes of $Ni_1-Ni_2-Ni_3$ and $Ni_4-Ni_5-Ni_6$, respectively.

3.4.2. Free Energy and Prefactor. In order to investigate the quantized Ni lattice effect on the rates, we have recast the QI formula in (1) into Arrhenius form, which consists of the free energy and the prefactor (17) and (18).

In the free energy calculations, firstly, we calculate the free energy profile for each step of the H hopping paths, $A_{hcp} \rightarrow A_{fcc} \rightarrow Oc_{sub} \rightarrow Te_{sub} \rightarrow A_{hcp}$ and $Oc_{inte} \rightarrow Te_{inte} \rightarrow Oc_{inte}$, with the reaction coordinate defined in Section 3.4.1. Then, we connect these free energy profiles one by one, the final free energy profiles for the whole processes are displayed in Figures 11 and 12.

Figures 11 and 12 display the calculated free energy profiles for the surface-subsurface and interior processes, respectively, with the quantized lattice, the classical lattice and the rigid one at room temperature (300 K). The corresponding free energy barriers, prefactors, and rates are tabulated in Table 5.

Figures 11 and 12 clearly show that the classical lattices always reduce the free energy barriers compared with the rigid lattices, however, the differences between the free energy barriers with the quantized lattices and the ones with the classical lattices are very small. For different processes;

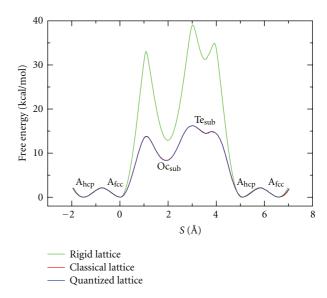


FIGURE 11: Free energy profiles with respect to the processes in Figure 9 at 300 K. The green, the red, and the blue lines correspond to the rigid, classical, and quantized lattices, respectively.

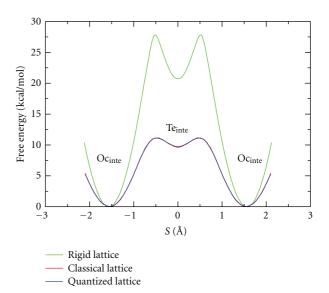


FIGURE 12: Free energy profiles with respect to the processes in Figure 10 at 300 K. The green, the red, and the blue lines correspond to the rigid, classical, and quantized lattices, respectively.

however, the relaxation effect on the free energies is very different. For hydrogen diffusion on Ni(111), the classical lattice only slightly lowers the free energy barrier, while it decreases the barriers by more than one-half in subsurface and interior processes. More careful analysis from Figure 11 reveals that the two preferred Ni(111) surface binding sites, that is, hcp and fcc hollows have symmetric wells, manifesting that the motions of Ni atoms in the layer beneath the surface have little influence on the surface free energies despite the fact that the Ni atoms beneath the hcp and fcc hollows have different arrangements. It is also found that the Oc_{sub} site has a deeper well than the Te_{sub} site and the well of the Te_{sub} site nearly disappears as relaxed Ni atoms

are considered. It manifests that the hydrogen at the Te_{sub} site is very unstable and can easily move to the Oc_{sub} site or resurface to the hcp site. In the interior processes, although the hydrogen in the Te_{inte} site is much less stable than in the Oc_{inte} site (see Figure 12), the well at the Te_{inte} is obvious. One thus expects that a two-step reaction process can be used for the reaction from one Oc_{inte} to the other.

Next, we consider the prefactor. Table 5 shows that the prefactors of the classical lattices are much smaller than those of rigid ones except for the process of H diffusion on Ni(111), and the prefactors of quantized lattices are always smaller than that of classical ones, but their amplitudes have the same order. This may be explained by the fact that the quantum motions of the lattice atoms can induce the dissipative effect on the tunneling degrees of freedom [62, 63], because the prefactor essentially incorporates the dynamical effect. It is well known that pure dissipation in the overdamping regime always hinders the reaction rates for a given reaction barrier. The present results thus are consistent with above analysis.

The rate is determined by both the prefactor and the free energy barrier. In Table 5, the rate with the rigid lattice is smaller than the one on the classical lattice, which is because the prefactor changes a little and the free energy determines the rate. However, the rate with the quantized lattice is smaller than that of the classical lattice, which is due to the fact that quantized lattice has a smaller prefactor while the free energies are similar. Generally speaking, for the quantized lattices, the rates are lower by 20%–40% when compared to the ones on the classical lattices.

Another important feature of the free energy is its temperature dependence. Figure 13 displays the free energy profiles with both H- and Ni-treated quantum mechanically at several temperatures. Generally speaking, the free energies have a slight difference at 300 K and 400 K, whereas this difference becomes pronounced for 100 K and 200 K, and the barrier positions move to the directions of shallow well for asymmetric reactions. These properties can be explained by the hydrogen tunneling effect. At lower temperatures, the tunneling plays a more important role. Indeed, the barrier heights decrease with decreasing temperature except for Oc_{sub} → Te_{sub} among 200 K to 400 K. This special case may be due to the special structure of the lattice. The thermal average displacements of Ni₁ and Ni₃ (in Figure 9) vertical to the Ni(111) surface increase with increasing temperature. Thus, H goes through reaction bottleneck easier at a higher temperature, which makes the barrier decrease. Figure 13 also displays that the free energy barriers of $Oc_{inte} \rightarrow Te_{inte}$ change little in the temperature range of 200-400 K, while those of the Te_{inte} → Oc_{inte} become smaller and smaller with decreasing temperature. The corresponding free energy barriers are 0.47, 1.09, 1.47, and 1.66 kcal/mol at 100, 200, 300, and 400 K, respectively. It manifests that the diffusing H atom may not equilibrate in the interior tetrahedral vacancy at very low temperatures.

3.4.3. Surface-Subsurface Transport. In the resurfacing process, $Te_{sub} \rightarrow A_{hcp}$ does not show an obvious barrier (see Figure 11), as the lattice atoms are treated quantum

mechanically. This step thus can be thought as a barrierless process. Table 6 tabulates the rate constants for the other resurfacing and subsurface processes in the temperature range of 100 to 600 K. We also list the available CVT/SCT results for $Oc_{sub} \rightarrow A_{fcc}$ and its reverse reaction [60]. Again, the CVT/SCT rates are close to the QI rates except at 100 K. We think our much bigger rate constant at 100 K is due to the contribution of tunneling.

3.4.4. Interior Migration. In the interior of bulk Ni, the two most stable sites to cage H are symmetric octahedral vacancies (see Figure 12). H diffusion between them has been measured experimentally [64-67]. Several theoretical calculations have also been proposed to investigate this diffusion process. Wimmer et al. [68] calculate the diffusion coefficient via two-step reactions Ocinte → Teinte → Ocinte by using a transition state theory together with accurate ab initio energies, while Wonchoba and Truhlar [60] consider the kinetic step as a direct process with a double maximum barrier and calculate the diffusion coefficient using the CVT/SCT. In the present QI calculations, Figure 13 has explicitly shown that the free energies have a well at the tetrahedral site from 200 K to 400 K. It is thus reasonable to assume that the diffusing H atom temporarily equilibrates in the tetrahedral site before jumping forward or backward to a neighboring octahedral site. The free energy well, however, becomes very shallow at 100 K. In this case, the direct reaction from the octahedral site to the other one may be acceptable. Here, we only calculate the diffusion coefficients via the two kinetic steps at 200–400 K.

The temperature dependence of the diffusion coefficients are commonly fitted to the Arrhenius equation

$$D(T) = D_0 \cdot \exp\left[\frac{-E_a}{RT}\right],\tag{27}$$

where R is the gas constant and D_0 and E_a are the preexponential factor and the activation energy, respectively. The QI calculations predict $D_0 = 3.93 \times 10^{-3} \, \text{cm}^2 \text{s}^{-1}$ and $E_a = 10.26 \, \text{kcal/mol}$. In the calculations, the rates of $Oc_{\text{inte}} \rightarrow Te_{\text{inte}}$ are used to obtain the diffusion coefficients for $Oc_{\text{inte}} \rightarrow Oc_{\text{inte}}$, because this process is much slower than that of $Te_{\text{inte}} \rightarrow Oc_{\text{inte}}$ and it determines the total reaction

Table 7 tabulates the pre-exponential factors and activation energies coming from available experiments and theories. It is found that both D_0 and E_a from the QI calculations are close to Ebisuzaki's experimental data [65]. Further tracking down the comparisons with experiments is nontrivial, because the accuracy of the diffusion coefficients is much dependent of the potential energy surface. However, we may make a quantitative comparison for the QI and CVT/SCT results. With use of the diffusion coefficients from 295 K to 300 K obtained by the CVT/SCT, Wonchoba and Truhlar [60] predict 11.1 kcal/mol for E_a , and 1.3 \times 10^{-3} cm²s⁻¹ for D_0 , respectively. These values are observably different from the QI calculations. E_a and D_0 are 0.8 kcal/mol larger and 3 times smaller than those from the QI calculations, respectively. The origin of these differences can be

TABLE 5: Free energies, prefactors, and rate constants.

Process (300 K)		ΔF (kcal/mol)	A_{QI} (s^{-1})	$k_{\mathrm{QI}}\ (\mathrm{s}^{-1})$
	a	2.19	1.58 (13)	4.07 (11)
$A_{fcc} \rightarrow A_{hcp}$	b	2.14	1.61 (13)	4.49 (11)
	С	2.14	1.27 (13)	3.47 (11)
	a	33.06	6.87 (13)	6.22 (-11)
$A_{fcc} \rightarrow Oc_{sub}$	b	13.79	2.85 (13)	2.64(3)
	С	13.75	2.29 (13)	2.23 (3)
	a	20.00	6.44 (13)	1.83 (-1)
$Oc_{sub} \rightarrow A_{fcc}$	b	5.40	2.10 (13)	2.62 (9)
	c	5.40	1.72 (13)	2.15 (9)
	a	34.92	4.29 (13)	1.67 (-12)
$A_{hcp} \rightarrow Te_{sub}$	b	14.92		
•	c	14.87		
Te _{sub} → A _{hcp}	a	3.25	5.13 (13)	2.28 (11)
	a	26.19	5.23 (13)	4.31 (-6)
$Oc_{sub} \rightarrow Te_{sub}$	b	7.83	1.86 (13)	3.51 (7)
	С	7.86	1.45 (13)	2.74 (7)
	a	7.83	8.17 (13)	1.51 (8)
$Te_{sub} \rightarrow Oc_{sub}$	b	1.75	1.91 (13)	1.05 (12)
	С	1.73	1.49 (13)	8.22 (11)
	a	27.82	5.12 (13)	2.86 (-7)
$Oc_{inte} \rightarrow Te_{inte}$	b	11.14	2.50 (13)	1.90 (5)
	c	11.17	1.75 (13)	1.32 (5)
	a	7.07	7.80 (13)	6.16 (8)
$Te_{inte} \rightarrow Oc_{inte}$	b	1.52	2.06 (13)	1.60 (12)
	c	1.47	1.53 (13)	1.36 (12)

a: The results for a rigid lattice.

Table 6: Rate constants (Unit: s^{-1} . Powers of 10 are in parentheses) for surface-subsurface processes. ^aThe QI results with a quantized lattice. ^bThe CVT/SCT results from [60].

	100 K	200 K	300 K	400 K	600 K
$A_{fcc} \rightarrow Oc_{sub}^{a}$	3.81 (-14)	1.14 (-1)	2.23 (3)	5.48 (5)	2.43 (8)
$A_{fcc} \rightarrow Oc_{sub}^{b}$	1.09 (-15)	1.23 (-1)	9.72 (3)	3.36 (6)	1.16 (9)
$Oc_{sub} \rightarrow A_{fcc}^{a}$	1.17 (6)	4.59 (7)	2.15 (9)	1.23 (10)	1.02 (11)
$Oc_{sub} \rightarrow A_{fcc}^{b}$	1.62 (5)	7.36 (7)	2.93 (9)	2.33 (10)	2.15 (11)
$Oc_{sub} \rightarrow Te_{sub}^{a}$	2.78 (-4)	1.99 (4)	2.74 (7)	1.18 (9)	2.49 (10)
$Te_{sub} \rightarrow Oc_{sub}^{a}$	7.24 (8)	4.68 (10)	8.22 (11)	2.00 (12)	4.13 (12)

Table 7: Arrhenius parameters for H diffusion in interior of bulk Ni. ^aThe QI diffusion coefficients for $Oc_{inte} \rightarrow Oc_{inte}$. ^bFrom [60]. ^cFrom [68]. ^dFrom [64]. ^eFrom [65]. ^fFrom [66]. ^gFrom [67].

		$D_0 \text{ (cm}^2\text{s}^{-1})$	E _a (kcal/mol)
Present QI ^a	200–400 K	3.93 (-3)	10.26
	295–300 K	1.3 (-3)	11.1
Wonchoba ^b (theoretical data)	300–627 K	7.8 (-4)	10.9
	627–1650 K	4.4 (-4)	10.2
Wimmer ^c (theoretical data)	273–1000 K	3.84 (-2)	10.92
Yamakawa ^d (experimental data)	220–350 K	1.9 (-3)	8.89
Ebisuzaki ^e (experimental data)	470–690 K	5.22 (-3)	9.56
Eichenauer ^f (experimental data)	660–930 K	6.73 (-3)	9.47
Katz ^g (experimental data)	670–1270 K	7.04 (-3)	9.43

b: The results for a classical lattice.

c: The results for a quantized lattice.

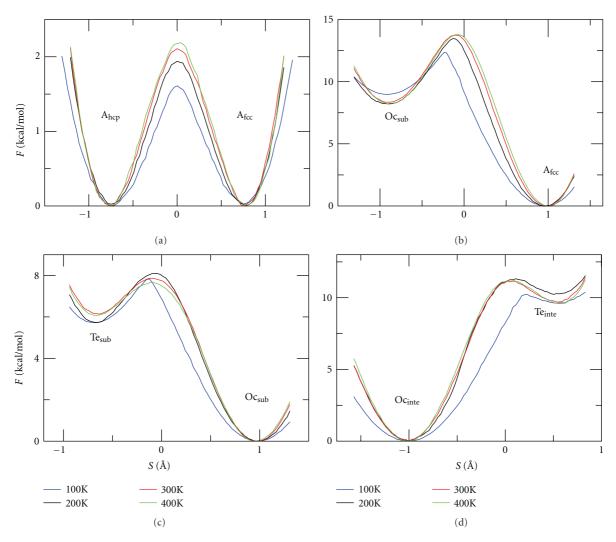


FIGURE 13: The temperature dependence of the free energies. The blue, the black, the red, and the green lines correspond to free energy profiles at 100 K, 200 K, 300 K, and 400 K, respectively.

explained by that Wonchoba and Truhlar have treated the processes $Oc_{inte} \rightarrow Te_{inte}$ and $Te_{inte} \rightarrow Oc_{inte}$ as a single kinetic step rather than as two kinetic steps, which results in a much longer tunneling path than that of the two steps. Compared with the results reported by Wimmer et al. [68], the activation energy is about 0.6 kcal/mol larger than the present one, and the pre-exponential factor is 10 times larger, which is also larger than all available experimental data. These differences may come from both the different potential energy surfaces and rate methods.

4. Conclusion

We have presented the basic principle of the quantum instanton (QI) approximation and its applications to chemical reactions from gas phase to surface systems. The applications demonstrate that the QI method makes it possible to treat hundreds of atoms because of the well-established techniques of imaginary time path integrals. For instance, more than 200

atoms have been incorporated in the present study of the H diffusion processes.

The QI approximation is a kind of "quantum transition state theory" in that there is no account of "recrossing" dynamics in the description. The recrossing effects on the quantum instanton rate constants have been quantified for several collinear reaction by Ceotto and Miller [25], and it is found especially evident for the collinear heavy-light-heavy reactions. Fortunately, the recrossing effects become generally less important in higher dimensions [69]. Therefore, the QI approach may become a suitable tool for the calculation of chemical reaction rate constants of complex systems.

Compared to conventional TST theories, the QI approximation involves two dividing surfaces, which are quantum analogs of the two turning point surfaces of the imaginary time trajectory in the semiclassical instanton theory. At high-temperature limit, these dividing surfaces coalesce into the one, the same as the dividing surface from Wigner's variational principle. In this case, the QI approximation becomes exactly the same as the classical TST. As the

tunneling corrections are incorporated, the CVT rates are consistent with the QI rates except at deep tunneling regime, where QI rates are generally greater than the rates from CVT with various tunneling corrections, since the CVT method uses an optimized tunneling path, while the QI method considers all tunneling paths and automatically gives each path its natural weight by the quantum Boltzmann factor. For the reaction of $H + CH_4 \rightarrow H_2 + CH_3$, accurate quantum dynamics rate constants are obtained with the MCTDH method. Compared to the MCTDH ones, the QI rate constants are larger by factors of about 2 to 3 over the temperature range 300–400 K. This difference may partly be due to the recrossing effect which is not considered in QI theory and partly arise from the use of the J-shifting approximation and the neglect of the vibrational angular momenta Hamiltonian in MCTDH method.

Acknowledgments

This work was financially supported by the National Science Foundation of China (Grant nos. 20833004 and 21073146), National Key Basic Research Foundation Program of China (2007CB815204), and the Scientific Research Foundation of Northwest A&F University (Grant no. Z109021103).

References

- [1] H. Eyring, "The activated complex in chemical reactions," *The Journal of Chemical Physics*, vol. 3, no. 2, pp. 63–71, 1935.
- [2] H. Eyring, "The theory of absolute reaction rates," *Transactions of the Faraday Society*, vol. 34, pp. 41–48, 1938.
- [3] E. Wigner, "The transition state method," *Transactions of the Faraday Society*, vol. 34, pp. 29–41, 1938.
- [4] G. A. Voth, D. Chandler, and W. H. Miller, "Time correlation function and path integral analysis of quantum rate constants," *Journal of Physical Chemistry*, vol. 93, no. 19, pp. 7009–7015, 1989.
- [5] G. A. Voth, D. Chandler, and W. H. Miller, "Rigorous formulation of quantum transition state theory and its dynamical corrections," *The Journal of Chemical Physics*, vol. 91, no. 12, pp. 7749–7760, 1989.
- [6] S. Jang and G. A. Voth, "A relationship between centroid dynamics and path integral quantum transition state theory," *Journal of Chemical Physics*, vol. 112, no. 20, pp. 8747–8757, 2000.
- [7] W. H. Miller, "Generalization of the linearized approximation to the semiclassical initial value representation for reactive flux correlation functions," *Journal of Physical Chemistry A*, vol. 103, no. 47, pp. 9384–9387, 1999.
- [8] E. Pollak and J. L. Liao, "A new quantum transition state theory," *Journal of Chemical Physics*, vol. 108, no. 7, pp. 2733– 2743, 1998.
- [9] J. Shao, J. L. Liao, and E. Pollak, "Quantum transition state theory: perturbation expansion," *Journal of Chemical Physics*, vol. 108, no. 23, pp. 9711–9725, 1998.
- [10] K. Yamashita and W. H. Miller, "'Direct' calculation of quantum mechanical rate constants via path integral methods: application to the reaction path Hamiltonian, with numerical test for the $H+H_2$ reaction in 3D," *The Journal of Chemical Physics*, vol. 82, no. 12, pp. 5475–5484, 1984.

- [11] J. W. Tromp and W. H. Miller, "New approach to quantum mechanical transition-state theory," *Journal of Physical Chemistry*, vol. 90, no. 16, pp. 3482–3485, 1986.
- [12] N. F. Hansen and H. C. Andersen, "A new formulation of quantum transition state theory for adiabatic rate constants," *The Journal of Chemical Physics*, vol. 101, no. 7, pp. 6032–6037, 1994.
- [13] G. Krilov, E. Sim, and B. J. Berne, "Quantum time correlation functions from complex time Monte Carlo simulations: a maximum entropy approach," *Journal of Chemical Physics*, vol. 114, no. 3, pp. 1075–1088, 2001.
- [14] E. Sim, G. Krilov, and B. J. Berne, "Quantum rate constants from short-time dynamics: an analytic continuation approach," *Journal of Physical Chemistry A*, vol. 105, no. 12, pp. 2824–2833, 2001.
- [15] W. H. Miller, Y. Zhao, M. Ceotto, and S. Yang, "Quantum instanton approximation for thermal rate constants of chemical reactions," *Journal of Chemical Physics*, vol. 119, no. 3, pp. 1329–1342, 2003.
- [16] T. Yamamoto and W. H. Miller, "On the efficient path integral evaluation of thermal rate constants within the quantum instanton approximation," *Journal of Chemical Physics*, vol. 120, no. 7, pp. 3086–3099, 2004.
- [17] Y. Zhao, T. Yamamoto, and W. H. Miller, "Path integral calculation of thermal rate constants within the quantum instanton approximation: application to the H+CH₄ → H₂+ CH₃ hydrogen abstraction reaction in full Cartesian space," *Journal of Chemical Physics*, vol. 120, no. 7, pp. 3100–3107, 2004
- [18] W. H. Miller, "Semiclassical limit of quantum mechanical transition state theory for nonseparable systems," *The Journal of Chemical Physics*, vol. 62, no. 5, pp. 1899–1906, 1975.
- [19] S. Coleman, "Fate of the false vacuum: semiclassical theory," *Physical Review D*, vol. 15, no. 10, pp. 2929–2936, 1977.
- [20] A. J. Leggett, S. Chakravarty, A. T. Dorsey, M. P. A. Fisher, A. Garg, and W. Zwerger, "Dynamics of the dissipative two-state system," *Reviews of Modern Physics*, vol. 59, no. 1, pp. 1–85, 1987.
- [21] R. A. Marcus, "On the analytical mechanics of chemical reactions. quantum mechanics of linear collisions," *The Journal of Chemical Physics*, vol. 45, no. 12, pp. 4493–4499, 1966.
- [22] E. A. Mccullough and R. E. Wyatt, "Dynamics of the collinear H + H₂ reaction. I. Probability density and flux," *The Journal of Chemical Physics*, vol. 54, no. 8, pp. 3578–3591, 1971.
 [23] D. G. Truhlar and A. Koppermann, "Exact and approximate
- [23] D. G. Truhlar and A. Koppermann, "Exact and approximate quantum mechanical reaction probabilities and rate constants for the collinear H + H₂ reaction," *The Journal of Chemical Physics*, vol. 56, no. 5, pp. 2232–2252, 1972.
- [24] T. V. George and W. H. Miller, "Classical S-matrix theory of reactive tunneling: linear H + H₂ collisions," *The Journal of Chemical Physics*, vol. 57, no. 6, pp. 2458–2467, 1972.
- [25] M. Ceotto and W. H. Miller, "Test of the quantum instanton approximation for thermal rate constants for some collinear reactions," *Journal of Chemical Physics*, vol. 120, no. 14, pp. 6356–6362, 2004.
- [26] C. Venkataraman and W. H. Miller, "The Quantum Instanton (QI) model for chemical reaction rates: the "simplest" QI with one dividing surface," *Journal of Physical Chemistry A*, vol. 108, no. 15, pp. 3035–3039, 2004.
- [27] Y. Li and W. H. Miller, "Different time slices for different degrees of freedom in Feynman path integration," *Molecular Physics*, vol. 103, no. 2-3, pp. 203–208, 2005.
- [28] T. Yamamoto and W. H. Miller, "Path integral evaluation of the quantum instanton rate constant for proton transfer in a polar

- solvent," *Journal of Chemical Physics*, vol. 122, no. 4, Article ID 044106, pp. 1–13, 2005.
- [29] M. Ceotto, S. Yang, and W. H. Miller, "Quantum reaction rate from higher derivatives of the thermal flux-flux autocorrelation function at time zero," *Journal of Chemical Physics*, vol. 122, no. 4, Article ID 044109, pp. 1–7, 2005.
- [30] J. Vaníček, W. H. Miller, J. F. Castillo, and F. J. Aoiz, "Quantum-instanton evaluation of the kinetic isotope effects," *Journal of Chemical Physics*, vol. 123, no. 5, Article ID 054108, pp. 1–14, 2005.
- [31] Y. Li and W. H. Miller, "Using a family of dividing surfaces normal to the minimum energy path for quantum instanton rate constants," *Journal of Chemical Physics*, vol. 125, no. 6, Article ID 064104, 2006.
- [32] S. Yang, T. Yamamoto, and W. H. Miller, "Path-integral virial estimator for reaction-rate calculation based on the quantum instanton approximation," *Journal of Chemical Physics*, vol. 124, no. 8, Article ID 084102, 2006.
- [33] J. Vaníček and W. H. Miller, "Efficient estimators for quantum instanton evaluation of the kinetic isotope effects: application to the intramolecular hydrogen transfer in pentadiene," *Journal of Chemical Physics*, vol. 127, no. 11, Article ID 114309, 2007.
- [34] M. Buchowiecki and J. Vaníček, "Direct evaluation of the temperature dependence of the rate constant based on the quantum instanton approximation," *Journal of Chemical Physics*, vol. 132, no. 19, Article ID 194106, 2010.
- [35] T. Zimmermann and J. Vaníček, "Three applications of path integrals: equilibrium and kinetic isotope effects, and the temperature dependence of the rate constant of the [1,5] sigmatropic hydrogen shift in (Z)-1,3-pentadiene," *Journal of Molecular Modeling*, vol. 16, no. 11, pp. 1779–1787, 2010.
- [36] K. F. Wong, J. L. Sonnenberg, F. Paesani et al., "Proton transfer studied using a combined ab initio reactive potential energy surface with quantum path integral methodology," *Journal of Chemical Theory and Computation*, vol. 6, no. 9, pp. 2566– 2580, 2010.
- [37] W. Wang, S. Feng, and Y. Zhao, "Quantum instanton evaluation of the thermal rate constants and kinetic isotope effects for SiH₄+H → SiH₃ + H₂ reaction in full Cartesian space," *Journal of Chemical Physics*, vol. 126, no. 11, Article ID 114307, 2007.
- [38] W. Wang and Y. Zhao, "Path integral evaluation of H diffusion on Ni(100) surface based on the quantum instanton approximation," *Journal of Chemical Physics*, vol. 130, no. 11, Article ID 114708, pp. 1–10, 2009.
- [39] W. Wang and Y. Zhao, "Quantum instanton evaluations of surface diffusion, interior migration, and surface-subsurface transport for H/Ni," *Journal of Chemical Physics*, vol. 132, no. 6, Article ID 064502, 2010.
- [40] B. J. Berne and D. Thirumalai, "On the simulation of quantum systems: path integral methods," *Annual Review of Physical Chemistry*, vol. 37, pp. 401–424, 1986.
- [41] R. P. Feynman and A. R. Hibbs, *Quantum Mechanics and Path Integrals*, McGraw-Hill, New York, NY, USA, 1965.
- [42] R. P. Feynman, Statistical Mechanics, Addison-Wesley, New York, NY, USA, 1972.
- [43] L. S. Schulman, Techniques and Applications of Path Integrals, John Wiley & Sons, New York, NY, USA, 1986.
- [44] M. Mezei, "Adaptive umbrella sampling: self-consistent determination of the non-Boltzmann bias," *Journal of Computational Physics*, vol. 68, no. 1, pp. 237–248, 1987.

- [45] C. Predescu and W. H. Miller, "Optimal choice of dividing surface for the computation of quantum reaction rates," *Journal of Physical Chemistry B*, vol. 109, no. 14, pp. 6491–6499, 2005.
- [46] J. Espinosa-García, "New analytical potential energy surface for the CH₄+H hydrogen abstraction reaction: thermal rate constants and kinetic isotope effects," *Journal of Chemical Physics*, vol. 116, no. 24, pp. 10664–10673, 2002.
- [47] D. L. Baulch, C. J. Cobos, R. A. Cox et al., "Evaluated kinetic data for combustion modelling," *Journal of Physical* and Chemical Reference Data, vol. 21, no. 3, pp. 411–734, 1992.
- [48] J. W. Sutherland, M. C. Su, and J. V. Michael, "Rate constants for H + CH₄, CH₃ + H₂, and CH₄ dissociation at high temperature," *International Journal of Chemical Kinetics*, vol. 33, no. 11, pp. 669–684, 2001.
- [49] S. Andersson, G. Nyman, A. Arnaldsson, U. Manthe, and H. Jonsson, "Comparison of quantum dynamics and quantum transition state theory estimates of the H + CH₄ reaction rate," *Journal of Physical Chemistry A*, vol. 113, no. 16, pp. 4468–4478, 2009.
- [50] J. Espinosa-García, J. Sansón, and J. C. Corchado, "The SiH₄ + H → SiH₃ + H₂ reaction: potential energy surface, rate constants, and kinetic isotope effects," *Journal of Chemical Physics*, vol. 109, no. 2, pp. 466–473, 1998.
- [51] K. D. Dobbs and D. A. Dixon, "Ab initio prediction of the activation energies for the abstraction and exchange reactions of H with CH₄ and SiH₄," *Journal of Physical Chemistry*, vol. 98, no. 20, pp. 5290–5297, 1994.
- [52] A. Goumri, W. J. Yuan, L. Ding, Y. Shi, and P. Marshall, "Experimental and theoretical studies of the reaction of atomic hydrogen with silane," *Chemical Physics*, vol. 177, no. 1, pp. 233–241, 1993.
- [53] T. N. Truong and D. G. Truhlar, "Effect of steps and surface coverage on rates and kinetic isotope effects for reactions catalyzed by metallic surfaces: chemisorption of hydrogen on Ni," *Journal of Physical Chemistry*, vol. 94, no. 21, pp. 8262– 8279, 1990.
- [54] J. V. Barth, "Transport of adsorbates at metal surfaces: from thermal migration to hot precursors," *Surface Science Reports*, vol. 40, no. 3, pp. 75–149, 2000.
- [55] T. N. Truong and D. G. Truhlar, "The effects of steps, coupling to substrate vibrations, and surface coverage on surface diffusion rates and kinetic isotope effects: hydrogen diffusion on Ni," *The Journal of Chemical Physics*, vol. 93, no. 3, pp. 2125–2138, 1990.
- [56] S. M. George, A. M. DeSantolo, and R. B. Hall, "Surface diffusion of hydrogen on Ni(100) studied using laser-induced thermal desorption," *Surface Science*, vol. 159, no. 1, pp. L425– L432, 1985.
- [57] D. R. Mullins, B. Roop, S. A. Costello, and J. M. White, "Isotope effects in surface diffusion: hydrogen and deuterium on Ni(100)," *Surface Science*, vol. 186, no. 1-2, pp. 67–74, 1987.
- [58] A. Lee, X. D. Zhu, L. Deng, and U. Linke, "Observation of a transition from over-barrier hopping to activated tunneling diffusion: H and D on Ni(100)," *Physical Review B*, vol. 46, no. 23, pp. 15472–15476, 1992.
- [59] T. S. Lin and R. Gomer, "Diffusion of ¹H and ²H on the Ni(111) and (100) planes," *Surface Science*, vol. 255, no. 1-2, pp. 41–60, 1991.
- [60] S. E. Wonchoba and D. G. Truhlar, "General potentialenergy function for H/Ni and dynamics calculations of surface diffusion, bulk diffusion, subsurface-to-surface transport, and

- absorption," *Physical Review B*, vol. 53, no. 16, pp. 11222–11241, 1996.
- [61] T. N. Truong, D. G. Truhlar, and B. C. Garrett, "Embedded diatomics-in-molecules: a method to include delocalized electronic interactions in the treatment of covalent chemical reactions at metal surfaces," *Journal of Physical Chemistry*, vol. 93, no. 25, pp. 8227–8239, 1989.
- [62] R. Baer and R. Kosloff, "Quantum dissipative dynamics of adsorbates near metal surfaces: a surrogate Hamiltonian theory applied to hydrogen on nickel," *Journal of Chemical Physics*, vol. 106, no. 21, pp. 8862–8875, 1997.
- [63] R. Baer, Y. Zeiri, and R. Kosloff, "Hydrogen transport in nickel (111)," *Physical Review B*, vol. 55, no. 16, pp. 10952–10974, 1997.
- [64] K. Yamakawa, "Diffusion of deuterium and isotope effect in nickel," *Journal of the Physical Society of Japan*, vol. 47, no. 1, pp. 114–121, 1979.
- [65] Y. Ebisuzaki, W. J. Kass, and M. O'Keeffe, "Diffusion and solubility of hydrogen in single crystals of nickel and nickelvanadium alloy," *The Journal of Chemical Physics*, vol. 46, no. 4, pp. 1378–1381, 1967.
- [66] W. Eichenauer, W. Loser, and H. Witte, "Solubility and rate of diffusion of hydrogen and deuterium in nickel and copper single crystals," Z Metallk, vol. 56, pp. 287–293, 1965.
- [67] L. Katz, M. Guinan, and R. J. Borg, "Diffusion of H₂, D₂, and T₂ in single-crystal Ni and Cu," *Physical Review B*, vol. 4, no. 2, pp. 330–341, 1971.
- [68] E. Wimmer, W. Wolf, J. Sticht et al., "Temperature-dependent diffusion coefficients from ab initio computations: hydrogen, deuterium, and tritium in nickel," *Physical Review B*, vol. 77, no. 13, Article ID 134305, 2008.
- [69] S. Chapman, S. M. Hornstein, and W. H. Miller, "Accuracy of transition state theory for the threshold of chemical reactions with activation energy. Collinear and three-dimensional H + H₂," *Journal of the American Chemical Society*, vol. 97, no. 4, pp. 892–894, 1975.

Hindawi Publishing Corporation Advances in Physical Chemistry Volume 2012, Article ID 951371, 9 pages doi:10.1155/2012/951371

Research Article

Improved Potential Energy Surface of Ozone Constructed Using the Fitting by Permutationally Invariant Polynomial Function

Mehdi Ayouz and Dmitri Babikov

Chemistry Department, Marquette University, Wehr Chemistry Building, Milwaukee, WI 53201-1881, USA

Correspondence should be addressed to Dmitri Babikov, dmitri.babikov@mu.edu

Received 7 July 2011; Accepted 23 August 2011

Academic Editor: Joel Bowman

Copyright © 2012 M. Ayouz and D. Babikov. This is an open access article distributed under the Creative Commons Attribution License, which permits unrestricted use, distribution, and reproduction in any medium, provided the original work is properly cited.

New global potential energy surface for the ground electronic state of ozone is constructed at the complete basis set level of the multireference configuration interaction theory. A method of fitting the data points by analytical permutationally invariant polynomial function is adopted. A small set of 500 points is preoptimized using the old surface of ozone. In this procedure the positions of points in the configuration space are chosen such that the RMS deviation of the fit is minimized. New *ab initio* calculations are carried out at these points and are used to build new surface. Additional points are added to the vicinity of the minimum energy path in order to improve accuracy of the fit, particularly in the region where the surface of ozone exhibits a shallow van der Waals well. New surface can be used to study formation of ozone at thermal energies and its spectroscopy near the dissociation threshold.

1. Introduction

The global potential energy surface (PES) for the ground electronic state of ozone,

$$O_3(\widetilde{X}) \longrightarrow O({}^3P) + O_2({}^3\Sigma_g^-),$$
 (1)

is now 10 years old. The old PES was based on the *ab initio* calculations of the electronic structure at the icMRCI+Q/cc-pVQZ level of theory using CASSCF(12,9) active space and was represented by a 3D-spline interpolation of the data on a structured rectangular grid [1, 2].

The *ab initio* data obtained at that level of theory contained two serious deficiencies. First, the computed dissociation energy $D_{\rm e}=1.027\,{\rm eV}$ was too low—about 847 cm⁻¹ lower than the experimental value available at that time (see below). Second, the surface exhibited an artificial barrier on its way to dissociation—about 47 cm⁻¹ above the threshold. In the improved, most popular version of that surface [3] an analytic correction function was added to the spline in order to (i) eliminate the barrier by taking into account the results of more accurate *ab initio* calculations [4, 5] carried out along the one-dimensional minimum energy

path to dissociation (MEP) and (ii) make the surface deeper in order to reproduce experimental value of the dissociation energy available at that time [6], $D_e = 1.132 \,\text{eV}$.

More accurate *ab initio* calculations of the electronic structure of O_3 were impossible 10 years ago but have become quite feasible nowadays. Furthermore, according to new experimental information [7, 8], the surface must be somewhat deeper, $D_e = 1.143 \, \text{eV}$. Clearly, there is an opportunity and a need of improving the existing PES of ozone.

During the last decade several attempts have been made [8–10] to assess the level of theory needed to construct an accurate PES of O₃ and obtain correct value of the dissociation energy without any empirical corrections, directly from the *ab initio* calculations. The main conclusion from the previous work was that the most important effect is due to the basis set size. It was also suggested that extrapolation to the complete basis set (CBS) limit might be necessary. In this paper we use new *ab initio* results obtained at the icMRCI+Q/CBS level of theory using CASSCF(12,9). Extrapolation to the CBS limit is done based on calculations with aug-cc-pVQZ and aug-cc-pV5Z basis sets at every point of the PES. Details of the electronic structure calculations will

be reported elsewhere [11]; here the focus is on construction of the accurate global analytic fit of the *ab initio* data points.

The problem is twofold. First, the ab initio points are still very expensive computationally. At the level of theory indicated above, the CPU time per point is about 5 hours. If the old method is employed (which is building a spline of data on a structured 3D grid), the number of points required is on order of 6,000. Simple math tells us that such calculations are still quite expensive. Furthermore, incorporation of larger active space and inclusion of spinorbit correction would further increase the computational cost, quite dramatically. Thus, reduction of the number of points computed ab initio is highly desirable. Second, the potential energy surface of ozone is rather complicated. In addition to the deep covalent well, it contains a shallow van der Waals (vdW) well in the asymptotic region of the PES. The vdW well is separated from the main well by a reef-like structure with top of the reef slightly below the dissociation threshold. Accurate reproduction of these features by the fitting function is highly desirable, because they are expected to affect the dynamics and spectroscopy of ozone.

The ozone molecule contains three electronically identical atoms, and its PES possesses the corresponding symmetry. It is wise to utilize this symmetry in order to construct an efficient and accurate analytic representation of the PES. We found that the fitting approach of Braams and Bowman [12] allows obtaining accurate representation of ozone PES with as few as 500–600 data points. If such small number of points is indeed sufficient, the electronic structure calculations can be carried out at a very high level of theory, which offers a very attractive method of building accurate PES of ozone and other highly symmetric molecules.

Note that the fitting approach of Braams and Bowman [12] does not require a structured grid. The data points can be anywhere on the PES. In this work we propose a simple and general method for generating a small set of optimally placed points. Two reasonable criteria for choosing good points are (a) minimizing RMS of the global fit and (b) emphasizing most important parts of the PES (e.g., the minimum of the well, or the transition state).

The paper is organized as follows. In Section 2 we give details of the fitting approach. Section 3 describes the procedure we used for generating a small set of pre-optimized data points for the following *ab initio* calculations. Results of the calculations are presented and discussed in Section 4. Conclusions are given in Section 5.

2. The Fitting Method

The fitting method used in this study has been introduced by Braams and Bowman [12] for treatment of larger polyatomic molecules, with up to 10 atoms. Their approach uses basis functions that are invariant with respect to permutations of identical atoms. To the best of our knowledge it has not yet been applied to fit the PES of a homonuclear triatomic molecule which represents, at the same time, the smallest and the most symmetric polyatomic molecule. In what follows we give details of this approach as applied to molecules involving three identical atoms, such as ozone molecule.

The first step is transformation from the set of three internuclear distances $r_{ij} = \{r_{12}, r_{23}, r_{31}\}$ to the set of three *Morse variables* $y_{ij} = \{y_{12}, y_{23}, y_{31}\}$ defined as

$$y_{ij} = \exp\left(-\frac{r_{ij}}{\lambda}\right). \tag{2}$$

Here y_{ij} is the Morse variable for the pair of *i*th and *j*th atoms; λ is a fixed parameter that possesses units of length and depends on the system. The choice of this parameter for ozone is described in the next section.

Using the Morse variables, the fitting function is expressed by the following expansion:

$$V_{\text{fit}}(y_{12}, y_{23}, y_{31}) = \sum_{i=0}^{J} V^{(i)}(y_{12}, y_{23}, y_{31}),$$
 (3)

where *J* is order of the polynomial fitting function. The explicit forms for the first five terms of this expansion are:

$$V^{(0)}(y_{12}, y_{23}, y_{31}) = C_{0},$$

$$V^{(1)}(y_{12}, y_{23}, y_{31}) = C_{1} \cdot [y_{12} + y_{23} + y_{31}],$$

$$V^{(2)}(y_{12}, y_{23}, y_{31}) = C_{2a} \cdot [y_{12} + y_{23} + y_{31}]^{2} + C_{2b} \cdot [y_{12}y_{23} + y_{23}y_{31} + y_{31}y_{12}],$$

$$V^{(3)}(y_{12}, y_{23}, y_{31}) = C_{3a} \cdot [y_{12} + y_{23} + y_{31}]^{3} + C_{3b} \cdot [y_{12} + y_{23} + y_{31}] + y_{31}y_{12}] + C_{3c} \cdot [y_{12}y_{23}y_{31}],$$

$$V^{(4)}(y_{12}, y_{23}, y_{31}) = C_{4a} \cdot [y_{12} + y_{23} + y_{31}]^{4} + C_{4b} \cdot [y_{12} + y_{23} + y_{31}]^{2} + C_{4c} \cdot [y_{12}y_{23}y_{31}] \cdot [y_{12} + y_{23} + y_{31}] + C_{4d} \cdot [y_{12}y_{23} + y_{23}y_{31} + y_{31}y_{12}]^{2},$$

$$V^{(5)}(y_{12}, y_{23}, y_{31}) = C_{5a} \cdot [y_{12} + y_{23} + y_{31}]^{5} + C_{5b} \cdot [y_{12} + y_{23} + y_{31}]^{5} + C_{5b} \cdot [y_{12} + y_{23} + y_{31}]^{3} + C_{5c} \cdot [y_{12} + y_{23} + y_{31}]^{2} + C_{5c} \cdot [y_{12} + y_{23} + y_{31}]^{2} + C_{5c} \cdot [y_{12} + y_{23} + y_{31}] + C_{5d} \cdot$$

Here C_0 is the zero-order coefficient, C_1 is the first-order coefficient, the triplet $\{C_{2a}, C_{2b}, C_{2c}\}$ represents a set of second-order coefficients, and so on. The functions $V^{(j)}(y_{12}, y_{23}, y_{31})$ are called monomials of jth order, because each of them contains only the terms of order j.

Equations (4) above show that the PES is expressed using various products of three permutationally invariant terms, namely, the first-order term,

$$p_1 = y_{12} + y_{23} + y_{31}, (5)$$

the second order term,

$$p_2 = y_{12}y_{23} + y_{23}y_{31} + y_{31}y_{12}, (6)$$

and the third order term,

$$p_3 = y_{12} y_{23} y_{31}. (7)$$

All possible products of these permutationally invariant terms are included in Equations (4) to build the permutationally invariant function $V_{\rm fit}(y_{12},y_{23},y_{31})$ for fitting the PES. Using notations of (5)–(7) this function can be reexpressed in the following useful form:

$$V_{\text{fit}}(p_{1}, p_{2}, p_{3})$$

$$= C_{0}p_{1}^{0}p_{2}^{0}p_{3}^{0}$$

$$+ C_{1}p_{1}^{1}p_{2}^{0}p_{3}^{0}$$

$$+ C_{2a}p_{1}^{2}p_{2}^{0}p_{3}^{0} + C_{2b}p_{1}^{0}p_{2}^{1}p_{3}^{0}$$

$$+ C_{3a}p_{1}^{3}p_{2}^{0}p_{3}^{0} + C_{3b}p_{1}^{1}p_{2}^{1}p_{3}^{0} + C_{3c}p_{1}^{0}p_{2}^{0}p_{3}^{1}$$

$$+ C_{3a}p_{1}^{3}p_{2}^{0}p_{3}^{0} + C_{3b}p_{1}^{1}p_{2}^{1}p_{3}^{0} + C_{3c}p_{1}^{0}p_{2}^{0}p_{3}^{1}$$

$$+ C_{4a}p_{1}^{4}p_{2}^{0}p_{3}^{0} + C_{4b}p_{1}^{2}p_{2}^{1}p_{3}^{0} + C_{4c}p_{1}^{1}p_{2}^{0}p_{3}^{1}$$

$$+ C_{4d}p_{1}^{0}p_{2}^{2}p_{3}^{0}$$

$$+ C_{5a}p_{1}^{5}p_{2}^{0}p_{3}^{0} + C_{5b}p_{1}^{3}p_{2}^{1}p_{3}^{0} + C_{5c}p_{1}^{2}p_{2}^{0}p_{3}^{1}$$

$$+ C_{5d}p_{1}^{1}p_{2}^{2}p_{3}^{0} + C_{5c}p_{1}^{0}p_{2}^{1}p_{3}^{1}.$$
(8)

The way in which the terms of (8) are combined is quite clear—according to their order, which also gives a natural method for truncating the expansion. The terms p_1^0 , p_2^0 , and p_3^0 are, of course, equal to unity but are included in (8) explicitly in order to emphasize the general structure of this expression. Namely, the term of each order contains all possible monomials of this order that can be formed from p_1 , p_2 , and p_3 . The relationship between the polynomial order J and the number of adjustable coefficients in the overall expansion, M, is given in Table 1.

Assume that the number of molecular geometries (the *ab initio* data points) used to construct the fit is N. Vector \mathbf{V} of length N is introduced that contains the values of *ab initio* energies at these points. Vector $\mathbf{V}_{\mathrm{fit}}$ of length N is introduced that contains the values of fit at these points. We also introduce vector \mathbf{C} of length M that contains a set of fitting coefficients for the polynomial of order J. Finally, the matrix \mathbf{A} of the size N-by-M is introduced that allows

obtaining values of the fit at the data points from the matrixvector product:

$$\mathbf{V}_{\mathrm{fit}} = \mathbf{AC}.$$
 (9)

The structure of matrix **A** follows directly from (8) above. Namely, the elements of matrix **A** can be expressed as:

$$A_{nm} = p_1^{\ell_1} p_2^{\ell_2} p_3^{\ell_3}, \tag{10}$$

where index n labels data points and defines p_1 , p_2 , and p_3 according to (5)–(7), while index m labels the terms of expansion in (8) and defines a set of powers ℓ_1 , ℓ_2 , and ℓ_3 . As introduced above, $1 \le n \le N$ and $1 \le m \le M$. For each given order of expansion j, a set of three powers in (10) has to satisfy the following monomial condition:

$$\ell_1 + 2\ell_2 + 3\ell_3 = j. \tag{11}$$

As introduced above, $0 \le j \le J$. This relation is illustrated in Table 2, where we listed all allowed sets of powers for orders up to the 5th. Using this approach the elements of matrix **A** can be easily generated for any set of data points and any order of the fitting polynomial.

Next, the deviation between the fitting function and the *ab initio* energies at the data points is minimized,

$$\min \|\mathbf{V} - \mathbf{AC}\|,\tag{12}$$

by finding the appropriate values of **C**. This can be formulated as a linear least squares fitting problem. In our numerical implementation, this problem is solved using subroutine DGELS of the LAPACK library [13]. Accuracy of the fit is measured by the root mean square (RMS) deviation defined as

RMS =
$$\frac{1}{N} \sum_{n=1}^{N} \sqrt{[V(n) - V_{\text{fit}}(n)]^2},$$
 (13)

with V(n) being the *ab initio* energy at the point n and $V_{\rm fit}(n)$ being the value of the fit at the same point, obtained from (8). This RMS deviation characterizes global quality of the fit. The local quality of the fit for each point n is given by the absolute deviation:

$$\Delta(n) = |V(n) - V_{\text{fit}}(n)|. \tag{14}$$

A FORTRAN subroutine has been developed to determine a set of adjustable coefficients \mathbf{C} for any given set of N data points and any given order J of the fitting function. This subroutine is general and can be used for any homonuclear triatomic molecule.

In addition to the internuclear distances $\{r_{12}, r_{23}, r_{31}\}$ and the Morse variables $\{y_{12}, y_{23}, y_{31}\}$, we extensively use one more set of the internal coordinates for the triatomic molecule: $\{\rho, \theta, \phi\}$ —the adiabatically adjusting principal axes hyperspherical (APH) coordinates [14]. These coordinates are not used in the fitting procedure, but they are very handy for graphical representation of the surface. Thus, the hyperradius ρ is used as an abscissa in Figures 1, 3 and 4 below. The full set of ρ, θ , and ϕ is used in Figure 5.

TABLE 1: The number of adjustable coefficients, M, versus the polynomial order, I	TABLE 1:	The number	of adjustable	coefficients, M	, versus the po	olynomial order, I.
---	----------	------------	---------------	-----------------	-----------------	---------------------

J	10	11	12	13	14	15	16	17	18	19	20
M	67	83	102	123	147	174	204	237	274	314	358

Table 2: Allowed values of the powers for various monomial terms, up to 5th order.

Manamial andan i	Coefficient		Powers		
Monomial order <i>j</i>	Coefficient	ℓ_1	ℓ_2	ℓ_3	
0	C_0	0	0	0	
1	C_1	1	0	0	
2	C_{2a}	2	0	0	
	C_{2b}	0	1	0	
	C_{3a}	3	0	0	
3	C_{3b}	1	1	0	
	C_{3c}	0	0	1	
	C_{4a}	4	0	0	
4	C_{4b}	2	1	0	
7	C_{4c}	1	0	1	
	C_{4d}	0	2	0	
	C_{5a}	5	0	0	
	C_{5b}	3	1	0	
5	C_{5c}	2	0	1	
	C_{5d}	1	2	0	
	C_{5e}	0	1	1	

Working with the APH coordinates, it is useful to remember that the small-amplitude motion along the hyper-radius ρ correlates with the symmetric stretching normal mode, while the large-amplitude motion along ρ describes dissociation, process (1). Small-amplitude motion along ϕ correlates with the asymmetric stretching normal mode, while the large-amplitude motion along ϕ describes pseudorotation [14]. The hyperangle θ correlates with the bending normal mode.

3. Generating Small Set of Preoptimized Points

Quite often, even before we start the computationally expensive *ab initio* calculations, we do already have some preliminary information about the PES. This information may come from the experiment (e.g., equilibrium structure, harmonic frequencies, dissociation energy), from the empirical forcefield or from the computationally inexpensive electronic structure calculations (e.g., CASPT2). In the case of ozone, we have an old surface [3], and we want to take full advantage of this information in order to minimize the number of points needed to construct an accurate fit.

Using the old surface of ozone [3], we experimented with polynomials of different orders, with different values of λ , and with different number of points in the data set. The polynomial of 16th order with $\lambda = 1.75$ Bohr was chosen. Such polynomial contains M = 204 adjustable parameters. We found that, when the number of data points

is around N = 500, the polynomial of 16th order has enough flexibility to reproduce all features of the complicated ozone PES, without showing artificial oscillations. Polynomials of lower-orders were not flexible enough and exhibited higher RMS deviations. Polynomials of higher-orders were more successful in fitting the data, but they showed artificial oscillations in the regions of sparse points. We searched for solution of this problem and found that the undesirable oscillations of the high order polynomials could be reduced by adding more data points. Finally, we have chosen to proceed with a small set of points, about 500, and the polynomial function of 16th order. The choice of number 500 was, of course, somewhat arbitrary. In what follows we will call these points the *fitting set*.

Next, we tried to find a way of choosing positions of points of the fitting set in a more or less optimal way with the purpose of obtaining the most accurate representation, by the polynomial of 16th order, of the relevant part of the PES. For our purposes (reaction dynamics at thermal energies) most relevant is the low energy part of the PES. Using the old surface we generated a very dense 3D grid of points in the configuration space. Points at energies higher than 0.2 eV above the dissociation threshold were removed as irrelevant, leaving approximately half million points in what we will call the reference set. The reference set of points is discrete, but, since it is very dense, it approximates reasonably well the continuous configuration space. At the first step the 500 points of the fitting set were placed randomly in the relevant part of the configuration space. Then we moved points of the fitting set, literally one by one, to new positions making sure that each such move maximizes accuracy of the surface representation. Accuracy of the surface representation was characterized by the RMS deviation between the fit and the old surface (computed using the reference set of points). Each possible position of the fitting point was evaluated by refitting the corresponding set of 500 fitting points and calculating the corresponding RMS deviation of the fit. The position that gives smallest RMS deviation was chosen, and the point was moved into that new position, after which the procedure was applied to the next point of the fitting set, and the next.

This procedure does not have to stop after all 500 points of the fitting set have been moved to new better positions. We tried to reiterate the whole set again and again, until the "memory" of the initial (arbitrary) placement of the fitting points has been lost.

Figures 1 and 2 illustrate this procedure. Figure 1(a) shows initial positions of the 500 fitting points in the configuration space. In this example the initial placement of points was intentionally done in the worst possible way. All points sit very close to each other in one remote region of the PES. Coverage of the configuration space is minimal, and the RMS deviation of the fit is huge, close to $5 \times 10^{12} \, \mathrm{cm}^{-1}$.

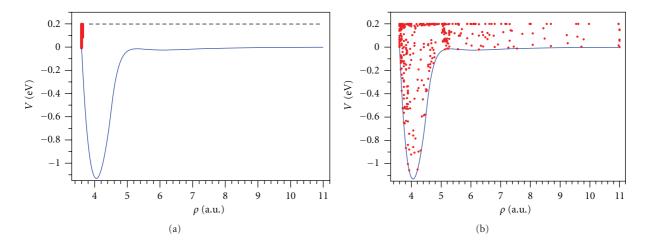


FIGURE 1: Illustration of the preoptimization procedure using the old surface of ozone. The MEP is shown as blue curve. The covalent well and the vdW well are seen. Horizontal axis gives the internal hyperradial coordinate ρ of O₃. The cut-off energy is shown by dashed line. The 500 data points are shown as red dots: (a) the initial placement of points according to the worst case scenario, (b) the final optimized set of points obtained after 5,000 iterations.

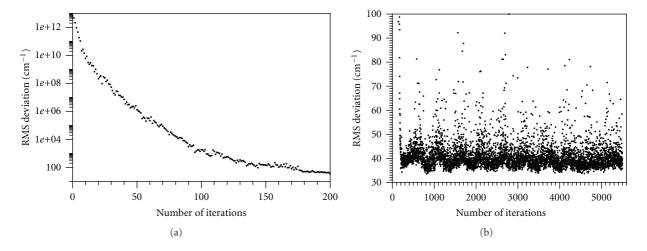


FIGURE 2: Improvement of the RMS deviation of the fit during the preoptimization procedure carried out using the old surface of ozone: (a) during the first 200 iterations (note the exponential scale), (b) during the 5,000 iterations, when the set of 500 fitting points is reoptimized 10 times. The gradual loss of memory of the initial placement of points is clearly seen.

Figure 2(a) shows that as points are moved one by one to their new better positions, the RMS deviation of the fit drops very quickly, roughly exponentially. After 200 points have been moved, the exponential fall regime transforms into an almost horizontal line regime, where the RMS deviation of the fit fluctuates in the range between 33 and $50\,\mathrm{cm}^{-1}$. Figure 2(b) shows that further iterations do not really improve the RMS deviation of the fit, but they promote the loss of "memory" of the initial placement of points. Figure 1(b) shows the final distribution of fitting points in the configuration space. Note that the final distribution of points in Figure 1(b) is not uniform. Some emphasis on the high energy part of the PES is clearly present, which means that this part of the PES is harder to fit accurately, compared to the well region at low energies. Some emphasis of the reef

region is also seen. This final fitting set is characterized by the RMS deviation of 36.0 cm^{-1} .

In order to characterize quality of the analytic fit itself, we computed the RMS deviation between the fitting function and the 500 data points of the fitting set. This value was only $33.0 \, \text{cm}^{-1}$.

One interesting observation that follows from the numerical experiments described above is that moving only a small number of points is sufficient in order to reduce the RMS deviation to a relatively low value. Further moves do not necessarily improve the RMS deviation. For example, in the worst case scenario presented in Figures 1 and 2, it was sufficient to move the first 200 points. In the less extreme tests we conducted, when the initial coverage was close to the uniform, we saw that moving about 100 points was enough.

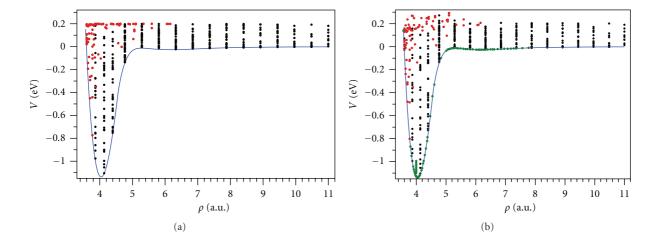


FIGURE 3: Illustration of partial preoptimization employed for accurate description of the asymptotic region. The fixed 400 points are shown by black dots. The optimized 100 points are shown by red dots. (a) Energies from the old PES, (b) Energies obtained in this work at the CBS level. The additional 70 points placed in the critical parts of the PES *a posteriori* are shown by green dots. The corresponding MEPs are shown by blue lines.

One can ask the question: would it be possible to use just those first 100 points and construct an accurate fit of the PES? The answer is no. We need more points than fitting coefficients, and our tests showed that the fitting function of 16th order is smooth only if we use about 500 points or more.

Detailed inspection of the final fit showed that although the covalent well was reproduced reasonably well, the fit of the MEP in the region of the vdW well was not really acceptable. Indeed, from Figure 1(b), we see that only a small number of fitting points ended up in the vdW region of the PES. In order to describe this part of the PES more accurately, one has to force the points to move into this part of PES, and cover it thoroughly, even if the RMS deviation of the global fit is not improved by such placement of points. This can be done, for example, by associating different fitting weights with different regions of the PES and we tried this approach. Another approach is to manually cover the asymptotic part of the PES with fitting points and forbid those points to move out. We found that this second method is easier to implement and ended up with the algorithm described in the next paragraph.

Based on the fact that moving just 100 points allows minimizing the RMS deviation of the fit, we spilt the set of 500 points onto two groups. The first 400 points were placed throughout the configuration space quasi-randomly (using a very sparse grid in the hyperspherical coordinates) and were not allowed to move. In Figure 3(a), these points are shown in black. About 80% of these points belong to the vdW region, while the 20% of them describe the main well. Positions of the remaining 100 points were optimized, using the method described above, in order to reduce the RMS deviation of the fit. Their final positions are shown in Figure 3(a) in red. The resultant RMS deviation between the fit and the reference set was 36.4 cm⁻¹. The RMS deviation between the fit and the fitting set of 500 points was only 36.0 cm⁻¹. These numbers are slightly higher (~9%)

compared to the case when all 500 points were optimized, but sacrificing slightly the global RMS deviation of the fit allows reproducing much better the vdW well region of the PES.

We would like to call a set of points obtained in this way a *preoptimized* set of points, because the points optimized using preliminary version of PES may not be equally optimal for the new accurate PES. However, it is obvious that preoptimizing a set of points is better than using an arbitrarily chosen set of points, especially if the *ab initio* calculations are computationally expensive.

We have to stress again that our pre-optimization procedure was carried out using the old surface of O₃, without doing any new *ab initio* calculations. The data points from the old surface are basically free, which allowed us to use them so liberally (i.e., repeatedly move points to new positions disregarding the old ones). We have to admit that if the old PES would not exist (which may be the case for new molecules), one option would be to actually compute points during pre-optimization. This would make the pre-optimization procedure more demanding computationally and would probably require employing more elegant approach to optimization, such as the steepest descend method.

Finally, the preoptimized set of points was used to carry out new *ab initio* calculations and construct new PES of ozone.

4. Results and Discussion

All *ab initio* calculations were carried out using, MOLPRO suite of the electronic structure codes [15]. The level of theory was icMR-CISD+Q using the CASSCF(12,9) active space. At each point of the PES, we carried out two independent calculations: first with aug-cc-pVQZ and second with aug-cc-pV5Z basis sets. Then, for each point of the PES, we

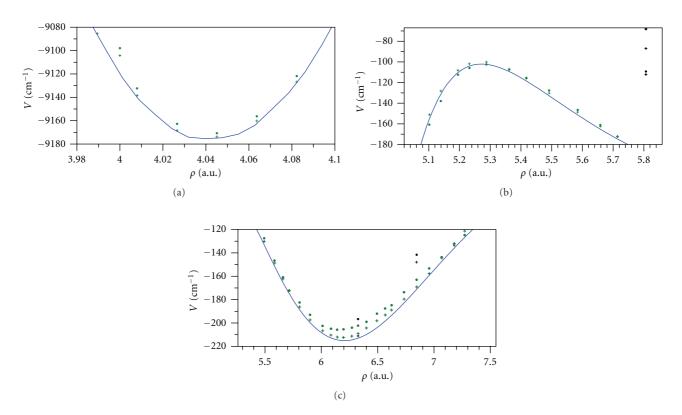


FIGURE 4: Three critical regions of new PES of ozone: (a) at the bottom of the covalent well, (b) near the top of the reef, (c) along the vdW well. The MEP is shown as blue line. Filled symbols show the data points; pluses show the values of the fit at these points. Deviations are small. Green color is used for points added to the fitting set *a posteriori*.

made extrapolation to the CBS limit using the following extrapolation formula [10]:

$$V_{\text{CBS}} = \frac{V_{\text{aug-cc-pvqz}} \cdot 4^3 - V_{\text{aug-cc-pv5z}} \cdot 5^3}{4^3 - 5^3}.$$
 (15)

The resultant value of the dissociation energy at the CBS limit is $D_{\rm e}=1.135\,{\rm eV}$, which is 871 cm⁻¹ higher than the dissociation energy of the old surface [1, 2]. This represents a dramatic improvement. New theoretical value of the dissociation energy is only 65 cm⁻¹ (8 meV) lower compared to the recent experimental value [7, 8].

We also tried calculations with aug-cc-pV6Z basis sets and made extrapolation based on the aug-cc-pV5Z and the aug-cc-pV6Z data. We found, however, that this adds only 3 meV (about 24 cm⁻¹) to the dissociation energy of ozone and decided not to follow this path. Calculations with larger active space CASSCF(18,12) and with incorporation of the spin-orbit correction are ongoing and will be reported elsewhere [11].

New data points at the CBS limit are shown in Figure 3(b). By comparing energies of the pre-optimized set of points (old PES, Figure 3(a)) to the set of new points computed in this work (Figure 3(b)), one can easily see that the two PESs are somewhat different, particularly in the regions above the well and in the vicinity of the transition state.

The CBS data points were fitted by the permutationally invariant polynomial of 16th order as explained in Section 2. The RMS deviation of the resultant fit was 26 cm⁻¹ which is,

in fact, slightly lower than the RMS deviation seen at the preoptimization step (Section 3). This result is quite encouraging and supports the idea (and efficiency) of pre-optimizing a set of data points prior to the massive *ab initio* calculations.

For the new analytic PES, we determined the MEP using the Newton-Raphson minimization method [16]. We inspected the MEP and found that, in its vicinity, the typical deviation of the fit from the data points was about 25 cm⁻¹, close to the global RMS deviation. We concluded that new surface can benefit from adding more points to the vicinity of the MEP. Note that the fitting method of Braams and Bowman [12] allows adding points to the fitting set a posteriori. Refitting an upgraded set of the data points is straightforward. We tried to add 4 points in the range of small values of ρ , 30 points close to the bottom of the covalent well, 14 points near the reef, and 22 points along the bottom of the vdW well—about 70 new points total. These additional points are shown in Figure 3(b) in green. Refitting the whole set of N = 570 points gave even better global RMS deviation of 22 cm⁻¹ and resulted in a much better description of the PES along the MEP. The final MEP is shown in Figure 3(b).

Detailed views of three critical regions of new PES are given in Figure 4. Figure 4(a) shows the bottom of the covalent well, while Figure 4(b) shows the reef and Figure 4(c) shows the vdW well. In these figures the minimum energy path is shown by the solid line, the values of *ab initio* energies at the data points are shown by filled symbols, while the

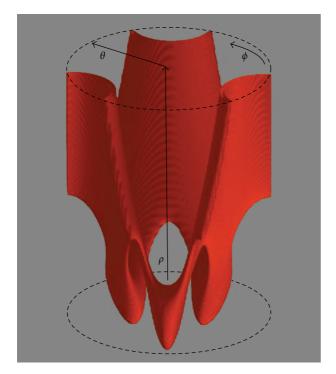


FIGURE 5: Global view of the ozone PES in three dimensions using the isoenergy surface at 0.2 eV and the internal hyperspherical coordinates $\{\rho,\theta,\phi\}$. The threefold symmetry is clearly seen. Each covalent well (at the bottom) is connected to two dissociation channels (at the top) through the narrow transition states. See text for details.

values of analytic fit at the data points are shown using plussigns. Deviations of the fit from the data are about 3 cm⁻¹ near the bottom of the covalent well, only 2 cm⁻¹ near the top of the reef, and about 7 cm⁻¹ near the bottom of the vdW well. These numbers demonstrate excellent accuracy of the analytic representation of the PES. On this new PES, the top of the reef is 102 cm⁻¹ below the dissociation threshold; the vdW well is 215 cm⁻¹ deep.

In Figure 5 we show an isoenergy surface for the PES of ozone in three dimensions. In this approach to PES visualization, the configuration space where the potential energy of the molecule is higher than a given cut-off value (here 0.2 eV above the dissociation threshold) is made transparent, while the configuration space classically accessible to the motion of nuclei at this energy is made visible as a 3D structure. The APH hyperspherical coordinates $\{\rho, \theta, \phi\}$ are used [14] in order to emphasize symmetry of the PES. The range of hyperradius in Figure 5 is the same as in Figure 3, namely, $3.5 < \rho <$ 11 Bohr. Recall that the hyperangles θ and ϕ correlate with bending and asymmetric stretching motions, respectively. Note that, due to the permutation symmetry of ozone, there are three identical covalent wells in the entire configuration space, which can be reached by changing the value of ϕ . Those are seen as three ellipsoidal-like lobes in the lower part of Figure 5. They are connected to three identical dissociation channels seen in the upper part of Figure 5. The reef structures discussed above (the transition states) are seen on

this picture as narrow bottlenecks connecting each covalent well to two dissociation channels. Figure 5 gives global view of the PES and permits seeing all its features simultaneously. We also see that fitting by the permutationally invariant polynomial function takes full advantage of symmetry of the molecule.

5. Conclusions

The approach of fitting the ab initio data by the permutationally invariant polynomial functions allows constructing accurate global PESs of symmetric molecules using relatively small number of points. Several features of the method contribute to reduction of the number of data points. First of all, analytic form of the fitting function takes the full advantage of symmetry and uses most efficiently every point computed ab initio. Redundant coverage of the configuration space is avoided. Second, this approach allows focusing on the most important part of the PES (here low energies) and avoids placing points into the irrelevant regions. Indeed, the high-energy regions of PESs are not only irrelevant to dynamics or spectroscopy but also harder to characterize ab initio. Third, the approach allows adding ab initio points one by one to the most important regions of the PES in order to improve representation of the surface there. This is very useful since in chemistry the transition state point is, usually, the most important. Finally, positions of the data points in the configuration space can be efficiently pre-optimized using available theoretical or experimental information. In our case an older PES of ozone was extremely useful.

It is true that such complete information as an older PES may not be available for every molecule in the nature, but for many important molecules the older PESs do exist. If unavailable, an approximate PES can be constructed using experimental data or the *ab initio* calculations at a reduced level of theory. In fact, the permutationally invariant polynomials of low order can be employed to construct an approximate PES quickly, since they contain very small number of fitting parameters (see Table 1) and require very few data points.

Acknowledgments

Joel Bowman and Bas Braams at Emory University are gratefully acknowledged for their invaluable advice on adopting the fitting approach. D. Babikov acknowledges support as Visiting Fellow at Emerson Center for Scientific Computation, Emory University. Qadir Timerghazin at Marquette University is acknowledged for his help in setting up the electronic structure calculations. This research was partially supported by the NSF Atmospheric Chemistry Program, grant number 0842530, and partially by the Air Force Office of Scientific Research, grant number FA9550-09-1-0604. We used resources of the National Energy Research Scientific Computing Center, which is supported by the Office of Science of the US Department of Energy under Contract no. DE-AC02-05CH11231.

References

- [1] R. Siebert, R. Schinke, and M. Bittererová, "Spectroscopy of ozone at the dissociation threshold: quantum calculations of bound and resonance states on a new global potential energy surface," *Physical Chemistry Chemical Physics*, vol. 3, no. 10, pp. 1795–1798, 2001.
- [2] R. Siebert, P. Fleurat-Lessard, R. Schinke, M. Bittererová, and S. C. Farantos, "The vibrational energies of ozone up to the dissociation threshold: dynamics calculations on an accurate potential energy surface," *Journal of Chemical Physics*, vol. 116, no. 22, pp. 9749–9767, 2002.
- [3] D. Babikov, B. K. Kendrick, R. B. Walker, R. T. Pack, P. Fleurat-Lesard, and R. Schinke, "Metastable states of ozone calculated on an accurate potential energy surface," *Journal of Chemical Physics*, vol. 118, no. 14, pp. 6298–6308, 2003.
- [4] R. Hernandez-Lamoneda, M. R. Salazar, and R. T. Pack, "Does ozone have a barrier to dissociation and recombination?" *Chemical Physics Letters*, vol. 355, no. 5-6, pp. 478–482, 2002.
- [5] P. Fleural-Lessard, S. Y. Grebenshchikov, R. Siebert, R. Schinke, and N. Halberstadt, "Theoretical investigation of the temperature dependence of the O+O2 exchange reaction," *Journal of Chemical Physics*, vol. 118, no. 2, pp. 610–621, 2003.
- [6] M. W. Chase Jr., C. A. Davies, J. R. Downey Jr., D. J. Frurip, R. A. McDonald, and A. N. Syverud, "JANAF thermochemical tables, third edition," *Journal of Physical and Chemical Reference Data*, vol. 14, supplement 1, 1985.
- [7] B. Ruscic, "Unpublished results obtained from active thermochemical tables (ATcT) based on the core (Argonne) thermochemical network," version 1.110; 2010.
- [8] F. Holka, P. G. Szalay, T. Müller, and V. G. Tyuterev, "Toward an improved ground state potential energy surface of ozone," *Journal of Physical Chemistry A*, vol. 114, no. 36, pp. 9927– 9935, 2010.
- [9] M. Tashiro and R. Schinke, "The effect of spin-orbit coupling in complex forming O(3P) + O2 collisions," *Journal of Chemical Physics*, vol. 119, no. 19, pp. 10186–10193, 2003.
- [10] R. Schinke and P. Fleurat-Lessard, "The transition-state region of the O(3P)+O2(3∑g-) potential energy surface," *Journal of Chemical Physics*, vol. 121, no. 12, pp. 5789–5793, 2004.
- [11] M. Ayouz and D. Babikov, unpublished.
- [12] B. J. Braams and J. M. Bowman, "Permutationally invariant potential energy surfaces in high dimensionality," *Interna*tional Reviews in Physical Chemistry, vol. 28, no. 4, pp. 577– 606, 2009.
- [13] LAPACK, "Linear algebra package, version 3.3.1," *Netlib*, http://www.netlib.org/lapack/.
- [14] D. Babikov, P. Zhang, and K. Morokuma, "Cyclic-N3. I. An accurate potential energy surface for the ground doublet electronic state up to the energy of the2A 2/2B1 conical intersection," *Journal of Chemical Physics*, vol. 121, no. 14, pp. 6743–6749, 2004.
- [15] H.-J. Werner, P. J. Knowles, R. Lindh et al., "MOLPRO, a package of *ab initio* programs," version 2009.1.
- [16] W. H. Press, S. A. Teukolsky, W. T. Vetterling, and B. P. Flannery, *Numerical Recipes*, Cambridge University Press, Cambridge, UK, 3rd edition, 2007.

Review Article

Potential Energy Surface of NO on Pt(997): Adsorbed States and Surface Diffusion

N. Tsukahara¹ and J. Yoshinobu²

 $^{1} Department \ of \ Advanced \ Material \ Sciences, \ The \ University \ of \ Tokyo, \ Kashiwa, \ Chiba \ 277-8561, \ Japan \ Sciences \ Advanced \ Material \ Sciences \ The \ University \ of \ Tokyo, \ Kashiwa, \ Chiba \ 277-8561, \ Japan \ Sciences \ Advanced \ Material \ Sciences \ The \ University \ One \ Science \ The \ University \ One \ Science \ The \ University \ One \ Tokyo, \ The \ University \ One \ One \ The \ University \ One \ On$

Correspondence should be addressed to J. Yoshinobu, yoshinobu@issp.u-tokyo.ac.jp

Received 31 May 2011; Revised 3 August 2011; Accepted 7 August 2011

Academic Editor: António Varandas

Copyright © 2012 N. Tsukahara and J. Yoshinobu. This is an open access article distributed under the Creative Commons Attribution License, which permits unrestricted use, distribution, and reproduction in any medium, provided the original work is properly cited.

The potential energy surface (PES) of NO on Pt(997) has been elucidated: the adsorption states and diffusion processes of NO on Pt(997) at low coverage were investigated by using infrared reflection absorption spectroscopy (IRAS) and scanning tunneling microscopy (STM). When NO molecules adsorb on a surface at a low temperature (11 K), each molecule transiently migrates on the surface from the first impact point to a possible adsorption site. We found that there are four stable adsorption sites for NO on Pt(997): a bridge site of the upper step, an fcc- (or hcp-) hollow site of the terrace, an on-top site of the terrace, and an fcc-hollow site of the lower step. At higher temperatures above 45 K, NO molecules start to migrate thermally to more stable adsorption sites on a terrace, and they are finally trapped at the bridge sites of the step, which are the most stable among the four sites.

1. Introduction

The elucidation of potential energy surface (PES) of adsorbed molecules on metal surfaces is quite important. In particular, surface diffusion of adsorbed atoms and molecules plays a vital role in various surface dynamical processes, such as heterogeneous chemical reactions, formation of self-assembled structures, and single atom manipulation by a scanning probe microscope [1]. Since an adsorbed molecule must encounter a reaction partner before a chemical reaction takes place, surface diffusion could be a rate-limiting process for surface chemical reactions. In particular, the adsorption of carbon monoxide (CO) and nitric monoxide (NO) on transition metal surfaces is a basic model for investigating the catalytic reaction on the automobile threeway catalyst, where the PES for CO and NO governs the migration of the molecules. Therefore, not only surface diffusion but also the adsorption states of CO and NO are important. So far, many studies of CO and NO on transition metal surfaces have been reported; NO adsorption on Pt(111) is one of the fundamental systems and there are many studies [2-10]. In addition, surface defects are often stable adsorption sites and active sites for NO dissociation

[11–13]. Therefore, the adsorption states and diffusion process of NO on a stepped Pt surface are even more important than that on a flat Pt surface.

In this review article, the adsorption states and the diffusion process of NO molecules on Pt(997) are discussed based on our recent investigations by infrared reflection absorption spectroscopy (IRAS) and scanning tunneling microscopy (STM).

Surface diffusion is classified into "thermal" and "transient" diffusion [1]. Thermal diffusion consists of stochastic site-to-site hopping motions of adsorbates driven by thermal fluctuation (Brownian motion). Based on Arrhenius-type rate theory, the hopping rate, k, is defined as follows:

$$k = A \exp\left(-\frac{E}{k_B T}\right),\tag{1}$$

where *E*, *T*, and *A* are the activation barriers to site-to-site hopping, substrate temperature, and preexponential factor, respectively. On the other hand, transient diffusion is the inevitable process upon adsorption [1, 14]. When an atom or a molecule is adsorbed on a surface, adsorption energy must be dissipated. Excitations of various vibrations of a

² The Institute for Solid State Physics, The University of Tokyo, Kashiwa, Chiba 277-8581, Japan

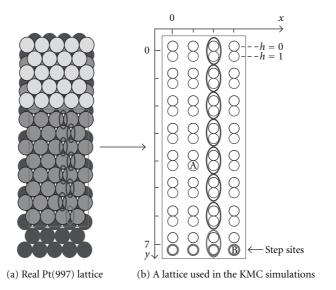


FIGURE 1: (a) A schematic drawing of Pt(997). (b) A lattice used in the present KMC simulation. The lattice size is about $280 \times 280 \text{ Å}^2$. Circles of thin lines represent the fcc- and hcp-hollow sites on the terrace, and circles of heavy lines represent the bridge sites on the step, respectively. Although the lattice of the (111) terrace is hexagonal, we virtually deformed the lattice into a tetragonal one to assign adsorption sites with Cartesian coordinates. The coordinates of adsorption sites on the terrace and the step are represented by (x, y, h, s) and (x, s), respectively. For example, the coordinates labeled "A" and "B" in the lattice are represented as (1, 4, 1, 0) and (3, 0), respectively [15].

substrate and an adsorbed molecule, electron-hole pair excitations, and transient motions of an adsorbate are possible dissipation paths. The transient diffusion is the translational migration of an adsorbate driven by its adsorption energy. This depends not on the substrate temperature, but on the interaction between adsorbates and the substrate. Energy dissipation of chemisorbed species is more efficient than that of physisorbed species because of the mixing of the electronic states in chemisorption. In addition, the PES of chemisorbed species is more complicated than that of physisorbed species. Therefore, chemisorbed species have a shorter diffusion length in transient diffusion than physisorbed species [1].

2. Experimental and Analysis Methods

All IRAS and STM experiments were carried out in an ultrahigh vacuum chamber. The base pressure of the chamber is less than 1×10^{-10} Torr.

A clean Pt(997) surface was carefully prepared by repeated cycles of Ne ion sputtering and annealing procedures in a preparation chamber. The Pt(997) surface has a periodic step-terrace structure (Figure 1(a)). The terrace has a (111) close-packed structure composed of nine rows of platinum atoms, and the monoatomic step is formed by a (111) microfacet. In the final cleaning procedure, the sample was exposed to 2×10^{-7} Torr O_2 with annealing at 1000 K to remove trace carbon contamination. Subsequently, the sample was flashed to 1300 K. The surface contaminations, mainly carbon, were reduced by repeated cycles of this oxidation procedure. The cleanness of the Pt(997) surface was confirmed by using low energy electron diffraction (LEED) and STM.

The sample was transferred to a measurement chamber in which the sample holder was connected to a liquid He/liquid $\rm N_2$ reservoir and surrounded by triple thermal shields. Gaseous NO molecules at 300 K ($k_BT\sim26$ meV) were introduced onto the cold sample surface through a pulse gas dosing system, at an angle of about 45° from the surface normal direction.

In IRAS measurements, the resolution and the number of accumulations were 4 cm⁻¹ and 500 scans, respectively. In time-resolved IRAS (TR-IRAS) measurements, the resolution was 4 cm⁻¹, the same as with the normal IRAS measurements. The measurement time of each spectrum was controlled by the number of accumulations. In this study, it was from 250 to 500 scans, which corresponds to a time increment from 50 to 100 s. When the valve of the pulse gas dosing system was opened, the time-resolved measurements were started, and a series of IRAS spectra were acquired as a function of the elapsed time. The exposure of NO molecules was controlled by the duration time of the pulse gas dosing system. The duration time (the open time of the valve) was in the order of ms (typically $2 \sim 5 \,\mathrm{ms}$) and much shorter than the measurement time. Details of the experiments are described in our previous papers [15–17].

In order to analyze the results of TR-IRAS in the range from 100 to 110 K, where the long range diffusion of NO across the terrace and the island formation occurs, Kinetic Monte Carlo (KMC) simulation was carried out. Here, the procedure of the present KMC simulation is described. The KMC simulation is performed with the lattice shown in Figure 1 with a periodic boundary condition. The migration of the adsorbed NO molecules is simulated using a lattice gas model [18, 19]. On the terraces and the steps, the arrays c(x, y, h, s) and $c_s(x, s)$ are defined, and the value of each

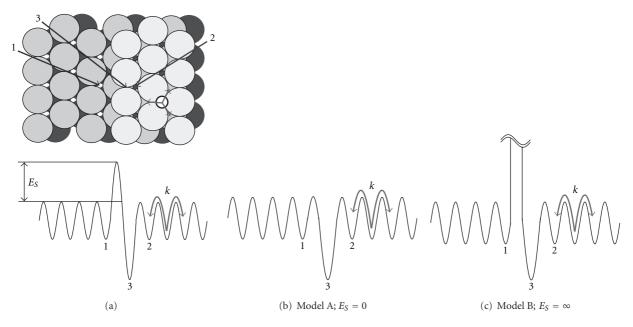


FIGURE 2: (a) A schematic drawing of Pt(997) around the step and its PES with ES barrier E_S . Sites 1, 2, and 3 are the HS site, HT site next to the BS site, and BS site, respectively. k is the NO does not adsorb, is the hcp-hollow site next to the HS site. k is the rate constant to migrate from a hollow site to a neighboring hollow site on the terrace. (b), (c) Models of PES in the KMC simulation. In model A, the rate constant from site 1 to site 3 is assumed to be the same as that from site 2 to site 3. In model B, the rate constant from site 1 to site 3 is assumed to be zero (infinite barrier).

element of the arrays is either 0 (empty) or 1 (occupied). In order to characterize the hopping processes of adsorbed NO, a rate constant k is assigned to each hopping motion. An NO molecule at a hollow site on the (111) terrace (HT species) migrates to a nearest neighbor HT site via a bridge site [13]. Therefore, the HT species has three nearest neighbors, meaning that three rate constants are required for one HT species. In this model, all the rate constants of hopping from the hollow to the nearest neighbor are assumed to be the same. A similar assumption was adopted in the previous study of CO on stepped Pt(111) surfaces [20–22].

In addition, the Ehrlich-Schwoebel (ES) effect [23, 24], which is shown in Figure 2, should be considered in the KMC simulation. If an atom or molecule approaches from a lower or an upper terrace to a step region, the PES across the step shows an asymmetric profile. In the case of CO on a stepped Pt(111) surface, a very large barrier on the route from a lower terrace to an upper step must be considered [20–22]. In order to incorporate the ES effect (Figure 2(a)) simply, two cases are considered: model A (Figure 2(b)) has no Schwoebel barrier, while model B (Figure 2(c)) has an infinite barrier. In model A, HT species on a lower terrace climb up to an upper step site. On the other hand, in model B, HT species on a lower terrace do not climb up to the upper step and are reflected by the ES barrier. Thus, the molecules can reach the step sites from one direction exclusively.

An adsorbate-adsorbate interaction was also taken into account in the simulation because HT species on Pt(111) form a $p(2 \times 2)$ structure [2–10]. Therefore, when they form the $p(2 \times 2)$ structure, energy modifications, which

are expressed by multiplying the rate constant k by a Boltzmann factor $\exp(-E_{\text{int}}/k_BT)$, must be considered. E_{int} is the interaction energy. The interaction is assumed only to be the factor lowering the potential energy minimum of the HT species [25–29]. In addition, all the rate constants whose processes reduce the distance between HT species to less than 5.54 Å are zero. This procedure represents the repulsive interaction between NO molecules. The value of 5.54 Å corresponds to the distance between hollow species in the $p(2 \times 2)$ structure on Pt(111).

The initial (t=0) distribution of NO molecules was determined stochastically. The details are described in our previous report [15]. Once the initial distribution was determined, repeated cycles of the standard KMC procedure were carried out until the elapsed time exceeded a preset value. In this study, 2000–100,000 cycles of the KMC step were carried out. Parameters r_s , k, and $E_{\rm int}$ were determined to fit the simulation with the experiment.

3. Adsorption States and Diffusion Kinetics

3.1. Adsorption States of NO Molecules on Pt(997). Figure 3 shows a series of IRAS spectra of NO molecules (0.017 ML) on Pt(997) as a function of substrate temperature. In Figure 3(a), four peaks are observed at 11 K. All peaks are derived from the stretching mode ν (N–O); there are four stable adsorption sites on Pt(997). Table 1 shows the assignment of the NO adsorption sites. The peaks at 1483 and 1689 cm⁻¹ are observed in the previous vibrational studies of NO on a flat Pt(111) at low temperatures and are assigned to the NO molecules at the threefold hollow

Adsorption site	ν(N–O)	(cm ⁻¹)	Adsorption energy (eV)	Abbreviation	
Adsorption site	Observed	Calculated*	rasorption energy (ev)	1001cviation	
Hollow (terrace)	1482 ~ 1484	1512 (fcc)	2.09 (fcc)	НТ	
Tionow (terrace)	1402 1404	1539 (hcp)	1.92 (hcp)	111	
On-top (terrace)	1689 ~ 1690	1683	1.61	OT	
Bridge (upper step)	1610 ~ 1630	1607	2.49	BS	
Hcp-hollow (lower step)	_	1188	0.87	_	
Fcc-hollow (lower step)	1385 ~ 1396	_	_	HS	

Table 1: Adsorbed states of NO on Pt(997). Observed and calculated energies are shown. *Details of DFT calculations are shown in our previous report [16].

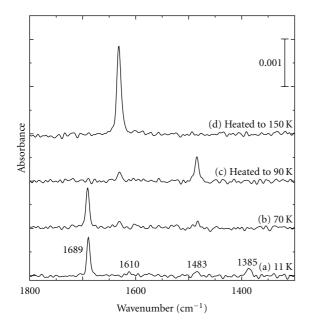


FIGURE 3: IRAS spectra of 0.017 ML NO on Pt(997) as a function of substrate temperature. (a) A spectrum after an NO gas injection at 11 K. (b) A spectrum after an NO gas injection at 70 K. (c) After heating the substrate from 70 K to 90 K, and cooling down to 70 K. (d) After heating the substrate from 70 K to 150 K, and cooling down to 70 K.

site and on-top site (HT and OT species) [6–10]. Other peaks at 1385 and 1610 cm⁻¹ have not been observed at NO on a flat Pt(111) surface; thus, they are related to the monoatomic step structure of Pt(997). By increasing the substrate temperature (Figures 3(b)–3(d)), the number of peaks is decreased. This is caused by the thermal diffusion of adsorbed NO. Adsorbed NO molecules thermally migrate on a surface to more stable adsorption sites. Thermal diffusion is discussed after the assignment of the four peaks in Figure 3(a).

Figure 4(a) shows an STM image of NO molecules (0.2 ML) on Pt(997) at 86 K. Adsorbed NO molecules are observed as protrusions on Pt(997). Since the substrate temperature in the STM result is almost the same as that in the IRAS result of Figure 3(c), the STM image should

contain two NO adsorption species (1483 and 1610 cm⁻¹). The protrusions on the terrace are HT species and they form a $p(2 \times 2)$ structure on the terrace, giving the 1483 cm⁻¹ peak. Therefore, the protrusions on the step edge correspond to the peak at 1610 cm⁻¹. By drawing a registry grid on the STM image, the protrusions on the step edge are located at the twofold bridge sites. Therefore, the stable adsorption site for NO molecules on the step edge is a twofold bridge site, and the peak at 1610 cm⁻¹ is assigned to NO at the bridge site of the upper step (BS species). Compared to the previous DFT calculation, the BS species is the most stable species, and the stretching frequency is 1607 cm⁻¹, which is in good agreement with the experimental results [16]. The other peak at 1385 cm⁻¹, which appears at 11 K, is assigned to the NO at the HS species shown in Figure 4(b). From the DFT calculation, there is a stable adsorption site at an HS (hcp) site as shown in Figure 4(b), and its calculated stretching frequency is 1188 cm⁻¹ [16]. This is smaller than the experimental result. We think that not the HS (hcp) site but the HS site is stable for the NO, which has stretching frequency of 1385 cm⁻¹. We think that HS species interact with the step edge more strongly than HT species. The hybridization between the Pt 5d state of the step edge and the NO 2π orbital increases the back donation of the electron from the Pt substrate to the 2π orbital compared to the NO on the terrace, and the electron back donation lowers the stretching frequency.

At 70 K, OT, HT, and BS species are observed by IRAS (Figure 3(b)), and HS species is not observed. This suggests that the HS species is the least stable among the four. By heating the substrate to 90 K, thermal diffusion of NO from OT sites is now activated. The peak of OT species disappears and the intensities of others are increased (Figure 3(c)). By heating the substrate to 150 K, all adsorbed NO molecules migrate to the BS sites (Figure 3(d)). Therefore, the most stable adsorption site for NO is the BS site, and the 2nd and 3rd most stable sites are the HT and OT sites, respectively. These results are in good agreement with the previous DFT calculation [16] and are summarized in Table 1.

3.2. Thermal Diffusion Processes of NO on Pt(997). Figure 5 shows a series of TR-IRAS spectra of NO on Pt(997) at 76 K,

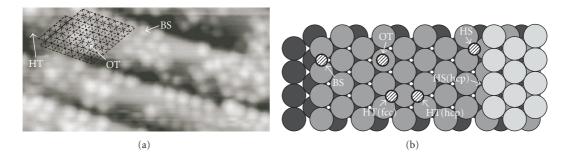


FIGURE 4: (a) An STM image of 0.2 ML NO on Pt(997) at 86 K. $V_s = -0.1 \text{ V}$, $I_t = 200 \text{ pA}$, $11 \text{ nm} \times 5.5 \text{ nm}$. The registry mesh is drawn based on adsorbed NO molecules on the terrace as a reference. The intersections correspond to the position of Pt atoms. (b) A schematic drawing of the adsorption sites of the NO on Pt(997). HT (fcc and hcp), OT, BS, and HS species are energetically stable. However, an HS (hcp) site is not stable.

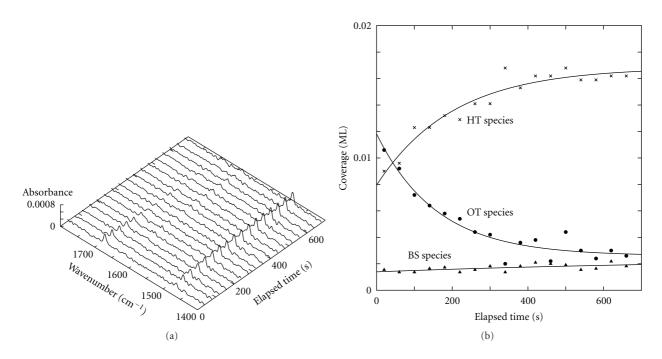


FIGURE 5: (a) A series of TR-IRAS spectra of NO on Pt(997) after an NO gas injection. (b) Change of the fractional coverage of each NO species as a function of the elapsed time. (Coverage: 0.02 ML, temperature: 76 K.).

and the coverage of OT, HT, and BS species as a function of elapsed time. The coverage of each species is defined as the ratio of the number of NO molecules at each site to the number of Pt atoms. The amount of OT species decreases and the amount of HT and BS species increases. The coverage change is estimated from the change of the peak intensities. The details are as follows: since the extinction coefficient of IR absorption by N-O stretching depends on the NO adsorption sites, the ratio of the extinction coefficient of OT species to that of HT and BS species is necessary to convert the peak intensity to the coverage. The coverage, whereby NO fully occupies the step site and the other sites are completely empty, is 0.056 ML. Note that the distance between neighboring NO molecules is about 5.5 Å, twice of the lattice constant of Pt substrate. Here, 1 ML is defined as the ratio of the number of adsorbed NO molecules to

the number of platinum atoms. We determined the coverage of BS species by comparing the peak intensity to that of 0.056 ML BS species (When all BS sites are occupied, the nearest-neighbor distance between NO molecules is about 5.5 Å. The dipole-dipole interaction should be considered in IRAS spectra and the peak could be slightly blue-shifted. However, we assume that the integrated intensity does not deviate from the simple proportional relation I_{BS} = $C_{\rm BS}N_{\rm BS}$ so much). In addition, the coverage of HT and OT species is also estimated by using the ratio of extinction coefficients. The total coverage of NO on Pt(997) is estimated by heating the substrate up to 150 K. After heating, all NO molecules migrate to BS sites and the only peak of BS species remains in the IRAS spectrum. Note that neither desorption nor dissociation of NO molecules occurs at 150 K [11-13].

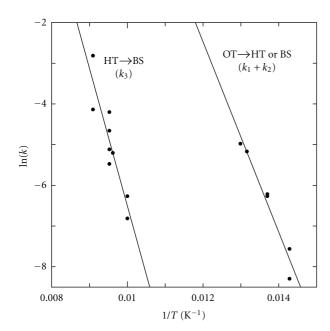


FIGURE 6: Arrhenius plots of the hopping processes of $k_1 + k_2$ and k_3 . $k_1 + k_2$ and k_3 are the rate constants to escape from an OT and an HT site, respectively.

Rate constants of the site-to-site hopping from the OT site to the HT and BS site are defined as k_1 and k_2 . The coverage change is analyzed based on first-order reaction kinetics, and k_1 and k_2 can be estimated from the following equations:

$$\frac{d\theta_{\rm OT}}{dt} = -(k_1 + k_2)\theta_{\rm OT},$$

$$\frac{d\theta_{\rm HT}}{dt} = k_1\theta_{\rm OT},$$

$$\frac{d\theta_{\rm BS}}{dt} = k_2\theta_{\rm OT}.$$
(2)

 $\theta_i(t)$ (i = OT, HT and BS) is the coverage of OT, HT, and BS species, respectively. Similar experiments were carried out in the temperature range from 70 K to 77 K, and the activation energies and preexponential factors of k_1 and k_2 are estimated. An Arrhenius plot for $k_1 + k_2$, which is the rate constant to escape from the OT site, is shown in Figure 6. The activation barrier and the preexponential factor are estimated to be about 200 meV and 2.0×10^{-11} s⁻¹, respectively. Since adsorbed NO molecules still remain in the terrace region in this temperature range, k_1 and k_2 are the rate constants of site-to-site hopping from the OT site to the neighboring HT or BS site, and long-range surface diffusion does not occur. Note that the $\theta_{\rm HT}(\infty)/\theta_{\rm BS}(\infty)$ is about $8 \sim 9$. We think that it depends on the terrace width of Pt(997), whose terrace is constructed by 9 atomic rows. This means that OT species only migrate to the nearest neighbor site (HT or BS), and the destinations depend on the initial position. OT species next to the step can only reach the step site. If a stepped Pt(111) surface, which has a longer terrace width

than Pt(997), is adopted, larger $\theta_{\rm HT}(\infty)/\theta_{\rm BS}(\infty)$ value than $8 \sim 9$ would be expected.

Figure 7 shows a series of TR-IRAS spectra of NO on Pt(997) at 105 K, and the coverage change of HT and BS species as a function of elapsed time. As the elapsed time increases, the peak intensity of HT species decreases and that of BS species increases. Long-range surface diffusion occurs at 105 K and all NO molecules migrate to the step edge. KMC simulation, which is described in Section 2, is adopted in the analysis. The parameters are the initial coverage $(\theta_{\text{total}}(0))$, the rate constant to escape from the HT site (k_3) , and the interaction energy between two NO molecules in the $p(2 \times 2)$ superstructure. From the analysis, we found that the model with no ES barrier shown in Figure 2(b) is much better than that with the infinite ES barrier model shown in Figure 2(c). The solid line in Figure 7(b) shows the result of KMC simulation based on the first model. The second model cannot fit the experimental data with any parameters; thus, fitting by the second model is not shown here. Despite the fact that hopping from the HT site on the lower terrace to the BS site involves ascending the monoatomic step, the first model, which has no ES barrier, is better as a model of NO diffusion on Pt(997). This is because of the stable adsorption site at the HS site. The details are discussed later. Similar TR-IRAS measurements are conducted in the range from 100 K to 110 K, and an Arrhenius plot for k_3 is shown in Figure 6. The activation barrier and the preexponential factor are estimated to be about 290 meV and 6.5×10^{11} s⁻¹, respectively.

Figure 8 shows IRAS spectra of NO on Pt(997) as a function of heating temperature. After heating the substrate to 45 K, the peak of the HS species diminishes, and only that of the BS species increases, and the others do not change. This indicates that all NO molecules at HS sites migrate to BS sites by ascending the monoatomic step, which supports the fact that no ES barrier is discussed above. We roughly estimated the barrier height as follows: since the HS species is observable at 40 K, the accommodation time of the HS site at 40 K is similar or longer than the measurement time at least. On the other hand, this diminishes immediately at 45 K; thus, the accommodation time of the HS site at 45 K is smaller than the measurement time. Therefore, assuming that the preexponential factor is 10¹¹ s⁻¹, the activation barrier to hopping from the HS site to the BS site is in the range from 110 meV to 120 meV.

3.3. Transient Diffusion Process of NO on Pt(997). Thermal diffusion of NO on Pt(997) does not occur at 11 K (Since the shape of the IRAS spectrum at 11 K did not change at all with increasing the elapsed time, we concluded that the site-to-site hopping of adsorbed NO molecules did not occur at 11 K.); the distribution of the adsorbed NO molecules on Pt(997) at 11 K is determined by the first collision point from the gas phase and the distance of transient diffusion from this collision point. We can estimate the distance of the transient diffusion of NO on Pt(997) from a series of IRAS spectra shown in Figure 3 [14]. We define the extinction coefficient of an adsorbed NO molecule as C_i (i = HS, HT, BS, OT). In

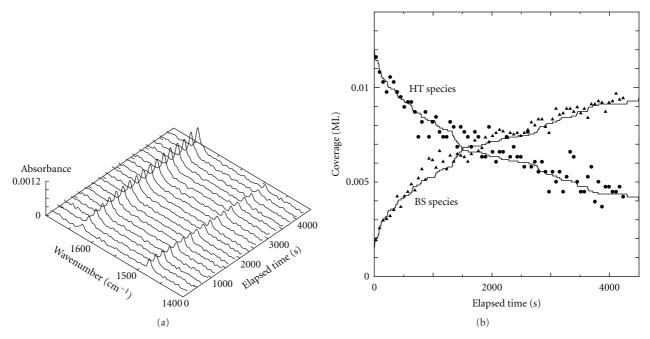


FIGURE 7: (a) A series of TR-IRAS spectra of NO on Pt(997) after an NO gas injection. (b) Change of the fractional coverage of each NO species as a function of the elapsed time. (Coverage: 0.017 ML, temperature: 105 K.).

all of the spectra of Figure 3, the total coverage of adsorbed NO is the same

$$\frac{I_{HS}(11)}{C_{HS}} + \frac{I_{HT}(11)}{C_{HT}} + \frac{I_{BS}(11)}{C_{BS}} + \frac{I_{OT}(11)}{C_{OT}}$$

$$= \frac{I_{HT}(70)}{C_{HT}} + \frac{I_{BS}(70)}{C_{BS}} + \frac{I_{OT}(70)}{C_{OT}}$$

$$= \frac{I_{HT}(90)}{C_{HT}} + \frac{I_{BS}(90)}{C_{BS}} = \frac{I_{BS}(150)}{C_{BS}},$$
(3)

where $I_i(T) = C_i N_i(T)$ is the peak intensity of adsorbed NO at site i, and $N_i(T)$ is the number of adsorbed NO molecules at site i. From these equations and the spectra of Figure 1, the ratio of extinction coefficients is estimated to be $C_{BS}/C_{HT} =$ 3.3 and $C_{\rm BS}/C_{\rm OT}=2.2$, respectively. We could not estimate $C_{\rm BS}/C_{\rm HS}$ from the spectrum of Figure 3(a). (Comparing the spectrum (a) with (c) in Figure 7, the peak position of BS species is slightly different. It seems that this is caused by the change of adsorption state of BS species, and the C_{BS} is also different between 11 K and 40 K.) However, the ratio of the number of NO in the step region (HS and BS) and that of NO in the terrace region (HT and OT) at 11 K is same as at 45 K, at which HS species diminishes. From the ratio of peak intensities at 45 K, the ratio of NO on the step to NO on the terrace is about 1:6.1. Based on a previous study of CO on Pt(997) [14], the simple model shown in Figure 9 is used to estimate the mean distance of transient diffusion. Therefore, the mean distance of transient diffusion is about 4.1 Å.

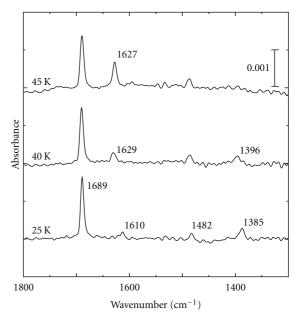


FIGURE 8: IRAS spectra of 0.027 ML NO on Pt(997) as a function of the heating temperature. NO molecules were adsorbed at 11 K.

4. Comparison with Other Studies

In this section, we discuss the above experimental results by comparison with the previous studies. In the He Atom Scattering (HAS) study of NO on Pt(111) [30], the activation barrier was estimated to be 510 meV, which is larger than our result (290 meV). However, their measurement was carried out on the macroscopic region and at higher temperatures

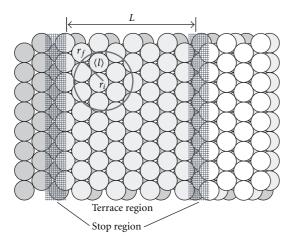


FIGURE 9: A schematic drawing for the estimation of transient diffusion length of NO on Pt(997). The shadowed regions and the other regions are regarded as the step region and the terrace region, respectively. r_i and r_f are an initial collision site and a final adsorption site, respectively. By considering the ratio of NO on the step to that on the terrace, the transient diffusion length $\langle l \rangle$ can be estimated based on Buffon's needle problem [2, 14].

 $(310 \sim 360 \, \text{K})$. Therefore, hopping across the step may be included and it could be the rate-limiting process. In addition, the dissociation of NO at the step site should occur above 200 K [11–13]. It is reasonable that the barrier height, 290 meV, is smaller than the HAS result.

In a previous IRAS and DFT study of NO on Pt(110) [25], the authors estimated the activation barrier to NO hopping. Hopping from the on-top site to the bridge site on the Pt atomic row is about 110 meV, and that from the hollow site, which is next to the bridge site on the atomic row to the bridge site on the atomic row, is about 230 meV. Their results are in agreement with our results.

The distance of transient diffusion of NO on Pt(997) is about 4.1 Å. On the other hand, that of CO on Pt(997) is about 6.8 Å [14], which is longer than that of NO. Physisorbed species, such as noble gas, transiently migrates in the order of hundreds of Å. CO and NO molecules chemisorb on the Pt surface, and their bonding is stronger than the physisorbed species. Chemisorbed CO and NO dissipate their adsorption energy to the substrate via mainly substrate phonon and electron-hole pair excitations. This results in a shorter length of transient diffusion. Comparing NO with CO, the transient diffusion length of NO is shorter than that of CO. This is caused by stronger coupling between NO and the Pt substrate. NO has an unpaired electron in the 2π orbital, which is empty in the case of CO. This unpaired electron makes the energy transfer from NO to the substrate efficient when NO molecules migrate on the surface. In addition, the shape of PES of NO is more complex than that of CO. The stable adsorption site of CO on Pt(997) is only an on-top site at low coverage, and the activation barrier to CO hopping is about 190 meV [20-22]. On the other hand, the number of stable adsorption sites for NO is larger than for CO, and the activation barrier to NO hopping is higher than

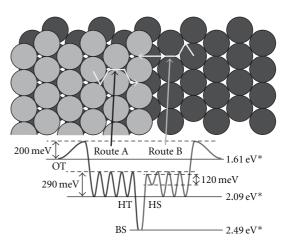


FIGURE 10: Potential energy surface of NO on Pt(997). *The adsorption energy is the result from the previous DFT studies [10, 16].

that of CO hopping. Therefore, this complicated PES shape results in the short length of NO transient diffusion.

Based on the IRAS experiments and the KMC simulation, PES of NO on Pt(997) is clarified. We conclude that the HT species can approach the step from both the upper and lower terraces. Although we cannot rule out the asymmetry of PES at the step, the NO molecules can easily migrate from a HS site to a BS site. This behavior is different from CO on a stepped Pt (111) surface, which has a large ES barrier [20–22]. NO molecules migrate to the upper step by climbing the activation barrier of about 120 meV. Figure 10 shows a schematic drawing of the routes for NO molecules from the terrace to the step and the shape of potential energy.

5. Summary

We have presented the PES of NO on Pt(997); the microscopic diffusion process of NO molecules on Pt(997) and the features of PES of NO, which are related to surface diffusion, are discussed. From the gas phase, NO collides with the Pt surface and transiently diffuses and reaches a stable adsorption site. The mean length of transient diffusion is about 4.1 Å. After the transient diffusion, thermal diffusion occurs at higher temperatures. First, NO molecules at HS sites thermally migrate up to the BS site. The activation barrier is about 120 meV. Secondly, OT species migrate to the neighboring HT or BS site. The activation barrier and the preexponential factor are about 200 meV and 2.0×10^{11} s⁻¹, respectively. Thirdly, the HT species start to diffuse on the terrace to the BS site, which is the most stable for NO. The activation barrier and the preexponential factor are about 290 meV and $6.5 \times 10^{11} \,\mathrm{s}^{-1}$, respectively. In addition, there is little ES effect on NO on Pt(997).

References

[1] J. V. Barth, "Transport of adsorbates at metal surfaces: from thermal migration to hot precursors," *Surface Science Reports*, vol. 40, no. 3, pp. 75–149, 2000.

- [2] W. A. Brown and D. A. King, "NO chemisorption and reactions on metal surfaces: a new perspective," *Journal of Physical Chemistry B*, vol. 104, no. 12, pp. 2578–2595, 2000.
- [3] H. Ibach and S. Lehwald, "Analysis of adsorption processes and surface reactions by vibration spectroscopy: adsorption of no on Pt(111)," *Surface Science*, vol. 76, no. 1, pp. 1–12, 1978.
- [4] J. L. Gland and B. A. Sexton, "Nitric oxide adsorption on the Pt(111) surface," *Surface Science*, vol. 94, no. 2-3, pp. 355–368, 1980.
- [5] B. E. Hayden, "An infra-red reflection absorption study of the adsorption of NO on Pt(111)," *Surface Science*, vol. 131, no. 2-3, pp. 419–432, 1983.
- [6] J. Yoshinobu and M. Kawai, "Adsorption and dimer formation of nitrogen monoxide on Pt(111) at low temperatur," *Chemistry Letters*, vol. 24, no. 7, p. 605, 1995.
- [7] I. Villegas, R. Gomez, and M. J. Weaver, "Nitric oxide as a probe adsorbate for linking Pt(111) electrochemical and model ultrahigh—vacuum interfaces using infrared spectroscopy," *Journal of Physical Chemistry*, vol. 99, no. 40, pp. 14832–14839, 1995.
- [8] M. Matsumoto, K. Fukutani, T. Okano et al., "Study of the adsorption structure of NO on Pt(111) by scanning tunneling microscopy and high-resolution electron energy-loss spectroscopy," *Surface Science*, vol. 454, no. 1, pp. 101–105, 2000.
- [9] M. Matsumoto, N. Tatsumi, K. Fukutani, and T. Okano, "Dynamical low-energy electron diffraction analysis of the structure of nitric oxide on Pt(1 1 1)," *Surface Science*, vol. 513, no. 3, pp. 485–500, 2002.
- [10] H. Aizawa, Y. Morikawa, S. Tsuneyuki, K. Fukutani, and T. Ohno, "A density-functional study of the atomic structures and vibrational spectra of NO/Pt(1 1 1)," *Surface Science*, vol. 514, no. 1–3, pp. 394–403, 2002.
- [11] V. K. Agrawal and M. Trenary, "An infrared study of NO adsorption at defect sites on Pt(111)," *Surface Science*, vol. 259, no. 1-2, pp. 116–128, 1991.
- [12] R. J. Mukerji, A. S. Bolina, W. A. Brown, Z. P. Liu, and P. Hu, "The temperature dependence of the adsorption of NO on Pt(211): a RAIRS and DFT investigation," *Journal of Physical Chemistry B*, vol. 108, no. 1, pp. 289–296, 2004.
- [13] E. H. G. Backus, A. Eichler, M. L. Grecea, A. W. Kleyn, and M. Bonn, "Adsorption and dissociation of NO on stepped Pt(533)," *Journal of Chemical Physics*, vol. 121, no. 16, pp. 7946–7954, 2004.
- [14] J. Yoshinobu, N. Tsukahara, F. Yasui, K. Mukai, and Y. Yamashita, "Lateral displacement by transient mobility in chemisorption of CO on Pt(1997)," *Physical Review Letters*, vol. 90, no. 24, pp. 248301–248301, 2003.
- [15] N. Tsukahara, K. Mukai, Y. Yamashita, and J. Yoshinobu, "Microscopic diffusion processes of NO on the Pt(997) surface," *Journal of Chemical Physics*, vol. 128, no. 5, Article ID 054701, 2008.
- [16] N. Tsukahara, K. Mukai, Y. Yamashita, J. Yoshinobu, and H. Aizawa, "Adsorption states of NO on the Pt(1 1 1) step surface," Surface Science, vol. 600, no. 17, pp. 3477–3483, 2006.
- [17] N. Tsukahara, K. Mukai, Y. Yamashita, and J. Yoshinobu, "Search for adsorption potential energy minima of NO on Pt(9 9 7) at 11 K," *Surface Science*, vol. 600, no. 18, pp. 3560–3563, 2006.
- [18] K. Binder and D. P. Landau, "Phase diagrams and critical behavior in Ising square lattices with nearest- and next-nearest-neighbor interactions," *Physical Review B*, vol. 21, no. 5, pp. 1941–1962, 1980.

- [19] M. Tringides and R. Gomer, "A Monte Carlo study of oxygen diffusion on the (110) plane of tungsten," *Surface Science*, vol. 145, no. 1, pp. 121–144, 1984.
- [20] J. E. Reutt-Robey, D. J. Doren, Y. J. Chabal, and S. B. Christman, "Microscopic co diffusion on a PT(111) surface by time-resolved infrared spectroscopy," *Physical Review Letters*, vol. 61, no. 24, pp. 2778–2781, 1988.
- [21] J. E. Reutt-Robey, Y. J. Chabal, D. J. Doren, and S. B. Christman, "CO diffusion on Pt(111) by time—resolved surface infrared spectroscopy," *Journal of Vacuum Science & Technology A*, vol. 7, no. 3, pp. 2227–2234, 1989.
- [22] J. E. Reutt-Robey, D. J. Doren, Y. J. Chabal, and S. B. Christman, "CO diffusion on Pt(111) with time-resolved Infrared-pulsed molecular beam methods: critical tests and analysis," *The Journal of Chemical Physics*, vol. 93, no. 12, pp. 9113–9129, 1990.
- [23] G. Ehrlich and F. G. Hudda, "Atomic view of surface self-diffusion: tungsten on tungsten," *The Journal of Chemical Physics*, vol. 44, no. 3, pp. 1039–1049, 1966.
- [24] R. L. Schwöebel and E. J. Shipsey, "Step motion on crystal surfaces," *Journal of Applied Physics*, vol. 37, no. 10, pp. 3682–3686, 1966.
- [25] W. A. Brown, R. K. Sharma, Q. Ge, and D. A. King, "Lateral potential energy surfaces for molecular chemisorption on metals from experiment and theory: NO on Pt{110} (1×2)," *Chemical Physics Letters*, vol. 299, no. 3-4, pp. 253–259, 1999.
- [26] C. Uebing and R. Gomer, "A Monte Carlo study of surface diffusion coefficients in the presence of adsorbate-adsorbate interactions. I. Repulsive interactions," *The Journal of Chemical Physics*, vol. 95, no. 10, pp. 7626–7635, 1991.
- [27] C. Uebing and R. Gomer, "A Monte Carlo study of surface diffusion coefficients in the presence of adsorbate-adsorbate interactions. II. Attractive interactions," *The Journal of Chemical Physics*, vol. 95, no. 10, pp. 7636–7640, 1991.
- [28] C. Uebing and R. Gomer, "A Monte Carlo study of surface diffusion coefficients in the presence of adsorbate-adsorbate interactions. III. Repulsive nearest-neighbor and attractive next-nearest-neighbor interactions," *The Journal of Chemical Physics*, vol. 95, no. 10, pp. 7641–7647, 1991.
- [29] C. Uebing and R. Gomer, "A Monte Carlo study of surface diffusion coefficients in the presence of adsorbate-adsorbate interactions. IV. Attractive nearest-neighbor and repulsive next-nearest-neighbor interactions," *The Journal of Chemical Physics*, vol. 95, no. 10, pp. 7648–7652, 1991.
- [30] M. Croci, C. Félix, G. Vandoni, W. Harbich, and R. Monot, "Chemisorption and macroscopic diffusion of NO on Pt(111)," *Surface Science*, vol. 307–309, pp. 460–464, 1994.

Hindawi Publishing Corporation Advances in Physical Chemistry Volume 2012, Article ID 268124, 13 pages doi:10.1155/2012/268124

Review Article

Exploring Multiple Potential Energy Surfaces: Photochemistry of Small Carbonyl Compounds

Satoshi Maeda,^{1,2} Koichi Ohno,³ and Keiji Morokuma^{2,4}

- ¹ The Hakubi Center, Kyoto University, Kyoto 606-8302, Japan
- ² Fukui Institute for Fundamental Chemistry, Kyoto University, Kyoto 606-8103, Japan
- ³ Toyota Physical and Chemical Research Institute, Nagakute, Aichi 480-1192, Japan

Correspondence should be addressed to Satoshi Maeda, smaeda@fukui.kyoto-u.ac.jp and Keiji Morokuma, keiji.morokuma@emory.edu

Received 20 June 2011; Accepted 9 August 2011

Academic Editor: Xinchuan Huang

Copyright © 2012 Satoshi Maeda et al. This is an open access article distributed under the Creative Commons Attribution License, which permits unrestricted use, distribution, and reproduction in any medium, provided the original work is properly cited.

In theoretical studies of chemical reactions involving multiple potential energy surfaces (PESs) such as photochemical reactions, seams of intersection among the PESs often complicate the analysis. In this paper, we review our recipe for exploring multiple PESs by using an automated reaction path search method which has previously been applied to single PESs. Although any such methods for single PESs can be employed in the recipe, the global reaction route mapping (GRRM) method was employed in this study. By combining GRRM with the proposed recipe, all critical regions, that is, transition states, conical intersections, intersection seams, and local minima, associated with multiple PESs, can be explored automatically. As illustrative examples, applications to photochemistry of formaldehyde and acetone are described. In these examples as well as in recent applications to other systems, the present approach led to discovery of many unexpected nonadiabatic pathways, by which some complicated experimental data have been explained very clearly.

1. Introduction

In order to theoretically unravel the entire photochemical reaction processes of a given system, one has to explore and characterize systematically several excited as well as the ground state potential energy surfaces (PESs). In the Franck-Condon (FC) approximation, a reaction starts from the FC point on an excited state PES. Then, the system undergoes either adiabatic or nonadiabatic pathways depending on a given excess energy and topographies on the PESs. In adiabatic paths, a bond reorganization occurs directly on the excited state PES through transition states (TSs). In nonadiabatic paths, on the other hand, the system makes nonadiabatic transition to a lower PES and then reacts on the lower PES. The system may cascade through several PESs via nonadiabatic transitions. Seams of intersection between two PESs often play a key role in various reactions [1–7]; near an intersection seam, nonadiabatic transitions

can take place efficiently. When the two states have the same spin and space symmetry, the intersection hyperspace consists of f-2 dimensions and is called "conical intersection (CI)," where f is the number of vibrational degrees of freedom. If the spin multiplicity and/or the space symmetry are different, the PESs cross simply in f-1 dimensional hyperspace. In this paper, both of these two types of intersections, that is, conical intersection and simple intersection seam, are denoted as "seam-of-crossing." In many kinetic studies, minimum energy structures on seam-of-crossing hyperspaces (MSXs) have been searched as critical points of nonadiabatic transitions. In short, to find all possible photochemical reaction pathways of a given system, systematic search for TSs and MSXs is required for all PESs below a given photon energy.

There have been considerable efforts on development of geometry optimization methods for MSXs [8–16] as well as for TSs [17–26]. A variety of geometry optimization

⁴ Department of Chemistry and The Cherry L. Emerson Center for Scientific Computation, Emory University, Atlanta, GA 30322, USA

techniques, such as the gradient minimization [17, 18], the Berny optimization [19, 20], the eigenvector following [21], the geometry direct inversion in the iterative subspace [22], and the rational function optimization [23], have been a great help to locate the exact saddle point starting from a guessed TS structure. MSX optimization methods can be classified into three types: constrained optimization methods [8–10], the direct gradient (DG) method [11, 12], and penalty function (PF) methods [13, 14]. These methods were compared systematically, and the former two were shown to converge more quickly than a PF method [15]. On the other hand, PF methods have a significant advantage that nonadiabatic coupling derivative vector (CDV) calculations are not required in optimization of MSXs of the conical intersection type. Recently, CDV calculations can be avoided even in constrained optimization methods and in the DG method by using the branching plane updating method [16]. These methods have been successfully applied to many theoretical analyses of photochemical reactions.

In general, geometry optimization requires a good initial guess. However, guesses of MSX structures are sometimes very difficult, because their shapes are often highly deviated from those of stable molecular structures. A similar problem sometimes arises also in the search for TSs on a single PES. To avoid this problem, many automated TS (or minimum energy path) search methods have been developed [27– 42]. Although most of these require guesses of a reaction mechanism such as key structures (product and intermediates) [27-34] or chemically relevant collective variables [35-37], some (relatively expensive) methods do not use any guess [38-42]. We also have developed two unique methods without needing any guess: the global reaction route mapping (GRRM) [43-45] method and the artificial force-induced reaction (AFIR) [46-48] method. GRRM can execute global mapping of reaction path networks of unimolecular isomerizations and dissociations on PESs of given atomic composition. AFIR can efficiently explore associative reaction paths among given reactants of multicomponent reactions. Although application of these automatic TS search methods to excited state PESs seems to be straightforward, it had not been successful probably because there are singular points in low-energy regions of excited state PESs due to conical intersections as discussed in Section 2.1. There has been no practical method for the automated MSX search either.

In this paper, we describe a recipe for exploring multiple PESs automatically. Two model functions, $F^{\rm AMF}$ and $F^{\rm SMF}$ [49, 50], are introduced for the TS search and the MSX search, respectively, in combination with the GRRM method. Although, in this study, it is applied to photochemical reactions, it can be applied to other nonadiabatic reactions such as ion-molecule reactions, organometallic reactions, and combustion reactions. Furthermore, the present recipe can adopt, instead of GRRM, any automated reaction path search method such as AFIR. In the present paper, we apply the proposed recipe with the GRRM method to photodissociation mechanisms of small carbonyl compounds such as formaldehyde $\rm H_2CO$ and acetone (CH₃)₂CO [49, 51].

2. Theory

2.1. Avoiding Model Function (AMF) Approach. Figure 1(a) schematically illustrates a one-dimensional cut of two coupled adiabatic PESs. Along the curve for the upper PES, there is a local minimum in the left-hand side and a conical intersection in the right-hand side. In the conical intersection, the adiabatic PES is singular due to the coupling between two diabatic surfaces. To eliminate the singular point from the adiabatic PES, we use the following avoiding model function in automated search:

$$F^{\text{AMF}}(\mathbf{Q}) = \frac{1}{2} \left(E^{\text{State 1}}(\mathbf{Q}) + E^{\text{State 2}}(\mathbf{Q}) \right)$$

$$+ \frac{1}{2} \sqrt{\left(E^{\text{State 1}}(\mathbf{Q}) - E^{\text{State 2}}(\mathbf{Q}) \right)^2 + 4U^2}, \qquad (1)$$

$$U(\mathbf{Q}) = \frac{\alpha}{2} \exp \left[-\left(\frac{E^{\text{State 1}}(\mathbf{Q}) - E^{\text{State 2}}(\mathbf{Q})}{\alpha} \right)^2 \right],$$

where **Q** is the atomic coordinates $\{Q_i\}$, $E^{\text{State 1}}(\mathbf{Q})$ is an adiabatic PES of the target (upper) state, $E^{\text{State 2}}(\mathbf{Q})$ is an adiabatic PES of the lower state, and α is a constant parameter. This F^{AMF} is very similar to the well-known equation for the diabatic/adiabatic transformation for two state systems, where $E^{\text{State }n}$ should be diabatic energies in the equation. In this study, adiabatic energies were substituted for $E^{\text{State }n}$. As seen in Figure 1(b), the model coupling function U in (1) changes the conical intersection region to an avoided crossing-like smooth curve. Thus, any automated search methods that require a smooth PES can be applied to F^{AMF} . TSs on F^{AMF} may be meaningless if the difference between F^{AMF} and $E^{State 1}$ is significant in TS regions, and therefore U was designed to have effects only in limited regions with a small energy gap. Hence, in TS regions F^{AMF} is often very similar to $E^{\text{State 1}}$. The accuracy (how well TSs on F^{AMF} reproduce TSs on $E^{State 1}$) depends on the value of α . To our experience, α should be about 1/10 of the vertical excitation energy of target reactions. In this study, we use $\alpha = 30 \text{ kJ/mol throughout.}$

An example is shown in Figure 1(c) for the direct dissociation channel of H₂CO on the S₁ PES. Starting from S₁-TS, the backward IRC (intrinsic reaction coordinate) reaches S₁-MIN, while the forward IRC crosses S₀/S₁-MSX (conical intersection) in a partially dissociated region. Behind these (true) critical structures, local minima and a saddle point on F^{AMF} (with $\alpha = 30 \text{ kJ/mol}$) are shown in black. As seen in Figure 1(c), the saddle point structure on F^{AMF} perfectly overlaps with S₁-TS (identical within convergence criteria of geometry optimization: maximum absolute gradient g_{MAX} = 6.0×10^{-5} hartree Å⁻¹, root mean square gradient $g_{RMS} =$ 4.0×10^{-5} hartree Å⁻¹, maximum absolute displacement $d_{\text{MAX}} = 3.0 \times 10^{-4} \text{ Å}$, root mean square displacement $d_{\text{RMS}} =$ 2.0×10^{-4} Å). S₁-MIN is also reproduced perfectly by the minimum on F^{AMF} . Moreover, on F^{AMF} , S_0/S_1 -MSX turned into a local minimum shown in black behind S₀/S₁-MSX. In other words, the conical intersection does not exist on F^{AMF} , which enables exploring the smooth F^{AMF} with an automated reaction path search method.

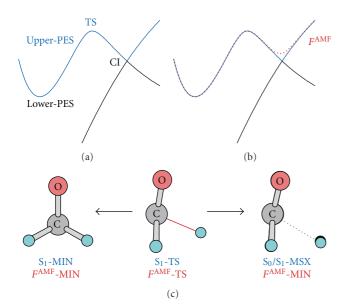


FIGURE 1: (a) A schematic one-dimensional curve of two coupled adiabatic PESs, (b) an example of $F^{\rm AMF}$ for the PESs in (a), and (c) comparisons between stationary points on $F^{\rm AMF}$ (with $\alpha=30\,{\rm kJ/mol}$) and those on the S₁-PES of H₂CO (see Section 2.4 for the ab initio calculation level). Each structure shown in (c) corresponds to S₁-MIN, S₁-TS, and S₀/S₁-MSX (conical intersection), respectively, and stationary structures on $F^{\rm AMF}$ are overlapped in black behind them. At S₁-MIN and S₁-TS, the stationary structures on $F^{\rm AMF}$ are identical to them within the convergence criteria (see text) of geometry optimization and cannot be seen. $F^{\rm AMF}$ -MIN can barely be seen behind S₀/S₁-MSX.

In short, TSs on an excited state (adiabatic) PES $E^{\text{State 1}}$ can be explored in two steps: a search for many TS-like structures as first-order saddles on F^{AMF} by an automated search method, optimization of true TSs on the PES $E^{\text{State 1}}$ using the TS-like structures as initial guesses. It should be noted that all TSs shown below are fully optimized first-order saddle points (true TSs) on adiabatic PESs.

2.2. Seam Model Function (SMF) Approach. In the automated search for MSXs, the following model function F^{SMF} is considered [49, 50]:

$$F^{\text{SMF}}(\mathbf{Q}) = \frac{1}{2} \left(E^{\text{State 1}}(\mathbf{Q}) + E^{\text{State 2}}(\mathbf{Q}) \right) + \frac{\left(E^{\text{State 1}}(\mathbf{Q}) - E^{\text{State 2}}(\mathbf{Q}) \right)^{2}}{\beta},$$
(2)

where \mathbf{Q} is the atomic coordinates $\{Q_i\}$, $E^{\text{State 1}}(\mathbf{Q})$ and $E^{\text{State 2}}(\mathbf{Q})$ are PESs of two target states, and β is a constant parameter. Minimization of F^{SMF} gives a geometry in which both the mean energy of the two states (the first term) and the energy gap between the two states (the second term) are small. Hence, minima on F^{SMF} can be good guesses of MSXs. Equation (2), which is also called penalty function (PF), or more complicated PFs have been employed in MSX geometry optimization [13, 14]. As discussed above, PF methods have a drawback concerned with convergence in MSX optimization

[15]. However, in automated searches, use of the PF has a significant advantage that the PF is a single smooth function, which permits the application of automated search methods developed for single PESs without any modification. Hence, we proposed the SMF approach which consists of two steps: (a) a search for many MSX-like structures as local minima on the PF using an automated search method and (b) determination of (true) MSX structures by using one of MSX optimization methods and MSX-like structures obtained in (a) as initial guesses.

Although smaller β gives better (more accurate) candidates, minimizations of $F^{\rm SMF}$ with smaller β need more optimization steps since at $\beta=0$ the function becomes singular. This is the cause of the slow convergence of a PF method observed in the systematic comparative study. To avoid this, use of relatively large β (typically $\beta\sim30-50\,{\rm kJ/mol}$) is recommended since the purpose of the first step (a) is to systematically collect many MSX-like structures as quick as possible. In this study, we use $\beta=30\,{\rm kJ/mol}$ throughout. It should be noted that all MSXs shown below are fully optimized true MSXs (the energy gap between two target states is smaller than $0.1\,{\rm kJ/mol}$ in all MSXs).

2.3. Global Reaction Route Mapping (GRRM) Method. In the GRRM method [43–45], global mapping of reaction path networks is executed by following the path network itself. To make such a search, one has to follow the paths in both uphill (minimum to saddle) and downhill (saddle to minimum) directions. The latter can be accomplished by following the IRC [52] using one of advanced steepest decent path methods [53–57]. The former, that is, uphill walk, had been difficult before 2004 until we proposed the anharmonic downward distortion following (ADDF) approach.

Many typical potential curves show a common feature that potential energy always become lower than the harmonic potential defined at the bottom of the curves in directions leading to TSs. Thus, reaction channels can be found by following ADD maxima starting from a local minimum on a PES. In many previous applications, the GRRM method based on the ADDF approach has found many unknown as well as nearly all known reaction channels automatically. The ADD maxima can be detected in multidimension by using the scaled hypersphere search (SHS) technique. Details of the SHS technique can be found in our previous papers [43–45].

Following all ADDs starting from all obtained local minima will provide an entire global map on PESs. Such a treatment called full-ADDF, denoted GRRM(*f*-ADDF), is very expensive, and its application is limited to small systems. An approach following only large ADDs, large-ADDF denoted GRRM(*l*-ADDF), is effective to survey lowenergy regions of PESs in large systems [58]. Another useful option for speedup is double-ended ADDF, denoted GRRM(*d*-ADDF), which confines the search area between given reactant and product geometries [33, 34].

2.4. Computational Methods Used in Applications. In this section, we summarize quantum chemical methods used in the applications in the following sections. For details, see original articles [49, 51].

In an application to H₂CO, GRRM(*f*-ADDF) was applied to *F*^{SMF} at the 3SA-CAS(4e,3o)-SCF/6-31G and 3SA-CAS(2e,3o)-SCF/6-31G levels, where SA stands for state-average and the averaged three states are S₀, S₁, and T₁. All obtained MSX-like structures were fully optimized at the 2S-CAS(12e,10o)-PT2/aug-cc-pVDZ level for the singlet states and at the SS-CAS(12e,10o)-PT2/aug-cc-pVDZ level for the triplet state, where 2S and SS stand for two-state averaged and single-state, respectively. In the state averaging, equal weights were used. All (known) TSs and local minima on these PESs were optimized at the same (CASPT2) levels.

In an application to $(CH_3)_2CO$, GRRM(d-ADDF) was applied to F^{SMF} and F^{AMF} at the 2SA-CAS(8e,7o)-SCF/6-31G and SS-CAS(8e,7o)-SCF/6-31G levels for the S₀, S₁, and T₁ states, respectively, where SS here stands for state-specific. In addition to $(CH_3)_2CO$, three isomers, $CH_2=C(OH)-CH_3$ (enol), ${}^{\bullet}CH_2-CH(O^{\bullet})-CH_3$ (biradical), and $CH_3-CO-CH_3$ (carbene), and a partially dissociated geometry $CH_3CO \cdot \cdot \cdot CH_3$ were considered as the end points for d-ADDF. All obtained MSX-like structures and TS-like structures were fully optimized at the 2S-CAS(8e,7o)-PT2/6-31+G* level for the singlet states and at the SS-CAS(8e,7o)-PT2/6-31+G* level for the triplet state. Local minima were optimized also at the same (CASPT2) levels.

Potential energies and gradients required for the searches as well as optimization were computed by the Molpro2006 program [59]. Using these quantities, all geometrical displacements were treated by the GRRM11 program [60].

3. Photodissociation of Formaldehyde

It was suggested experimentally that the photodissociation of H_2CO at low-photon energies occurs on the S_0 PES after an internal conversion (IC) from the S_1 PES [61–65]. Hence, dynamics as well as stationary points on the ground state S_0 PES have been studied extensively by theoretical calculations [39, 40, 43–45, 66–89]. The focuses in early studies had been on the following two channels:

$$H_2CO \longrightarrow CO + H_2,$$
 (3)

$$H_2CO \longrightarrow HCO + H,$$
 (4)

The TS for the channel (3), which is often called "tight-TS," was already determined in 1974 by ab initio calculations [67]. The radical dissociation (4) can occur both from the S_0 PES and from the T_1 PES, and hence the T_1 PES has also been studied [90, 91]. Knowledge of the higher singlet states was rather scarce until very recently [92, 93]. A new channel for the molecular products was experimentally proposed in 1993 [94]; the channel is often represented as

$$H_2CO \longrightarrow HCO \cdots H \longrightarrow CO + H_2,$$
 (5)

where one of H atoms, once partially dissociated, roams around the HCO fragment and finally abstracts the other H atom to generate $CO + H_2$. This speculation was confirmed in 2004 by combined experimental and theoretical studies [95]. Since its discovery, this channel named "roaming" has

been a hot topic as a new type of reaction mechanism [96–98], and it has been found in many reactions having implications to atmospheric chemistry [99–108] and combustion chemistry [88, 109, 110].

The IC was postulated to occur in the potential well of H₂CO in many previous studies. However, recently, several MSXs were found outside the potential well of H_2CO : two S_0/T_1 -MSXs were located in the potential well of hydroxycarbene HCOH [111, 112], a S₀/S₁-MSX was located in a partially dissociated H · · · HCO region [113]. In 2009, we explored multiple PESs for the S_0 , S_1 , and T_1 states by the SMF-GRRM approach [49]. The potential energy profile we discovered is presented in Figure 2, where the high-energy regions for $H_2O \cdots C$ and $H_2C \cdots O$ are not shown. The two S_0/T_1 -MSXs of HCOH [111, 112] are denoted as S_0/T_1 -MSX2 and S_0/T_1 -MSX3, and the partially dissociated S_0/S_1 -MSX [113] is shown as S_0/S_1 -MSX1. As seen in this figure, to isomerize on the T_1 PES or to partially dissociate on the S₁ PES, the system has to overcome a significant barrier. At low-photon energies ($<32\,000\,\mathrm{cm}^{-1}=383\,\mathrm{kJ}\,\mathrm{mol}^{-1}$), these barriers are not accessible. Hence, these known MSXs are not likely involved in the low-energy photodissociation process.

In addition to known MSXs, some new MSX structures were discovered in the automated search. One of those, S_0/T_1 -MSX1, was discovered in the potential well of H_2CO . Adopting this new S₀/T₁-MSX1 and known excited state TSs [111, 114], we proposed the entire mechanism for the lowenergy photolysis as follows. After the photoexcitation the system oscillates around the S₁-MIN for a long time since there is no S₀/S₁-MSX in the potential well and the lowest S_1/T_1 -MSX1 is higher than the photon energies. The S_1/T_1 intersystem crossing (ISC) may be able to take place by trickling down from S₁ to T₁ at all the geometries, while the molecule in the S_1 state spends a long time oscillating around S₁-MIN, because PESs for the S₁ and T₁ states are very close and nearly parallel to each other in energy at any place in the basin of S₁-MIN. Although the probability at each geometry may be small because the spin-orbital coupling between the two states belonging to the same electronic configuration is small, the integrated probability over a long time could be substantial. Once the system comes down to T₁ from the S₁-MIN basin region, the T₁/S₀ ISC via the newly found S_0/T_1 -MSX1 (390 kJ mol⁻¹) can take place in this H₂CO basin. This mechanism based on the CASPT2 energetics is consistent with the result obtained by the MRCISD(Q)/AV5Z calculations, where relative energy values of the three important barriers, that is, the S₁ (C–H bond scission) barrier, the T_1 barrier, and S_0/T_1 -MSX1, are 456.4, 413.1 and 397.7 kJ/mol, respectively, at the MRCISD(Q)/AV5Z level [114]. After the transition to S_0 , the dynamics on the S₀ PES should start in the H₂CO basin and propagate via the tight-TS or the roaming pathway to give the $CO + H_2$ product.

After the proposal of this mechanism, direct CASSCF dynamics studies have been conducted for the molecular dissociation at medium excitation energies [115, 116]. By these simulations, molecular dissociations involving an ISC or a direct IC in the partially dissociated $H \cdot \cdot \cdot HCO$ region were proposed. These paths undergo a C–H bond dissociation

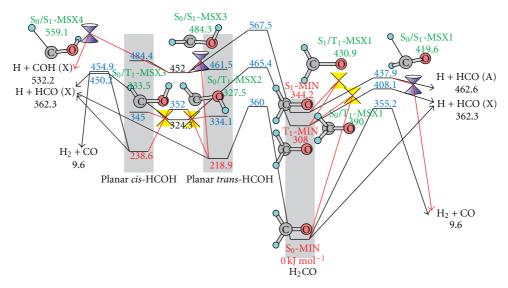


FIGURE 2: A CASPT2 potential energy profile (in kJ/mol) for the three low lying S_0 , S_1 , and T_1 states of H_2CO [49]. Reprinted with permission from [49]. Copyright 2009 American Chemical Society.

on either the T_1 or S_1 PESs. Obviously, the S_1 dissociation needs sufficient (medium) photon energies to overcome the S₁ barrier. The other path involving the partial dissociation on the T₁ PES may happen via tunneling or zero-pointenergy effect even at the low photon energies. However, this (molecular dissociation involving the T_1 dissociation) was shown to be a very minor process in recent three-state trajectory surface hopping (3S-TSH) simulations including the S_0 , S_1 , and T_1 states [117]. In the 3S-TSH simulations, highly accurate (analytically fitted) PESs were employed and the hopping was treated by Tully's fewest switches algorithm. The 3S-TSH simulations demonstrated that the above decay mechanism involving the S₁-T₁ trickling down mechanism followed by the T_1 - S_0 ISC through S_0/T_1 -MSX1 in the potential well of H₂CO is the major process before the molecular dissociation. Furthermore, they discovered a new unexpected (but minor) dynamics in which the system once decays down to the So PES and then isomerize to HCOH on the S₀ PES before the dissociation. Surprisingly, in such trajectories, the system hops up to the T₁ PES and then hops down to the S_0 PES through S_0/T_1 -MSX1 or S_0/T_1 -MSX2. This is energetically certainly allowed in Figure 2.

4. Photodissociation of Acetone

Another example is an application to $(CH_3)_2CO$ [51]. Photolysis of acetone is one of the most extensively studied photochemical reactions [118]. The CC bond dissociation, called "Norrish type I reaction" $(CH_3)_2CO \rightarrow CH_3CO + CH_3$, has been the main focus of many theoretical and experimental studies [119–133]. Roaming was also suggested experimentally [102], which was proposed to proceed on the S_0 PES as $(CH_3)_2CO \rightarrow CH_3CO \cdots CH_3 \rightarrow CO + CH_3-CH_3$.

In early experimental studies [119–121], it was proposed that the Norrish type I dissociation occurs on the T_1 PES

(the T_1 path) after an ISC from the S_1 PES, as long as the photon energy exceeds the barrier of the CC bond breaking on the T₁ PES. A theoretical calculation at the CASSCF level indicated that the ISC happens around a S₁/T₁-MSX structure located below the T₁ barrier, and the T₁ path was suggested to be the most preferable channel (at least in terms of potential energy) [122]. However, in later combined femtosecond laser experimental and theoretical studies [123– 125], it was suggested that the dissociation occurs through the S₁ barrier (the S₁ path) before the ISC takes place when photon energies are larger than the S_1 barrier. The S₁ path was then confirmed by another femtosecond laser study at 195 nm (613 kJ/mol) [126–128]. Relevant stationary structures for the S₁ path were examined by CASPT2 and MRCISD(Q) calculations [132]. We revisited [51] the PESs of (CH₃)₂CO for two purposes: to find nonadiabatic paths to the S₀ PES systematically for the roaming channel and to explain the conflict between the fast S_1/T_1 ISC proposed by CASSCF calculations and the experimentally observed S₁ path which overcomes the S₁ barrier much higher than the CASSCF S_1/T_1 -MSX.

Figure 3 presents a potential energy profile for the three low lying S_0 , S_1 , and T_1 states. For isomerizations on the S_1 and T_1 PESs, only the lowest channels for the $(CH_3)_2CO \leftrightarrow CH_2=C(OH)-CH_3$ reaction $(S_1\text{-}TS2)$ and $T_1\text{-}TS2$ are shown in the profile. As seen in this figure, these excited state isomerizations have higher barriers and must be minor channels compared to the CC bond dissociations $(S_1\text{-}TS1)$ and $T_1\text{-}TS1)$. We should note that the $S_1/T_1\text{-}MSX$ is much higher in energy than $T_1\text{-}TS1$ on the CASPT2 PESs in contrast to the case of the CASSCF calculations reported previously. Hence, if photon energy is higher than the S_1 barrier $(S_1\text{-}TS1)$, the most favorable path is the direct dissociation. This explains the recent femtosecond laser experimental observation very well. Below the S_1 barrier, there is no exit channel from the S_1 PES. Hence and also because of very small spin-orbit

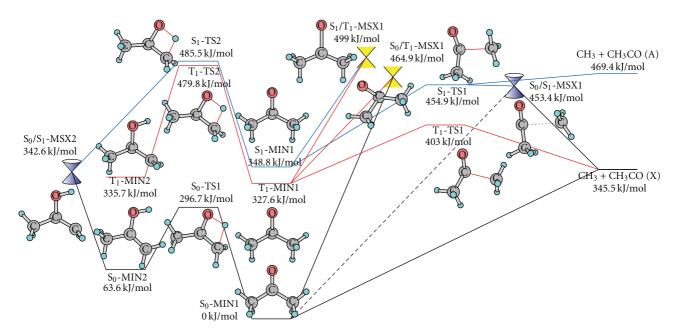


FIGURE 3: A CASPT2 potential profile for the three low lying states $(S_0, S_1, \text{ and } T_1)$ of $(CH_3)_2CO$ [51]. Reprinted with permission from [51]. Copyright 2010 American Chemical Society.

coupling between the S_1 and T_1 states, we proposed that the ISC occurs very slowly by trickling down from S_1 to T_1 while the molecule in the S₁ state spends a long time oscillating around S₁-MIN1. This may be able to happen because PESs for the S₁ and T₁ states are very close and nearly parallel to each other in energy at any place in the basin of S₁-MIN1, similarly to the case of H₂CO. There are some experimental evidences showing that the S_1/T_1 ISC is very slow [134]; recent time-resolved mass spectrometry and photoelectron spectroscopy experiments and direct dynamics simulations suggested that the system decays from the FC region to the S₁ minimum within 30 femtoseconds and then stays on the S₁ PES more than 100 picoseconds at 253–288 nm (473– 415 kJ/mol) excitations [135, 136]. After coming down to the T_1 PES, the system can overcome the T_1 barrier to undergo the Norrish type I reaction.

In Figure 3, several decay paths can be found from the S_1 PES to the S_0 PES. Unlike H_2CO , S_0/T_1 -MSX1 in the potential well of (CH₃)₂CO is much higher in energy than T₁-TS1. The lowest path to the S₀ PES undergoes a dissociation on the S1 PES through S1-TS1 followed by a nonadiabatic transition in the nearly dissociated geometry through S_0/S_1 -MSX1 and a recombination on the S_0 PES. The roaming dynamics was observed at 230 nm (520 kJ/mol) [102], at which the direct CC bond dissociation on the S₁ PES is the dominant path of the Norrish type I reaction. Hence, this is the most likely path to produce the ground state (CH₃)₂CO. At this photon energy, the excited state isomerization to the enol species followed by an IC through S₀/S₁-MSX2 and an enol-keto isomerization on the S₀ PES may be a minor channel to the ground state (CH₃)₂CO before the roaming dynamics may take place.

5. S_0/T_1 Intersection Space

One can find candidates of saddle points on seam-of-crossing hyperspaces (SPSXs) as saddles on $F^{\rm SMF}$. Minimum energy paths on seam-of-crossing hyperspaces (MEPSXs) starting from SPSXs were suggested to be useful for understanding dynamical trajectories crossing a high-energy region of a seam-of-crossing hyperspace [12]. In this section, SPSXs and MEPSXs for the S_0/T_1 intersection spaces of $H_2{\rm CO}$ and $({\rm CH_3})_2{\rm CO}$ are discussed because of their significance in the generation of the S_0 species. The optimization method for SPSXs from SMF (or guessed) structures and an algorithm to calculate an MEPSX from a SPSX are described in our previous paper [16].

Figure 4(a) shows a MEPSX for the S_0/T_1 intersection space of H_2CO at the CASPT2 level. The MEPSX was calculated from two SPSXs. Along the MEPSX, all points have the S_0/T_1 energy gap less than 1.0 kJ/mol. As seen in this figure, the S_0/T_1 intersection space was found to be connected from the HCOH area through the S_0/T_1 -MSX1 geometry to the partially dissociated region. It follows that the S_0/T_1 ISC may take place not only at S_0/T_1 -MSX1 but also with variety of geometries in this very wide intersection space.

Integration of an MEPSX with CASPT2 is expensive, and we also tested and used the UB3LYP method using Gaussian09 program [137]. At first, the MEPSX for H_2CO by the UB3LYP method is shown in Figure 4(b). For H_2CO the MEPSX by UB3LYP is similar to the one by the CASPT2 method. Therefore, we adopted the UB3LYP method for $(CH_3)_2CO$. Figure 5 shows two MEPSXs (a) for $H_2C=C(OH)CH_3 \leftrightarrow (CH_3)_2CO \leftrightarrow CH_3CO + CH_3$ and (b) for $CH_3-CO-CH_3 \leftrightarrow (CH_3)_2CO \leftrightarrow CH_3CO + CH_3$. Another MEPSX from an MSX of the ${}^{\bullet}CH_2-CH(O^{\bullet})-CH_3$ form (not shown) is directly connected to the partially dissociated

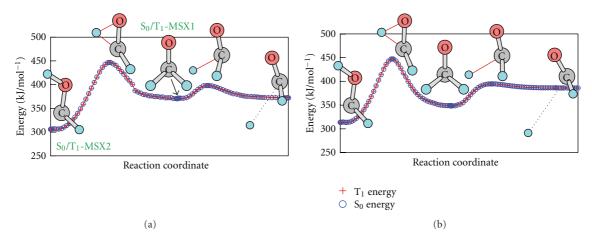


FIGURE 4: (a) A S_0/T_1 -MEPSX curve for HCOH \leftrightarrow H₂CO \leftrightarrow HCO + H at the CASPT2 level (see Section 2.4 for details of the CASPT2 calculations) and (b) a S_0/T_1 -MEPSX curve for the same reaction at the UB3LYP/aug-cc-pVDZ level.

 $CH_3CO \cdot \cdot \cdot CH_3$ region through only one SPSX structure, that is, it does not enter the potential well of $(CH_3)_2CO$. In contrast to Figure 4, these intersection spaces lie in a very high-energy region in the potential well of $(CH_3)_2CO$. Only outside the potential well, the intersection space comes down to a low-energy region. Thus, the S_0/T_1 ISC is expected to be much slower in $(CH_3)_2CO$ than the case of H_2CO , although $(CH_3)_2CO$ also has a very wide S_0/T_1 intersection space.

6. A Merit of Automated Search

The most significant advantage of the present approach is that unexpected pathways can be discovered. Geometry optimization has been a very powerful mean to locate exact MSXs and TSs starting from guessed geometries. However, a guess structure leads only to a TS or a MSX anticipated from it. On excited state PESs, molecules frequently take unexpected geometries that are very different from those of stable ground state molecules. Hence, the advantage of the present method without guess is very helpful in analyses of photochemical reactions.

We already reported some unexpected paths discovered by the present recipe. The first is the S₀/T₁ ISC path for H₂CO as discussed above [49]. The second is an H-atom roundtrip path discovered in photolysis of methyl-ethylketone CH₃C(O)C₂H₅ [138]. In this path, on the S₁ PES, an H atom in the ethylgroup at first transfers to the O atom to undergo an S₀/S₁ IC in a conical intersection of a diradical isomer, and then the H atom comes back to the original position on the S₀ PES, and finally the molecule dissociates into $CH_3CO + C_2H_5$ or $C_2H_5CO + CH_3$ on the S_0 PES. This path explained an experimental photodissociation quantum yields measurements very well. The third is the discovery for the first time of the excited state roaming pathway, which we found in photolysis of NO₃ [107, 108]. Here, one of the O atoms in NO₃ partially dissociates on the first excited doublet (D₁) PES and then roams around the NO₂ fragment before producing O₂ + NO on either the D₁ PES or the ground state D₀ PES. This mechanism

also explained very well recent experimental results giving two channels, one with hot O_2 and the other with cold O_2 [105, 106]. Unexpected nonadiabatic ignition paths of unsaturated hydrocarbons were also discovered by the SMF-AFIR approach very recently [50].

7. Conclusion and Perspective

We reviewed our recipe to explore multiple PESs systematically by using an automated reaction path search method which has been used for the ground state (smooth) PESs [49, 50]. In this paper, it was applied together with the GRRM method [43–45] to small carbonyl compounds to study their photodissociation mechanisms. In an application to H₂CO [49], we discovered a new nonadiabatic (S₀/T₁ ISC) path to reproduce the ground state species in the potential well of H₂CO. This path was recently confirmed by extensive 3S-TSH simulations using very accurate PESs [117]. For (CH₃)₂CO [51], many possible nonadiabatic decay paths from the S₁ PES were systematically located, and new insight into the slow S₁/T₁ ISC and new nonadiabatic paths to the ground state PES were obtained.

Three or more states may couple simultaneously in some reactions. An extension of the present approaches is straightforward since both (1) and (2) are similar to the equation for the diabatic/adiabatic transformation, although we have not yet made systematic tests for such cases.

Dynamic effects may play a significant role in many reactions. Although direct dynamics is very useful in simulations with moderate accuracies [139], it is still too expensive to find all the reaction events of a given system including slow events. There are many powerful approaches applied to ground state PESs to accelerate a dynamics for known mechanisms [140–142]. A prior mechanism search by the present approach followed by such accelerated dynamics may be a solution in the future for theoretical solving complicated reaction mechanisms. The present method can also be connected to the analytical PES fitting approach [143–146] which enabled the recent extensive 3S-TSH simulations of

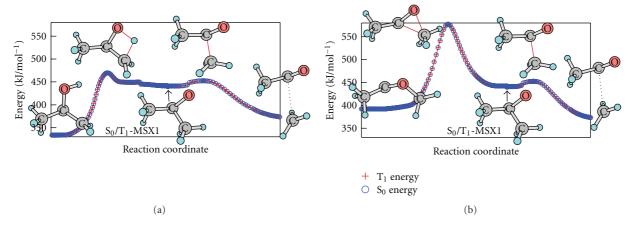


FIGURE 5: (a) A S_0/T_1 -MEPSX curve for $H_2C=C(OH)CH_3 \leftrightarrow (CH_3)_2CO \leftrightarrow CH_3CO + CH_3$ and (b) a S_0/T_1 -MEPSX curve for $CH_3-CO-CH_3 \leftrightarrow (CH_3)_2CO \leftrightarrow CH_3CO + CH_3$, at the UB3LYP/6-31+G* level.

H₂CO [117]. This approach permits the execution of highly accurate simulations, although applications are limited to small systems including less than 20 atoms. In constructing an analytical PES, prior knowledge about the mechanisms obtained by the present approach will be very useful for effective sampling of the PES data with the least number of ab initio calculations, avoiding exhaustive sampling on a perfect grid covering all configurations. One technical but significant issue in this approach is how to represent the square root topology of conical intersections, and several approaches have been proposed [147–150].

Our particular interest is to apply the present approach to multiple PESs described by combined quantum mechanical and molecular mechanical (QM/MM) calculations [151–154]. We have already reported automated reaction path search on the ground state PES of the QM/MM-ONIOM method [155] by combined microiteration [156, 157] and GRRM methods [158], where use of AFIR instead of GRRM has already been possible. This development is expected to greatly expand the applicability of the present approach to large systems.

Acknowledgements

This work is partly supported by a grant from Japan Science and Technology Agency with a Core Research for Evolutional Science and Technology (CREST) in the area of high-performance computing for multiscale and multiphysics phenomena at Kyoto University as well as a grant from US AFOSR (Grant no. FA9550-10-1-0304) at Emory University.

References

- [1] F. Bernardi, M. Olivucci, and M. A. Robb, "Potential energy surface crossings in organic photochemistry," *Chemical Society Reviews*, vol. 25, no. 5, pp. 321–328, 1996.
- [2] D. R. Yarkony, "Conical intersections: diabolical and often misunderstood," *Accounts of Chemical Research*, vol. 31, no. 8, pp. 511–518, 1998.

- [3] D. Schröder, S. Shaik, and H. Schwarz, "Two-state reactivity as a new concept in organometallic chemistry," *Accounts of Chemical Research*, vol. 33, no. 3, pp. 139–145, 2000.
- [4] A. L. Sobolewski, W. Domcke, C. Dedonder-Lardeux, and C. Jouvet, "Excited-state hydrogen detachment and hydrogen transfer driven by repulsive $1\pi\sigma^*$ states: a new paradigm for nonradiative decay in aromatic biomolecules," *Physical Chemistry Chemical Physics*, vol. 4, no. 7, pp. 1093–1100, 2002.
- [5] R. Poli and J. N. Harvey, "Spin forbidden chemical reactions of transition metal compounds. New ideas and new computational challenges," *Chemical Society Reviews*, vol. 32, no. 1, pp. 1–8, 2003.
- [6] B. G. Levine and T. J. Martínez, "Isomerization through conical intersections," *Annual Review of Physical Chemistry*, vol. 58, pp. 613–634, 2007.
- [7] S. Nanbu, T. Ishida, and H. Nakamura, "Future perspectives of nonadiabatic chemical dynamics," *Chemical Science*, vol. 1, pp. 663–674, 2010.
- [8] N. Koga and K. Morokuma, "Determination of the lowest energy point on the crossing seam between two potential surfaces using the energy gradient," *Chemical Physics Letters*, vol. 119, no. 5, pp. 371–374, 1985.
- [9] M. R. Manaa and D. R. Yarkony, "On the intersection of two potential energy surfaces of the same symmetry. Systematic characterization using a Lagrange multiplier constrained procedure," *The Journal of Chemical Physics*, vol. 99, no. 7, pp. 5251–5256, 1993.
- [10] J. M. Anglada and J. M. Bofill, "A reduced-restricted-quasi-Newton-Raphson method for locating and optimizing energy crossing points between two potential energy surfaces," *Journal of Computational Chemistry*, vol. 18, no. 8, pp. 992–1003, 1997.
- [11] M. J. Bearpark, M. A. Robb, and H. Bernhard Schlegel, "A direct method for the location of the lowest energy point on a potential surface crossing," *Chemical Physics Letters*, vol. 223, no. 3, pp. 269–274, 1994.
- [12] F. Sicilia, L. Blancafort, M. J. Bearpark, and M. A. Robb, "New algorithms for optimizing and linking conical intersection points," *Journal of Chemical Theory and Computation*, vol. 4, no. 2, pp. 257–266, 2008.

- [13] C. Ciminelli, G. Granucci, and M. Persico, "The photoisomerization mechanism of azobenzene: a semiclassical simulation of nonadiabatic dynamics," *Chemistry*, vol. 10, no. 9, pp. 2327–2341, 2004.
- [14] B. G. Levine, J. D. Coe, and T. J. Martínez, "Optimizing conical intersections without derivative coupling vectors: application to multistate multireference second-order perturbation theory (MS-CASPT2)," *Journal of Physical Chemistry B*, vol. 112, no. 2, pp. 405–413, 2008.
- [15] T. W. Keal, A. Koslowski, and W. Thiel, "Comparison of algorithms for conical intersection optimisation using semiem-pirical methods," *Theoretical Chemistry Accounts*, vol. 118, no. 5-6, pp. 837–844, 2007.
- [16] S. Maeda, K. Ohno, and K. Morokuma, "Updated branching plane for finding conical intersections without coupling derivative vectors," *Journal of Chemical Theory and Computation*, vol. 6, no. 5, pp. 1538–1545, 2010.
- [17] J. W. McIver Jr. and A. Komornicki, "Structure of transition states in organic reactions. General theory and an application to the cyclobutene-butadiene isomerization using a semiempirical molecular orbital method," *Journal of the American Chemical Society*, vol. 94, no. 8, pp. 2625–2633, 1972.
- [18] A. Komornicki, K. Ishida, K. Morokuma, R. Ditchfield, and M. Conrad, "Efficient determination and characterization of transition states using ab-initio methods," *Chemical Physics Letters*, vol. 45, no. 3, pp. 595–602, 1977.
- [19] H. B. Schlegel, "Optimization of equilibrium geometries and transition structures," *Journal of Computational Chemistry*, vol. 3, no. 2, pp. 214–218, 1982.
- [20] Ö Farkas and H. B. Schlegel, "Methods for optimizing large molecules. II. Quadratic search," *Journal of Chemical Physics*, vol. 111, no. 24, pp. 10806–10814, 1999.
- [21] C. J. Cerjan and W. H. Miller, "On finding transition states," The Journal of Chemical Physics, vol. 75, no. 6, pp. 2800–2801, 1981.
- [22] P. Császár and P. Pulay, "Geometry optimization by direct inversion in the iterative subspace," *Journal of Molecular Structure*, vol. 114, no. 1-2, pp. 31–34, 1984.
- [23] A. Banerjee, N. Adams, J. Simons, and R. Shepard, "Search for stationary points on surfaces," *Journal of Physical Chemistry*, vol. 89, no. 1, pp. 52–57, 1985.
- [24] H. B. Schlegel, "Exploring potential energy surfaces for chemical reactions: an overview of some practical methods," *Journal of Computational Chemistry*, vol. 24, no. 12, pp. 1514– 1527, 2003.
- [25] F. Jensen, *Introduction to Computational Chemistry*, John Wiley & Sons, Chichester, UK, 2nd edition, 2007.
- [26] H. B. Schlegel, "Geometry optimization," Wiley Interdisciplinary Reviews: Computational Molecular Science, vol. 1, no. 5, pp. 790–809, 2011.
- [27] T. A. Halgren and W. N. Lipscomb, "The synchronous-transit method for determining reaction pathways and locating molecular transition states," *Chemical Physics Letters*, vol. 49, no. 2, pp. 225–232, 1977.
- [28] M. J. S. Dewar, E. F. Healy, and J. J. P. Stewart, "Location of transition states in reaction mechanisms," *Journal of* the Chemical Society, Faraday Transactions 2: Molecular and Chemical Physics, vol. 80, no. 3, pp. 227–233, 1984.
- [29] R. Elber and M. Karplus, "A method for determining reaction paths in large molecules: application to myoglobin," *Chemical Physics Letters*, vol. 139, no. 5, pp. 375–380, 1987.
- [30] G. Henkelman, B. P. Uberuaga, and H. Jónsson, "Climbing image nudged elastic band method for finding saddle points

- and minimum energy paths," *Journal of Chemical Physics*, vol. 113, no. 22, pp. 9901–9904, 2000.
- [31] W. Ren and E. Vanden-Eijnden, "String method for the study of rare events," *Physical Review B*, vol. 66, no. 5, Article ID 052301, 2002.
- [32] B. Peters, A. Heyden, A. T. Bell, and A. Chakraborty, "A growing string method for determining transition states: comparison to the nudged elastic band and string methods," *Journal of Chemical Physics*, vol. 120, no. 17, pp. 7877–7886, 2004.
- [33] S. Maeda and K. Ohno, "A new approach for finding a transition state connecting a reactant and a product without initial guess: applications of the scaled hypersphere search method to isomerization reactions of HCN, (H₂O)₂, and alanine dipeptide," *Chemical Physics Letters*, vol. 404, no. 1–3, pp. 95–99, 2005.
- [34] S. Maeda and K. Ohno, "Conversion pathways between a fullerene and a ring among C₂₀ clusters by a sphere contracting walk method: remarkable difference in local potential energy landscapes around the fullerene and the ring," *Journal of Chemical Physics*, vol. 124, no. 17, Article ID 174306, 2006.
- [35] M. Černohorský, S. Kettou, and J. Koča, "VADER: new soft-ware for exploring interconversions on potential energy surfaces," *Journal of Chemical Information and Computer Sciences*, vol. 39, no. 4, pp. 705–712, 1999.
- [36] A. Laio and M. Parrinello, "Escaping free-energy minima," *Proceedings of the National Academy of Sciences of the United States of America*, vol. 99, no. 20, pp. 12562–12566, 2002.
- [37] S. K. Burger and P. W. Ayers, "Dual grid methods for finding the reaction path on reduced potential energy surfaces," *Journal of Chemical Theory and Computation*, vol. 6, no. 5, pp. 1490–1497, 2010.
- [38] J. Q. Sun and K. Ruedenberg, "Gradient extremals and steepest descent lines on potential energy surfaces," *The Journal of Chemical Physics*, vol. 98, no. 12, pp. 9707–9714, 1993.
- [39] K. Bondensgård and F. Jensen, "Gradient extremal bifurcation and turning points: an application to the H₂CO potential energy surface," *Journal of Chemical Physics*, vol. 104, no. 20, pp. 8025–8031, 1996.
- [40] W. Quapp, M. Hirsch, O. Imig, and D. Heidrich, "Searching for saddle points of potential energy surfaces by following a reduced gradient," *Journal of Computational Chemistry*, vol. 19, no. 9, pp. 1087–1100, 1998.
- [41] K. K. Irikura and R. D. Johnson, "Predicting unexpected chemical reactions by isopotential searching," *Journal of Physical Chemistry A*, vol. 104, no. 11, pp. 2191–2194, 2000.
- [42] E. M. Müller, A. de Meijere, and H. Grubmüller, "Predicting unimolecular chemical reactions: chemical flooding," *Journal of Chemical Physics*, vol. 116, no. 3, pp. 897–905, 2002.
- [43] K. Ohno and S. Maeda, "A scaled hypersphere search method for the topography of reaction pathways on the potential energy surface," *Chemical Physics Letters*, vol. 384, no. 4–6, pp. 277–282, 2004.
- [44] S. Maeda and K. Ohno, "Global mapping of equilibrium and transition structures on potential energy surfaces by the scaled hypersphere search method: applications to ab initio surfaces of formaldehyde and propyne molecules," *Journal of Physical Chemistry A*, vol. 109, no. 25, pp. 5742–5753, 2005.
- [45] K. Ohno and S. Maeda, "Global reaction route mapping on potential energy surfaces of formaldehyde, formic acid, and their metal-substituted analogues," *Journal of Physical Chemistry A*, vol. 110, no. 28, pp. 8933–8941, 2006.

- [46] S. Maeda and K. Morokuma, "Communications: a systematic method for locating transition structures of A+B → X type reactions," *Journal of Chemical Physics*, vol. 132, no. 24, Article ID 241102, 2010.
- [47] S. Maeda, S. Komagawa, M. Uchiyama, and K. Morokuma, "Finding reaction pathways for multicomponent reactions: the passerini reaction is a four-component reaction," *Angewandte Chemie*, vol. 50, no. 3, pp. 644–649, 2011.
- [48] S. Maeda and K. Morokuma, "Finding reaction pathways of type A + B → X: toward systematic prediction of reaction mechanisms," *Journal of Chemical Theory and Computation*, vol. 7, no. 8, pp. 2335–2345, 2011.
- [49] S. Maeda, K. Ohno, and K. Morokuma, "Automated global mapping of minimal energy points on seams of crossing by the anharmonic downward distortion following method: a case study of H₂CO," *Journal of Physical Chemistry A*, vol. 113, no. 9, pp. 1704–1710, 2009.
- [50] S. Maeda, R. Saito, and K. Morokuma, "Finding minimum structures on the seam of crossing in reactions of type A + B → X: exploration of nonadiabatic ignition pathways of unsaturated hydrocarbons," *Journal of Physical Chemistry Letters*, vol. 2, no. 8, pp. 852–857, 2011.
- [51] S. Maeda, K. Ohno, and K. Morokuma, "A theoretical study on the photodissociation of acetone: insight into the slow intersystem crossing and exploration of nonadiabatic pathways to the ground state," *Journal of Physical Chemistry Letters*, vol. 1, no. 12, pp. 1841–1845, 2010.
- [52] K. Fukui, "A formulation of the reaction coordinate," *Journal of Physical Chemistry*, vol. 74, no. 23, p. 4161, 1970.
- [53] K. Ishida, K. Morokuma, and A. Komornicki, "The intrinsic reaction coordinate. An ab initio calculation for HNC → HCN and H⁻ + CH4 → CH₄ + H⁻," *The Journal of Chemical Physics*, vol. 66, no. 5, pp. 2153–2156, 1976.
- [54] K. Müller and L. D. Brown, "Location of saddle points and minimum energy paths by a constrained simplex optimization procedure," *Theoretica Chimica Acta*, vol. 53, no. 1, pp. 75–93, 1979.
- [55] M. Page and J. W. McIver Jr., "On evaluating the reaction path Hamiltonian," *The Journal of Chemical Physics*, vol. 88, no. 2, pp. 922–935, 1988.
- [56] C. Gonzalez and H. Bernhard Schlegel, "An improved algorithm for reaction path following," *The Journal of Chemical Physics*, vol. 90, no. 4, pp. 2154–2161, 1989.
- [57] H. P. Hratchian and H. B. Schlegel, "Using Hessian updating to increase the efficiency of a Hessian based predictor-corrector reaction path following method," *Journal of Chemical Theory and Computation*, vol. 1, no. 1, pp. 61–69, 2005.
- [58] S. Maeda and K. Ohno, "Structures of water octamers (H₂O)₈: exploration on ab initio potential energy surfaces by the scaled hypersphere search method," *Journal of Physical Chemistry A*, vol. 111, no. 20, pp. 4527–4534, 2007.
- [59] H.-J. Werner, P. J. Knowles, F. R. Manby et al., MOL-PRO, version 2006.1, a package of ab initio programs, http://www.molpro.net.
- [60] S. Maeda, Y. Osada, K. Morokuma, and K. Ohno, GRRM11, http://kmweb.fukui.kyoto-u.ac.jp/~smaeda/GRRM_PR000 .html.
- [61] W. M. Gelbart, M. L. Elert, and D. F. Heller, "Photodissociation of the formaldehyde molecule: does it or doesn't it?" Chemical Reviews, vol. 80, no. 5, pp. 403–416, 1980.
- [62] C. B. Moore and J. C. Weisshaar, "Formaldehyde photochemistry," *Annual Review of Physical Chemistry*, vol. 34, pp. 525– 555, 1983.

- [63] D. J. Clouthier and D. A. Ramsay, "The spectroscopy of formaldehyde and thioformaldehyde," *Annual Review of Physical Chemistry*, vol. 34, pp. 31–58, 1983.
- [64] W. H. Green Jr., C. B. Moore, and W. F. Polik, "Transition states and rate constants for unimolecular reactions," *Annual Review of Physical Chemistry*, vol. 43, no. 1, pp. 591–626, 1992.
- [65] C. B. Moore, "A spectroscopist's view of energy states, energy transfers, and chemical reactions," *Annual Review of Physical Chemistry*, vol. 58, pp. 1–33, 2007.
- [66] D. M. Hayes and K. Morokuma, "Theoretical studies of carbonyl photochemistry. I. ab initio potential energy surfaces for the photodissociation H₂CO* → H + HCO," *Chemical Physics Letters*, vol. 12, no. 4, pp. 539–543, 1972.
- [67] R. L. Jaffe, D. M. Hayes, and K. Morokuma, "Photodissociation of formaldehyde-4: potential energy surfaces for H₂CO* → H₂ + CO," *The Journal of Chemical Physics*, vol. 60, no. 12, pp. 5108–5109, 1974.
- [68] J. A. Hernandez and R. Carbo, "Theoretical-study of formaldehyde photodissociation," *Journal de Chimie Physique et de Physico-Chimie Biologique*, vol. 72, no. 9, pp. 959–960, 1975.
- [69] R. L. Jaffe and K. Morokuma, "MCSCF potential energy surface for photodissociation of formaldehyde," *The Journal* of Chemical Physics, vol. 64, no. 12, pp. 4881–4886, 1976.
- [70] J. D. Goddard and H. F. Schaefer, "The photodissociation of formaldehyde: potential energy surface features," *The Journal* of *Chemical Physics*, vol. 70, no. 11, pp. 5117–5134, 1979.
- [71] N. C. Handy and S. Carter, "An improved potential surface for formaldehyde," *Chemical Physics Letters*, vol. 79, no. 1, pp. 118–124, 1981.
- [72] R. Schinke, "Rotational state distributions of H₂ and CO following the photofragmentation of formaldehyde," *The Journal of Chemical Physics*, vol. 84, no. 3, pp. 1487–1491, 1986
- [73] G. E. Scuseria and H. F. Schaefer, "The photodissociation of formaldehyde: a coupled cluster study including connected triple excitations of the transition state barrier height for H₂CO → H₂ + CO," *The Journal of Chemical Physics*, vol. 90, no. 7, pp. 3629–3636, 1989.
- [74] Y. T. Chang, C. Minichino, and W. H. Miller, "Classical trajectory studies of the molecular dissociation dynamics of formaldehyde: H₂CO → H₂+CO," *The Journal of Chemical Physics*, vol. 96, no. 6, pp. 4341–4355, 1992.
- [75] L. Deng, T. Ziegler, and L. Fan, "A combined density functional and intrinsic reaction coordinate study on the ground state energy surface of H₂CO," *The Journal of Chemical Physics*, vol. 99, no. 5, pp. 3823–3835, 1993.
- [76] W. Chen, W. L. Hase, and H. B. Schlegel, "Ab initio classical trajectory study of H₂CO → H₂+CO dissociation," *Chemical Physics Letters*, vol. 228, no. 4-5, pp. 436–442, 1994.
- [77] G. H. Peslherbe and W. L. Hase, "Semiempirical MNDO, AM1, and PM3 direct dynamics trajectory studies of formaldehyde unimolecular dissociation," *Journal of Chemical Physics*, vol. 104, no. 20, pp. 7882–7894, 1996.
- [78] H. Nakano, K. Nakayama, K. Hirao, and M. Dupuis, "Transition state barrier height for the reaction H₂CO → H₂+CO studied by multireference Møller-Plesset perturbation theory," *Journal of Chemical Physics*, vol. 106, no. 12, pp. 4912–4917, 1997.
- [79] F. Jensen, "Stationary points on the H₂CO potential energy surface: dependence on theoretical level," *Theoretical Chemistry Accounts*, vol. 99, no. 5, pp. 295–300, 1998.
- [80] D. Feller, M. Dupuis, and B. C. Garrett, "Barrier for the $H_2CO \rightarrow H_2+CO$ reaction: a discrepancy between high-level

- electronic structure calculations and experiment," *Journal of Chemical Physics*, vol. 113, no. 1, pp. 218–226, 2000.
- [81] X. Li, J. M. Millam, and H. B. Schlegel, "Ab initio molecular dynamics studies of the photodissociation of formaldehyde, H₂CO → H₂ + CO: direct classical trajectory calculations by MP2 and density functional theory," *Journal of Chemical Physics*, vol. 113, no. 22, pp. 10062–10067, 2000.
- [82] H. B. Schlegel, S. S. Iyengar, X. Li et al., "Ab initio molecular dynamics: propagating the density matrix with Gaussian orbitals. III. Comparison with Born-Oppenheimer dynamics," *Journal of Chemical Physics*, vol. 117, no. 19, pp. 8694– 8704, 2002.
- [83] T. Yonehara and S. Kato, "Role of isomerization channel in unimolecular dissociation reaction H₂CO → H₂+CO: Ab initio global potential energy surface and classical trajectory analysis," *Journal of Chemical Physics*, vol. 117, no. 24, pp. 11131–11138, 2003.
- [84] X. Zhang, S. Zou, L. B. Harding, and J. M. Bowman, "A global ab initio potential energy surface for formaldehyde," *Journal* of *Physical Chemistry A*, vol. 108, no. 41, pp. 8980–8986, 2004.
- [85] X. Zhang, J. L. Rheinecker, and J. M. Bowman, "Quasiclassical trajectory study of formaldehyde unimolecular dissociation: H₂ CO → H₂ + CO, H + HCO," *Journal of Chemical Physics*, vol. 122, no. 11, Article ID 114313, 8 pages, 2005.
- [86] T. Yonehara and S. Kato, "Quantum dynamics study on multichannel dissociation and isomerization reactions of formaldehyde," *Journal of Chemical Physics*, vol. 125, no. 8, Article ID 084307, 2006.
- [87] J. M. Bowman and X. Zhang, "New insights on reaction dynamics from formaldehyde photodissociation," *Physical Chemistry Chemical Physics*, vol. 8, no. 3, pp. 321–332, 2006.
- [88] L. B. Harding, S. J. Klippenstein, and A. W. Jasper, "Ab initio methods for reactive potential surfaces," *Physical Chemistry Chemical Physics*, vol. 9, no. 31, pp. 4055–4070, 2007.
- [89] S. Maeda and K. Ohno, "A new global reaction route map on the potential energy surface of H₂CO with unrestricted level," *Chemical Physics Letters*, vol. 460, no. 1–3, pp. 55–58, 2008.
- [90] Y. Yamaguchi, S. S. Wesolowski, T. J. Van Huis, and H. F. Schaefer, "The unimolecular dissociation of H₂CO on the lowest triplet potential-energy surface," *Journal of Chemical Physics*, vol. 108, no. 13, pp. 5281–5288, 1998.
- [91] H. M. Yin, S. H. Kable, X. Zhang, and J. M. Bowman, "Signatures of H₂CO photodissociation from two electronic states," *Science*, vol. 311, no. 5766, pp. 1443–1446, 2006.
- [92] K. K. Baeck, "The analytic gradient for the equation-of-motion coupled-cluster energy with a reduced molecular orbital space: an application for the first excited state of formaldehyde," *Journal of Chemical Physics*, vol. 112, no. 1, pp. 1–4, 2000.
- [93] J. B. Simonsen, N. Rusteika, M. S. Johnson, and T. I. Sølling, "Atmospheric photochemical loss of H and H₂ from formaldehyde: the relevance of ultrafast processes," *Physical Chemistry Chemical Physics*, vol. 10, no. 5, pp. 674–680, 2008.
- [94] R. D. Van Zee, M. F. Foltz, and C. B. Moore, "Evidence for a second molecular channel in the fragmentation of formaldehyde," *Journal of Chemical Physics*, vol. 99, no. 3, pp. 1664–1673, 1993.
- [95] D. Townsend, S. A. Lahankar, S. K. Lee et al., "The roaming atom: straying from the reaction path in formaldehyde decomposition," *Science*, vol. 306, no. 5699, pp. 1158–1161, 2004.

- [96] A. G. Suits, "Roaming atoms and radicals: a new mechanism in molecular dissociation," *Accounts of Chemical Research*, vol. 41, no. 7, pp. 873–881, 2008.
- [97] N. Herath and A. G. Suits, "Roaming radical reactions," Journal of Physical Chemistry Letters, vol. 2, no. 6, pp. 642–647, 2011.
- [98] J. M. Bowman and B. C. Shepler, "Roaming radicals," *Annual Review of Physical Chemistry*, vol. 62, pp. 531–553, 2011.
- [99] P. L. Houston and S. H. Kable, "Photodissociation of acetaldehyde as a second example of the roaming mechanism," *Proceedings of the National Academy of Sciences of the United States of America*, vol. 103, no. 44, pp. 16079–16082, 2006.
- [100] B. C. Shepler, B. J. Braams, and J. M. Bowman, "Quasiclassical trajectory calculations of acetaldehyde dissociation on a global potential energy surface indicate significant non-transition state dynamics," *Journal of Physical Chemistry A*, vol. 111, no. 34, pp. 8282–8285, 2007.
- [101] B. R. Heazlewood, M. J. T. Jordan, S. H. Kable et al., "Roaming is the dominant mechanism for molecular products in acetaldehyde photodissociation," *Proceedings of the National Academy of Sciences of the United States of America*, vol. 105, no. 35, pp. 12719–12724, 2008.
- [102] V. Goncharov, N. Herath, and A. G. Suits, "Roaming dynamics in acetone dissociation," *Journal of Physical Chemistry A*, vol. 112, no. 39, pp. 9423–9428, 2008.
- [103] C. Chen, B. Braams, D. Y. Lee, J. M. Bowman, P. L. Houston, and D. Stranges, "Evidence for vinylidene production in the photodissociation of the allyl radical," *Journal of Physical Chemistry Letters*, vol. 1, no. 12, pp. 1875–1880, 2010.
- [104] E. Kamarchik, L. Koziol, H. Reisler, J. M. Bowman, and A. I. Krylov, "Roaming pathway leading to unexpected water + vinyl products in C₂H₄OH dissociation," *Journal of Physical Chemistry Letters*, vol. 1, no. 20, pp. 3058–3065, 2010.
- [105] M. P. Grubb, M. L. Warter, A. G. Suits, and S. W. North, "Evidence of roaming dynamics and multiple channels for molecular elimination in NO₃ photolysis," *The Journal of Physical Chemistry Letters*, vol. 1, pp. 2455–2458, 2010.
- [106] M. P. Grubb, M. L. Warter, K. M. Johnson, and S. W. North, "Ion imaging study of NO₃ radical photodissociation dynamics: characterization of multiple reaction pathways," *Journal of Physical Chemistry*, vol. 115, no. 15, pp. 3218–3226, 2011.
- [107] H. Xiao, S. Maeda, and K. Morokuma, "Excited-state roaming dynamics in photolysis of a nitrate radical," *Journal of Physical Chemistry Letters*, vol. 2, no. 9, pp. 934–938, 2011.
- [108] S. W. North, "Roaming in the dark," *Nature Chemistry*, vol. 3, no. 7, pp. 504–505, 2011.
- [109] A. Fernández-Ramos, J. A. Miller, S. J. Klippenstein, and D. G. Truhlar, "Modeling the kinetics of bimolecular reactions," *Chemical Reviews*, vol. 106, no. 11, pp. 4518–4584, 2006.
- [110] L. B. Harding and S. J. Klippenstein, "Roaming radical pathways for the decomposition of alkanes," *Journal of Physical Chemistry Letters*, vol. 1, no. 20, pp. 3016–3020, 2010.
- [111] P. Zhang, Applications of electronic structure theory in the study of molecular processes, Ph.D. thesis, Emory University, 2005.
- [112] B. C. Shepler, E. Epifanovsky, P. Zhang, J. M. Bowman, A. I. Krylov, and K. Morokuma, "Photodissociation dynamics of formaldehyde initiated at the T_1/S_0 minimum energy crossing configurations," *Journal of Physical Chemistry A*, vol. 112, no. 51, pp. 13267–13270, 2008.
- [113] M. Araujo, B. Lasorne, M. J. Bearpark, and M. A. Robb, "The photochemistry of formaldehyde: internal conversion and

- molecular dissociation in a single step?" *Journal of Physical Chemistry A*, vol. 112, no. 33, pp. 7489–7491, 2008.
- [114] P. Zhang, S. Maeda, K. Morokuma, and B. J. Braams, "Photochemical reactions of the low-lying excited states of formaldehyde: T₁/S₀ intersystem crossings, characteristics of the S₁ and T₁ potential energy surfaces, and a global T₁ potential energy surface," *Journal of Chemical Physics*, vol. 130, no. 11, Article ID 114304, 2009.
- [115] M. Araújo, B. Lasorne, A. L. Magalhães, G. A. Worth, M. J. Bearpark, and M. A. Robb, "The molecular dissociation of formaldehyde at medium photoexcitation energies: a quantum chemistry and direct quantum dynamics study," *Journal of Chemical Physics*, vol. 131, no. 14, Article ID 144301, 2009.
- [116] M. Arauéjo, B. Lasorne, A. L. Magalhaes, M. J. Bearpark, and M. A. Robb, "Controlling product selection in the photodissociation of formaldehyde: direct quantum dynamics from the S₁ barrier," *Journal of Physical Chemistry A*, vol. 114, no. 45, pp. 12016–12020, 2010.
- [117] B. Fu, B. C. Shepler, and J. M. Bowman, "hree-state trajectory surface hopping studies of the photodissociation dynamics of formaldehyde on ab initio potential energy surfaces," *Journal* of the American Chemical Society, vol. 133, no. 20, pp. 7957– 7968, 2011.
- [118] Y. Haas, "Photochemical α-cleavage of ketones: revisiting acetone," *Photochemical and Photobiological Sciences*, vol. 3, no. 1, pp. 6–16, 2004.
- [119] R. A. Copeland and D. R. Crosley, "Radiative, collisional and dissociative processes in triplet acetone," *Chemical Physics Letters*, vol. 115, no. 4-5, pp. 362–368, 1985.
- [120] H. Zuckermann, B. Schmitz, and Y. Haas, "Dissociation energy of an isolated triplet acetone molecule," *Journal of Physical Chemistry*, vol. 92, no. 17, pp. 4835–4837, 1988.
- [121] S. W. North, D. A. Blank, J. Daniel Gezelter, C. A. Longfellow, and Y. T. Lee, "Evidence for stepwise dissociation dynamics in acetone at 248 and 193 nm," *The Journal of Chemical Physics*, vol. 102, no. 11, pp. 4447–4460, 1995.
- [122] D. Liu, W. H. Fang, and X. Y. Fu, "An ab initio study on photodissociation of acetone," *Chemical Physics Letters*, vol. 325, no. 1–3, pp. 86–92, 2000.
- [123] E. W. G. Diau, G. Kötting, and A. H. Zewail, "Femto-chemistry of norrish type-1 reactions. I. Experimental and theoretical studies of acetone and related ketones on the s1 surface," *ChemPhysChem*, vol. 2, no. 5, pp. 273–293, 2001.
- [124] E. W. G. Diau, C. Kötting, T. I. Sølling, and A. H. Zewail, "Femtochemistry of Norrish type-I reactions. III. Highly excited ketones—theoretical," *ChemPhysChem*, vol. 3, no. 1, pp. 57–78, 2002.
- [125] T. I. Sølling, E. W. G. Diau, C. Kötting, S. de Feyter, and A. H. Zewail, "Femtochemistry of Norrish type-I reactions. IV. Highly excited ketones—experimental," *ChemPhysChem*, vol. 3, no. 1, pp. 79–97, 2002.
- [126] W. K. Chen, J. W. Ho, and P. Y. Cheng, "Ultrafast photodissociation dynamics of the acetone 3s Rydberg state at 195 nm: a new mechanism," *Chemical Physics Letters*, vol. 380, no. 3-4, pp. 411–418, 2003.
- [127] W. K. Chen, J. W. Ho, and P. Y. Cheng, "Ultrafast photodissociation dynamics of acetone at 195 nm. I. Initial-state, intermediate, and product temporal evolutions by femtosecond mass-selected multiphoton ionization spectroscopy," *Journal of Physical Chemistry A*, vol. 109, no. 31, pp. 6805–6817, 2005.
- [128] W. K. Chen and P. Y. Cheng, "Ultrafast photodissociation dynamics of acetone at 195 nm: II. Unraveling complex

- three-body dissociation dynamics by femtosecond timeresolved photofragment translational spectroscopy," *Journal* of *Physical Chemistry A*, vol. 109, no. 31, pp. 6818–6829, 2005.
- [129] H. Somnitz, M. Fida, T. Ufer, and R. Zellner, "Pressure dependence for the CO quantum yield in the photolysis of acetone at 248 nm: a combined experimental and theoretical study," *Physical Chemistry Chemical Physics*, vol. 7, no. 18, pp. 3342–3352, 2005.
- [130] V. Khamaganov, R. Karunanandan, A. Rodriguez, and J. N. Crowley, "Photolysis of CH₃C(O)CH₃ (248 nm, 266 nm), CH₃C(O)C₂H₅ (248 nm) and CH₃C(O)Br (248 nm): pressure dependent quantum yields of CH₃ formation," *Physical Chemistry Chemical Physics*, vol. 9, no. 31, pp. 4098–4113, 2007.
- [131] R. Nádasdi, G. Kovács, I. Szilágyi et al., "Exciplex laser photolysis study of acetone with relevance to tropospheric chemistry," *Chemical Physics Letters*, vol. 440, no. 1–3, pp. 31– 35, 2007.
- [132] I. Antol, M. Eckert-Maksić, M. Ončák, P. Slavíček, and H. Lischka, "Photodissociation pathways of acetone upon excitation into the 3s Rydberg state: adiabatic versus diabatic mechanism," Collection of Czechoslovak Chemical Communications, vol. 73, no. 11, pp. 1475–1494, 2008.
- [133] H. Somnitz, T. Ufer, and R. Zellner, "Acetone photolysis at 248 nm revisited: pressure dependence of the CO and CO₂ quantum yields," *Physical Chemistry Chemical Physics*, vol. 11, no. 38, pp. 8522–8531, 2009.
- [134] T. Shibata and T. Suzuki, "Photofragment ion imaging with femtosecond laser pulses," *Chemical Physics Letters*, vol. 262, no. 1-2, pp. 115–119, 1996.
- [135] N. Rusteika, K. B. Møller, and T. I. Sølling, "New insights on the photodynamics of acetone excited with 253–288 nm femtosecond pulses," *Chemical Physics Letters*, vol. 461, no. 4–6, pp. 193–197, 2008.
- [136] R. Y. Brogaard, T. I. Sølling, and K. B. Møller, "Initial dynamics of the Norrish Type I reaction in acetone: probing wave packet motion," *Journal of Physical Chemistry A*, vol. 115, no. 15, pp. 556–561, 2011.
- [137] M. J. Frisch, G. W. Trucks, H. B. Schlegel et al., "Gaussian 09 Revision A.2," Wallingford CT, 2009.
- [138] R. Nádasdi, G. L. Zügner, M. Farkas, S. Dōbé, S. Maeda, and K. Morokuma, "Photochemistry of methyl ethyl ketone: quantum yields and S₁/S₀-diradical mechanism of photodissociation," *ChemPhysChem*, vol. 11, no. 18, pp. 3883–3895, 2010.
- [139] B. Lasorne, G. A. Worth, and M. A. Robb, "Excited-state dynamics," Wiley Interdisciplinary Reviews: Computational Molecular Science, vol. 1, no. 3, pp. 460–475, 2011.
- [140] J. Kästner, "Umbrella sampling," Wiley Interdisciplinary Reviews: Computational Molecular Science, vol. 1, no. 6, pp. 932–942, 2011.
- [141] H. Hu and W. Yang, "Free energies of chemical reactions in solution and in enzymes with ab initio quantum mechanics/molecular mechanics methods," *Annual Review of Physical Chemistry*, vol. 59, pp. 573–601, 2008.
- [142] A. Barducci, M. Bonomi, and M. Parrinello, "Metadynamics," Wiley Interdisciplinary Reviews: Computational Molecular Science, vol. 1, no. 5, pp. 826–843, 2011.
- [143] G. C. Schatz, "The analytical representation of electronic potential-energy surfaces," *Reviews of Modern Physics*, vol. 61, no. 3, pp. 669–688, 1989.
- [144] M. A. Collins, "Molecular potential-energy surfaces for chemical reaction dynamics," *Theoretical Chemistry Accounts*, vol. 108, no. 6, pp. 313–324, 2002.

- [145] J. M. Bowman, B. J. Braams, S. Carter et al., "Ab-initio-based potential energy surfaces for complex molecules and molecular complexes," *Journal of Physical Chemistry Letters*, vol. 1, no. 12, pp. 1866–1874, 2010.
- [146] J. M. Bowman, G. Czakó, and B. Fu, "High-dimensional ab initio potential energy surfaces for reaction dynamics calculations," *Physical Chemistry Chemical Physics*, vol. 13, no. 18, pp. 8094–8111, 2011.
- [147] C. R. Evenhuis, X. Lin, D. H. Zhang, D. Yarkony, and M. A. Collins, "Interpolation of diabatic potential-energy surfaces: quantum dynamics on ab initio surfaces," *Journal of Chemical Physics*, vol. 123, no. 13, Article ID 134110, 12 pages, 2005.
- [148] Z. H. Li, R. Valero, and D. G. Truhlar, "Improved direct diabatization and coupled potential energy surfaces for the photodissociation of ammonia," *Theoretical Chemistry Accounts*, vol. 118, no. 1, pp. 9–24, 2007.
- [149] Z. Wang, I. S. K. Kerkines, K. Morokuma, and P. Zhang, "Analytical potential energy surfaces for N₃ low-lying doublet states," *Journal of Chemical Physics*, vol. 130, no. 4, Article ID 044313, 2009.
- [150] X. Zhu and D. R. Yarkony, "On the representation of coupled adiabatic potential energy surfaces using quasidiabatic Hamiltonians: description of accidental seams of conical intersection," *Molecular Physics*, vol. 108, no. 19-20, pp. 2611–2619, 2010.
- [151] A. Warshel and M. Levitt, "Theoretical studies of enzymatic reactions: dielectric, electrostatic and steric stabilization of the carbonium ion in the reaction of lysozyme," *Journal of Molecular Biology*, vol. 103, no. 2, pp. 227–249, 1976.
- [152] U. C. Singh and P. A. Kollman, "A combined ab initio quantum mechanical and molecular mechanical method for carrying out simulations on complex molecular systems: applications to the CH₃Cl + Cl⁻ exchange reaction and gas phase protonation of polyethers," *Journal of Computational Chemistry*, vol. 7, no. 6, pp. 718–730, 1986.
- [153] M. J. Field, P. A. Bash, and M. Karplus, "A combined quantum mechanical and molecular mechanical potential for molecular dynamics simulations," *Journal of Computational Chemistry*, vol. 11, no. 6, pp. 700–733, 1990.
- [154] F. Maseras and K. Morokuma, "IMOMM—a new integrated ab-initio plus molecular mechanics geometry optimization scheme of equilibrium structures and transition-states," *Journal of Computational Chemistry*, vol. 16, no. 9, pp. 1170–1179, 1995.
- [155] M. Svensson, S. Humbel, R. D. J. Froese, T. Matsubara, S. Sieber, and K. Morokuma, "ONIOM: a multilayered integrated MO + MM method for geometry optimizations and single point energy predictions. A test for Diels-Alder reactions and Pt(P(t-Bu)₃)₂ + H₂ oxidative addition," *Journal of Physical Chemistry*, vol. 100, no. 50, pp. 19357–19363, 1996.
- [156] T. Vreven, K. Morokuma, Ö Farkas, H. B. Schlegel, and M. J. Frisch, "Geometry optimization with QM/MM, ONIOM, and other combined methods. I. Microiterations and constraints," *Journal of Computational Chemistry*, vol. 24, no. 6, pp. 760–769, 2003.
- [157] T. Vreven, M. J. Frisch, K. N. Kudin, H. B. Schlegel, and K. Morokuma, "Geometry optimization with QM/MM methods II: explicit quadratic coupling," *Molecular Physics*, vol. 104, pp. 701–714, 2006.
- [158] S. Maeda, K. Ohno, and K. Morokuma, "An automated and systematic transition structure explorer in large flexible

molecular systems based on combined global reaction route mapping and microiteration methods," *Journal of Chemical Theory and Computation*, vol. 5, no. 10, pp. 2734–2743, 2009.

Hindawi Publishing Corporation Advances in Physical Chemistry Volume 2012, Article ID 572148, 20 pages doi:10.1155/2012/572148

Research Article

Ab Initio Potential Energy Surfaces for Both the Ground (\widetilde{X}^1A') and Excited (\widetilde{A}^1A'') Electronic States of HSiBr and the Absorption and Emission Spectra of HSiBr/DSiBr

Anyang Li,^{1,2} Sen Lin,¹ and Daiqian Xie¹

- ¹ Institute of Theoretical and Computational Chemistry, Key Laboratory of Mesoscopic Chemistry, School of Chemistry and Chemical Engineering, Nanjing University, Nanjing 210093, China
- ² Institute of High Performance Computing and Applications, Chongqing University of Posts and Telecommunications, Chongqing 400065, China

Correspondence should be addressed to Daigian Xie, dqxie@nju.edu.cn

Received 27 May 2011; Accepted 14 July 2011

Academic Editor: Xinchuan Huang

Copyright © 2012 Anyang Li et al. This is an open access article distributed under the Creative Commons Attribution License, which permits unrestricted use, distribution, and reproduction in any medium, provided the original work is properly cited.

Ab initio potential energy surfaces for the ground (\tilde{X}^1A') and excited (\tilde{A}^1A'') electronic states of HSiBr were obtained by using the single and double excitation coupled-cluster theory with a noniterative perturbation treatment of triple excitations and the multireference configuration interaction with Davidson correction, respectively, employing an augmented correlation-consistent polarized valence quadruple zeta basis set. The calculated vibrational energy levels of HSiBr and DSiBr of the ground and excited electronic states are in excellent agreement with the available experimental band origins. In addition, the absorption and emission spectra of HSiBr and DSiBr were calculated using an efficient single Lanczos propagation method and are in good agreement with the available experimental observations.

1. Introduction

Silylenes and its halogenated analogs are important reactive intermediates in the chemical vapor deposition of silicon thin films [1] and plasma etching process [2]. The identification and quantification of such intermediates could help make these processes more efficient, so that they have attracted much attention in experimental and theoretical studies [3–17]. However, because these radicals are typically short-lived and highly reactive, it is difficult to monitor them. Due to the lack of comprehensive spectroscopic signatures for these species, the detailed mechanism of such semiconductor growth processes is still not fully understood.

In this work, we focus on the monobromosilylene (HSiBr) system, which was first detected by Herzberg and Verma in 1964 [3]. Both absorption and emission spectra of HSiBr in the 410–600 nm were obtained by flash photolysis of SiH $_3$ Br. The vibrational fundamentals and geometries for both the ground and excited states were confirmed after vibrational and rotational analyses of the spectra. Although

no spin splittings were observed, the occurrence of subbands with $\Delta K=0$ and ± 2 led them to assume that the electronic transition was triplet-singlet. Subsequently in 1965, these electronic transitions were confirmed to be $\widetilde{A}^1A''-\widetilde{X}^1A'$ by Hougen and Watson via an "axis-switching" mechanism [4]. The spectra of the $\widetilde{A}^1A''-\widetilde{X}^1A'$ system of jet-cooled HSiBr and its deuterated analog were obtained about 15 years ago by Harjanto et al. [8] using pulsed electric discharge techniques, and the r_0 structures for the ground and excited states were determined from the rotational analyses of the 0_0^0 band. Later in 2001, 26/51 ground state vibrational levels of HSiBr/DSiBr were observed by Hostutler et al. [13] from the single vibronic level dispersed fluorescence spectra of jet-cooled HSiBr/DSiBr by laser excitation of selected bands.

Unlike HSiF and HSiCl, only a few theoretical studies have been reported for monobromosilylene (HSiBr) [6, 13]. In 1979, Gilchrist et al. [6] determined the geometrical structures and bending potentials for the excited state \tilde{A}^1A'' of HSiBr by fitting the Herzberg and Verma's data [3] and also obtained the H–Si stretching frequency(ν'_1 = 1785 cm⁻¹),

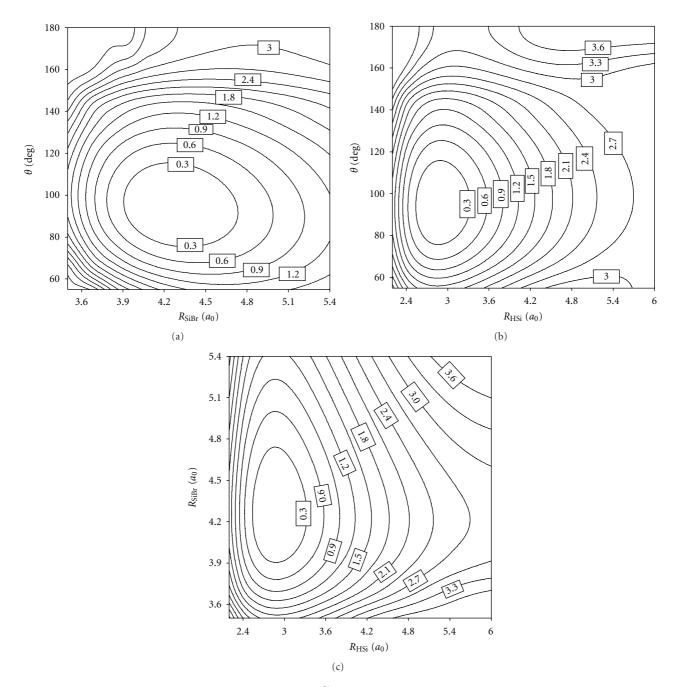


FIGURE 1: Contour plots of the potential energy surface of HSiBr(\widetilde{X}^1A') in the internal coordinates. (a) Contour plot at $R_{\text{HSi}} = 2.869 \, a_0$. (b) Contour plot at $R_{\text{SiBr}} = 4.257 \, a_0$. (c) Contour plot at $\theta = 93.9^\circ$. Contours are spaced by 0.3 eV with the zero defined at the HSiBr(\widetilde{X}^1A') minimum.

which is agreement with the later experimental value of 1787 cm⁻¹ [8]. In order to ascertain the validity of their refined force constants, Hostutler et al. [13] calculated the independent ground and excited state structures at B3LYP level with 6-311G(3df,3pd) basis set in 2001. To our best knowledge, however, no potential energy surface (PES) has been reported for either the ground or excited electronic state of HSiBr. The lack of reliable PESs will hinder our understanding of the spectroscopy of this important

molecule, particularly for highly excited vibrational levels which can be probed by emission spectroscopy.

In the present work, we extend our previous studies on the HGeCl [18], HGeBr [19], and HSiCl [20] systems by reporting accurate *ab initio* PESs for both the ground (\tilde{X}^1A') and excited (\tilde{A}^1A'') electronic states of HSiBr using the coupled cluster singles and doubles with perturbative triples method [CCSD(T)] and the internally contracted multireference configuration interaction method with the

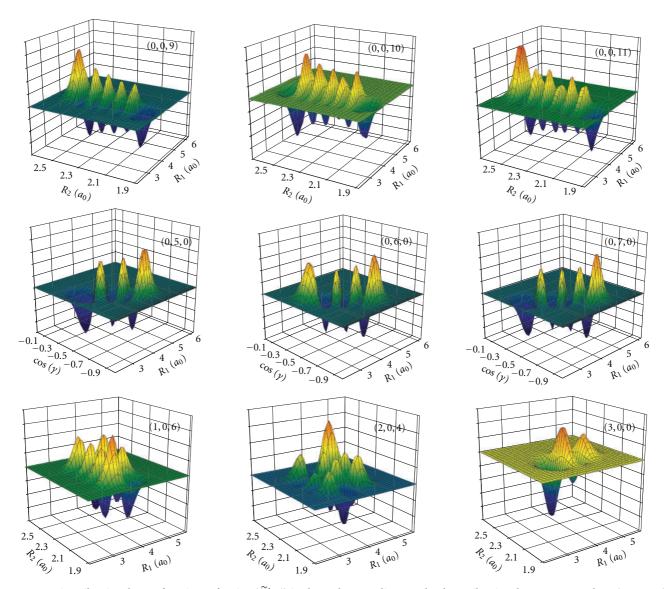


FIGURE 2: Nine vibrational wave functions of HSiBr (\tilde{X}^1A') in the Radau coordinates. The three vibrational quantum numbers (n_1, n_2, n_3) represent the H–Si stretching, bending, and Si–Br stretching modes, respectively.

Table 1: Geometrical parameters for the ground and excited states of HSiBr.

Electronic state	Method	$R_e(\mathrm{HSi})$ (Å)	$R_e(SiCl)$ (Å)	$\theta_e(\mathrm{HSiCl})$ (°)
	CCSD(T)/AVQZ ^a	1.518	2.253	93.9
	B3LYP/6-311G(3df,3pd) ^b	1.524	2.2674	94.3
\widetilde{X}^1A'	Expt. ^c	1.561	2.231	102.9
	Expt. ^d	1.518	2.237	93.4
	Expt. ^b	1.503	2.235	92.8
	CAS/MRCI +Q/AVQZ ^a	1.499	2.219	117.7
$\widetilde{A}^1A^{\prime\prime}$	B3LYP/6-311G(3df,3pd) ^b	1.5014	2.2339	115.9
AA	Expt. ^c	1.499	2.208	116.6
	Expt. ^d	1.497	2.208	116.4

^aThis work.

^bReference [13].

^cReference [3].

^dReference [8].

Table 2: Calculated vibrational energy levels (in cm $^{-1}$) and comparison with available experimental results for HSiBr (\widetilde{X}^1A').

(n_1, n_2, n_3)	This work	Expt. [13]	(n_1, n_2, n_3)	This work	Expt. [13]
(0,0,0)	0.0		(2,0,4)	5509.4	
(0,0,1)	409.3	412.4	(1, 1, 7)	5528.3	
(0, 1, 0)	770.3	772.0	(1,0,9)	5569.3	
(0,0,2)	815.7		(0,7,1)	5668.2	5682.0
(0, 1, 1)	1176.7	1181.4	(0,6,3)	5706.5	
(0,0,3)	1219.5		(1,5,0)	5710.5	5717.8
(0, 2, 0)	1536.4	1540.7	(3,0,0)	5717.7	
(0, 1, 2)	1580.4		(0,5,5)	5742.8	
(0,0,4)	1620.7		(1, 4, 2)	5757.7	
(0, 2, 1)	1939.7	1946.3	(0,4,7)	5775.7	
(1,0,0)	1977.6	1976.2	(2, 2, 1)	5782.7	
(0,1,3)	1981.3		(0, 3, 9)	5803.7	
(0,0,5)	2019.3		(1,3,4)	5818.1	
(0,3,0)	2296.3	2301.1	(0, 2, 11)	5825.5	
(0,2,2)	2340.4		(0, 1, 13)	5841.9	
(0, 1, 4)	2379.5		(2, 1, 3)	5846.3	
(1,0,1)	2387.6	2386.7	(0, 0, 15)	5856.9	
(0,0,6)	2415.3		(1,2,6)	5871.6	
(0,3,1)	2696.4	2705.5	(2,0,5)	5908.4	
(1,1,0)	2734.8	2733.2	(1, 1, 8)	5917.0	
(0,2,3)	2738.3		(1,0,10)	5954.3	
(0,1,5)	2775.2		(0, 8, 0)	6017.4	6031.9
(1,0,2)	2794.6		(0,7,2)	6053.0	
(0,0,7)	2808.6		(0,6,4)	6088.9	
(0,4,0)	3050.2	3058.2	(1,5,1)	6090.2	
(0,3,2)	3094.0		(0,5,6)	6114.8	
(0,2,4)	3133.6		(2,3,0)	6124.3	
(1,1,1)	3142.2		(3,0,1)	6127.9	
(0,1,6)	3168.3		(0,4,8)	6153.1	
(1,0,3)	3198.9		(1,4,3)	6154.7	
(0,0,8)	3199.0		(0,3,10)	6179.7	
(0,4,1)	3447.0	3457.2	(2,2,2)	6183.3	
(1,2,0)	3487.7	3485.1	(0, 2, 12)	6198.7	
(0,3,3)	3489.0		(1,3,5)	6209.7	
(0,2,5)	3526.3		(0, 1, 14)	6213.5	
(1, 1, 2)	3546.5		(0, 0, 16)	6230.2	
(0,1,7)	3558.8		(2,1,4)	6244.6	
(0,0,9)	3586.6		(1,2,7)	6260.2	
(1,0,4)	3600.7		(1,1,9)	6300.1	
(0,5,0)	3798.7	3808.9	(2,0,6)	6307.4	
(0,4,2)	3841.5		(1,0,11)	6336.5	
(2,0,0)	3880.9	3881.4	(0,8,1)	6399.6	
(0,3,4)	3881.4	000111	(0,7,3)	6435.9	
(1,2,1)	3893.8		(1,6,0)	6441.1	6449.8
(0,2,6)	3916.5		(3,1,0)	6444.6	0117.0
(0, 1, 8)	3946.4		(0,6,5)	6471.3	
(1,1,3)	3948.1		(2,3,1)	6485.0	
(0,0,10)	3971.4		(0,5,7)	6503.3	
(1,0,5)	3999.9		(0,5,7) $(1,5,2)$	6516.2	
(0,5,1)	4192.1	4202.9	(0,4,9)	6530.9	
(0, 5, 1)	4174.1	4202.7	(0,4,7)	0.2.0.2	

Table 2: Continued.

(n_1, n_2, n_3)	This work	Expt. [13]	(n_1, n_2, n_3)	This work	Expt. [13]
(0,4,3)	4233.3		(3,0,2)	6534.2	
(1,3,0)	4234.5	4234.5	(1, 4, 4)	6546.1	
(0,3,5)	4271.0		(0, 3, 11)	6552.8	
(2,0,1)	4288.1		(0, 2, 13)	6569.5	
(1, 2, 2)	4298.7		(2, 2, 3)	6581.6	
(0, 2, 7)	4304.0		(0, 1, 15)	6584.2	
(0, 1, 9)	4331.1		(1, 3, 6)	6598.5	
(1, 1, 4)	4347.0		(0,0,17)	6607.9	
(0, 0, 11)	4353.3		(2, 1, 5)	6639.7	
(1,0,6)	4396.5		(1, 2, 8)	6646.9	
(0,6,0)	4542.4	4557.8	(1, 1, 10)	6682.9	
(0, 5, 2)	4583.4		(2,0,7)	6701.0	
(2, 1, 0)	4622.1		(1,0,12)	6716.0	
(0,4,4)	4622.9		(0, 9, 0)	6748.4	
(1,3,1)	4639.7		(0, 8, 2)	6780.7	
(0, 3, 6)	4658.2		(2,4,0)	6813.7	
(0,2,8)	4688.8		(0,7,4)	6816.7	
(1,2,3)	4689.3		(1,6,1)	6844.5	
(2,0,2)	4703.9		(0,6,6)	6849.9	
(0, 1, 10)	4712.9		(3,1,1)	6850.7	
(0,0,12)	4732.6		(2,3,2)	6878.2	
(1,1,5)	4743.4		(0,5,8)	6879.5	
(1,0,7)	4790.4		(0,4,10)	6904.1	
(0,6,1)	4932.4	4946.5	(1,5,3)	6915.1	
(0,5,3)	4972.4	1710.3	(0,3,12)	6923.2	
(0,3,3) $(1,4,0)$	4975.2	4979.2	(1,4,5)	6931.1	
(0,4,5)	5009.6	1777.2	(0, 2, 14)	6938.4	
(2,1,1)	5025.1		(3,0,3)	6942.6	
(0,3,7)	5042.9		(0,1,16)	6956.2	
(0,3,7) $(1,3,2)$	5042.9		(2,2,4)	6977.2	
(0,2,9)	5070.6		(2,2,4) $(1,3,7)$	6985.0	
(0,2,3) $(1,2,4)$	5086.3		(0,0,18)	6995.9	
(0,1,11)	5091.9		(1,2,9)	7026.1	
(2,0,3)			(2,1,6)	7036.7	
(0,0,13)	5107.7 5109.4			7062.3	
			(1,1,11)		
(1,1,6)	5137.2		(2,0,8)	7092.1 7093.0	
(1,0,8)	5181.3	F220 1	(1,0,13)		
(0,7,0)	5282.0	5229.1	(0,9,1)	7126.0	
(0,6,2)	5320.5		(0,8,3)	7160.2	
(0,5,4)	5358.4		(3,2,0)	7166.8	7176.0
(1,4,1)	5359.0		(1,7,0)	7167.4	7176.8
(2,2,0)	5380.0		(0,7,5)	7195.0	
(0,4,6)	5394.0		(2,4,1)	7207.6	
(2,1,2)	5423.5		(0,6,7)	7226.1	
(0,3,8)	5424.7		(1,6,2)	7244.4	
(1,3,3)	5445.8		(3,1,2)	7251.9	
(0,2,10)	5449.5		(0,5,9)	7252.9	
(0,1,12)	5468.1		(2,3,3)	7269.8	
(1, 2, 5)	5480.3		(0, 4, 11)	7274.5	
(0,0,14)	5483.9		(0, 3, 13)	7291.1	

Table 3: Calculated vibrational energy levels (in cm $^{-1}$) and comparison with available experimental results for DSiBr (\widetilde{X}^1A').

(n_1,n_2,n_3)	This work	Expt. [13]	(n_1,n_2,n_3)	This work	Expt. [13]
(0,0,0)	0.0		(0,4,7)	4959.8	
(0,0,1)	405.0	407.99	(1, 5, 2)	4976.7	4981.7
(0, 1, 0)	562.0	561.8	(2, 1, 4)	4985.7	
(0,0,2)	807.2	812.4	(1,0,9)	4990.3	
(0, 1, 1)	965.0	968.5	(3,0,2)	5011.6	
(0, 2, 0)	1122.1	1121.3	(0, 2, 10)	5015.8	
(0,0,3)	1206.8		(2,4,0)	5021.4	
(0, 1, 2)	1365.4	1371.5	(0,7,3)	5042.3	
(1,0,0)	1439.7	1439.5	(0,0,13)	5059.6	
(0, 2, 1)	1523.2	1528.7	(1, 3, 5)	5067.1	
(0,0,4)	1603.9		(0, 5, 6)	5117.4	
(0,3,0)	1678.9	1679.6	(1,6,1)	5122.4	
(0,1,3)	1763.1		(2,2,3)	5131.8	
(1,0,1)	1844.7	1844.9	(1, 1, 8)	5145.2	
(0, 2, 2)	1921.7	1927.9	(3, 1, 1)	5150.8	
(1, 1, 0)	1995.5	1998.2	(0,3,9)	5178.6	
(0,0,5)	1998.5		(0, 8, 2)	5193.6	5214
(0,3,1)	2078.2	2081.7	(1, 4, 4)	5217.6	
(0, 1, 4)	2158.2		(0, 1, 12)	5224.9	
(0,4,0)	2232.4	2236.2	(2,0,6)	5231.3	
(1,0,2)	2247.0		(1,7,0)	5266.0	
(0,2,3)	2317.5		(0,6,5)	5273.0	
(0,0,6)	2390.6		(2, 3, 2)	5276.1	
(1, 1, 1)	2398.5	2400.3	(3, 2, 0)	5288.9	
(0, 3, 2)	2474.8	2482.7	(1, 2, 7)	5299.6	
(1, 2, 0)	2549.2		(0,4,8)	5339.2	
(0, 1, 5)	2550.8		(0,9,1)	5343.4	5363.5
(0,4,1)	2629.8	2634.1	(1,5,3)	5366.1	
(1,0,3)	2646.6		(1,0,10)	5371.0	
(0, 2, 4)	2710.7		(2, 1, 5)	5378.2	
(0,0,7)	2780.0		(0, 2, 11)	5390.9	
(0,5,0)	2782.3	2788.9	(3,0,3)	5411.2	
(1, 1, 2)	2798.8	2799.4	(2,4,1)	5418.3	
(2,0,0)	2840.4	2843.8	(0,7,4)	5427.0	
(0,3,3)	2868.8		(0,0,14)	5431.1	
(0, 1, 6)	2940.8		(1, 3, 6)	5452.4	
(1,2,1)	2950.2	2950.2	(0, 10, 0)	5491.4	5505.5
(0,4,2)	3024.6	3034.7	(0,5,7)	5497.7	
(1,0,4)	3043.7	000117	(1,6,2)	5512.7	5522.2
(1,3,0)	3099.5	3096.8	(2,2,4)	5524.6	0022.2
(0,2,5)	3101.4	20,010	(1,1,9)	5526.5	
(0,0,8)	3166.8		(4,0,0)	5534.9	
(0,5,1)	3178.0	3185.8	(3, 1, 2)	5551.2	
(0,3,1) $(1,1,3)$	3196.4	3133.0	(0,3,10)	5554.7	
(2,0,1)	3245.4		(2,5,0)	5557.8	
(2,0,1) $(0,3,4)$	3260.2		(0,8,3)	5579.1	
(0, 3, 4) (0, 1, 7)	3328.3		(0, 0, 3) $(0, 1, 13)$	5596.6	
(0, 1, 7) (0, 6, 0)	3329.1	3337.6	(0,1,13) $(1,4,5)$	5603.6	
(0,0,0) (1,2,2)	3348.4	3351.7	(2,0,7)	5620.9	
(1, 2, 2) (2, 1, 0)	3390.1	JJJ1./	(0,6,6)	5654.3	

Table 3: Continued.

(n_1, n_2, n_3)	This work	Expt. [13]	(n_1, n_2, n_3)	This work	Expt. [13]
(0,4,3)	3416.8		(1,7,1)	5657.5	
(1,0,5)	3438.4		(2,3,3)	5669.3	
(0, 2, 6)	3489.5		(1, 2, 8)	5681.5	
(1, 3, 1)	3498.5	3497.9	(3, 2, 1)	5689.9	
(0,0,9)	3550.8		(0,4,9)	5716.2	
(0,5,2)	3571.1	3583.3	(0, 9, 2)	5729.9	5753.4
(1, 1, 4)	3591.4		(1,0,11)	5748.6	
(1,4,0)	3646.2	3646.9	(1, 5, 4)	5752.8	
(2,0,2)	3647.6		(0, 2, 12)	5763.8	
(0,3,5)	3649.0		(2, 1, 6)	5768.1	
(0, 1, 8)	3713.1		(1, 8, 0)	5800.3	
(0, 6, 1)	3723.1	3734.1	(0, 0, 15)	5802.6	
(1, 2, 3)	3744.0		(3,0,4)	5808.4	
(2, 1, 1)	3793.0		(0,7,5)	5808.9	
(0,4,4)	3806.4		(2, 4, 2)	5812.3	
(1,0,6)	3830.5		(3, 3, 0)	5826.3	
(0,7,0)	3873.1	3885.2	(1, 3, 7)	5834.9	
(0,2,7)	3875.0		(0,5,8)	5875.6	
(1,3,2)	3894.7	3894.3	(0,10,1)	5879.2	5899.5
(0,0,10)	3931.9	00,110	(1,6,3)	5900.3	20,,,,
(2,2,0)	3937.5		(1,1,10)	5904.6	
(0,5,3)	3961.5		(2,2,5)	5914.8	
(1,1,5)	3983.8		(0,3,11)	5928.5	
(0,3,6)	4035.2		(4,0,1)	5939.1	
(0,3,0) $(1,4,1)$	4043.3		(3,1,3)	5949.2	
(2,0,3)	4047.3		(2,5,1)	5952.8	
(0,1,9)	4095.1		(0,8,4)	5962.3	
(0,6,2)	4114.5	4131.2	(0,0,4) $(0,1,14)$	5967.2	
(0,0,2) $(1,2,4)$	4136.9	4131.2	(1,4,6)	5986.7	
(1, 5, 0)	4189.3	4194.7	(2,0,8)	6007.6	
(2,1,2)	4193.0	11/1./	(0,11,0)	6026.6	6040.2
(0,4,5)	4193.5		(0,6,7)	6033.0	0040.2
(3,0,0)	4204.5		(1,7,2)	6046.0	6058.04
(1,0,7)	4219.9		(2,3,4)	6060.0	0030.04
(0,2,8)	4257.9		(1,2,9)	6060.3	
(0,7,1)	4265.5	4279.1	(4,1,0)	6071.0	
(1,3,3)	4288.2	42/7.1	(3,2,2)	6088.4	
(0,0,11)	4310.4		(2,6,0)	6090.7	
(0,0,11) $(2,2,1)$	4338.4		(2,0,0) $(0,4,10)$	6091.0	
(2,2,1) $(0,5,4)$	4349.4		(0, 9, 3)	6113.9	
				6122.9	
(1,1,6)	4373.7	1226.2	(1,0,12)		
(0,8,0)	4414.6	4226.2	(0,2,13)	6135.4	
(0,3,7)	4418.9	4442.1	(1,5,5)	6136.7	
(1,4,2)	4437.4	4442.1	(2,1,7)	6155.4	
(2,0,4)	4444.4		(0,0,16)	6177.2	
(0,1,10)	4474.4		(0,7,6)	6188.6	
(2,3,0)	4481.3		(1,8,1)	6190.1	
(0,6,3)	4503.2		(3,0,5)	6203.0	
(1,2,5)	4527.1		(2,4,3)	6203.3	
(0,4,6)	4577.8		(1,3,8)	6214.4	
(1,5,1)	4584.4		(3,3,1)	6225.4	
(2, 1, 3)	4590.7		(0, 5, 9)	6251.1	

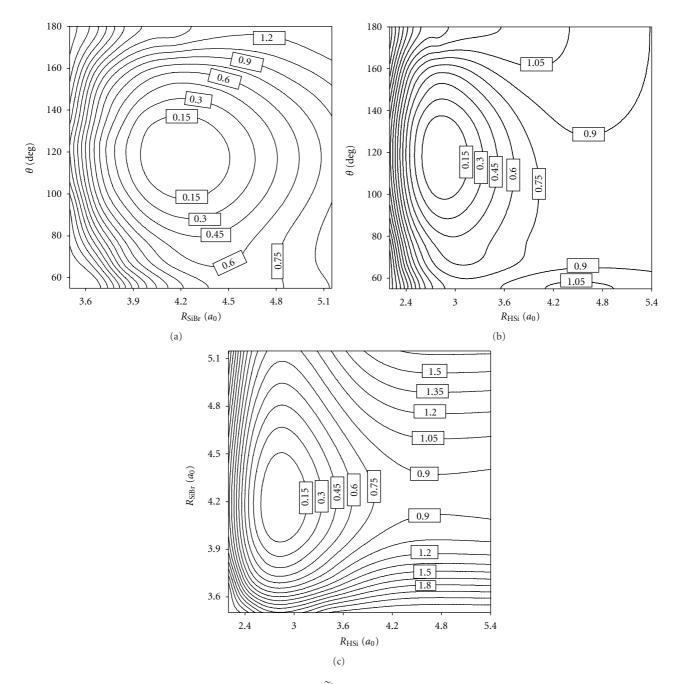


FIGURE 3: Contour plots of the potential energy surface of HSiBr (\widetilde{A}^1A'') in the internal coordinates. (a) Contour plot at $R_{\text{HSi}} = 2.833 \, a_0$. (b) Contour plot at $R_{\text{SiBr}} = 4.193 \, a_0$. (c) Contour plot at $\theta = 117.7^{\circ}$. Contours are spaced by 0.15 eV with the zero defined at the HSiBr(\widetilde{A}^1A'') minimum.

Davidson correction for higher excitations (MRCI + Q), respectively, employing an augmented correlation-consistent polarized valence quadruple zeta (AVQZ) basis set. The vibrational energy levels on both the two electronic states as well as the absorption and emission spectra were calculated and compared with the available experimental data. The reasonable good agreement between our results and experimental data demonstrates that the PESs are very accurate. This paper is organized as follows. In Section 2, we describe the details of the *ab initio* calculations and the analytical representation of the PESs and transition dipole

moments, as well as the quantum mechanical method to calculate the vibrational energy levers. Section 3 discusses the main features of the PESs, vibrational states, and electronic spectra, respectively. A brief conclusion is summarized in Section 4.

2. Computational Details

2.1. Potential Energy Surfaces and Transition Dipole Moment Surface. Ab initio calculations were carried out to determine the potential energy surfaces (PESs) for both the \widetilde{X}^1A' and

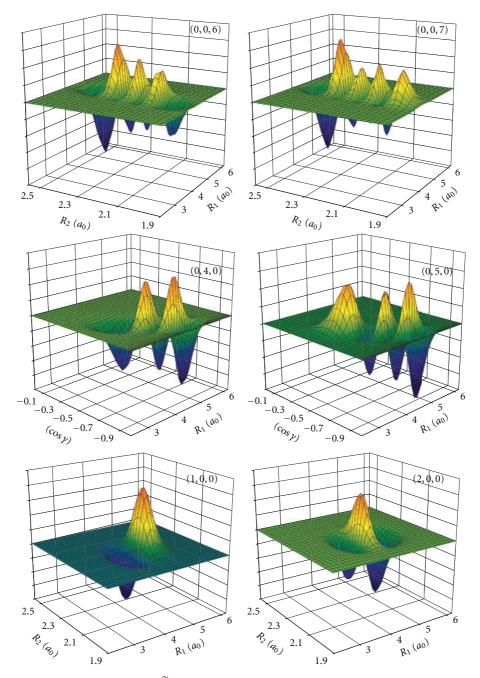


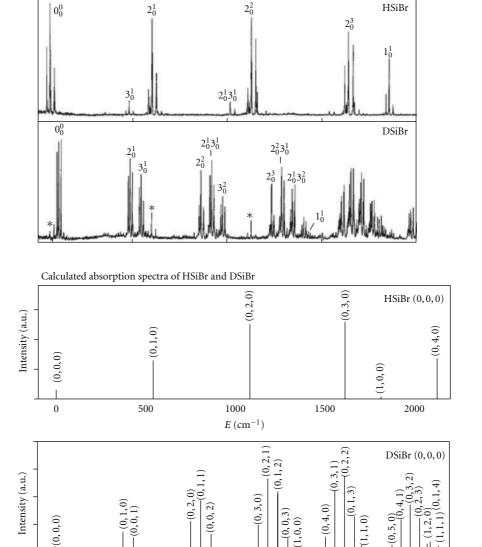
FIGURE 4: Six vibrational wave functions of HSiBr (\tilde{A}^1A'') in the Radau coordinates. The three vibrational quantum numbers (n_1, n_2, n_3) represent the H–Si stretching, bending, and Si–Br stretching modes, respectively.

 $\widetilde{A}^1A^{\prime\prime}$ states of HSiBr by using the MOLPRO [21] suite of quantum chemistry programs. The corresponding transition dipole moment surfaces were also calculated in this work.

The two PESs were constructed independently. For the closed-shell ground (\widetilde{X}^1A') electronic state, the single-reference RCCSD(T) method [22] was employed with Dunning's AVQZ basis set [23], which generates a total of 223 cGTOs, and the core electrons were frozen in all the *ab initio* calculations. A nonuniform and truncated direct product grid in the internal coordinates (R_{HSi} , R_{SiBr} , θ) was

selected for the calculations of PES, where $R_{\rm HSi}$ and $R_{\rm SiBr}$ are the H–Si and Si–Br internuclear distances, respectively, and θ is the enclosed bond angle \angle HSiBr. For the two radial coordinates, we have chosen 17 points covering the H–Si radial coordinate from 2.2 a_0 to 6.5 a_0 and 15 points in the Si–Br radial coordinate from 3.2 a_0 to 5.4 a_0 . In the angle coordinate, 12 points ranging from 55° to 180° were used. This gives a total of 3060 geometry-unique points.

In the case of the open-shell excited electronic state (\tilde{A}^1A'') of HSiBr, which can not be adequately treated



Experimental LIF spectra of HSiBr and DSiBr by Harjanto et al.

FIGURE 5: Calculated stick absorption spectra for the $\widetilde{A}^1A'' \leftarrow \widetilde{X}^1A'$ transition from the lowest vibrational level $\widetilde{X}(0, 0, 0)$ of HSiBr and DSiBr with the corresponding portion of the experimental LIF spectrum [8] (on the top of the calculated ones), respectively.

1000

 $E (cm^{-1})$

1500

by single electronic configuration, the MRCI + Q [24–26] calculations were carried out using the Dunning's AVQZ basis set. After primary test calculations, the state-averaged complete active space self-consistent field (SA-CASSCF) [27, 28] for equally weighted $1^1A^{\prime\prime}$ and $2^1A^{\prime\prime}$ states were employed with a large active space (18 active electrons in 12 active orbitals) to further consider the core-valence correlation effect [15, 18–20]. The remnant sixteen core orbitals were kept doubly occupied but fully optimized. Based on the CASSCF natural orbitals, the subsequent MRCI + Q calculations were carried out for the full valence active space (12 electrons in 9 orbitals), where core-valence and core-core correlations were also included by single and

0

500

double excitations from three 2p orbitals of Si in each configuration state function. The total number of contracted configurations is about 8.3×10^8 . A relatively extensive range is also chosen for the *ab initio* points. In particular, sixteen points from 2.2 to $5.5\,a_0$ for $R_{\rm HSi}$ and fourteen points from 3.25 to $5.15\,a_0$ for $R_{\rm SiBr}$ were selected. In the angle direction, twelve points were used ranging from 55 to 180° . A total of 2688 geometry-unique points were generated.

2000

In addition, we have also calculated the non-zero $(\widetilde{A}^1A'' - \widetilde{X}^1A')$ transition dipole moment, which is perpendicular to the molecular plane, using the MRCI + Q method with the AVTZ basis set.

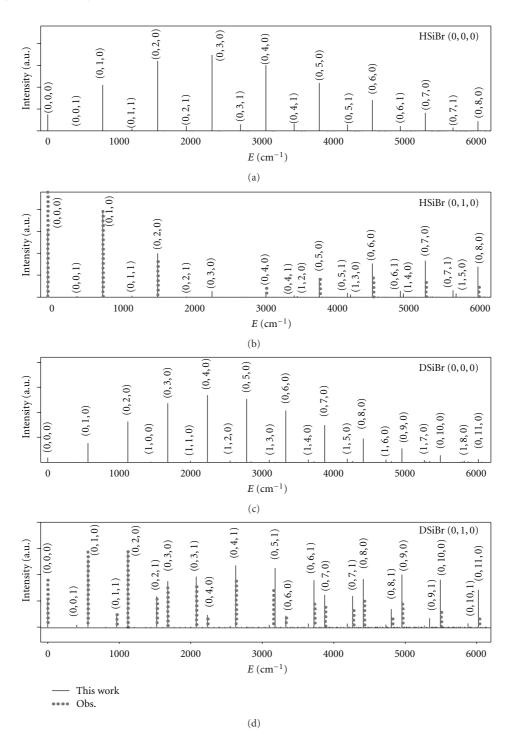


FIGURE 6: Calculated stick emission spectra for the $\widetilde{A}^1A'' \to \widetilde{X}^1A'$ transition from (0,0,0) and (0,1,0) vibrational levels of HSiBr and DSiBr. The experimental spectra were taken from [13].

Finally, the potential energies and the transition dipole moment at any arbitrary point were obtained using the three-dimensional cubic spline interpolation. The corresponding FORTRAN codes are available upon request.

2.2. Vibrational Energy Levels. The vibrational energy levels were obtained by solving the vibrational Hamiltonian with the total angular momentum J=0 in Radau coordinates

$$(R_1, R_2, \gamma),$$

$$\hat{H} = -\frac{\hbar^2}{2m_1} \frac{\partial^2}{\partial R_1^2} - \frac{\hbar^2}{2m_2} \frac{\partial^2}{\partial R_2^2}$$

$$-\frac{\hbar^2}{2} \left(\frac{1}{m_1 R_1^2} + \frac{1}{m_2 R_2^2} \right) \left(\frac{\partial^2}{\partial \gamma^2} + \cot \gamma \frac{\partial}{\partial \gamma} \right) + V(R_1, R_2, \gamma),$$

$$(1)$$

(1, 2, 6)

(0,9,0)

(n_1,n_2,n_3)	This work	Expt. [13]	(n_1, n_2, n_3)	This work	Expt. [13]
(1,0,8)	4606.5		(0, 10, 2)	6264.2	6286.9
(3,0,1)	4609.4		(1, 1, 11)	6279.5	
(0, 2, 9)	4638.2		(1, 6, 4)	6285.0	
(0,7,2)	4655.2	4673.4	(0, 3, 12)	6300.5	
(1, 3, 4)	4679.0		(2, 2, 6)	6302.5	
(0,0,12)	4686.2		(1, 9, 0)	6332.2	
(1,6,0)	4729.1	4736.7	(0, 1, 15)	6339.0	
(0,5,5)	4734.6		(4,0,2)	6339.4	
(2, 2, 2)	4736.4		(0, 8, 5)	6342.3	
(3, 1, 0)	4747.9		(2,5,2)	6344.9	
(1, 1, 7)	4760.8		(3, 1, 4)	6346.0	
(0,3,8)	4800.0		(3,4,0)	6359.9	
(0, 8, 1)	4805.5	4824	(1, 4, 7)	6366.9	
(1, 4, 3)	4828.9		(2,0,9)	6391.5	
(2,0,5)	4839.1		(0,6,8)	6409.3	
(0, 1, 11)	4851.0		(0, 11, 1)	6412.8	6433.9
(2, 3, 1)	4880.2		(1,7,3)	6431.7	
(0,6,4)	4889.5		(1, 2, 10)	6435.9	

4966.8

(2,3,5)

(0,4,11)

Table 3: Continued.

where m_1 and m_2 are the atomic mass of H and Br, respectively. The transformation between the Radau coordinates (R_1, R_2, γ) and the internal coordinates $(R_{HSi}, R_{SiBr}, \theta)$ is well documented [29]. The vibrational wave functions were represented in a direct product discrete variable representation (DVR) [30] grid, and the vibrational energy levels were calculated using the Lanczos algorithm [31], which generates the eigenvalues of the Hamiltonian by a three-term recursion. Extensive convergence tests were carried out to ascertain the accuracy of the results against the number of recursion steps and grid size. When eigenfunctions were required, the Lanczos recursion was repeated to assemble the wave functions of interest.

4914.7

4954.1

For the ground electronic state, R_1 was represented by 50 potential optimized DVR (PODVR) [32, 33] grid points derived from the one-dimensional Hamiltonian, in which the two other coordinates were fixed at their equilibrium values. The other radial coordinate R_2 was represented by 30 PODVR grid points from the corresponding one-dimensional Hamiltonian. For the angular variable, 80 Gauss-Legendre [34] grid points were used. The converged vibrational energy levels below 7500 cm⁻¹ were generated by performing about 7000 Lanczos recursion steps with a cutoff of 4.0 eV for the potential energy.

In the case of the excited electronic state of HSiBr, different parameters were used for calculating the vibrational states. The PODVR grids for R_1 and R_2 consist of 50 and 30 points, respectively. 80 Gauss-Legendre grid points in the interval [0°, 180°] were used for γ . The converged vibrational energy levels below 6000 cm⁻¹ were generated by performing about 5000 Lanczos recursion steps with a cutoff of 2.5 eV for the potential energy.

2.3. Absorption and Emission Spectra. The absorption and emission spectra can be evaluated as

6448.0

6463.7

$$\Sigma(\omega) \propto |\langle \Phi_n | \mu | \Psi_{n'} \rangle|^2,$$
 (2)

where μ is the transition dipole moment and Φ_n and $\Psi_{n'}$ are the vibrational wave functions of the ground and excited electronic states, respectively. The transition amplitude $\langle \Phi_n | \mu | \Psi_{n'} \rangle$ can be calculated directly from the vibrational wave functions, but, in this work, we have used an efficient single Lanczos propagation (SLP) method [35, 36]. This method is particularly efficient for calculating emission from multiple excited state levels, because it requires no explicit construction and storage of the vibrational wave functions, and it has been proved successful in a number of systems [37].

For the calculation of electronic spectra, the Hamiltonians for both the ground and excited electronic states need to be represented by the same DVR grid. For both absorption and emission spectra, 60 sine-DVR points were employed to cover the R_1 range of [2.10, 8.00] a_0 and 40 sine-DVR points for the R_2 range of [1.7, 2.7] a_0 . For γ , an eighty-point Gauss-Legendre DVR grid was used.

3. Results and Discussions

3.1. Ground (\tilde{X}^1A') State Potential and Vibrational Energy Levels. Figure 1 displays the contour plots of the ground electronic state PES of HSiBr in the internal coordinates (R_{HSi} , R_{SiBr} , θ). Figures 1(a), 1(b), and 1(c) show the dependence of the potential on R_{SiBr} and θ with R_{HSi} fixed at its equilibrium value of 2.869 a_0 , on R_{HSi} and θ with R_{SiBr} fixed at its equilibrium value of 4.257 a_0 , and on the two bond

Table 4: Calculated vibrational energy levels (in cm $^{-1}$) and comparison with available experimental results for HSi 79 Br (\widetilde{A}^1A'').

(n_1,n_2,n_3)	This work	Expt. [8]	(n_1,n_2,n_3)	This work	Expt. [8]
(0,0,0)	0.0		(0,7,0)	3471.9	
(0,0,1)	416.5	416.54	(0, 2, 6)	3497.2	
(0, 1, 0)	541.8	535.31	(1, 1, 3)	3546.3	
(0,0,2)	828.8		(0,0,9)	3590.8	
(0, 1, 1)	956.6	949.37	(0, 3, 5)	3619.6	
(0, 2, 0)	1081.1	1059.20	(1, 2, 2)	3634.3	
(0,0,3)	1237.5		(1, 3, 1)	3710.8	3641.02
(0, 1, 2)	1367.1		(0, 4, 4)	3724.3	
(0, 2, 1)	1492.9	1470.89	(0, 1, 8)	3742.1	
(0,3,0)	1613.0	1569.07	(1, 4, 0)	3766.1	3675.59
(0, 0, 4)	1642.7		(0,5,3)	3806.0	
(0, 1, 3)	1774.4		(0,6,2)	3841.9	
(1,0,0)	1813.7	1786.96	(2,0,1)	3842.1	3784.87
(0, 2, 2)	1900.2		(1,0,5)	3846.1	
(0,3,1)	2021.1	1977.88	(0,7,1)	3872.3	
(0,0,5)	2043.6		(0, 2, 7)	3883.8	
(0,4,0)	2126.6	2060.57	(2,1,0)	3894.6	3828.00
(0, 1, 4)	2178.3		(1, 1, 4)	3947.3	
(1,0,1)	2227.7	2200.77	(0,0,10)	3963.8	
(0, 2, 3)	2304.8		(0,3,6)	4009.5	
(1, 1, 0)	2321.3	2286.15	(1, 2, 3)	4036.3	
(0,3,2)	2424.6		(0, 9, 0)	4076.1	
(0,0,6)	2439.2		(1, 3, 2)	4112.0	
(0,4,1)	2531.4		(0, 1, 9)	4119.3	
(0, 1, 5)	2577.7		(1, 4, 1)	4165.5	
(0,5,0)	2614.0	2526.79	(1,5,0)	4196.8	4069.35
(1,0,2)	2637.7		(1,0,6)	4240.2	
(0, 2, 4)	2706.7		(2,0,2)	4247.4	
(1, 1, 1)	2733.5	2697.66	(0, 2, 8)	4264.0	
(1, 2, 0)	2819.9	2770.59	(2, 1, 1)	4299.7	4229.06
(0,3,3)	2825.4		(0,0,11)	4331.9	
(0,0,7)	2829.2		(2, 2, 0)	4339.7	4261.83
(0,4,2)	2931.4		(1, 1, 5)	4344.0	
(0, 1, 6)	2971.8		(0, 10, 0)	4359.5	
(0,5,1)	3015.5		(0, 3, 7)	4393.4	
(1,0,3)	3044.0		(1, 2, 4)	4434.8	
(0,6,0)	3065.2		(0, 9, 1)	4481.3	
(0, 2, 5)	3104.6		(0, 1, 10)	4487.9	
(1, 1, 2)	3141.7		(1,3,3)	4510.3	
(0,0,8)	3212.6		(1,0,7)	4628.7	
(0, 3, 4)	3224.6		(0, 2, 9)	4637.9	
(1, 2, 1)	3229.2	3179.44	(2,0,3)	4649.2	
(1, 3, 0)	3305.3	3235.83	(0, 0, 12)	4695.3	
(0,4,3)	3328.9		(2, 1, 2)	4700.6	4681.50
(0, 1, 7)	3360.0		(2, 2, 1)	4734.1	4645.25
(0,5,2)	3412.1		(1, 1, 6)	4735.8	
(2,0,0)	3432.9		(2,3,0)	4766.4	4620.91
(1,0,4)	3447.0		(0,3,8)	4770.9	
(0,6,1)	3448.6		(3,0,0)	4797.7	

Table 5: Calculated vibrational energy levels (in cm $^{-1}$) and comparison with available experimental results for HSi 81 Br ($\widetilde{A}^{1}A^{\prime\prime}$).

(n_1,n_2,n_3)	This work	Expt. [8]	(n_1,n_2,n_3)	This work	Expt. [8]
(0,0,0)	0.0		(0,7,0)	3471.2	
(0,0,1)	415.1	415.23	(0, 2, 6)	3489.5	
(0,1,0)	541.8	535.31	(1, 1, 3)	3542.3	
(0,0,2)	826.1		(0,0,9)	3579.7	
(0, 1, 1)	955.2	947.95	(0, 3, 5)	3613.0	
(0,2,0)	1081.0	1059.20	(1, 2, 2)	3631.6	
(0,0,3)	1233.5		(1,3,1)	3709.4	3639.63
(0,1,2)	1364.4		(0,4,4)	3718.9	
(0, 2, 1)	1491.4	1469.44	(0, 1, 8)	3732.2	
(0,3,0)	1612.8	1569.07	(1,4,0)	3765.7	3675.25
(0,0,4)	1637.4		(0,5,3)	3801.9	
(0,1,3)	1770.3		(0,6,2)	3839.6	
(1,0,0)	1813.7	1786.96	(2,0,1)	3839.8	3783.65
(0, 2, 2)	1897.4		(1,0,5)	3840.8	
(0,3,1)	2019.6	1976.42	(0,7,1)	3870.7	
(0,0,5)	2037.1		(0, 2, 7)	3874.9	
(0,4,0)	2126.4	2060.57	(2, 1, 0)	3894.4	3828.00
(0, 1, 4)	2173.0		(1, 1, 4)	3942.1	
(1,0,1)	2226.4	2199.43	(0,0,10)	3951.7	
(0,2,3)	2300.7		(0,3,6)	4001.8	
(1,1,0)	2321.2	2286.15	(1,2,3)	4032.3	
(0,3,2)	2421.8		(0,9,0)	4075.0	
(0,0,6)	2431.5		(1,3,2)	4105.7	
(0,4,1)	2529.9		(0,1,9)	4110.7	
(0,1,5)	2571.2		(1,4,1)	4164.2	
(0,5,0)	2613.8	2526.79	(1,5,0)	4192.3	4068.67
(1,0,2)	2635.0		(1,0,6)	4232.6	
(0,2,4)	2701.4		(2,0,2)	4245.0	
(1,1,1)	2732.1	2696.27	(0,2,8)	4254.1	
(1,2,0)	2819.5	2770.59	(2,1,1)	4298.5	4228.03
(0,3,3)	2819.8	27,010	(0,0,11)	4318.7	1220,00
(0,0,7)	2822.1		(2,2,0)	4337.6	4261.15
(0,4,2)	2928.6		(1,1,5)	4339.3	
(0,1,6)	2964.1		(0, 10, 0)	4357.6	
(0,5,1)	3014.0		(0,3,7)	4384.6	
(1,0,3)	3040.1		(1,2,4)	4429.7	
(0,6,0)	3065.0		(0,9,1)	4475.9	
(0,2,5)	3098.1		(0,1,10)	4479.5	
(1,1,2)	3139.0		(1,3,3)	4506.4	
(0,0,8)	3202.6		(1,0,7)	4620.7	
(0,3,4)	3219.2		(0,2,9)	4631.5	
(1,2,1)	3227.8	3177.99	(2,0,3)	4645.6	
(1, 2, 1) $(1, 3, 0)$	3305.2	3235.83	(0,0,12)	4681.2	
(0,4,3)	3324.8	3233.03	(0,0,12) $(2,1,2)$	4698.3	4620.59
(0,4,3) $(0,1,7)$	3351.1		(2,1,2) $(2,2,1)$	4728.2	4643.80
(0, 1, 7) (0, 5, 2)	3409.3		(2,2,1) $(1,1,6)$	4733.0	1013.00
(0, 3, 2) (2, 0, 0)	3432.9		(2,3,0)	4761.0	4679.78
(2,0,0) $(1,0,4)$	3441.8		(2,3,0) $(0,3,8)$	4765.2	40/7./0
(0,6,1)	3447.7		(3,0,0)	4797.7	

Table 6: Calculated vibrational energy levels (in cm $^{-1}$) and comparison with available experimental results for DSi 79 Br (\tilde{A}^1A'').

(n_1,n_2,n_3)	This work	Expt. [8]	(n_1,n_2,n_3)	This work	Expt. [8]
(0,0,0)	0.0	0.00	(0,9,0)	3320.2	
(0, 1, 0)	377.8	376.41	(0,1,7)	3333.7	
(0,0,1)	436.3	434.34	(1,2,3)	3336.5	3291.73
(0, 2, 0)	755.7	750.48	(0,8,1)	3351.9	
(0, 1, 1)	811.7	806.10	(2,1,1)	3367.4	
(0,0,2)	869.0	864.77	(0,7,2)	3391.1	
(0,3,0)	1133.0	1121.95	(1,1,4)	3398.8	
(0, 2, 1)	1187.1	1174.58	(0,0,8)	3411.2	
(0,1,2)	1243.0	1231.27	(0,6,3)	3436.6	
(0,0,3)	1298.7	1290.48	(2,0,2)	3444.3	
(1,0,0)	1344.7	1325.55	(1,0,5)	3467.4	
(0,4,0)	1508.1	1490.30	(0,5,4)	3487.2	
(0,3,1)	1560.6	1540.58	(1,6,0)	3505.6	3436.43
(0, 2, 2)	1614.5	1594.60	(0,4,5)	3541.7	
(0, 1, 3)	1670.4	1651.70	(1,5,1)	3560.7	3498.71
(1, 1, 0)	1710.6	1688.70	(0,3,6)	3600.2	
(0,0,4)	1725.9	1711.77	(1,4,2)	3619.1	3562.48
(1,0,1)	1775.9	1754.76	(2,3,0)	3637.3	3579.61
(0,5,0)	1879.8	1855.22	(0,10,0)	3639.9	
(0,4,1)	1930.6	1902.26	(0,2,7)	3665.9	
(0,3,2)	1982.5	1953.86	(1,3,3)	3680.7	3628.07
(0,2,3)	2036.6	2008.99	(0,9,1)	3682.0	
(1,2,0)	2075.8	2048.42	(2,2,1)	3710.5	3659.77
(0,1,4)	2093.2	2067.22	(0,8,2)	3721.3	000,,,,
(1, 1, 1)	2138.0	2112.79	(0,1,8)	3739.9	
(0,0,5)	2151.5		(1,2,4)	3743.4	
(1,0,2)	2203.3	2180.27	(3,0,0)	3744.8	
(0,6,0)	2247.6	2215.53	(0,7,3)	3763.4	
(0,5,1)	2295.8	2259.58	(2,1,2)	3785.2	
(0,4,2)	2345.3	2308.59	(0,6,4)	3810.7	
(0,3,3)	2397.7	2361.47	(1,1,5)	3811.2	
(1,3,0)	2439.7	2404.43	(0,0,9)	3821.2	
(0,2,4)	2452.7	2418.10	(1,7,0)	3845.6	
(1,2,1)	2499.6	2467.46	(0,5,5)	3863.0	
(0,1,5)	2511.6	2107.10	(2,0,3)	3863.8	
(1,1,2)	2562.1	2533.19	(1,0,6)	3883.8	
(0,0,6)	2575.1	2333.17	(1,6,1)	3899.5	
(0,0,0) (2,0,0)	2596.0		(0,4,6)	3925.6	
(2,0,0) (0,7,0)	2611.0	2569.98	(1,5,2)	3958.2	
(0,7,0) $(1,0,3)$	2627.3	2601.43	(2,4,0)	3975.7	3905.52
					3903.32
(0,6,1)	2655.6	2610.98	(0,3,7)	3983.0	
(0,5,2)	2701.8	2657.51	(1,4,3)	4019.3	2007.77
(0,4,3)	2752.3	2755 51	(2,3,1)	4049.0	3987.77
(1,4,0)	2800.5	2755.51	(0,2,8)	4059.3	
(0,3,4)	2805.8	2017 20	(3,1,0)	4070.9	
(1,3,1)	2858.5	2817.20	(1,3,4)	4082.4	
(0,2,5)	2862.9	2001 62	(2,2,2)	4126.0	
(1,2,2)	2919.2	2881.69	(1,2,5)	4148.9	
(0, 1, 6)	2926.0		(3,0,1)	4164.5	
(2,1,0)	2945.8		(2,1,3)	4199.2	

Table 6: Continued.

(n_1,n_2,n_3)	This work	Expt. [8]	(n_1,n_2,n_3)	This work	Expt. [8]
(0, 8, 0)	2969.5	2912.85	(1,1,6)	4218.7	
(1, 1, 3)	2982.6	2948.95	(0,0,10)	4224.0	
(0,0,7)	2995.4		(1,8,0)	4229.4	
(0,7,1)	3008.8		(2,0,4)	4278.5	
(2,0,1)	3022.2		(1,7,1)	4287.6	
(1,0,4)	3048.5	2999.16	(1,0,7)	4296.8	
(0,6,2)	3051.0	3018.34	(2,5,0)	4305.2	4220.97
(0,5,3)	3099.2		(1,6,2)	4348.7	
(0,4,4)	3151.3		(2,4,1)	4380.0	4306.79
(1,5,0)	3156.5	3100.27	(3,2,0)	4395.1	
(0,3,5)	3206.7		(1,5,3)	4412.0	
(1,4,1)	3212.9	3161.61	(2,3,2)	4455.8	
(0, 2, 6)	3267.2		(3,1,1)	4486.9	
(1, 3, 2)	3272.4	3225.27	(3,0,2)	4581.6	
(2, 2, 0)	3293.1		(4,0,0)	4763.6	

lengths with the bond angle fixed at its equilibrium value of 93.9°, respectively. The equilibrium geometry of HSiBr at the ground electronic state PES was found to be located at $R_{\rm HSi} = 2.869\,a_0$, $R_{\rm SiBr} = 4.257\,a_0$, and $\theta = 93.9^\circ$, which is very similar to that of HSiCl [20], except that the Si–Br bond is longer than the Si–Cl bond. Our results are compared in Table 1 with the previous experimental and theoretical results. It is clear that our equilibrium geometry is in good agreement with the experimental and theoretical values [3, 8, 13].

The calculated vibrational levels for the ground electronic state (\widetilde{X}^1A') of HSiBr up to $7300\,\mathrm{cm}^{-1}$ are listed in Table 2, together with the available experimental values. The vibrational energy levels are assigned with three vibrational quantum numbers (n_1, n_2, n_3) , representing the H–Si stretching, bending, and Si–Br stretching vibrational modes, respectively. By inspecting the nodal structures of the corresponding wave functions, the assignment of the vibrational levels can be achieved. The plots of nine wave functions of HSiBr are given in Figure 2, in which the nodal structures are clearly visible. The ease of the assignment suggests that the vibration of HSiBr is largely regular with weak intramodal coupling in this spectral region.

From Table 2, it is apparent that the calculated vibrational energy levels reproduce the available experimental data very well. The fundamental frequencies of v_1 = 1977.6 cm⁻¹, v_2 = 770.3 cm⁻¹, and v_3 = 409.3 cm⁻¹ are in excellent agreement with the experimental values [13] of 1976.2, 772.0, and 412.4 cm⁻¹, respectively. The good theory-experiment agreement is held all the way to the highest experimentally assigned level (1, 7, 0) near 7200 cm⁻¹.

The vibrational energy levels of DSiBr have also been obtained on the same *ab initio* ground electronic state PES. The calculated vibrational levels up to 6500 cm⁻¹ are compared with the available experimental data in Table 3. As expected, the substitution by the more massive deuterium not only lowers the energies of the H–Si stretching and bending vibrations, but also decreases the Si–Br stretching vibrational frequency to a small extent. Again, the calculated

results are in excellent agreement with experiment. The calculated fundamental vibrational frequencies for the D–Si stretching, Si–Br stretching, and bending modes (1439.8, 405.0, and 562.0 cm⁻¹) are very close to the experimental values [13] (1439.5, 407.99, and 561.8 cm⁻¹), respectively. As a whole, Tables 2 and 3 show that all the calculated vibrational energy levels for HSiBr/DSiBr are within a reasonable error of the observed values, demonstrating the high accuracy of our *ab initio* ground electronic state PFS

3.2. Excited (\widetilde{A}^1A'') State Potential and Vibrational Energy Levels. Figure 3 displays the PES for the excited electronic state (\widetilde{A}^1A'') in the HSiBr internal coordinates (R_{HSi} , R_{SiBr} , θ). The equilibrium geometry was found to be located at $R_{\text{HSi}} = 2.833\,a_0$, $R_{\text{SiBr}} = 4.193\,a_0$, and $\theta = 117.7^\circ$. In comparison with the ground state, neither the H–Si nor Si–Br bond length changes significantly, but the bending angle is extended by about 20°. One can see from Table 1 that the equilibrium geometry is consonant with the experimental and previous theoretical values [3, 8, 13].

The calculated vibrational levels for the excited (\widetilde{A}^1A'') electronic states of HSi⁷⁹Br, HSi⁸¹Br, DSi⁷⁹Br, and DSi⁸¹Br are presented in Tables 4, 5, 6, and 7, together with the available experimental results. The energies given in the tables are relative to the ground (0, 0, 0) vibrational level on this PES. Figure 4 displays six vibrational wave functions of HSiBr on the excited electronic states. The nodal structures of the wave functions are clearly shown. The theory-experiment agreement is typically very good. For example, the calculated fundamental frequencies of the H-Si stretching, Si-79Br stretching, and bending modes (1813.71, 416.50, and 541.83 cm⁻¹) are in reasonably good agreement with the experimental values (1786.96, 416.54, and 535.31 cm⁻¹) [8]. As expected, the substitution by deuterium lowers the energies of the vibrational frequencies. Since the ⁷⁹Br/⁸¹Br ratio is much smaller than D/H, the effect

Table 7: Calculated vibrational energy levels (in cm $^{-1}$) and comparison with available experimental results for DSi 81 Br ($\widetilde{A}^{1}A^{\prime\prime}$).

(n_1,n_2,n_3)	This work	Expt. [8]	(n_1,n_2,n_3)	This work	Expt. [8]
(0,0,0)	0.0		(0,9,0)	3316.96	
(0,1,0)	377.2	375.87	(0,1,7)	3328.73	
(0,0,1)	435.4	433.44	(1,2,3)	3331.48	3287.52
(0,2,0)	754.5	749.44	(0,8,1)	3347.95	
(0,1,1)	810.3	804.70	(2,1,1)	3365.97	
(0,0,2)	867.4	863.00	(0,7,2)	3385.94	
(0,3,0)	1131.1	1120.41	(1,1,4)	3394.50	
(0,2,1)	1185.2	1173.11	(0,0,8)	3404.45	
(0,1,2)	1240.9	1228.93	(0,6,3)	3430.85	
(0,0,3)	1296.2	1287.74	(2,0,2)	3442.10	
(1,0,0)	1344.7	1325.55	(1,0,5)	3462.55	
(0,4,0)	1505.5	1488.35	(0,5,4)	3480.95	
(0,3,1)	1558.1	1538.21	(1,6,0)	3503.64	3435.14
(0,2,2)	1611.8	1591.74	(0,4,5)	3535.04	
(0,1,3)	1667.5	1648.49	(1,5,1)	3557.80	3496.22
(1,1,0)	1710.2	1688.30	(0,3,6)	3593.33	
(0,0,4)	1722.6	1708.21	(1,4,2)	3615.41	3558.80
(1,0,1)	1774.9	1753.76	(2,3,0)	3636.40	3578.93
(0,5,0)	1876.7	1852.96	(0,10,0)	3638.85	
(0,4,1)	1927.5	1899.48	(0,2,7)	3658.95	
(0,3,2)	1979.2	1950.57	(1,3,3)	3676.39	3623.67
(0,2,3)	2033.1	2005.19	(0,9,1)	3677.72	
(1,2,0)	2074.9	2047.70	(2,2,1)	3708.72	3658.01
(0,1,4)	2089.5	2063.10	(0,8,2)	3715.75	
(1,1,1)	2136.6	2111.59	(0,1,8)	3732.91	
(0,0,5)	2147.3		(1,2,4)	3739.87	
(1,0,2)	2201.3	2178.17	(3,0,0)	3743.44	
(0,6,0)	2244.0	2213.29	(0,7,3)	3757.02	
(0,5,1)	2292.3	2256.47	(2,1,2)	3782.58	
(0,4,2)	2341.5	2304.82	(0,6,4)	3804.27	
(0,3,3)	2393.6	2357.25	(1,1,5)	3805.53	
(1,3,0)	2438.4	2403.33	(0,0,9)	3813.63	
(0,2,4)	2448.4	2413.45	(1,7,0)	3843.74	
(1,2,1)	2497.8	2465.64	(0,5,5)	3856.71	
(0,1,5)	2507.2		(2,0,3)	3859.58	
(1,1,2)	2559.8	2530.70	(1,0,6)	3878.06	
(0,0,6)	2570.0		(1,6,1)	3896.57	
(2,0,0)	2596.0		(0,4,6)	3919.12	
(0,7,0)	2607.0	2567.71	(1,5,2)	3954.23	
(1,0,3)	2624.4	2598.32	(2,4,0)	3974.67	3904.78
(0,6,1)	2651.7	2607.55	(0,3,7)	3976.09	
(0,5,2)	2697.5	2653.40	(1,4,3)	4014.57	
(0,4,3)	2747.7		(2,3,1)	4046.99	3985.91
(1,4,0)	2798.8	2754.28	(0,2,8)	4051.56	
(0,3,4)	2800.9		(3,1,0)	4070.65	
(1,3,1)	2856.1	2815.08	(1,3,4)	4076.68	
(0,2,5)	2857.9		(2,2,2)	4120.45	
(1,2,2)	2916.3	2878.97	(1,2,5)	4143.05	
(0,1,6)	2920.8		(3,0,1)	4163.28	
(2,1,0)	2945.5		(2,1,3)	4195.41	

Table 7: Continued.

(n_1, n_2, n_3)	This work	Expt. [8]	(n_1,n_2,n_3)	This work	Expt. [8]
(0,8,0)	2965.5	2911.19	(1,1,6)	4212.47	
(1,1,3)	2979.3	2945.37	(0,0,10)	4215.55	
(0,0,7)	2989.5		(1,8,0)	4224.77	
(0,7,1)	3004.8		(2,0,4)	4273.99	
(2,0,1)	3021.1		(1,7,1)	4283.27	
(1,0,4)	3044.6	3014.23	(1,0,7)	4290.27	
(0,6,2)	3046.3	2994.71	(2,5,0)	4304.18	4220.13
(0,5,3)	3094.0		(1,6,2)	4343.48	
(0,4,4)	3145.7		(2,4,1)	4377.84	4304.76
(1,5,0)	3154.6	3098.96	(3,2,0)	4392.57	
(0,3,5)	3200.8		(1,5,3)	4406.13	
(1,4,1)	3210.3	3159.24	(2,3,2)	4452.59	
(0,2,6)	3261.2		(3,1,1)	4485.40	
(1,3,2)	3269.0	3221.96	(3,0,2)	4579.21	
(2,2,0)	3292.5		(4,0,0)	4763.54	

of the ⁸¹Br substitution on vibrational energies of HSiBr is much less pronounced.

3.3. Absorption Spectra. The $\widetilde{A}^1A'' \leftarrow \widetilde{X}^1A'$ electronic transition of HSiBr involves an electron promotion from a silicon-based nonbonding σ orbital to an unoccupied outof-plane Si 3p orbital [13]. The only non-zero transition dipole is perpendicular to the molecular plane, and it varies smoothly with the three coordinates in the Franck-Condon region. As shown in Figure 5, the calculated $\widetilde{A}^1 A'' \leftarrow \widetilde{X}^1 A'$ absorption spectra from the lowest state \tilde{X} (0, 0, 0) of both HSiBr and DSiBr were found to contain a relatively small number of vibronic bands. The spectral positions of the vibronic bands of HSiBr and DSiBr are consistent with the experimental spectra obtained with the laser-induced fluorescence technique [8]. Since the experimental LIF spectrum may often be composed of several different fragment portions which were recorded under different experimental conditions and involve the influence of rotational structures, some observable bands cannot be reproduced in our calculations. Considering the approximately 20° change in the bending equilibrium angle, it is anticipated that the absorption is dominated by excitation in the bending mode. Indeed, the calculated absorption spectrum for HSiBr is dominated by the $(0, n_2, 0)$ progression. On the other hand, the spectrum of DSiBr is more complex than that of HSiBr. Besides the $(0, n_2, 0)$ progression, the $(0, 0, n_3)$ band and some combination bands are of comparable intensities. In addition, several weaker bands such as (1,0,0), (1,1,0), and (1, 1, 1) are visible.

3.4. Emission Spectra. The calculated $\widetilde{A}^1A'' \to \widetilde{X}^1A'$ emission spectra from the (0,0,0) and (0,1,0) vibrational states of the excited electronic state of HSiBr and DSiBr and the comparison with the available experimental observations are shown in Figure 6. The spectra are concentrated in the spectral region within $6000\,\mathrm{cm}^{-1}$ above the band origin,

and it is clear that the experimental emission spectra of Hostutler et al. [13] are well reproduced by the calculated ones. As shown in this figure, the emission spectra from the vibrational state $\widetilde{A}(0, 1, 0)$ of HSiBr is dominated by the $(0, n_2, 0)$ progression. The good agreement between theory and experiment again suggests that both the ground and excited state PESs are quite reliable. Also shown in Figure 6, the calculated emission spectra from the vibrational state of $\widetilde{A}(0, 0, 0)$ is also dominated by the $(0, n_2, 0)$ progression.

The essential features of the spectra are similar for the two isotopomers, but the DSiBr spectra are more congested than that of HSiBr due to the larger mass of deuterium. One can see from Figure 6 that the emission spectrum from $\tilde{A}(0, 0, 0)$ of DSiBr is featured by the dominated $(0, n_2, 0)$ 0) and weaker $(1, n_2, 0)$ progressions. The large bending excitation is due to the about 20° increase in the bond angle upon electronic excitation. In the same figure, the calculated emission spectrum from the $\tilde{A}(0, 1, 0)$ of DSiBr is compared to the experimental data of Hostutler et al. [13] As expected, the spectrum bending progressions are dominated, with 0 and 1 quanta in the Si-Br mode, respectively. The overall agreement with the experiment is very good. These emission spectra show that the spectral pattern is quite sensitive to the vibrational state from which the emission originates. These observations are very similar to those in our previous work about HSiCl [20].

4. Conclusions

In this work, we have reported accurate *ab initio* PESs for both the ground (\widetilde{X}^1A') and excited electronic states (\widetilde{A}^1A'') of HSiBr, as well as the $\widetilde{A}^1A''-\widetilde{X}^1A'$ transition dipole moment. By spline interpolation of numerous *ab initio* points which were obtained at high *ab initio* level of theory, the nonempirical three-dimensional potential energy surfaces and transition dipole moment function were constructed. Some low-lying vibrational energy levels of

both HSiBr and DSiBr were determined using the Lanczos recursion method. The calculated results are in good agreement with the available experimental data, demonstrating the good quality of both the ground and excited state PESs. In addition, the absorption and emission spectra of HSiBr/DSiBr were calculated using an efficient single Lanczos propagation method, and the resulting spectra were found to be fairly consistent with experimental observations. Similar to HSiCl, the approximately 20° difference in the HSiBr equilibrium bending angle in the two electronic states leads to significant bending excitations in both absorption and emission spectra. Our theoretical results reported provide necessary insight into the vibrational dynamics of the HSiBr molecule in its ground and excited electronic states.

Acknowledgments

D.X. acknowledges support from the National Natural Science Foundation of China (Grant Nos. 20725312 and 91021010), from the Ministry of Science and Technology (2007CB815201), and from the Fundamental Research Funds for the Central Universities (1114020503).

References

- [1] J. M. Jasinski, B. S. Meyerson, and B. A. Scott, "Mechanistic studies of chemical vapor-deposition," *Annual Review of Physical Chemistry*, vol. 38, no. 1, pp. 109–140, 1987.
- [2] S. K. Murad, S. P. Beaumont, and C. D. W. Wilkinson, "New chemistry for selective reactive ion etching of InGaAs and InP over InAlAs in SiCl₄/SiF₄/HBr plasmas," *Applied Physics Letters*, vol. 67, no. 18, pp. 2660–2662, 1995.
- [3] G. Herzberg and R. D. Verma, "Spectra & structures of free HSiCl & HSiBr radicals," *Canadian Journal of Physics*, vol. 42, no. 3, pp. 395–432, 1964.
- [4] J. T. Hougen and J. K. G. Watson, "Anomalous rotational line intensities in electronic transitions of polyatomic moleculesaxis-switching," *Canadian Journal of Physics*, vol. 43, no. 2, pp. 298–320, 1965.
- [5] N. L. Shinkle and J. B. Coon, "A variable reduced mass model for quasi-linear molecules with application to HSiBr," *Journal of Molecular Spectroscopy*, vol. 40, no. 2, pp. 217–227, 1971.
- [6] W. A. Gilchrist, E. Reyna, and J. B. Coon, "Geometrical structures, bending potentials, and vibrational frequencies v_1 for 1 A" states of HSiBr, HSiCl, and DSiCl," *Journal of Molecular Spectroscopy*, vol. 74, no. 3, pp. 345–360, 1979.
- [7] J. I. Steinfeld, "Reactions of photogenerated free radicals at surfaces of electronic materials," *Chemical Reviews*, vol. 89, no. 6, pp. 1291–1301, 1989.
- [8] H. Harjanto, W. W. Harper, and D. J. Clouthier, "Resolution of anomalies in the geometry and vibrational frequencies of monobromosilylene (HSiBr) by pulsed discharge jet spectroscopy," *The Journal of Chemical Physics*, vol. 105, no. 23, pp. 10189–10200, 1996.
- [9] W. W. Harper and D. J. Clouthier, "Reinvestigation of the HSiCl electronic spectrum: experimental reevaluation of the geometry, rotational constants, and vibrational frequencies," *The Journal of Chemical Physics*, vol. 106, no. 23, pp. 9461– 9473, 1997.
- [10] W. W. Harper, E. A. Ferrall, R. K. Hilliard, S. M. Stogner, R. S. Grev, and D. J. Clouthier, "Laser spectroscopic detection of

- the simplest unsaturated silylene and germylene," *Journal of the American Chemical Society*, vol. 119, no. 35, pp. 8361–8362, 1997.
- [11] W. W. Harper, D. A. Hostutler, and D. J. Clouthier, "Pulsed discharge jet spectroscopy of DSiF and the equilibrium molecular structure of monofluorosilylene," *The Journal of Chemical Physics*, vol. 106, no. 11, pp. 4367–4375, 1997.
- [12] D. A. Hostutler, D. J. Clouthier, and R. H. Judge, "Single vibronic level emission spectroscopy of jet-cooled HSiF and DSiF," *The Journal of Chemical Physics*, vol. 114, no. 24, pp. 10728–10732, 2001.
- [13] D. A. Hostutler, N. Ndiege, D. J. Clouthier, and S. W. Pauls, "Emission spectroscopy, harmonic vibrational frequencies, and improved ground state structures of jet-cooled monochloro—and monobromosilylene (HSiCl and HSiBr)," *The Journal of Chemical Physics*, vol. 115, no. 12, pp. 5485–5491, 2001.
- [14] B. S. Tackett and D. J. Clouthier, "Structural and spectroscopic trends in the ground states of the monohalosilylenes: emission spectroscopy of jet-cooled HSiI and DSiI," *The Journal of Chemical Physics*, vol. 118, no. 6, pp. 2612–2619, 2003.
- [15] D. K. W. Mok, E. P. F. Lee, F. T. Chau, and J. M. Dyke, "Franck-Condon simulation of the single vibronic level emission spectra of HSiF and DSiF including anharmonicity," *The Journal of Chemical Physics*, vol. 120, no. 3, pp. 1292–1305, 2004
- [16] B. S. Tackett, D. J. Clouthier, J. N. Landry, and W. Jager, "Fourier transform microwave spectroscopy of HSiBr: exploring the Si-Br bond through quadrupole hyperfine coupling," The Journal of Chemical Physics, vol. 122, no. 21, Article ID 214314, 6 pages, 2005.
- [17] D. W. K. Mok, E. P. F. Lee, F. T. Chau, and J. M. Dyke, "Franck-Condon simulations including anharmonicity of the $A^1A''-X^1A'$ absorption and single vibronic level emission spectra of HSiCl and DSiCl," *Journal of Chemical Theory and Computation*, vol. 5, no. 3, pp. 565–579, 2009.
- [18] S. Lin, D. Xie, and H. Guo, "Ab initio potential energy surfaces for both the ground (X^1A') and excited (X^1A') and excited (A^1A'') electronic states of HGeCl and the absorption and emission spectra of HGeCl/DGeCl," *The Journal of Chemical Physics*, vol. 129, no. 15, Article ID 154313, 11 pages, 2008.
- [19] S. Lin, D. Xie, and H. Guo, "Ab initio potential energy surfaces for both the ground (X¹A') and excited (A¹A'') electronic states of HGeBr and the absorption and emission spectra of HGeBr/DGeBr," *Journal of Physical Chemistry A*, vol. 113, no. 26, pp. 7314–7321, 2009.
- [20] S. Lin and D. Q. Xie, "New *ab initio* potential energy surfaces for both the ground (X¹A') and excited (A¹A") electronic states of HSiCl and the absorption and emission spectra of of HSiCl/DSiCl," *Journal of Computational Chemistry*, vol. 32, no. 8, pp. 1694–1702, 2011.
- [21] MOLPRO, a package of ab initio programs designed by H.-J. Werner, P. J. Knowles, R. D. Amos et al., version 2006.1.
- [22] C. Hampel, K. A. Peterson, and H. J. Werner, "A comparison of the efficiency and accuracy of the quadratic configuration-interaction (QCISD), coupled cluster (CCSD), and Brueckner coupled cluster (BCCD) methods," *Chemical Physics Letters*, vol. 190, no. 1-2, pp. 1–12, 1992.
- [23] T. H. Dunning Jr., "Gaussian basis sets for use in correlated molecular calculations. I. The atoms boron through neon and hydrogen," *The Journal of Chemical Physics*, vol. 90, no. 2, pp. 1007–1023, 1989.

- [24] S. R. Langhoff and E. R. Davidson, "Configuration interaction calculations on nitrogen molecule," *International Journal of Quantum Chemistry*, vol. 8, no. 1, pp. 61–72, 1974.
- [25] P. J. Knowles and H.-J. Werner, "An efficient method for the evaluation of coupling coefficients in configuration interaction calculations," *Chemical Physics Letters*, vol. 145, no. 6, pp. 514–522, 1988.
- [26] H.-J. Werner and P. J. Knowles, "An efficient internally contracted multiconfiguration-reference configuration interaction method," *The Journal of Chemical Physics*, vol. 89, no. 9, pp. 5803–5814, 1988.
- [27] P. J. Knowles and H.-J. Werner, "An efficient second-order MCSCF method for long configuration expansions," *Chemical Physics Letters*, vol. 115, no. 3, pp. 259–267, 1985.
- [28] H.-J. Werner and P. J. Knowles, "A second order multiconfiguration SCF procedure with optimum convergence," *The Journal of Chemical Physics*, vol. 82, no. 11, pp. 5053–5063, 1985.
- [29] B. R. Johnson and W. P. Reinhardt, "Adiabatic separations of stretching and bending vibrations: application to H₂O," *The Journal of Chemical Physics*, vol. 85, no. 8, pp. 4538–4556, 1986.
- [30] J. C. Light, I. P. Hamilton, and J. V. Lill, "Generalized discrete variable approximation in quantum mechanics," *The Journal* of Chemical Physics, vol. 82, no. 3, pp. 1400–1409, 1985.
- [31] C. Lanczos, "An iteration method for the solution of the eigenvalue problem of linear differential and integral operators," *Journal of Research of the National Bureau of Standards*, vol. 45, no. 4, pp. 255–282, 1950.
- [32] J. Echave and D. C. Clary, "Potential optimized discrete variable representation," *Chemical Physics Letters*, vol. 190, no. 3-4, pp. 225–230, 1992.
- [33] H. Wei and T. Carrington, "The discrete variable representation of a triatomic Hamiltonian in bond length-bond angle coordinates," *The Journal of Chemical Physics*, vol. 97, no. 5, pp. 3029–3037, 1992.
- [34] J. V. Lill, G. A. Parker, and J. C. Light, "Discrete variable representations and sudden models in quantum scattering theory," *Chemical Physics Letters*, vol. 89, no. 6, pp. 483–489, 1982.
- [35] R. Q. Chen and H. Guo, "A single Lanczos propagation method for calculating transition amplitudes," *The Journal of Chemical Physics*, vol. 111, no. 22, pp. 9944–9951, 1999.
- [36] R. Q. Chen and H. Guo, "A single Lanczos propagation method for calculating transition amplitudes. II. Modified QL and symmetry adaptation," *The Journal of Chemical Physics*, vol. 114, no. 4, pp. 1467–1472, 2001.
- [37] H. Guo, R. Chen, and D. Xie, "Calculation of transition amplitudes with a single Lanczos propagation," *Journal of Theoretical and Computational Chemistry*, vol. 1, no. 1, pp. 173–185, 2002.

Hindawi Publishing Corporation Advances in Physical Chemistry Volume 2012, Article ID 164752, 19 pages doi:10.1155/2012/164752

Review Article

Constructing Potential Energy Surfaces for Polyatomic Systems: Recent Progress and New Problems

J. Espinosa-Garcia, M. Monge-Palacios, and J. C. Corchado

Departamento de Química Física, Universidad de Extremadura, 06071 Badajoz, Spain

Correspondence should be addressed to J. Espinosa-Garcia, joaquin@unex.es

Received 11 May 2011; Accepted 14 July 2011

Academic Editor: Laimutis Bytautas

Copyright © 2012 J. Espinosa-Garcia et al. This is an open access article distributed under the Creative Commons Attribution License, which permits unrestricted use, distribution, and reproduction in any medium, provided the original work is properly cited.

Different methods of constructing potential energy surfaces in polyatomic systems are reviewed, with the emphasis put on fitting, interpolation, and analytical (defined by functional forms) approaches, based on quantum chemistry electronic structure calculations. The different approaches are reviewed first, followed by a comparison using the benchmark $H + CH_4$ and the $H + NH_3$ gas-phase hydrogen abstraction reactions. Different kinetics and dynamics properties are analyzed for these reactions and compared with the available experimental data, which permits one to estimate the advantages and disadvantages of each method. Finally, we analyze different problems with increasing difficulty in the potential energy construction: spin-orbit coupling, molecular size, and more complicated reactions with several maxima and minima, which test the soundness and general applicability of each method. We conclude that, although the field of small systems, typically atom-diatom, is mature, there still remains much work to be done in the field of polyatomic systems.

1. Introduction

At the heart of chemistry lies the knowledge of the reaction mechanism at atomic or molecular levels, that is, the motion of the nuclei in the potential field due to the electrons and nuclei. When the separation of the nuclear and electronic motions is possible, that is, within the Born-Oppenheimer (BO) approximation [1], the potential energy surface (PES) is the electronic energy (which includes electronic kinetic and Coulomb interaction energy) plus nuclear repulsion of a given adiabatic electronic state as a function of geometry. The PES is then the effective potential energy for the nuclear motion when the system is in that electronic state.

The actual knowledge of the chemical reactivity is based on quantum mechanical first principles, and the complete construction of the PES represents a very important challenge in theoretical chemistry. For small reactive systems (three or four atoms), the PES construction is a relatively mature field, although even today new surfaces are still being developed for atom-diatom systems [2–6] using highlevel *ab initio* calculations. For instance, one of the latest atom-diatom surfaces has been developed in the present year by Jiang et al. [6] for the H + HBr hydrogen abstrac-

tion reaction. *Ab initio* calculations were performed based on the multireference configuration interaction (MRCI) method including Davidson's correction using augmented correlation-consistent-polarized valence X-tuple zeta basis sets, with X up to 5, extrapolating the energies to the complete basis set (CBS) limit, and taking into account the spin-orbit correction. In order to define the complete configuration space for the BrH₂ system, *ab initio* calculations were performed at more than 12000 geometries. Then, a three-dimensional cubic spline interpolation was employed to yield the ground-state PES for this system. As can be seen, the computational effort (correlation energy + basis set + number of points) is enormous, and doing this for larger systems is still clearly prohibitive.

The extension to larger reactive systems (more than 4 atoms) is an open and promising field, although computationally very costly. Thus, for polyatomic systems of n atoms, with 3n-6 internal degrees of freedom, if one needs m configurations for each degree of freedom, one would need a total of $m^{(3n-6)}$ evaluations of the energy. For instance, taking a typical value of m of 10, for the H + CH₄ hydrogen abstraction reaction 10^{12} evaluations would be needed. This implies too much computer time to perform

ab initio calculations with chemical accuracy (1 kcal mol⁻¹) and becomes totally unaffordable if one aims to achieve spectroscopic accuracy (1 cm⁻¹).

The accuracy of the kinetics and dynamics description of a chemical reaction depends, aside from the quality of the PES, on the dynamics method used. If the motion of the nuclei on the PES is determined by the Hamilton equations in the phase-space configuration, the dynamics methods are classical or quasiclassical trajectory (QCT) approaches [7], and if the system is described by the Schrödinger equation (time dependent or time independent), the dynamics methods are quantum mechanical (QM) [8]. Finally, variational transition-state theory with multidimensional tunneling contribution (VTST/MT) can be derived from a dynamical approach by statistical mechanics and provides an excellent and affordable method to calculate thermal rate and state-selected constants [9].

In sum, electronic structure theory, dynamics methods, and constructed potential energy surfaces are the keystones of the theoretical study of chemical reactivity. Recent years have seen a spectacular development in these strongly related disciplines, paving the way towards chemical accuracy in polyatomic systems and toward spectroscopic accuracy in smaller problems. The scope of this paper is the construction of potential energy surfaces for bimolecular gasphase polyatomic reactive systems in their electronic groundstate. Section 2 describes different methods of constructing potential energy surfaces, with especial focus on the methodological approach developed by our research group. Section 3 presents a library of PESs available for the scientific community, and Section 4 presents some results for the H + CH₄ benchmark polyatomic system and the H + NH₃ reaction, which permits us to compare results from different methods. Section 5 is devoted to analyzing the treatment of the peculiarities found in some reactions that entail additional challenges to the construction of potential energy surfaces, such as spin-orbit coupling, the molecular size, and the presence of various maxima and minima. Finally, Section 6 summarizes the main conclusions of the paper.

2. Constructing Potential Energy Surfaces

The construction of potential energy surfaces in reactive systems began with the dawn of Quantum Chemistry when different quantum approaches were used, basically empirical or semiempirical. In present days, the data needed for this construction are obtained from high-level *ab initio* calculations, although density functional theory (DFT) methods are also widely used, especially in the case of larger molecular systems.

As is well known, and this special issue is a clear indication of it, the construction of PESs has a long tradition in theoretical and computational chemistry, and an exhaustive review of the literature is beyond the scope of the present paper (see, for instance, a recent review in [10]). Here we only highlight some important contributions with the aim that the reader will get an overall perspective on this wide field of research.

The most straightforward procedure to describe a reactive system is from electronic structure calculations carried out "on the fly," sometimes also called "direct dynamics" [11], where every time the dynamics algorithm requires an energy, gradient, or Hessian, it is computed from electronic structure calculations or molecular mechanics methods. The advantage of this approach is the direct application of electronic structure calculations to dynamics problems without intermediaries, but when chemical accuracy is needed, very high-level ab initio calculations are required, and hence the time and computational cost are very high. For polyatomic systems, such an approach is still prohibitive. A recent example is the direct dynamics trajectory study of the formaldehyde cation with molecular hydrogen gas-phase reaction [12]. Even using a modest MP2/6-311G(d,p) ab initio level, which yields a barrier only 0.5 kcal mol⁻¹ below the benchmark value, the ≈9600 trajectories required about 2.5 CPU years on a small Linux cluster. In this regard, one has to keep in mind that QCT calculations require a large number of trajectories to adequately sample the events and obtain results that from a purely statistical point of view are tolerable, that is, with very small errors. Note that the time devoted to the QCT calculation is negligible in this time scale.

The alternative to direct dynamics calculations is to construct a mathematical PES, that is, developing an algorithm that can provide the potential energy for any given geometry of the system without depending on "on-the-fly" electronic structure computations. In this sense, three basic approaches have been considered: fitting, interpolation, or analytical (defined by functional forms). In fact, the fitting and analytical procedures share the idea of functional form, and this analytical function needs to be fitted to theoretical information. This classification is therefore arbitrary, and other possibilities can be found in the literature [10]. We think, however, that it can help the reader get a better general view of this field. The interpolation methods have been widely applied in the construction of potential energy surfaces, and different strategies have been developed [9, 10, 13–15]. Thus, Collins et al. [14, 16, 17] developed and applied a method for generating potential energy surfaces using a modified Shepard interpolation. The PES at any configuration (Z) is represented by a weighted average of Taylor series $T_i(R)$:

$$V = \sum_{i=1}^{N \text{data}} w_i(Z) T_i(R), \tag{1}$$

where N_{data} is the number of molecular configurations whose energy and its first (gradient) and second (Hessian) derivatives have been evaluated, $w_i(Z)$ is the normalized weighting factor, R is a set of internal coordinates, and the Taylor series are expanded around the point i:

$$T_{i}(R) = V(R) + \sum_{k=1}^{3n-6} \frac{\partial V}{\partial R_{k}} [R_{k} - R_{k}(i)] + \frac{1}{2!} \sum_{k=1}^{3n-6} \sum_{j=1}^{3n-6} [R_{k} - R_{k}(i)] \frac{\partial^{2} V}{\partial R_{k} \partial R_{j}} [R_{j} - R_{j}(i)].$$
(2)

The use of the energy and its first and second derivatives makes the method very robust, but computationally very expensive, especially if very high-level ab initio calculations are needed for a correct description of the reactive system. For instance, very recently a new PES for the H + CH₄ gas-phase reaction has been developed by Collins by interpolation of 30000 data points obtained with high-level ab initio calculations [18]. The ab initio calculations took about 600 days on a workstation with 8 CPU cores in total, while the evaluations of the potential values on all the grids for this reaction took 400 days. Three advantages of this method are the following: first, that the interpolated function agrees precisely with the values of the data points; second, that new electronic structure points may be incorporated in the process to improve the PES; third, that the PES is invariant to the permutation or exchange of indistinguishable nuclei. However, Shepard interpolation often yields slight oscillations in equipotential contours and vibrational frequencies (second derivatives of the energy); that is, the potential energy surface is not smooth enough to provide smooth changes in the vibrational frequencies. This is a limitation when one wants to compute tunneling effects at low energies, since the barrier to tunnel through is unrealistic.

Fitting methods, such as the interpolated ones considered above, have been widely used in the construction of potential energy surfaces [19–21], and they have been recently reviewed [10]. Thus, for instance, a fitting procedure widely used is based on the many-body expansion (MBE) method [22], amplified by Varandas [23] in the so-called double many-body expansion (DMBE) method. The potential is given by a sum of terms corresponding to atoms, diatoms, triatoms, and tetra-atoms and a series of adjustable coefficients. Another fitting procedure has been developed and applied by Bowman et al. [24–27], in which the *ab initio* data are globally fitted to a permutational symmetry invariant polynomial. The function describing the PES has the form

$$V = p(x) + \sum_{i < j} q_{i,j}(x) \cdot y_{i,j},$$
 (3)

where x is an n-dimensional vector, depending on n internuclear distances, with components $x_{i,j} = \exp(-r_{ij})$, r_{ij} being the distance between nuclei i and j, and $y_{i,j}$ given by

$$y_{i,j} = \frac{e^{-r_{i,j}}}{r_{i,j}},\tag{4}$$

and p(x) and q(x) are polynomials constructed to satisfy the permutation symmetry with respect to the indistinguishable nuclei. For instance, for the CH_5^+ polyatomic system [28], the PES was least-squares fitted to 20 639 *ab initio* energies, obtained at the MP2/cc-pVTZ level. This fit contains 2303 coefficients and an rms fitting error of 51 cm⁻¹. Bowman and coworkers have developed 16 of such PESs for polyatomic systems, and they have been recently revised [27]. In general, the fitting approach is linear least squares, and therefore these surfaces do not exactly reproduce the *ab initio* data.

The third alternative consists of the analytical surfaces defined by functional forms. In this method the *ab initio* data are fitted to a valence bond (VB) functional form, augmented with molecular mechanics (MM) terms which give great flexibility to the potential energy surface. These VB/MM functional forms have a long history in the development of potential energy surfaces [29–33], although at first the surfaces were semiempirical in the sense that theoretical and experimental data were used in the fitting procedure. This has been the methodological approach developed by our group [10, 34, 35].

The first surfaces were developed for the H + CH₄ hydrogen abstraction reaction, as a paradigm of polyatomic systems [29–33]. The potential energy for a given geometry, V, is given by the sum of three terms: stretching potential, $V_{\rm stretch}$, harmonic bending term, $V_{\rm harm}$, and anharmonic out-of-plane potential, $V_{\rm op}$,

$$V = V_{\text{stretch}} + V_{\text{harm}} + V_{\text{op}}.$$
 (5)

The stretching potential is the sum of four London-Eyring-Polanyi (LEP) terms, each one corresponding to a permutation of the four methane hydrogens:

$$V_{\text{stretch}} = \sum_{i=1}^{4} V_3(R_{\text{CH}_i}, R_{\text{CH}_B}, R_{\text{H}_i \text{H}_B}), \tag{6}$$

where R is the distance between the two subscript atoms, H_i stands for one of the four methane hydrogens, and H_B is the attacking H atom. Although the functional form of the V_3 LEP potential is well known, we will recall it for the sake of completeness:

$$\begin{split} V_3\big(R_{\text{CH}_i},R_{\text{CH}_B},R_{\text{H}_i\text{H}_B}\big) &= Q\big(R_{\text{CH}_i}\big) + Q\big(R_{\text{CH}_B}\big) + Q\big(R_{\text{H}_i\text{H}_B}\big) \\ &- \sqrt{\frac{1}{2}\big[J\big(R_{\text{CH}_i}\big) - J\big(R_{\text{H}_i\text{H}_B}\big)\big]^2 + \frac{1}{2}\big[J\big(R_{\text{H}_i\text{H}_B}\big) - J\big(R_{\text{CH}_B}\big)\big]^2 + \frac{1}{2}\big[J\big(R_{\text{CH}_B}\big) - J\big(R_{\text{CH}_i}\big)\big]^2}, \\ Q(R_{XY}) &= \frac{E^1(R_{XY}) + E^3(R_{XY})}{2}, \\ J(R_{XY}) &= \frac{E^1(R_{XY}) - E^3(R_{XY})}{2}, \end{split}$$

$$E^{1}(R_{XY}) = D_{XY}^{1} \left\{ \exp\left(-2\alpha_{XY} \left[R_{XY} - R_{XY}^{e}\right]\right) - 2\exp\left(-\alpha_{XY} \left[R_{XY} - R_{XY}^{e}\right]\right) \right\},$$

$$E^{3}(R_{XY}) = D_{XY}^{3} \left\{ \exp\left(-2\alpha_{XY} \left[R_{XY} - R_{XY}^{e}\right]\right) + 2\exp\left(-\alpha_{XY} \left[R_{XY} - R_{XY}^{e}\right]\right) \right\},$$

$$(7)$$

where there are 12 fitting parameters, four for each of the three kinds of bond, R_{CH_1} , R_{CH_B} , and $R_{\text{H}_i\text{H}_B}$. In particular, these are the singlet and triplet dissociation energies, D_{XY}^1 and D_{XY}^3 , the equilibrium bond distance, R_{XY}^e , and the Morse parameter, α_{XY} . The Morse parameter for the CH_i bonds, α_{CH} , however, is not taken as a constant but rather as a function of the CH distances,

$$\alpha_{\rm CH} = a_{\rm CH} + b_{\rm CH} \left(\frac{\tanh \left[c_{\rm CH} \left(\overline{R} - R_{\rm CH}^e \right) \right] + 1}{2} \right), \quad (8)$$

with \overline{R} being the average R_{CH_i} distance,

$$\overline{R} = \frac{1}{4} \sum_{i=1}^{4} R_{\text{CH}_i}.$$
 (9)

In this way, α_{CH} changes smoothly from its value at methane, $a_{\text{CH}} + (b_{\text{CH}}/2)$, to its value at the methyl radical, $a_{\text{CH}} + b_{\text{CH}}$, as the reaction evolves. Therefore, 14 parameters are required to describe the stretching potential.

One of the problems with this functional was that the equilibrium C–H distances for the reactants, saddle point, and products are the same, leading to a very rigid surface. Chakraborty et al. [36], for the $H + C_2H_6$ reaction, included a modification to endow the surface with greater flexibility. The reference C–H bond distance is transformed smoothly from reactant to product using the following equation:

$$R_{\text{CH}}^{o} = P_1 R_{\text{CH},R}^{o} + (1 - P_1) R_{\text{CH},P}^{o}, \tag{10}$$

where P_1 is

$$P_1 = \prod_{i=1}^{4} T_1(R_{\text{CH}_i}), \tag{11}$$

which is symmetric with respect to all the four hydrogen atoms and goes to zero as one of the hydrogen atoms is abstracted, and T_1 is a geometry-dependent switching function, given by

$$T_1(R_{\text{CH}_i}) = 1 - \tanh[w_1(R_{\text{CH}_i} - w_2)],$$
 (12)

where w_1 and w_2 are adjustable parameters. Therefore, this adds 2 new parameters (total 16 parameters) to describe the stretching potential.

The V_{harm} term is the sum of six harmonic terms, one for each bond angle in methane:

$$V_{\text{harm}} = \frac{1}{2} \sum_{i=1}^{3} \sum_{j=i+1}^{4} k_{ij}^{0} k_{i} k_{j} \left(\theta_{ij} - \theta_{ij}^{0} \right)^{2}, \tag{13}$$

where k_{ij}^0 and k_i are force constants and θ_{ij}^0 are the reference angles. The k_{ij}^0 force constants are allowed to evolve from their value in methane, k^{CH_4} , to their value in methyl, k^{CH_3} , which are two parameters of the fit, by means of switching functions:

$$k_{ij}^{0} = k^{\text{CH}_4} + k^{\text{CH}_4} \left[S_1(R_{\text{CH}_i}) S_1(R_{\text{CH}_j}) - 1 \right] + \left(k^{\text{CH}_4} - k^{\text{CH}_3} \right) \left| S_2(R_{\text{CH}_i}) S_2(R_{\text{CH}_j}) - 1 \right|,$$
(14)

while k_i is a function of both the R_{CH_i} and $R_{H_iH_B}$ distances:

$$k_{i} = A_{1} \exp \left[-A_{2} (R_{\text{CH}_{i}} - R_{\text{CH}}^{e})^{2} \right],$$

$$A_{1} = 1 - \exp \left[-aa_{1} (R_{\text{H}_{i}\text{H}_{B}})^{2} \right],$$

$$A_{2} = aa_{2} + aa_{3} \exp \left[-aa_{4} \left(R_{\text{H}_{i}\text{H}_{B}} - R_{\text{H}_{i}\text{H}_{B}}^{e} \right)^{2} \right].$$
(15)

Thus, four adjustable parameters are involved in the definition of k_i .

The reference angles are also allowed to change from their value at methane, $\tau = 109.47^{\circ}$, or arccosine (-1/3), to methyl, 120° or $2\pi/3$ radians, by means of switching functions [37]:

$$\theta_{ij}^{0} = \operatorname{acos}\left(-\frac{1}{3}\right) + \left[\operatorname{acos}\left(-\frac{1}{3}\right) - \frac{\pi}{2}\right] \left[S_{\varphi}(R_{\mathrm{CH}_{i}})S_{\varphi}(R_{\mathrm{CH}_{j}}) - 1\right] + \left[\operatorname{acos}\left(-\frac{1}{3}\right) - \frac{2\pi}{3}\right] \left[S_{\theta}(R_{\mathrm{CH}_{k}})S_{\theta}(R_{\mathrm{CH}_{l}}) - 1\right].$$

$$(16)$$

Finally, the switching functions are given by

$$\begin{split} S_{1}(R_{\text{CH}_{i}}) &= 1 - \tanh\left[\alpha_{1}^{s}(R_{\text{CH}_{i}} - R_{\text{CH}}^{e})(R_{\text{CH}_{i}} - \beta_{1}^{s})^{8}\right], \\ S_{2}(R_{\text{CH}_{i}}) &= 1 - \tanh\left[\alpha_{2}^{s}(R_{\text{CH}_{i}} - R_{\text{CH}}^{e})(R_{\text{CH}_{i}} - \beta_{2}^{s})^{6}\right], \\ S_{\varphi}(R_{\text{CH}_{i}}) &= 1 - \tanh\left\{A_{\varphi}(R_{\text{CH}_{i}} - R_{\text{CH}}^{e})\exp\left[B_{\varphi}(R_{\text{CH}_{i}} - C_{\varphi})^{3}\right]\right\}, \\ S_{\theta}(R_{\text{CH}_{i}}) &= 1 - \tanh\left\{A_{\theta}(R_{\text{CH}_{i}} - R_{\text{CH}}^{e})\exp\left[B_{\theta}(R_{\text{CH}_{i}} - C_{\theta})^{3}\right]\right\}, \end{split}$$

$$(17)$$

involving 10 more adjustable parameters. In total, 16 terms need to be fitted for the calibration of the V_{harm} potential.

The $V_{\rm op}$ potential is a quadratic-quartic term whose aim is to correctly describe the out-of-plane motion of methyl:

$$V_{\rm op} = \sum_{i=1}^{4} f_{\Delta_i} \sum_{\substack{j=1\\j \neq i}}^{4} \left(\Delta_{ij}\right)^2 + \sum_{i=1}^{4} h_{\Delta_i} \sum_{\substack{j=1\\j \neq i}}^{4} \left(\Delta_{ij}\right)^4.$$
 (18)

The force constants, f_{Δ_i} and h_{Δ_i} , have been incorporated into a new switching function which is such that V_{op} vanishes at the methane limit and which directs the change of the methyl fragment from pyramidal to planar as the reaction evolves:

$$f_{\Delta_i} = [1 - S_3(R_{\text{CH}_i})] f_{\Delta},$$

 $h_{\Delta_i} = [1 - S_3(R_{\text{CH}_i})] h_{\Delta},$ (19)

$$S_3(R_{\text{CH}_i}) = 1 - \tanh \left| \alpha_3^s (R_{\text{CH}_i} - R_{\text{CH}}^e) (R_{\text{CH}_i} - \beta_3^s)^2 \right|,$$

with f_{Δ} , h_{Δ} , α_3^s , and β_3^s being the only parameters of $V_{\rm op}$ that enter the fitting process. Δ_{ij} is the angle that measures the deviation from the reference angle:

$$\Delta_{ij} = \operatorname{acos}\left(\frac{\left(\vec{r_k} - \vec{r_j}\right) \times \left(\vec{r_l} - \vec{r_j}\right)}{\left\|\left(\vec{r_k} - \vec{r_j}\right) \times \left(\vec{r_l} - \vec{r_j}\right)\right\|} \frac{\vec{r_i}}{\left\|\vec{r_i}\right\|}\right) - \theta_{ij}^0, \quad (20)$$

where $\vec{r_i}$, $\vec{r_j}$, $\vec{r_k}$, and $\vec{r_l}$ are vectors going from the carbon atom to the i, j, k, and l hydrogen atoms, respectively, and θ_{ij}^0 are the reference angles defined in (16). The first term to the right of (20) is therefore the angle between the CH_i bond and a vector perpendicular to the plane described by the j, k, and l hydrogen atoms and centred at the j atom. To correctly calculate Δ_{ij} , the motion from k to l has to be clockwise from the point of view of the i atom.

In the case of the H + CH₄ reaction the CH₃ radical product is planar. What happens if the product presents a nonplanar geometry? In these cases of CX₃ products, we have modified the reference angle θ_{ij}^o in (13) and (20). Thus, the original expression,

$$\theta_{ij}^{o} = \tau + \left(\tau - \frac{\pi}{2}\right) \left[S_{\varphi}(R_{\mathrm{CX}_{i}}) \cdot S_{\varphi}(R_{\mathrm{CX}_{j}}) - 1\right] + \left(\tau - \frac{2\pi}{3}\right) \left[S_{\vartheta}(R_{\mathrm{CX}_{k}}) \cdot S_{\vartheta}(R_{\mathrm{CX}_{i}}) - 1\right], \tag{21}$$

where $\tau = 109.47^{\circ}$, is replaced by

$$\theta_{ij}^{o} = \tau + (\tau - \tau_1) \left[S_{\varphi}(R_{\text{CX}_i}) \cdot S_{\varphi}(R_{\text{CX}_j}) - 1 \right]$$

$$+ (\tau - \tau_2) \left[\left[S_{\theta}(R_{\text{CX}_k}) \cdot S_{\theta}(R_{\text{CX}_l}) - 1 \right],$$
(22)

where τ_2 is the bending angle in the non-planar product, and τ_1 is related to τ_2 by the expression,

$$\tau_1 = \pi - \arcsin \left[\frac{\sin(\tau_2/2)}{\sin(\pi/3)} \right]. \tag{23}$$

In these cases of non-planar products, CX₃, this correction would add new parameters in the fitting procedure.

The PES, therefore, depends on at least 36 parameters, 16 for the stretching, 16 for the harmonic term, and 4 for the out-of-plane potential. These 36 parameters give great flexibility to the PES, while keeping the VB/MM functional form physically intuitive.

In the case of the H + CH₄ reaction the CH₄ reactant presents T_d symmetry. What happens if the reactant presents a different symmetry? For instance, ammonia presents symmetry $C_{3\nu}$, characterized by an inversion mechanism through

a planar structure with symmetry D_{3h} . The functional form (5) used for the H + CH₄ reaction cannot be applied without modification to any kind of system . Thus, when this potential is applied to the study of the H + NH₃ \rightarrow H₂ + NH₂ reaction, a major drawback was observed [38], namely that it wrongly describes the NH₃ inversion reaction, predicting that the planar ammonia (D_{3h} symmetry), which is a saddle point to the ammonia inversion, is about 9 kcal mol⁻¹ more stable than the pyramidal structure (C_{3v} symmetry).

In the original expression for the $H + CH_4$ reaction (5), the $V_{\rm op}$ term was added to obtain a correct description of the out-of-plane bending in the methyl radical, $580\,{\rm cm}^{-1}$. However, Yang and Corchado [38] noted that this term leads to unphysical behaviour along the ammonia inversion path. To avoid this drawback, our laboratory recently developed [39] a new PES where the $V_{\rm op}$ term is removed:

$$V = V_{\text{stretch}} + V_{\text{harm}}.$$
 (24)

Consequently, each of the 16 parameters is required for the stretching terms and the harmonic bending terms of the PES which were fitted to high-level *ab initio* CCSD(T)/cc-pVTZ calculations.

In sum, starting from a basic functional form, this form must be adapted to each particular case, looking for the greatest flexibility and suitability for the problem under study. This has been the main aim of the modifications on the original functional form (5), described by (10)–(12), (22), (23), and (24). While this could represent a disadvantage with respect to the fitting or interpolation methods, because new functional forms must be developed in each case, it also represents an advantage, because simple stepwise modifications can give great flexibility to the surface.

Once the functional form is available, the fitting procedure is started. A very popular approach for fitting a function is the least-squares method, which, using some local optimization algorithm, gives values of the parameters that minimize (locally) the function

$$R = \sum_{x} |E(x) - F(x, p)|^{2}, \qquad (25)$$

where E(x) is the *ab initio* energy associated with a particular molecular configuration specified by "x" and F(x, p) is the energy predicted by the analytical function at the same molecular configuration, which depends on a set of m parameters denoted as p.

One must note, however, that any fitting procedure has certain limitations. First, due to the large number of parameters, it is very hard to find a global minimum for the fit, which accurately describes the entire surface. Second, due to the nature of the linear least-square method, the result is dependent on the initial parameters; third, since we use a mathematical approach without physical intuition, one usually obtains a number of distinct sets of mathematical parameters, all equally probable and good at reproducing the complete system. To make matters worse, as noted by Banks and Clary [40], while the differences between these parameter sets may be small, the dynamics information obtained from them can vary notably. This is especially

true because small changes in the energy derivatives can cause large changes in dynamical properties of the PES. One therefore requires an extremely accurate fit to the topology of the given points to obtain an acceptable set of parameters.

To solve at least partially some of the above problems, we adopt a different approach [41]. Firstly, we will try to obtain the values of the parameters that minimize the function

$$R = \sum_{x} w_{x}^{e} \left| E(x) - F(x, p) \right|^{2} + \sum_{x} w_{x}^{g} \left| g(x) - \frac{\partial F(x, p)}{\partial x} \right|^{2} + \sum_{x} w_{x}^{H} \left| H(x) - \frac{\partial^{2} F(x, p)}{\partial x^{2}} \right|^{2},$$

$$(26)$$

where g(x) denotes the gradients (first derivative of the energy), H(x) the Hessian elements (second derivatives of the energy), and w_x^e , w_x^g , and w_x^H are weights. In practice, the gradients enter the fitting process only at the stationary points, and the Hessian elements by means of the harmonic vibrational frequencies at selected points. Secondly, the choice of the number of points to be fitted is critical, and this strategy allows this number to be reduced drastically (see more details in the original paper [41]). We begin by choosing the stationary points (reactants, products, saddle point, and intermediate complexes) as data points. The geometry, energy, and frequencies are fitted and, thus, indirectly, the first and second derivatives of the energy. It is necessary to remember that if the information included was only the energy, a mesh of m^{3n-6} points would be required. However, when the information included is not only the energy at a stationary point but also the first and second derivatives, only one point is needed to reproduce each stationary point configuration. Moreover, additional points on the minimum energy path are included. Thus, with the inclusion of the stationary points and representative points on the reaction path, we search for a good reproduction of the topology of the path connecting reactants to products. Finally, we add the energy of a point not on the reaction path to describe zones of the reaction valley relevant to tunneling dynamics and rotational excitation of the products. The fitting procedure is currently automated on a computer with no user intervention except to analyze the results and, when called for, to change the weights.

This strategy presents certain advantages over other methods. The first is transferability of the functional form and the fitted parameters. Since one can regard VB/MM as some kind of highly specific MM force field, it can be expected that some of the fitting parameters are transferable to a similar system, although obviously the parameter values are system specific. In our group we have used this feature to obtain, for example, the PES for the $F + CH_4$ reaction [42] using as the starting point the analytical PES for H + CH₄ [43]. Secondly, the PESs are guaranteed to some extent to have the capability of reproducing the energetic interactions of the chemical system in region not included in the fit. For example, high-energy collisions might require knowledge of the PES at very high energies that may not have been sampled in the fitting process. An interpolation method cannot ensure the absence of spurious wells or unphysical

repulsive regions when nearby points are absent, while MM force fields can. Thirdly, VB/MM PES parameters can be refitted so as to fine-tune the PES using additional data (e.g., higher *ab initio* calculations at selected points) at a low computational cost. Furthermore, VB/MM surfaces and their energy derivatives (when they can be analytically calculated) are usually smoother than interpolated surfaces. As was mentioned above, Shepard interpolation sometimes gives discontinuities in the derivatives, which is a highly undesirable feature for kinetics and dynamics studies.

Thus, our research group has developed economical alternatives for constructing analytical PESs of polyatomic systems, which basically are VB/MM-type surfaces. This strategy of seeking an optimal tradeoff of time and computational cost has been successfully used in several gasphase hydrogen abstraction reactions of five [44, 45], six [42, 43, 46–52], and seven [53] atoms. In general, a good correspondence between kinetics and dynamics theoretical results and experimental measurements is found. In the first phase of our research, theoretical and experimental information was used in the fitting procedure, making the analytical surface semiempirical in nature, which was a serious problem and a limitation in kinetics and dynamics studies. However, in the last few years, our surfaces have been fitted exclusively to very high-level ab initio calculations, avoiding the aforementioned limitations.

3. Library of Potential Energy Surfaces

The FORTRAN codes and the fitted parameters of the polyatomic potential energy surfaces developed by our group are available, free of charge, for the scientific community, and can be downloaded from the POTLIB library [54]: http://comp.chem.umn.edu/potlib/ or http://users.ipfw.edu/DUCHOVIC/POTLIB2001, or obtained from the authors upon request.

4. Applications

(a) The $H + CH_4$ Reaction. The gas-phase $H + CH_4 \rightarrow H_2 + CH_3$ hydrogen abstraction reaction, as well as its deuterated isotopomers, is the prototype polyatomic reactive system and has been widely studied both theoretically and experimentally [10]. The construction of its PES has a long history, and it is one of the few reactive systems for which different approaches to the construction have been developed, which permits a direct comparison.

We will focus attention, except otherwise stated, on the three most recent and accurate surfaces for this reactive system, which were constructed with different strategies. Chronologically, in 2006 Zhang et al. [55, 56] developed the family of ZBBi surfaces, using the invariant polynomial method, based on the fitting to more than 20000 *ab initio* energies at the RCCSD(T)/aug-cc-pVTZ level. In 2009 we developed [41] an analytical PES, CBE surface, which is a VB/MM functional form, and the 36 parameters are fitted using exclusively high-level electronic structure calculations at the CCSD(T)/cc-pVTZ level. Very recently, in 2011,

TABLE 1: CH₅ saddle point properties.^a

	Fitting (ZBB3) ^b	Analytical (CBE) ^c	Interpolated (ZFWCZ) ^d
Barrier height	14.78	15.01	15.03
Geometry			
R(C–H')	1.409	1.390	1.399
$R(H'-H_B)$	0.901	0.973	0.895
<h-c-h'< td=""><td>102.8</td><td>106.8</td><td>103.1</td></h-c-h'<>	102.8	106.8	103.1
$<$ C $-$ H $'$ $-$ H $_B$	180.0	180.0	180.0
Vibrational frequencies			
	3289	3173	3223
	3289	3173	3223
	3104	3036	3073
	1726	1833	1784
	1434	1443	1442
	1434	1443	1442
	1078	1173	1115
	1078	1173	1115
	1062	1085	1062
	440	542	522
	440	542	522
	1320i	1488i	1467i

^aEnergy in kcal mol^{-1} , geometry in Å and degrees, and vibrational frequency in cm⁻¹; ^b[55]; ^c[41]; ^d[18].

Zhou et al. [18] constructed a full-dimensional surface using the modified Shepard interpolation scheme based on 30000 data points at the CCSD(T)/aug-cc-pVTZ level the ZFWCZ surface. The energy, geometry and vibrational frequencies of the saddle point are summarized in Table 1 for the three surfaces. Comparing the wide range of properties, we conclude that the three surfaces present excellent agreement, with small differences in the CBE with respect to the other two surfaces in the <H-C-H' bending angle, \approx 3°, and in the ZBB3 compared to the other two surfaces in the imaginary frequency, $\approx 100 \, \text{cm}^{-1}$. The three surfaces present a colinear saddle point, 180.0°, with a similar barrier height, with small differences, ± 0.2 kcal mol⁻¹, that is, within the chemical accuracy, and very close to the best estimation predicted at the CCSD(T)/aug-cc-pVQZ level, 14.87 kcal mol^{-1} [57].

The best macroscopic measure of the accuracy of a potential energy surface is probably the rate constant, at least in the thermal bottleneck region. When we compare different dynamics methods using the same surface, the dynamics approach is tested, and when we compare theoretical and experimental results, both the dynamics method and the surface are tested. Figure 1 plots the thermal rate coefficients computed with accurate fulldimensional quantum dynamics approaches, on the analytical CBE surface; a very accurate interpolation surface developed by Wu et al., WWM surface [57–59], which used the modified Shepard interpolated method developed by Collins et al., based on CCSD(T)/cc-pVQZ or CCSD(T)/aug-cc-pVQZ ab initio calculations; and

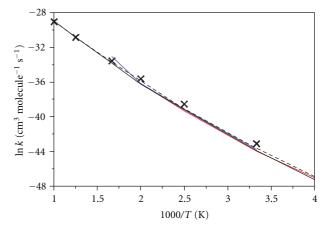


FIGURE 1: Arrhenius plots of $\ln k$ (cm³ molecule $^{-1}$ s $^{-1}$) for the forward thermal rate coefficients of the H + CH4 reaction against the reciprocal of temperature (K), in the range 250–1000 K. Black line: MCDTH quantum calculations on the CBE surface; red line: MCDTH quantum calculations on the WWM surface; blue line: quantum calculations on the ZBB2 surface; black dashed line: VTST/MT calculations on the CBE surface; crosses: experimental values [60].

a fitted surface, named ZBB2, an earlier version of the ZBB3 surface developed by Bowman et al. In the same figure, there also appear the results obtained with the variational transition-state theory with multidimensional tunneling effect [41] and the experimental data [60] for comparison. First, with quantum dynamics approaches, the rate coefficients obtained with the three surfaces agree almost perfectly in the common temperature range. Second, when the rate coefficients are obtained using different dynamics approaches, VTST/MT and MCDTH (multiconfigurational time-dependent Hartree approach [58, 59]) on the same CBE surface, excellent agreement is found, and both reproduce the experimental information in the common temperature range. These results indicate, first, that VTST/MT is a powerful and computationally economic tool for the kinetics study of polyatomic systems, with results comparable to those obtained with computationally more expensive quantum dynamical methods. Second, the CBE surface is accurate at least in the region of low energies, which is the most relevant region for thermal rate coefficient calculations and, therefore, provides a satisfactory description of the reaction path and the transition-state region.

Next, we analyze some dynamics properties where different surfaces have been used and compared with the sparse experimental data. We focus on the $H + CD_4 \rightarrow HD + CD_3$ reaction because there is more experimental information available for comparison. The product energy partitioning has been experimentally obtained by Valentini's group. [61] only for the vibration and rotation of the HD product, and this same group found that more than 95% of the HD product is formed in the $\nu'=0$ and $\nu'=1$ vibrational states. These results appear in Table 2, together with the QCT results on the analytical CBE and the fitted ZBB1 [55] surfaces. The QCT calculations on these two PESs show excellent

Table 2: HD product energy partitioning and vibrational distribution (percentages) for the $H + CD_4$ reaction at 1.52 eV.

Surface	f'_{vib} (HD)	$f'_{\rm rot}$ (HD)	$HD \\ (\nu' = 0)$	$HD \\ (\nu' = 1)$
Analyticala	18	18	84	15
Fitted ^b	22	18	78	22
Exp.c	7	9	≥	95

^aCBE surface, [41] ^bZBB1 surface, [55] ^cValentini et al. [61].

agreement for the HD product energy partitioning as well as for the HD vibrational distribution. In this latter case, the QCT results reproduce the experimental evidence, but, in the first case, they strongly contrast with the experimental measurements, which measure an internal excitation of the HD product of 7% and 9% for vibration and rotation, respectively. The agreement between the results from the two surfaces leads us to think that the discrepancies with experiment are mainly due to the dynamical method, that is, to limitations of the QCT approach. Experimental problems, however, cannot be totally ruled out, as was recently observed by Hu et al. [62], who suggested that the conclusions from Valentini et al.'s CARS experimental study might need to be reinterpreted.

The product angular distribution is, doubtless, one of the most sensitive dynamics features with which to test the quality of the potential energy surface, but experimentally it is very difficult to measure in some cases. When the Photoloc technique is used, the laboratory speed depends on both the scattering angle and the speed of the CD₃ product, which is influenced by the HD coproduct internal energy distribution. Uncertainties in this quantity could produce errors in the scattering angle.

Camden et al. [63] reported the first study of the stateto-state dynamics differential cross-section at high energies $(1.95 \,\mathrm{eV})$ for the H + CD₄ gas-phase reaction using the Photoloc technique. They found that the CD₃ products are sideways/forward scattered with respect to the incident CD₄, suggesting a stripping mechanism (note that in the original papers [63–65] the CD₃ product is measured with respect to the incident H). Later, this same laboratory [64, 65] reported new experimental studies, also at high energy (1.2 eV), finding the same experimental behaviour. Experimentally, state-to-state dynamics studies are difficult to perform at low energies for the title reaction, because the H atoms, which are produced in a photolysis process, are hot. Only very recently have Zhang et al. [66] reported crossed molecular beam experiments for the H + CD₄ reaction at lower collision energies, ranging from 0.72 to 1.99 eV. Note that the lower value, 0.72 eV, is close to the barrier height, and consequently its dynamics will be influenced mainly by the transitionstate region. Figure 2(a) plots these experimental results. A backward angle is clearly observed at low energies (rebound mechanism), changing towards sideways when the energy increases (stripping mechanism).

This is an excellent opportunity to test the quality of the PES and the dynamics methods (Figures 2(b)–2(d)). Only two surfaces have been used to study this problem

theoretically: an analytical surface from our group (versions 2002 [43, 67] and 2008, labeled here as CBE [41, 68]), using both QCT and QM calculations, and an "on-thefly" B3LYP/631G(d,p) density functional theory surface [65], using QCT calculations. At low energies, ≈ 0.7 eV, our analytical surfaces, PES-2002 and CBE, using QCT and QM methods (Figures 2(b) and 2(c)), show backward scattering, associated with a rebound mechanism, reproducing the recent experimental data [66]. The B3LYP "on-the-fly" surface using QCT calculations (Figure 2(d)) yields a more sideways scattering, with large uncertainties, in contrast with experiment. These differences could be due to the poor statistics on the B3LYP surface [65] and to the severe underestimation of the barrier heights, about 5 kcal mol⁻¹ lower than the best ab initio calculations. This low barrier artificially permits reactive trajectories with larger impact parameters, favouring the sideways scattering region. When this error in the barrier height is corrected, our PES-2002 and, more noticeably in the better CBE surface, the low impact parameters are favoured, and this explains the rebound mechanism. Note that, interestingly, this experimental behaviour was already predicted by our group in 2006 [67] before the experimental data were available.

At higher collision energies, as they increase from 1.06 to 1.99 eV, Zhang et al. [66] found a shift of the product angular distribution from backwards to sideways. This behaviour agrees qualitatively with the previous observations of Camden et al. [63-65], although these latter workers found a clear sideways distribution at 1.21 and 1.95 eV, with practical extinction of the backward signal. This may have been due to the use of the Photoloc technique, which neglects the internal energy contribution of the HD co-product, and, as the authors themselves recognized in 2006, "clearly a more detailed picture of the differential cross section is desirable but it will have to await more experimental work." The QCT results using the analytical CBE surface (Figure 2(b)) reproduce the new experimental evidence. QM calculations on the same CBE surface [68] (Figure 2(c)) give more sideways scattering than the QCT calculations and experiment, although it is not clear whether this is due to significant quantum effects or simply are an artifact of the reduced dimensionality approach in the QM calculations.

Note that QCT calculations on the old PES-2002 surface also predicted the subsequently experimentally observed behaviour [66]—backwards-sideways scattering. However, they contradicted the experimental information available at the time the study was carried out-in 2006. In addition, since direct-dynamics OCT calculations at the B3LYP/631G(d,p) level showed sideways scattering, reproducing the experimental measurements [63–65], the validity of the analytical PES-2002 was questioned. The recent experiments of Zhang et al. [66], however, changed the whole picture and now the direct-dynamics QCT calculations at low collision energies are questioned because of, as noted above, the presence of reactive trajectories with erroneously large impact parameters due to the underestimation of the barrier height. In the case of higher collision energies, however, this error in the barrier should be of less concern than at lower energies.

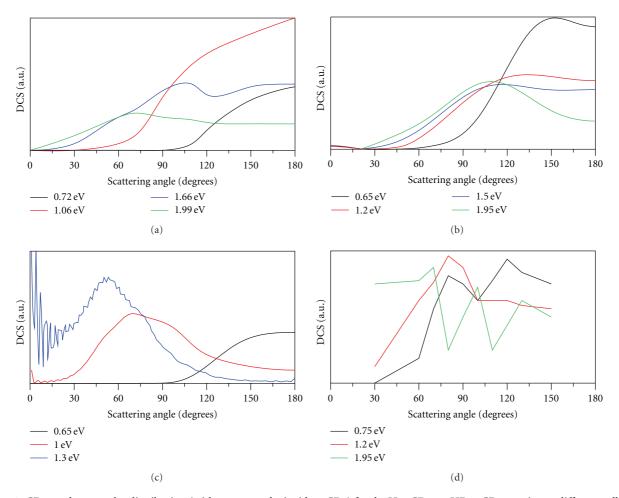


FIGURE 2: CD_3 product angular distribution (with respect to the incident CD_4) for the $H + CD_4 \rightarrow HD + CD_3$ reaction at different collision energies. (a) Experimental results from [64]; (b) QCT angular distribution on the CBE analytical surface [66]; (c) QM angular distribution on the CBE analytical surface [66]; (d) QCT angular distribution on the B3LYP "on-the-fly" surface [65].

Very recently, Zhou et al. [18] have performed an exhaustive analysis of the total reaction probabilities and integral cross-section using quantum dynamics calculations on the three most recent surfaces: fitted ZBB3, analytical CBE, and interpolated ZFWCZ surfaces, with collision energies up to 1.7 eV. Figure 3 plots the integral cross-section results. At collision energies up to 1.0 eV, the three surfaces show satisfactory agreement, while at higher energies of collision, the CBE surface overestimates this dynamics property, while the remaining two surfaces show good agreement. This could be attributed to deficiencies of the CBE surface at high energies. This is not surprising since the calibration of the CBE surface was done thinking of thermal behaviour. The information used during the fit focused on the reaction path and reaction valley, and higher energy areas were neither sampled nor weighted sufficiently. Therefore, as the collision energy increases, the accuracy of the CBE surface diminishes.

Finally, another severe test of the quality of the PES is the study of the effect of the vibrational excitation on the dynamics. In fact, the dynamics of a vibrationally excited polyatomic reaction presents a challenge both theoretically and experimentally. Camden et al. [69] carried out the

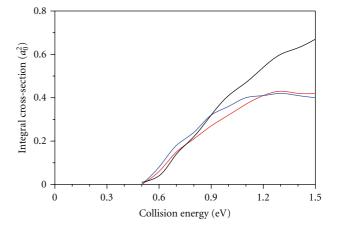


FIGURE 3: Quantum mechanical integral cross-section (a_o^2) versus collision energy (eV) for the H + CH₄ \rightarrow H₂ + CH₃ reaction on the CBE (black line), ZBB3 (blue line), and ZFWCZ (red line) surfaces.

first experimental study on the effect of the C–H stretch excitation on the gas-phase $H + CH_4$ hydrogen abstraction

reaction. They found that the excitation of the asymmetric C–H stretch mode enhances the reaction cross-section by a factor of 3.0 ± 1.5 with respect to the ground-state methane, and this enhancement is practically independent of the collision energies for the three cases analyzed—1.52, 1.85, and 2.20 eV. In the following year, 2006, two theoretical papers on this issue were published: one by Xie et al. [56] using QCT calculations on the ZBB3 surface, and another from our laboratory [70] also using QCT calculations on the older analytical PES-2002 surface. At 1.52 eV, the theoretical results are close, with computed enhancement factors of 2.3 and 1.9, respectively, both of them within the experimental uncertainties. Note that our more recent CBE surface also predicts an enhancement factor of 1.9 (unpublished results).

(b) The H + NH₃ Reaction. The reaction of hydrogen atom with ammonia is a typical five-body reactive system, and presents a rare opportunity to study both intermolecular and intramolecular dynamics. For the intermolecular case, the gas-phase H + NH₃ \rightarrow H₂ + NH₂ hydrogen abstraction reaction is similar to the H + CH₄ reaction. It presents a barrier height of 14.5 kcal mol⁻¹ and a reaction exoergicity of 5.0 kcal mol⁻¹, as compared to 14.87 and an endoergicity of 2.88 kcal mol⁻¹, respectively, for the H + CH₄ analogue. Also, the inversion of ammonia between two pyramidal structures ($C_{3\nu}$ symmetry) passing through a planar structure (D_{3h} symmetry, which is a saddle point) is an example of intramolecular dynamics [71] with a barrier height in the range 5.20–5.94 kcal mol⁻¹, depending on the level of calculation.

Only three potential energy surfaces have been developed for the H + NH₃ system. In 2005, Moyano and Collins [72] developed an interpolation potential energy surface for the ammonia inversion, and the hydrogen abstraction and exchange reactions of H + NH₃ using a modified Shepard interpolated scheme based on 2000 data points calculated at the CCSD(T)/aug-cc-pVDZ level (PES1 version) or as singlepoint calculations at the CCSD(T)/aug-cc-pVTZ (PES2 version) level. The first and second derivatives of the energy were calculated by finite differences in the energy. Previously, in 1997, our group constructed the first surface for the hydrogen abstraction reaction exclusively, CE-1997 [44], which was fitted to a combination of experimental and theoretical information that is, it was semiempirical in nature, which represents a limitation for dynamics studies. Moreover, as was previously noted, recently Yang and Corchado [38] reported a major drawback of the CE-1997, namely that it describes incorrectly the NH₃ inversion motion, predicting incorrectly that the planar ammonia (D_{3h} symmetry) is about 9 kcal mol⁻¹ more stable than the pyramidal structure $(C_{3\nu}$ symmetry). To correct this behaviour of the NH₃ inversion, together with its semiempirical character, a new analytical potential energy surface, named EC-2009, was recently developed by our group [39], describing simultaneously the hydrogen abstraction and ammonia inversion reactions. This EC-2009 surface is basically a valence bondmolecular mechanics (VB/MM) surface, given by (24), and was fitted exclusively to very high level ab initio calculations

TABLE 3: NH₄ hydrogen abstraction saddle point properties.^a

	Interpolated (MC) ^b	Analytical (EC-2009) ^c	Ab initio ^d
Barrier height	14.64	14.48	14.73
Geometry			
R(N-H')	1.323	1.279	1.308
$R(H'-H_B)$	0.900	0.868	0.890
$<$ C $-$ H $'$ $-$ H $_B$	160.8	180.0	158.4
Vibrational frequencies			
	3450	3444	3478
	3350	3373	3384
	2057	1861	1888
	1527	1623	1566
	1174	1497	1280
	1047	1080	1063
	650	622	677
	629	581	506
	1371i	1602i	1662i

^aEnergy in kcal mol⁻¹, geometry in Å and degrees, and vibrational frequency in cm⁻¹; ^b[72]; ^c [39]; ^d [39], at the CCSD(T)/cc-pVTZ level.

at the CCSD(T)/cc-pVTZ level. Note that the first derivatives of this surface are analytical, which implies a significant reduction in the computer time required for dynamical calculations as well as more accurate derivatives than is possible with numerical methods.

We begin by analyzing the hydrogen abstraction reaction. Table 3 lists the energy, geometry, and vibrational frequencies of the saddle point, with the interpolated MC (PES2 version) and the analytical EC-2009 surfaces. Using as target the CCSD(T)/cc-pVTZ *ab initio* level, the two surfaces present similarities, although important differences must be noted. First, while the interpolated MC surface reproduces the *ab initio* N–H′–H bend angle, the analytical surface yields a collinear approach. However, in previous papers [73, 74], we demonstrated that this was not a serious problem in the kinetics and dynamics description of the system. Second, the imaginary frequency obtained with the MC surface differs by about 300 cm⁻¹ from the *ab initio* value.

For the two surfaces, Figure 4 shows the energy along the minimum energy path $(V_{\rm MEP})$ and the ground-state vibrationally adiabatic potential curve (V_a^G) , which is defined as the sum of the potential and vibrational zero-point energies along the reaction path. Note that *s* is the reaction coordinate, being zero at the saddle point, positive in the product channel, and negative in the reactant channel. Firstly, the $V_{\rm MEP}$ curve is smooth and shows no oscillations in either surface. However, V_a^G shows significant oscillations when computed for the interpolated surface. The reason is that the potential energy surface is not smooth enough to provide smooth changes in the frequencies (second derivatives of the energy). The situation becomes worse as one moves away from the saddle point and approaches areas where little ab initio information for interpolation is available. Thus, the bump in V_a^G at around s = -1 a.u. is due to wild oscillations

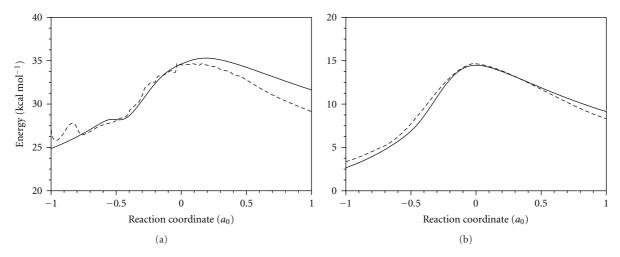


FIGURE 4: Potential energy (b) and vibrational ground-state energy (a) along the reaction path of the $H + NH_3 \rightarrow H_2 + NH_2$ reaction computed using the EC-2009 (solid lines) and MC (dashed lines) surfaces. The zero of energy is set to the equilibrium potential energy of the reactants.

of the frequencies that lead to unphysical values of V_a^G for |s| > 1. This is a limitation when one wants to compute the tunneling effect at low energies (see below), since the barrier to tunnel through is totally unrealistic.

Figure 5 plots the thermal rate coefficients computed with the VTST/MT approach on both surfaces, where tunneling was estimated using the least-action tunneling (LAT) method [75, 76], together with experimental values [77] for comparison. In the common temperature range, 490–1780 K, both surfaces reproduce the experimental data, which is a test of both the surface and the dynamical method. The differences between the rates for the two surfaces are relatively small, 40% at 600 K, and diminishing as temperature increases. At low temperatures, the differences between the two surfaces increase, with the rates computed on the MC surface being 92% larger than the ones with the EC-2009 surface at 200 K. In this low temperature regime, where tunneling is important, the analytical EC-2009 surface is more accurate due to the unrealistic oscillations in the adiabatic reaction path on the MC surface, which negatively influence the tunneling.

The integral cross-sections in the range 10–30 kcal mol⁻¹ have been evaluated using quasi-classical trajectory (QCT) calculations on both surfaces [72, 78] and are plotted in Figure 6. As apparent from this figure, both surfaces agree reasonably, showing typical threshold behaviour, starting from 10 kcal mol⁻¹ and increasing with the translational energy. Unfortunately, there is no experimental data for comparison, and we think that these theoretical results might stimulate experimental work on this little studied system.

Finally, the angular distributions of the H₂ product with respect to the incident H atom has only been determined using the EC-2009 surface [78]. Figure 7 plots this property for collision energies of 25 and 40 kcal mol⁻¹. At 25 kcal mol⁻¹, the scattering distribution is in the sidewaysbackward hemisphere, associated with a rebound mechanism and low impact parameters. When the collision energy increases, 40 kcal mol⁻¹, the scattering is shifted slightly

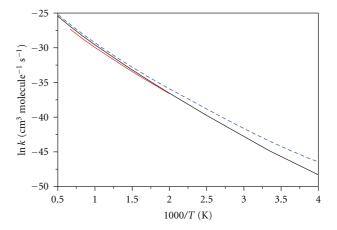


FIGURE 5: Arrhenius plots of $\ln k$ (cm³ molecule⁻¹ s⁻¹) for the forward thermal rate coefficients of the $H + NH_3 \rightarrow H_2 + NH_2$ reaction against the reciprocal of temperature (K) in the range 200–2000 K. Solid black line: analytical EC-2009; dashed blue line: interpolated MC; dotted red line: experimental values from [77].

towards the sideways hemisphere, due to larger impact parameters.

As was mentioned above, the EC-2009 surface describes, in addition to the aforementioned hydrogen abstraction reaction, the ammonia inversion, an example of interesting intramolecular dynamics. Figure 8 plots the equipotential contours in the two significant coordinates, r(N-H) bond length and <H-N-H angle, for the analytical EC-2009 PES and the CCSD(T)/cc-pVTZ *ab initio* level, for comparison. As seen, the contours are smooth and the analytical PES reproduces the fitted *ab initio* data points [39].

A very stringent test of the quality of this surface is the ammonia splitting, which demands spectroscopic accuracy. The inversion motion is represented by a symmetric double-well potential. As a consequence of the perturbation originating this double well, a splitting of each degenerate vibrational

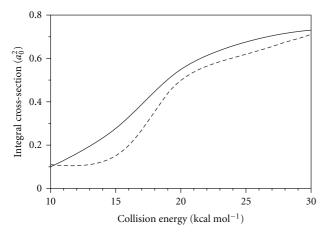


FIGURE 6: QCT reaction cross-section (a_0^2) versus the collision energy (kcal mol⁻¹) for the H + NH₃ \rightarrow H₂ + NH₂ reaction computed using the analytical EC-2009 (solid line) and interpolated MC (dashed line) surfaces.

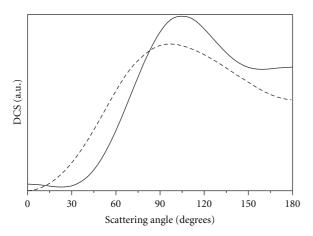


FIGURE 7: H_2 product angular distribution (with respect to the incident H) for the H + NH₃ \rightarrow H₂ + NH₂ reaction at 25 kcal·mol⁻¹ (solid line) and 40 kcal mol⁻¹ (dashed line), computed using QCT calculations on the EC-2009 surface.

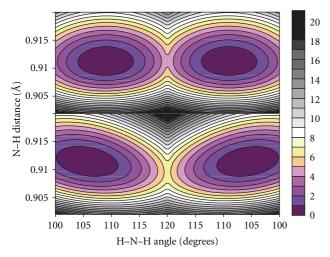


FIGURE 8: Ammonia inversion reaction. Contour plots of the analytical EC-2009 (upper panel) and CCSD(T)/ccpVTZ *ab initio* surface (lower panel).

level into two levels appears, ΔE , due to quantum mechanical tunneling [71], and the splitting increases rapidly with the vibrational number. The splitting ΔE can be computed from the tunneling rate of inversion, k_{tunn} , which is in turn obtained from the imaginary action integral, $\theta(E)$, using the WKB approximation [79]:

$$\Delta E_0 = \frac{k_{\text{tunn}}}{2c},$$

$$k_{\text{tunn}} = \frac{2c\nu_2}{\pi} \exp[-\theta(E)],$$
(27)

with c being the speed of light and v_2 the eigenvalue associated with the inversion mode of ammonia, 1113 cm⁻¹. Figure 9 plots this path for ammonia where the first two pairs of split eigenvalues are superimposed. The computed splitting is listed in Table 4 together with experimental values [80] for comparison. The EC-2009 results overestimate the experimental values. The reason for the discrepancy mainly lies in the shape of the PES, although other factors such as the tunneling calculation cannot be discarded. Indeed, we found [39] that the overestimation we obtain in tunneling splitting is due to our barrier to inversion being slightly lower and thinner than those of other studies. Unfortunately, tunneling splitting is so sensitive to the shape of the PES that a few tenths of kcal·mol⁻¹ give rise to a factor of four in the computed splitting. With respect to the effect of isotopic substitution, for the ND3 case we obtain a value $\Delta E = 0.37 \, \text{cm}^{-1}$. Although this is greater than the experimentally reported value, 0.05 cm⁻¹ [81], it correctly predicts about one order of magnitude reduction upon isotopic substitution. In sum, despite the enormous effort required for the construction of the potential energy surface, it does not suffice to obtain spectroscopic accuracy, and our surface can only give a qualitative description of the splitting in ammonia.

5. When the Problems Increase

The benchmark $H + CH_4$ hydrogen abstraction reaction, with five light atoms and a single heavy atom, which allows a large number of very high-level *ab initio* calculations to be performed, gives the impression of the process being a "piece of cake" regarding polyatomic bimolecular reactions. However, it still presents kinetics and dynamics differences depending on the potential energy used and discrepancies with the experimental measures. Then, what will the case be when more complicated systems are studied? In this section we will analyze some problems which can appear alone or in combination in the study of polyatomic systems and strongly complicate the construction of potential energy surfaces.

5.1. The Spin-Orbit Problem and Multisurface Dynamics. This is a typical problem, for instance, in reactions involving halogen atoms, X(²P), with molecular systems, R–H:

$$X(^{2}P) + H-R \longrightarrow XH + R \quad (X = F, Cl, Br).$$
 (28)

The halogen atom presents two spin-orbit electronic states, ${}^{2}P_{3/2}$ and ${}^{2}P_{1/2}$, with a splitting of 404 cm⁻¹ (1.1 kcal mol⁻¹),

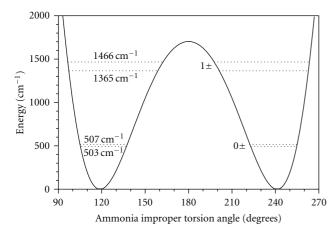


FIGURE 9: Classical potential for the ammonia inversion path obtained from the EC-2009 surface. The first two pairs of eigenvalues are shown.

Table 4: Eigenvalues of ammonia inversion (in cm⁻¹).

ν_2	EC-2009 ^a	Exp.b
0+	0.00	0.00
0^-	3.64	0.79
1+	861.39	932.43
1-	962.90	968.12
2+	1533.36	1598.47
2-	1942.29	1822.18

^a[39]; ^b[80].

882 cm⁻¹ (2.5 kcal mol⁻¹), and 3685 cm⁻¹ (3.5 kcal mol⁻¹) for F, Cl, and Br, respectively. A priori, the smaller the separation, the greater the possibility of the reaction coming from the two states, which complicates the PES construction and the dynamics study.

This problem affects all the previously described theoretical methods to develop surfaces, because it is a problem intrinsic to the initial information required: the quantum mechanical calculations. For this problem, relativistic calculations would be needed, which would immensely increase the computational cost and would make these calculations impractical in polyatomic systems. In addition, new functional forms for the analytical functions need to be developed to include the coupling between states and its dependence on coordinates [82, 83], in order to make it possible to include nonadiabatic effects and hopping between surfaces in the dynamics study of these multistate systems.

In the case of atom-diatom reactions, some results have shed light on the spin-orbit problem, although some theory/experiment controversies still persist. For instance, for the well-studied $F(^2P_{3/2}, ^2P_{1/2}) + H_2$ reaction, Alexander et al. [82, 84] found that the reactivity of the excited s-o state of F is small, 10–25% of the reactivity of the ground s-o state, and concluded that the overall dynamics of the F + H_2 reaction could be well described by calculations on a single, electronically adiabatic PES, although for a

direct comparison with experiment the coupling between the ground and excited s-o surfaces must be considered.

For the analogue $Cl(^2P_{3/2}, ^2P_{1/2}) + H_2$ reaction, because of the larger energy separation, one would expect that the reaction could evolve on the ground-state adiabatic surface, with the contribution of the chlorine excited state, ²P_{1/2}, being practically negligible according to the Born-Oppenheimer (BO) approach. However, recently a theory/experiment controversy has arisen on this issue. Thus, Lee and Liu [85-87] demonstrated experimentally the contrary for the $Cl + H_2$ reaction; that is, the excited chlorine atom (Cl*) is more reactive to H₂ than the ground-state chlorine (Cl) by a factor of at least \approx 6. In any case, even taking into account experimental error bars, the authors were confident about the reactivity relationship Cl* > Cl, which could have a significant effect on the temperature dependence of the thermal rate coefficients. The authors interpreted this surprising result by postulating a nonadiabatic transition (breakdown of the BO approximation) from the excited Cl* to the ground-state Cl surface by either electrostatic or spin-orbit coupling in the entrance channel. This experimental study initiated a major theoretical and experimental debate on the influence of the excited Cl* in the reactivity of the Cl + H₂ reaction. Different laboratories [88–93] performed theoretical/experimental studies of the validity of the BO approximation in this reaction, concluding that the adiabatically allowed reaction $(Cl(^{2}P_{3/2}) + H_{2})$ will dominate the adiabatically forbidden reaction ($Cl(^{2}P_{1/2})$ + H₂). Hence, these results are in direct contrast with the experiment of Liu et al. [85-87], suggesting that this experiment claiming high reactivity of Cl* needs to be reexamined.

In the case of polyatomic systems, this level of sophistication has not been achieved and would still be computationally prohibitive. Thus, some approaches have been considered to take into account, indirectly, the s-o effect in the construction of the PES and the dynamics study. First, for thermochemical or rate coefficient calculations, the s-o effect on the multiple electronic states is taken into account by the electronic partition function of the reactants in the usual expression

$$Qe = 4 + 2\exp\left(-\frac{\varepsilon}{k_B T}\right),\tag{29}$$

where ε is the s-o splitting of the halogen atom. Second, there is an additional effect on the barrier height (Figure 10). In fact, if we assume that along the entire reaction path the states are fully quenched, considering the s-o effect would lower the energy of the s-o ground state of the halogen atom by $1/3 \varepsilon$ below its nonrelativistic energy, increasing the barrier height by this amount. This represents 0.38, 0.83, and 1.17 kcal mol⁻¹, respectively, for F, Cl, and Br. Our group considered these approaches in the construction of the surface for the F(2 P) + CH₄ [42], Cl(2 P) + CH₄ [49], and Cl(2 P) + NH₃ [94, 95] reactions. Note, however, that this approach is to some extent incoherent in the sense that as we move away from the saddle point towards reactants the energy asymptotically tends to zero, the energy of the lower state of the halogen atom. However, as we move from the

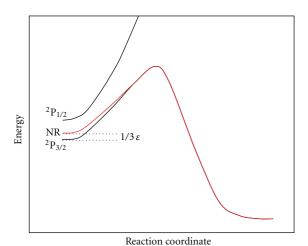


FIGURE 10: Schematic representation of the potential energy along the reaction path for a reaction with spin/orbit effects on the reactants. Red line: nonrelativistic calculations.

saddle point towards reactants, it should tend asymptotically to $1/3 \varepsilon$ until it reaches the point where the two states interact. From that point towards the reactants, the surface has to tend to zero. There is therefore a gap of up to $1/3 \varepsilon$ between the exact result and our approximation results. However, we can assume that this gap is sufficiently small and is located so far from the dynamically important regions of the surface that we can safely neglect it. Moreover, in our analytical surfaces, the changes in the energy can be fitted in order to change the slope of the reaction path so that this asymptotic behaviour can be corrected. In addition, in the latter case of the Cl(²P) + NH₃ reaction, because of the presence of wells in the reactant channel (see below), this gap occurs before the system reaches the well in the region connecting the well with reactants, and its influence on the kinetics and dynamics is entirely negligible.

5.2. The Molecular "Size" Problem. Obviously, the cost of calculating the quantum chemical information needed to build the PES increases exponentially with the number of electrons involved, and it is still a prohibitive task for large molecules and heavy atoms. Thus, for instance, while the H + CH₄ benchmark reaction involves five light hydrogen atoms with only eleven electrons, when thirdrow atoms are considered, for instance, H + SiH₄, nineteen electrons are involved, or when larger systems are considered, for instance, H + CCl₄, four heavy chlorine atoms and 75 electrons must be included in the calculations. This represents an enormous computational effort, and that is prohibitive if high-level ab initio calculations are used to obtain chemical accuracy. Obviously, fitting or interpolation approaches, based on grids of 20000-30000 data points or direct dynamics calculations are still unaffordable, although more economical alternatives could be used to calculate the quantum mechanical data, such as the "dual level" technique, where the geometries and vibrational frequencies are calculated at a lower ab initio or DFT level and the energies are

calculated as single points on these geometries at a higher quantum mechanical level. Even so, the computational effort would be enormous.

In these complicated cases with a large number of electrons, our strategy to build the PES, based on a smaller number of ab initio calculations, represents an interesting and practical alternative. Thus, our laboratory has constructed surfaces for several five-body systems, $H + NH_3$ [39, 44], 11 electrons, $F + NH_3$ [45], 19 electrons, and $Cl(^2P) +$ NH₃ [94, 95], 27 electrons; six-body systems, H + SiH₄ [46], 19 electrons, H + GeH₄ [96], 37 electrons, $Cl(^{2}P) + CH_{4}$ [49], 27 electrons, Br(²P) + CH₄ [51], 45 electrons, H + CCl₄ [52, 97], 75 electrons; one of seven bodies, OH + CH₄ [53], 19 electrons. In addition, we have also studied reactions with asymmetrically substituted methane, H + CH₃Cl and Cl + CHClF₂ [98, 99], which represent another challenge in the PES construction for polyatomic systems, because in addition to the aforementioned problems, the possibility of several reaction channels needs to be taken into account. Although the older surfaces were semiempirical, that is, they combined theoretical and experimental information in the fitting procedure due to computational limitations at that time, the newer surfaces, those developed from 2007 onward, are based exclusively on quantum mechanical information: $H + CH_4$ [41], $H + CCl_4$ [97], $H + NH_3$ [39], and $Cl(^2P) +$ NH₃ [95].

It is noteworthy that the functional form has remained almost unchanged, being that of the $H + CH_4$ reaction, adding different modifications following the requirements of the systems under study. Thus, for the five-body systems we removed the dependency on one of the hydrogen atoms of CH_4 , and for the seven-body system, $OH + CH_4$, we added additional Morse and harmonic terms to describe the OH bond and <HOH angle, while for the asymmetric reactions we allowed the four atoms bonded to the carbon atom to vary independently. In addition, we improved the analytical form when building the $CI + NH_3$ surface by allowing the equilibrium N-H distance to vary along the reaction path [95].

5.3. Reactions with More Complicated Topology. The last problem analyzed in this section is that associated with the presence of several maxima and minima in the polyatomic reaction. As was recently noted by Clary [100], "reactions with several maxima and minima in the potential energy surface present the severest challenge to calculating and fitting potential energy surfaces and carrying out quantum dynamics calculations."

Basically, taking into account the topology of the potential energy surface and independently of whether the reaction is exothermic, endothermic, or thermoneutral, the bimolecular reactions can be classified into three broad categories (Figure 11): reactions with a single barrier (Figure 11(a)); barrierless reactions (Figure 11(b)), and reactions with more complicated potentials (e.g., Figures 11(c) and 11(d)). We focus on this last case with polyatomic systems (n > 4). Obviously, the existence of wells in the entry and exit channels is associated with the presence of heavy atoms,

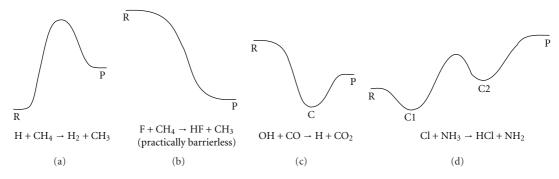


FIGURE 11: Schematic representation of the potential energy along the reaction path for different types of bimolecular reactions. R, P and C denote, respectively, reactants, products, and intermediate complexes. In all the cases, the vertical axis represents the energy and the horizontal axis the reaction coordinate.

especially halogen atoms, which favour the formation of intermediate complexes, either van der Waals or hydrogenbonded complexes. Thus, bimolecular reactions with a complicated topology, as shown in Figures 11(c) or 11(d), also tend to pose several of the problems considered above, that is, the increase of the number of electrons involved and the spin-orbit problem. In addition, the presence of several maxima and minima requires a fine evaluation of the energies, gradients, and Hessians needed for a correct description of the PES. This, obviously, represents a complication in the construction of the PES, and only very few global surfaces have as yet been developed [26, 95].

We finish this section by describing the most complicated surface analyzed by our group [95]: the analytical potential energy surface for the Cl(²P) + NH₃ polyatomic reaction, which presents several wells in the entry and exit channels, with a topology showed in Figure 11(d). Different intermediate complexes were found in the entry and exit channels at the CCSD(T)/cc-pVTZ level, and the intrinsic reaction path was calculated (energies, gradients, and Hessians) starting from the saddle point. With respect to the barrier height, one of the most difficult energy properties of a PES to estimate, different laboratories report electronic structure calculations using different levels (correlation energy and basis sets) [94, 95, 101-103]. Gao et al. [102] constructed the reaction path using the MPWB1K density functional (DFT) method [104], finding a barrier of 5.2 kcal mol⁻¹, and, using different correlation energy levels and basis sets, despite, they reported values in the range $4.8-6.2 \,\mathrm{kcal} \,\mathrm{mol}^{-1}$. Xu and Lin [103] performed a computational study of the mechanisms and kinetics of the reaction. The geometries of the stationary points were optimized using the B3LYP DFT method, and their energies were refined with the modified Gaussian-2 (G2M) theory. They obtained a value of 7.2 kcal mol⁻¹, in contrast with the preceding values. Finally, we [94] obtained a barrier height of 7.6 kcal mol⁻¹ at the CCSD(T)/cc-pVTZ level and of 5.8 kcal mol⁻¹ [95] at a higher level, CCSD(T) = FULL/aug-cc-pVTZ, close to Gao et al.'s result. These results illustrate the dramatic influence of the electronic correlation and basis set on the correct description of the barrier, and it must be borne in mind that small differences in the saddle point produce large deviations in the kinetics and dynamics analysis. To further

complicate the study of this reaction, the spin-orbit coupling must be considered, since the chlorine atom has two low-lying fine structure electronic states, $^2P_{1/2}$ and $^2P_{3/2}$, with a separation of $\varepsilon=882\,\mathrm{cm}^{-1}\approx\!2.5\,\mathrm{kcal\,mol}^{-1}$. As discussed above, the spin-orbit coupling was taken into account in our nonrelativistic calculations in two ways: first, in the electronic partition function of the reactant (29), and second, by adding one-third of the split between the two states, that is, $0.8\,\mathrm{kcal\,mol}^{-1}$, to the barrier height, where we have assumed that the s-o coupling is essentially fully quenched at the saddle point. With this correction, our best estimate of the barrier height was $6.6\,\mathrm{kcal\,mol}^{-1}$.

With all this information, an analytical PES was constructed and kinetics information was obtained using VTST/MT methods [95]. The results agree well with experimental values of the rate coefficients and equilibrium constants, showing that the wells have little influence on the kinetics of the reaction. This is mainly due to the fact that VTST/MT for this reaction, whose reaction path is lower in energy than the products, assumes that tunneling has no effect. Therefore, kinetics is controlled by the properties of a transition state, which is located near the saddle point. In addition, calculations of the recrossing of the transition state that the presence of wells could cause showed that it is very small. Therefore, only the saddle point region determines the reaction probabilities.

An exhaustive dynamics study using QCT and QM methods is currently in progress in our group and should be published soon. From the results it seems that the reaction cross-sections show significant values at very low collision energies using both methodologies. In order to analyze to what extent the presence of wells (especially the well on the reactant side) is responsible for this behaviour, further studies will be carried out with a model surface similar to the Cl + NH₃ from which the wells have been removed. Note that the latter study is possible because of the availability of an analytical surface that can be refitted to remove the wells without significantly modifying other regions of the PES, which is an added value to this kind of analytical PES. These kinds of study can help us to understand the dynamics of such a complicated system and whether transition-state theory, which (as noted above) assumes that only the saddle point region is significant, needs to be challenged.

6. Final Remarks

The construction of potential energy surfaces in polyatomic reactive systems represents a major theoretical challenge, with a very high computational and human time cost. Based on high-level electronic structure calculations, fitting, interpolation, and analytical (defined by functional forms) approaches have been developed and applied in the kinetics and dynamics (classical, quasi-classical, and quantum mechanical) study of these reactions. However, in spite of the enormous progress in the last 20–30 years in theoretical algorithms and computational power, the construction of potential energy surfaces in polyatomic systems has still not reached the level of accuracy achieved for the triatomic systems.

The quality of these surfaces is still an open and debatable question, and even for the benchmark $H + CH_4$ polyatomic reaction, which involves only five light hydrogen atoms and eleven electrons, small differences are found depending on the PES construction and the dynamics method. Unfortunately, the problems will increase for other important chemical systems, where some effects are present such as spin-orbit coupling, increase in the number of electrons and molecular size, or potentials with more complicated topology. In these cases, the kinetics and dynamics results will be even more strongly dependent on the quality of the PES. In the last few decades, there has been much theoretical effort on the part of various laboratories, but there is still much to do in this research field.

Throughout this paper, the emphasis has been put on the strategy developed by our group which has constructed about 15 surfaces for polyatomic systems of five, six and seven bodies. These are freely available for download from the POTLIB websites, http://comp.chem.umn.edu/POTLIB/or http://users.ipfw.edu/DUCHOVIC/POTLIB2001/, or can be requested from the authors.

The analytical surfaces developed in our group are based on a basic functional form with slight modifications to suit it to each of the systems studied. In this sense, they are very specialized force fields, with mathematical functions that allow further improvements to be introduced. For example, adding terms to describe anharmonicity, modemode coupling, or an improved dependence of the constants of the fit on the reaction coordinate are possibilities, which can improve the functional form.

The inclusion of additional reaction channels, such as the exchange reactions in methane or ammonia, is another pending matter in work on our surfaces. This would open up the possibility of analyzing competitive channels and could lead to a better understanding of the behaviour of complex reactions.

An additional advantage of this approach is the negligible computational cost of the evaluation of the potential energy surface and its derivatives, which is a very desirable feature when one wants to apply expensive QM methods for the study of these reactions. Undoubtedly, with the evolution of computer resources, eventually a point will be reached when direct dynamics calculations using high *ab initio* levels will be feasible. However, until then, the possibility of having

an analytical function that can describe the potential energy with reasonable accuracy is the fastest option. In recent years ad hoc surfaces have been constructed which only reproduce a single kinetics or dynamics property but do not provide a complete description of the reaction system. However, the aim of our work is to build a PES that reproduces at least qualitatively all the kinetics and dynamics features of the reactive system. Obviously a quantitative description of all kinetics and dynamics properties will be the final goal, and with this target in mind in our group we have adopted a flexible functional form that can be easily improved and adapted to other similar systems.

Acknowledgments

This work has been partially supported in recent years by the Junta de Extremadura, Spain, and Fondo Social Europeo (Projects nos. 2PR04A001, PRI07A009, and IB10001). One of the authors (M.Monge-Palacios) thanks Junta de Extremadura (Spain) for a scholarship.

References

- [1] M. Born and R. Oppenheimer, "Zur quantentheorie der molekeln," *Annals of Physics*, vol. 84, pp. 457–484, 1927.
- [2] C. N. Ramachandran, D. De Fazio, S. Cavalli, F. Tarantelli, and V. Aquilanti, "Revisiting the potential energy surface for the He + H₂⁺ → HeH⁺ + H reaction at the full configuration interaction level," *Chemical Physics Letters*, vol. 469, no. 1–3, pp. 26–30, 2009.
- [3] F. George and S. Kumar, "Ab initio ground and the first excited adiabatic and quasidiabatic potential energy surfaces of H⁺ + CO system," *Chemical Physics*, vol. 373, no. 3, pp. 211–218, 2010.
- [4] T. Tanaka and T. Takayanagi, "Quantum reactive scattering calculations of H + F₂ and Mu + F₂ reactions on a new *ab initio* potential energy surface," *Chemical Physics Letters*, vol. 496, no. 4–6, pp. 248–253, 2010.
- [5] W. Skomorowski, F. Pawlowski, T. Korona, R. Moszynski, P. S. Zuchowski, and J. M. Hutson, "Interaction between LiH molecule and Li atom from the state-of-the-art electronic structure calculations," *Journal of Chemical Physics*, vol. 134, p. 114109, 2011.
- [6] B. Jiang, Ch. Xie, and D. Xie, "New ab iniito potential energy surface for BrH₂ and rate constants for the H + HBr → H₂ + Br abstraction reaction," *Journal of Chemical Physics*, vol. 134, p. 114301, 2011.
- [7] M. Karplus, R. N. Porter, and R. D. Sharma, "Exchange reactions with activation energy. I. Simple barrier potential for (H, H₂)," *Journal of Chemical Physics*, vol. 43, no. 9, pp. 3259–3287, 1965.
- [8] D.J. Kouri, Y. Sun et al., "New time-dependent and time-independent computational methods for molecular collisions," in *Mathematical Frontiers in Computational Chemical Physics*, D. G. Truhlar, Ed., pp. 207–244, Springer, New York, NY, USA, 1988.
- [9] A. Fernandez-Ramos, J. A. Miller, S. J. Klippenstein, and D. G. Truhlar, "Modeling the kinetics of bimolecular reactions," *Chemical Reviews*, vol. 106, pp. 4518–4584, 2006.
- [10] T. V. Albu, J. Espinosa-García, and D. G. Truhlar, "Computational chemistry of polyatomic reaction kinetics and

- dynamics: the quest for an accurate CH_5 potential energy surface," *Chemical Reviews*, vol. 107, no. 11, pp. 5101–5132, 2007.
- [11] W. L. Hase, K. Song, and M. S. Gordon, "Direct dynamics simulations," *Computing in Science and Engineering*, vol. 5, no. 4, pp. 36–44, 2003.
- [12] J. Liu, K. Song, W. L. Hase, and S. L. Anderson, "Direct dynamics trajectory study of the reaction of formaldehyde cation with D₂: vibrational and zero-point energy effects on quasiclassical trajectories," *Journal of Physical Chemistry A*, vol. 109, no. 50, pp. 11376–11384, 2005.
- [13] T.-S. Ho and H. Rabitz, "A general method for constructing multidimensional molecular potential energy surfaces from ab initio calculations," *Journal of Chemical Physics*, vol. 104, no. 7, pp. 2584–2597, 1996.
- [14] M. A. Collins, "Molecular potential-energy surfaces for chemical reaction dynamics," *Theoretical Chemistry Accounts*, vol. 108, no. 6, pp. 313–324, 2002.
- [15] T.-S. Ho and H. Rabitz, "Reproducing kernel Hilbert space interpolation methods as a paradigm of high dimensional model representations: application to multidimensional potential energy surface construction," *Journal of Chemical Physics*, vol. 119, no. 13, pp. 6433–6442, 2003.
- [16] J. Ischtwan and M. A. Collins, "Molecular potential energy surfaces by interpolation," *Journal of Chemical Physics*, vol. 100, no. 11, pp. 8080–8088, 1994.
- [17] M. A. Addicoat and M. A. Collins, "Potential energy surfaces: the forces of chemistry," in *Tutorials in Molecular Reaction Dynamics*, M. Brouard and C. Vallance, Eds., p. 28, RSC Publishing, Cambridge, UK, 2010.
- [18] Y. Zhou, B. Fu, C. Wang, M. A. Collins, and D. H. Zhang, "Ab initio potential energy surface and quantum dynamics for the $H+CH_4 \rightarrow H_2+CH_3$," *Journal of Chemical Physics*, vol. 134, pp. 64323–64330, 2011.
- [19] J. N. Murrell, S. Carter, S. C. Farantos, P. Huxley, and A. J. C. Varandas, *Molecular Potential Energy Functions*, Wiley, Chistester, UK, 1984.
- [20] G. C. Schatz, "The analytical representation of electronic potential-energy surfaces," *Reviews of Modern Physics*, vol. 61, no. 3, pp. 669–688, 1989.
- [21] J. M. Bowman and G. C. Schatz, "Theoretical studies of polyatomic bimolecular reaction dynamics," *Annual Review of Physical Chemistry*, vol. 46, no. 1, pp. 169–195, 1995.
- [22] K. Sorbie and J. N. Murrell, "Theoretical study of the $O(^{1}D)+H_{2}(^{1}S_{g})$ reactive quenching process," *Molecular Physics*, vol. 31, pp. 905–920, 1976.
- [23] A. J. C. Varandas, "Four-atom bimolecular reactions with relevance in environmental chemistry," *International Reviews in Physical Chemistry*, vol. 19, no. 2, pp. 199–245, 2000.
- [24] A. Brown, B. J. Braams, K. Christoffel, Z. Jin, and J. M. Bowman, "Classical and quasiclassical spectral analysis of CH₅⁺ using an ab initio potential energy surface," *Journal of Chemical Physics*, vol. 119, no. 17, pp. 8790–8793, 2003.
- [25] Z. Jin, B. J. Braams, and J. M. Bowman, "An ab initio based global potential energy surface describing CH₃⁺ → CH₃⁺ + H₅," *Journal of Physical Chemistry A*, vol. 110, no. 4, pp. 1569– 1574, 2006.
- [26] B. J. Braams and J. M. Bowman, "Permutationally invariant potential energy surfaces in high dimensionality," *International Reviews in Physical Chemistry*, vol. 28, no. 4, pp. 577– 606, 2009.
- [27] J. M. Bowman, G. Czako, and B. Fu, "High-dimensional ab initio potential energy surfaces for reaction dynamics

- calculations," *Physical Chemistry Chemical Physics*, vol. 13, no. 18, pp. 8094–8111, 2011.
- [28] A. B. McCoy, B. J. Braams, A. Brown, X. Huang, Z. Jin, and J. M. Bowman, "Ab initio diffusion monte carlo calculations of the quantum behavior of CH₅⁺ in full dimensionality," *Journal of Physical Chemistry A*, vol. 108, no. 23, pp. 4991–4994, 2004.
- [29] T. Valencich and D. L. Bunker, "Energy-dependent cross sections for the tritium-methane hot atom reactions," *Chemical Physics Letters*, vol. 20, no. 1, pp. 50–52, 1973.
- [30] L. M. Raff, "Theoretical investigations of the reaction dynamics of polyatomic systems: chemistry of the hot atom (T* + CH₄) and (T* + CD₄) systems," *Journal of Chemical Physics*, pp. 2220–2244, 1970.
- [31] R. Steckler, K. J. Dykema, F. B. Brown, G. C. Hancock, D. G. Truhlar, and T. Valencich, "A comparative study of potential energy surfaces for CH₃ + H₂ → CH₄ + H," *Journal of Chemical Physics*, vol. 87, no. 12, pp. 7024–7035, 1987.
- [32] T. Joseph, R. Steckler, and D. G. Truhlar, "A new potential energy surface for the CH₃ + H₂ → CH₄ + H reaction: calibration and calculations of rate constants and kinetic isotope effects by variational transition state theory and semiclassical tunneling calculations," *Journal of Chemical Physics*, vol. 87, no. 12, pp. 7036–7049, 1987.
- [33] M. J. T. Jordan and R. G. Gilbert, "Classical trajectory studies of the reaction CH₄ +H → CH₃ + H₂," *Journal of Chemical Physics*, vol. 102, no. 14, pp. 5669–5682, 1995.
- [34] J. Espinosa-García and J. C. Corchado, "Global surfaces and reaction-path potentials. Applications of variational transition-state theory," *Recent Research Development in Physical Chemistry*, vol. 1, pp. 165–192, 1997.
- [35] J. Espinosa-Garcia, "Analysis of economical strategies for the construction of potential energy surfaces," *Trends in Physical Chemistry*, vol. 8, pp. 49–73, 2000.
- [36] A. Chakraborty, Y. Zhao, H. Lin, and D. G. Truhlar, "Combined valence bond-molecular mechanics potentialenergy surface and direct dynamics study of rate constants and kinetic isotope effects for the H + C₂H₆ reaction," *Journal* of Chemical Physics, vol. 124, no. 4, pp. 44315–44328, 2006.
- [37] R. J. Duchovic, W. L. Hase, and H. B. Schlegel, "Analytic function for the H + CH₃

 CH₄ potential energy surface,"

 Journal of Physical Chemistry, vol. 88, no. 7, pp. 1339–1347, 1984.
- [38] M. Yang and J. C. Corchado, "Seven-dimensional quantum dynamics study of the H + NH₃ → H₂ + NH₂ reaction," *Journal of Chemical Physics*, vol. 126, no. 21, pp. 214312–214321, 2007.
- [39] J. Espinosa-Garcia and J. C. Corchado, "Analytical potential energy surface and kinetics of the NH₃ + H → NH2 + H₂ hydrogen abstraction and the ammonia inversion reactions," *Journal of Physical Chemistry A*, vol. 114, no. 12, pp. 4455–4463, 2010.
- [40] S. T. Banks and D. C. Clary, "Reduced dimensionality quantum dynamics of Cl + CH₄ → HCl + CH₃ on an ab initio potential," *Physical Chemistry Chemical Physics*, vol. 9, no. 8, pp. 933–943, 2007.
- [41] J. C. Corchado, J. L. Bravo, and J. Espinosa-Garcia, "The hydrogen abstraction reaction H + CH₄. I. New analytical potential energy surface based on fitting to ab initio calculations," *Journal of Chemical Physics*, vol. 130, no. 18, pp. 184314–184323, 2009.
- [42] C. Rángel, M. Navarrete, and J. Espinosa-García, "Potential energy surface for the F(²P_{3/2}, ²P_{1/2}) + CH₄ hydrogen abstraction reaction. Kinetics and dynamics study," *Journal of Physical Chemistry A*, vol. 109, no. 7, pp. 1441–1448, 2005.

- [43] J. Espinosa-García, "New analytical potential energy surface for the CH₄ + H hydrogen abstraction reaction: thermal rate constants and kinetic isotope effects," *Journal of Chemical Physics*, vol. 116, no. 24, pp. 10664–10673, 2002.
- [44] J. C. Corchado and J. Espinosa-García, "Analytical potential energy surface for the NH₃ + H → NH₂ + H₂ reaction: application of variational transition-state theory and analysis of the equilibrium constants and kinetic isotope effects using curvilinear and rectilinear coordinates," *Journal of Chemical Physics*, vol. 106, no. 10, pp. 4013–4021, 1997.
- [45] J. Espinosa-García and J. C. Corchado, "Analytical surface for the reaction with no saddle-point NH₃ + F → NH₂ + FH. Application of variational transition state theory," *Journal of Physical Chemistry A*, vol. 101, no. 40, pp. 7336–7344, 1997.
- [46] J. Espinosa-García, J. Sansón, and J. C. Corchado, "The SiH₄ + H → SiH₃ + H₂ reaction: potential energy surface, rate constants, and kinetic isotope effects," *Journal of Chemi*cal Physics, vol. 109, no. 2, pp. 466–473, 1998.
- [47] J. Espinosa-García and J. C. García-Bernáldez, "Analytical potential energy surface for the CH₄ + O(³P) → CH₃ + OH reaction. Thermal rate constants and kinetic isotope effects," *Physical Chemistry Chemical Physics*, vol. 2, no. 10, pp. 2345–2351, 2000.
- [48] J. Espinosa-García, J. L. Bravo, and C. Rangel, "New analytical potential energy surface for the F(²P) + CH₄ hydrogen abstraction reaction: kinetics and dynamics," *Journal of Physical Chemistry A*, vol. 111, no. 14, pp. 2761–2771, 2007.
- [49] J. C. Corchado, D. G. Truhlar, and J. Espinosa-García, "Potential energy surface, thermal, and state-selected rate coefficients, and kinetic isotope effects for Cl + CH₄ → HCl + CH₃," *Journal of Chemical Physics*, vol. 112, no. 21, pp. 9375–9389, 2000.
- [50] C. Rangel, M. Navarrete, J. C. Corchado, and J. Espinosa-García, "Potential energy surface, kinetics, and dynamics study of the Cl + CH₄ → HCl + CH₃ reaction," *Journal of Chemical Physics*, vol. 124, no. 12, pp. 124306–124324, 2006.
- [51] J. Espinosa-García, "Potential energy surface for the CH₃ + HBr → CH₄ + Br hydrogen abstraction reaction: thermal and state-selected rate constants, and kinetic isotope effects," *Journal of Chemical Physics*, vol. 117, no. 5, pp. 2076–2086, 2002
- [52] C. Rangel and J. Espinosa-García, "Potential energy surface for the CCl₄ + H → CCl₃ + ClH reaction: kinetics and dynamics study," *Journal of Chemical Physics*, vol. 122, no. 13, pp. 134315–134319, 2005.
- [53] J. Espinosa-García and J. C. Corchado, "Potential energy surface for a seven-atom reaction. Thermal rate constants and kinetic isotope effects for CH₄ + OH," *Journal of Chemical Physics*, vol. 112, no. 13, pp. 5731–5739, 2000.
- [54] R.J. Duchovic, Y.L. Volobuev, G.C. Lynch et al., "POLTLIB," 2001.
- [55] X. Zhang, B. J. Braams, and J. M. Bowman, "An ab initio potential surface describing abstraction and exchange for H + CH₄," *Journal of Chemical Physics*, vol. 124, no. 2, pp. 021104– 021108, 2006.
- [56] Z. Xie, J. M. Bowman, and X. Zhang, "Quasiclassical trajectory study of the reaction $H + CH_4$ ($\nu_3 = 0.1$) $\rightarrow CH_3 + H_2$ using a new ab initio potential energy surface," *Journal of Chemical Physics*, vol. 125, no. 13, pp. 133120–133127, 2006.
- [57] T. Wu, H. J. Werner, and U. Manthe, "Accurate potential energy surface and quantum reaction rate calculations for the $\rm H+CH_4\rightarrow H_2+CH_3$ reaction," *Journal of Chemical Physics*, vol. 124, no. 16, pp. 164307–164318, 2006.

- [58] F. Huarte-Larrañaga and U. Manthe, "Quantum dynamics of the CH₄ + H → CH₃ + H₂ reaction: full-dimensional and reduced dimensionality rate constant calculations," *Journal of Physical Chemistry A*, vol. 105, no. 12, pp. 2522–2529, 2001.
- [59] G. Schiffel, U. Manthe, and G. Nyman, "Full-dimensional quantum reaction rate calculations for H + CH₄ → H₂ + CH₃ on a recent potential energy surface," *Journal of Physical Chemistry A*, vol. 114, no. 36, pp. 9617–9622, 2010.
- [60] J. W. Sutherland, M. C. Su, and J. V. Michael, "Rate constants for H + CH₄, CH₃ + H₂, and CH₄ dissociation at high temperature," *International Journal of Chemical Kinetics*, vol. 33, no. 11, pp. 669–684, 2001.
- [61] G. J. Germann, Y. D. Huh, and J. J. Valentini, "State-to-state dynamics of atom + polyatom abstraction reactions. II. The H + CD₄ → HD(v',J') + CD₃ reaction," *Journal of Chemical Physics*, vol. 96, no. 8, pp. 1957–1966, 1992.
- [62] W. Hu, G. Lendvay, D. Troya et al., "H + CD4 abstraction reaction dynamics: product energy partitioning," *Journal of Physical Chemistry A*, vol. 110, no. 9, pp. 3017–3027, 2006.
- [63] J. P. Camden, H. A. Bechtel, and R. N. Zare, "Dynamics of the simplest reaction of a carbon atom in a tetrahedral environment," *Angewandte Chemie*, vol. 42, no. 42, pp. 5227–5230, 2003.
- [64] J. P. Camden, H. A. Bechtel, D. J. A. Brown et al., "A reinterpretation of the mechanism of the simplest reaction at an sp 3-hybridized carbon atom: H + CD₄ → CD₃ + HD," *Journal of the American Chemical Society*, vol. 127, no. 34, pp. 11898–11899, 2005.
- [65] J. P. Camden, W. Hu, H. A. Bechtel et al., "H + CD₄ abstraction reaction dynamics: excitation function and angular distributions," *Journal of Physical Chemistry A*, vol. 110, no. 2, pp. 677–686, 2006.
- [66] W. Zhang, Y. Zhou, G. Wu et al., "Depression of reactivity by the collision energy in the single barrier H + CD₄ → HD + CD₃ reaction," Proceedings of the National Academy of Sciences of the United States of America, vol. 107, no. 29, pp. 12782–12785, 2010.
- [67] C. Rangel, J. Sansón, J. C. Corchado, J. Espinosa-Garcia, and G. Nyman, "Product angular distribution for the H + CD₄ → HD + CD₃ reaction," *Journal of Physical Chemistry* A, vol. 110, no. 37, pp. 10715–10719, 2006.
- [68] J. Espinosa-García, G. Nyman, and J. C. Corchado, "The hydrogen abstraction reaction H+ CH₄. II. Theoretical investigation of the kinetics and dynamics," *Journal of Chemical Physics*, vol. 130, no. 18, pp. 184315–184323, 2009.
- [69] J. P. Camden, H. A. Bechtel, D. J. A. Brown, and R. N. Zare, "Effects of C-H stretch excitation on the H + CH₄ reaction," *Journal of Chemical Physics*, vol. 123, no. 13, pp. 134301– 134309, 2005.
- [70] C. Rangel, J. C. Corchado, and J. Espinosa-García, "Quasiclassical trajectory calculations analyzing the reactivity and dynamics of asymmetric stretch mode excitations of methane in the H + CH₄ reaction," *Journal of Physical Chemistry A*, vol. 110, no. 35, pp. 10375–10383, 2006.
- [71] C. H. Townes and A. L. Schawlow, Microwave Spectroscopy, McGraw-Hill, New York, NY, USA, 1955.
- [72] G. E. Moyano and M. A. Collins, "Interpolated potential energy surface for abstraction and exchange reactions of NH₃ + H and deuterated analogues," *Theoretical Chemistry Accounts*, vol. 113, no. 4, pp. 225–232, 2005.
- [73] J. Espinosa-García, "Capability of LEPS surfaces to describe the kinetics and dynamics of non-collinear reactions," *Jour-nal of Physical Chemistry A*, vol. 105, no. 1, pp. 134–139, 2001.

- [74] J. Espinosa-García, "Capability of LEP-type surfaces to describe noncollinear reactions. 2. Polyatomic systems," *Journal of Physical Chemistry A*, vol. 105, no. 38, pp. 8748–8755, 2001.
- [75] B. C. Garrett and D. G. Truhlar, "A least-action variational method for calculating multidimensional tunneling probabilities for chemical reactions," *Journal of Chemical Physics*, vol. 79, no. 10, pp. 4931–4938, 1983.
- [76] R. Meana-Pañeda, D. G. Truhlar, and A. Fernández-Ramos, "Least-action tunnelling transmission coefficient for polyatomic reactions," *Journal of Chemical Theory and Computation*, vol. 6, no. 1, pp. 6–17, 2010.
- [77] T. Ko, P. Marshall, and A. Fontijn, "Rate coefficients for the H + NH₃ reaction over a wide temperature range," *Journal of Physical Chemistry*, vol. 94, no. 4, pp. 1401–1404, 1990.
- [78] J. Espinosa-García and J. C. Corchado, "Quasi-classical trajectory calculations of the hydrogen abstraction reaction H + NH₃," *Journal of Physical Chemistry A*, vol. 114, no. 21, pp. 6194–6200, 2010.
- [79] A. M. Hapern, B. R. Ramachandran, and E. D. Glendening, "The inversion potential of ammonia: an intrinsic reaction coordinate calculation for student investigation," *Journal of Chemical Education*, vol. 84, no. 6, pp. 1067–1072, 2007.
- [80] V. Špirko, "Vibrational anharmonicity and the inversion potential function of NH₃," *Journal of Molecular Spectroscopy*, vol. 101, no. 1, pp. 30–47, 1983.
- [81] V. M. Devi, P. P. Das, K. N. Rao, S. Urban, D. Papouseck, and V. Spirko, "The diode laser spectrum of the V_2 band of 14 ND₃ and 15 ND₃," *Journal of Molecular Spectroscopy*, vol. 88, pp. 293–299, 1981.
- [82] M. H. Alexander, D. E. Manolopoulos, and H. J. Werner, "An investigation of the F + H₂ reaction based on a full ab initio description of the open-shell character of the F(²P) atom," *Journal of Chemical Physics*, vol. 113, no. 24, pp. 11084–11100, 2000.
- [83] G. Capecchi and H. J. Werner, "Ab initio calculations of coupled potential energy surfaces for the Cl(²P_{3/2}, ²P_{1/2}) + H₂ reaction," *Physical Chemistry Chemical Physics*, vol. 6, no. 21, pp. 4975–4983, 2004.
- [84] M. H. Alexander, H. J. Werner, and D. E. Manolopoulos, "Spin-orbit effects in the reaction of F(²P) with H₂," *Journal of Chemical Physics*, vol. 109, no. 14, pp. 5710–5713, 1998.
- [85] S. H. Lee, "State-specific excitation function for $Cl(^2P) + H_2$ (v = 0,j): effects of spin-orbit and rotational states," *Journal of Chemical Physics*, vol. 110, no. 17, pp. 8229–8232, 1999.
- [86] S.-H. Lee and K. Liu, "Exploring the spin-orbit reactivity in the simplest chlorine atom reaction," *Journal of Chemical Physics*, vol. 111, no. 14, pp. 6253–6259, 1999.
- [87] F. Dong, S. H. Lee, and K. Liu, "Direct determination of the spin-orbit reactivity in CI(²P_{3/2}, ²P_{1/2}) + H₂/D₂/HD reactions," *Journal of Chemical Physics*, vol. 115, no. 3, pp. 1197–1204, 2001.
- [88] M. H. Alexander, G. Capecchi, and H. J. Werner, "Theoretical study of the validity of the Born-Oppenheimer approximation in the CL + $H_2 \rightarrow HCL + H$ reaction," *Science*, vol. 296, no. 5568, pp. 715–718, 2002.
- [89] N. Balucani, D. Skouteris, L. Cartechini et al., "Differential cross sections from quantum calculations on coupled ab initio potential energy surfaces and scattering experiments for Cl(²P) + H₂ reactions," *Physical Review Letters*, vol. 91, no. 1, pp. 013201–013204, 2003.
- [90] M. H. Alexander, G. Capecchi, and H.-J. Werner, "Details and consequences of the nonadiabatic coupling in the Cl(²P) + H² reaction," *Faraday Discussions*, vol. 127, pp. 59–72, 2004.

- [91] E. Garand, J. Zhou, D. E. Manolopoulos, M. H. Alexander, and D. M. Neumark, "Nonadiabatic interactions in the Cl + H₂ reaction probed by CIH₂ and CID₂ photoelectron imaging," *Science*, vol. 319, no. 5859, pp. 72–75, 2008.
- [92] D. M. Neumark, "Slow electron velocity-map imaging of negative ions: applications to spectroscopy and dynamics," *Journal of Physical Chemistry A*, vol. 112, no. 51, pp. 13287– 13301, 2008.
- [93] X. Wang, W. Dong, C. Xiao et al., "The extent of non-born-oppenheimer coupling in the reaction of Cl(²P) with *para*-H₂," *Science*, vol. 322, no. 5901, pp. 573–576, 2008.
- [94] M. Monge-Palacios and J. Espinosa-Garcia, "Reaction-path dynamics calculations of the Cl + NH₃ hydrogen abstraction reaction: the role of the intermediate complexes," *Journal of Physical Chemistry A*, vol. 114, no. 12, pp. 4418–4426, 2010.
- [95] M. Monge-Palacios, C. Rangel, J. C. Corchado, and J. Espinosa-Garcia, "Analytical potential energy surface for the reaction with intermediate complexes NH₃ + Cl → NH₂ + HCl: application to the kinetics study," *International Journal of Quantum Chemistry*. In press.
- [96] J. Espinosa-García, "Analytical potential energy surface for the GeH₄ + H → GeH₃ + H₂ reaction: thermal and vibrational-state selected rate constants and kinetic isotope effects," *Journal of Chemical Physics*, vol. 111, no. 20, pp. 9330–9336, 1999.
- [97] J. Espinosa-García, C. Rangel, M. Monge-Palacios, and J. C. Corchado, "Kinetics and dynamics study of the H + CCl₄ → HCl(v', j')+ CCl₃ reaction," *Theoretical Chemistry Accounts*, vol. 128, pp. 743–755, 2010.
- [98] C. Rangel and J. Espinosa-García, "Analytical potential energy surface describing abstraction reactions in asymmetrically substituted polyatomic systems of type CX₃Y + A → products," *Journal of Physical Chemistry A*, vol. 110, no. 2, pp. 537–547, 2006.
- [99] C. Rangel and J. Espinosa-García, "Potential energy surface for asymmetrically substituted reactions of type CWXYZ + A. kinetics study," *Journal of Physical Chemistry A*, vol. 111, no. 23, pp. 5057–5062, 2007.
- [100] D. C. Clary, "Theoretical studies on bimolecular reaction dynamics," *Proceedings of the National Academy of Sciences* of the United States of America, vol. 105, no. 35, pp. 12649– 12653, 2008.
- [101] S. Kondo, K. Tokuhashi, A. Takahashi, and M. Kaise, "Ab initio study of reactions between halogen atoms and various fuel molecules by Gaussian-2 theory," *Journal of Hazardous Materials*, vol. 79, no. 1-2, pp. 77–86, 2000.
- [102] Y. Gao, I. M. Alecu, P.-C. Hsieh, B. P. Morgan, P. Marshall, and L. N. Krasnoperov, "Thermochemistry is not a lower bound to the activation energy of endothermic reactions: a kinetic study of the gas-phase reaction of atomi-chlorine with ammonia," *Journal of Physical Chemistry A*, vol. 110, no. 21, pp. 6844–6850, 2006.
- [103] Z. F. Xu and M. C. Lin, "Computational studies on the kinetics and mechanisms for NH₃ reactions with ClOx (x = 0-4) radicals," *Journal of Physical Chemistry A*, vol. 111, no. 4, pp. 584–590, 2007.
- [104] Y. Zhao and D. G. Truhlar, "Hybrid meta density functional theory methods for thermochemistry, thermochemical kinetics, and noncovalent interactions: the MPW1B95 and MPWB1K models and comparative assessments for hydrogen bonding and van der Waals interactions," *Journal of Physical Chemistry A*, vol. 108, no. 33, pp. 6908–6918, 2004.